Nanowires for thermoelectric energy conversion

Nanowires for thermoelectric energy conversion

Proefschrift

ter verkrijging van de graad van doctor aan de Technische Universiteit Eindhoven, op gezag van de rector magnificus prof.dr.ir. F.P.T. Baaijens, voor een commissie aangewezen door het College voor Promoties, in het openbaar te verdedigen op dinsdag 10 maart 2020 om 16:00 uur

door

Daniel Vakulov

geboren te Taganrog, Rusland

Dit proefschrift is goedgekeurd door de promotoren en de samenstelling van de promotiecommissie is als volgt:

voorzitter:	prof. dr. ir. G.M.W. Kroesen
1e promotor:	prof. dr. E.P.A.M. Bakkers
copromotor:	prof. dr. P.A. Bobbert
leden:	prof. dr. T. Schäpers (Rheinisch-Westfälische Technische Hochschule)
	prof. dr. M.A. Loi (Rijksuniversiteit Groningen)
	prof. dr. E.H. Brück (Technische Universiteit Delft)
	prof. dr. I. Zardo (Universität Basel)
	dr. J.E.M. Haverkort

Het onderzoek of ontwerp dat in dit proefschrift wordt beschreven is uitgevoerd in overeenstemming met de TU/e Gedragscode Wetenschapsbeoefening.

PhD thesis, Eindhoven University of Technology

Daniel Vakulov, March 2019

Cover design by Mr. Sandman ®

Printed by: Proefschriftmaken || www.proefschriftmaken.nl

A catalogue record is available from the Eindhoven University of Technology Library

ISBN: 978-90-386-4999-3

The research described in this thesis was funded by the European Research Council under grant number ERC HELENA 617256 (applicant: Erik P.A.M. Bakkers)

Contents

Chapter 1. Introduction.

1.1. Impact of the energy generation on climate change.

Climate change is a major global challenge affecting the planet Earth and its inhabitants[1]. The current warming trend must be considered because most of it is the result of human activity and proceeding at a rate that is unprecedented over decades[2]. Generally, energy demand is increasing globally, resulting in the escalation of greenhouse gas emissions. The aforementioned trend will be continuing, driven by a rising population and economic growth[3]. Recent studies predict that if the world keeps consuming fossil fuel, average surface temperatures will have risen between 2°C and 6°C by the end of the 21st-century[4], resulting in the melting of ice in the arctic regions. It has been estimated that if all the ice in the world is molten due to climate change, it will result in a drastic rise of the sea level[5], as shown in Figure 1.1. It looks like we might have to look for another place to call home if the sea levels would rise tomorrow. Climate change, thus, presents increasing challenges for renewable energy generation.

Figure 1.1. – The predicted rise of the world sea level (of approximately 65 meters) due to climate change. Adapted from reference 5.

In order to prevent such irreversible consequences, certain steps toward sustainable energy production must be taken. To illustrate this challenge, the energy generation and consumption in the USA are shown in Figure 1.2.

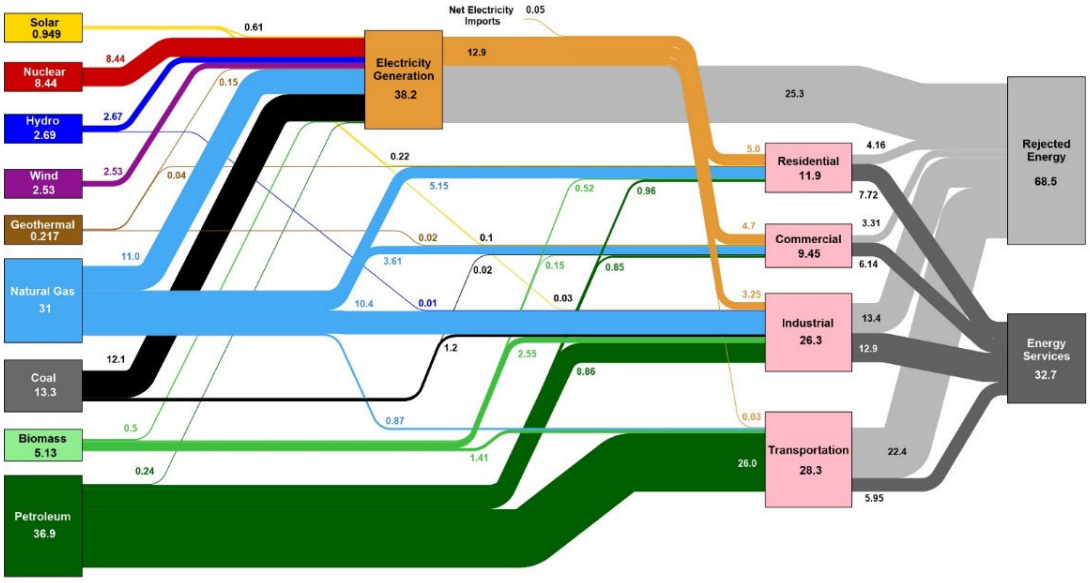

Figure 1.2. – The energy flow chart released by Lawrence Livermore National Laboratory details the sources and consumption of energy (in percentage) in the USA, and how much waste exists (2018). Adapted from reference 6.

Based on the diagram, it can be concluded that petroleum (36.9 % of the total produced energy) remains the primary source of energy for transportation (26.0 %) and industrial use (8.86 %). Surprisingly, 'old' and 'dirty' coal so far contributes up to 12.1 % to the electricity generation. However, cleaner but still exhaustible energy source like natural gas (31.0 % of the total produced energy) is extensively used for electricity generation (11.0 %), as well as for industrial (10.4 %) and residential purposes (11.9 %). Renewable sources generate around 6.4% of the total produced energy. Hydro and wind energy sources create about 2.6 % and 2.5 % of the energy, respectively, while the contribution of solar energy giving almost 1% of the total energy. Despite the positive contribution of renewable energy sources, it can be concluded that nearly 70% of the produced energy is rejected in the form of heat[6]. Most of the rejected energy is coming from electrical generation and transportation. Even if only a relatively small percentage of the waste heat can be converted into electricity, it will have a beneficial effect on climate change and slow down the rise of the surface temperature. Thus, besides using renewable energy sources, such as wind, geothermal, hydro, and solar power, it is essential to gain back rejected energy via the concept of energy harvesting. Recently, many efforts have been made in developing large-scale energy harvesting systems like solar power, windmills, and hydroelectric plants. Here we are focusing on the small-scale energy harvesters that can be used in autonomous devices and which are expected to become core components of zero-energy systems.

1.2. Energy harvesting for autonomous devices and systems.

Energy harvesting is a vital focus of the 21st century due to the increased demand for energy. Typically, energy harvesting is assigned to the accumulation of energy from

the environment; this energy would otherwise be lost. Commonly, motion (vibrations, wind, etc.), light (photovoltaic), heat, and chemical energy (biodiesel, fuel cells, etc.) can be used as energy harvesting sources, as shown in Figure 1.3. There are physical effects involved in energy transitions. For instance, in the case of motion, three mechanisms are available, particularly electromagnetic, piezoelectric, and electrostatic. Electromagnetic harvesters transform the energy from electromagnetic fields to electrical[7]. Piezoelectric harvesters convert the kinetic energy in the form of vibrations into electricity[8]. The electrostatic potential energy that results from Coulomb forces can be converted into electrical energy using electrostatic harvesters. The typical output of these generators is in the range of a few μW[9–11]. Thermal harvesters use the thermoelectric effect (Seebeck effect), and light harvesters employ the photovoltaic effect. The efficiency of commercially available large-scale solar panels is up to 22.8 % [12].

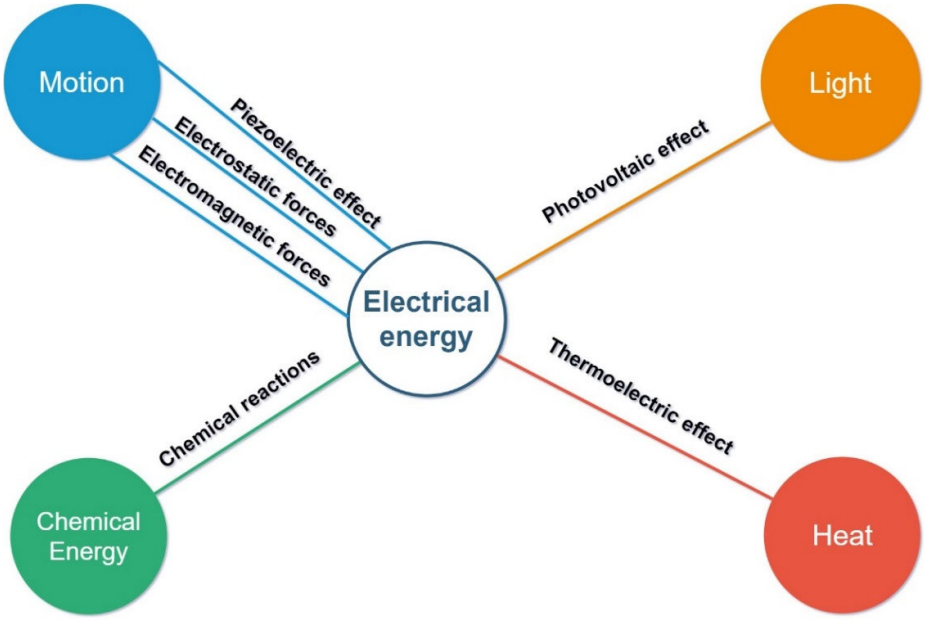

Figure 1.3. – Categories of energy harvesting sources.

Nowadays, large scale harvesting power plants (solar cell farms and windmills) are widespread since they can provide a significant amount of electrical power[12]. In contrast, the energy output of small-scale harvesters (electromagnetic, electrostatic, thermoelectric harvesters) is relatively low (in the range from nanowatts to hundreds of milliwatts); nevertheless, these harvesters are promising for autonomous devices and zero-energy systems. Such systems will have a positive impact on sustainable energy[13]. In this thesis, we focus on thermoelectric energy generators, which can find an application on the Internet of Things (IoT) devices and zero-energy systems[14].

1.3. Thermoelectricity and thermoelectric efficiency.

In thermoelectric energy harvesting, the Seebeck effect is used into convert heat to electricity[15]. Currently, the efficiency of commercially available thermoelectric

generators (TEGs) is up to 10%[16]. It is necessary to increase the thermoelectric figure of merit ZT to make an efficient and modest thermoelectric generator. It has been predicted that the use of low-dimensional structures could help to increase efficiency. These aspects are addressed in the next section.

The thermoelectric efficiency of a material is defined as[17]:

$$Z = S^2 \cdot \frac{\sigma \cdot A}{l} \cdot \frac{l}{\kappa \cdot A} = S^2 \frac{\sigma}{\kappa}, \tag{1.1}$$

where σ is the electric conductivity, A and l are geometrical parameters (cross-sectional area and length of wire, respectively), S the Seebeck coefficient, and κ the thermal conductivity. The SI unit of Z is [K^{-1}], so it is often multiplied by the temperature T to form the dimensionless number ZT, which is referred to as the figure of merit (see Eq. (1.2)).

$$ZT = S^2 \frac{\sigma}{\kappa} \cdot T \,. \tag{1.2}$$

It can be concluded from Eq. (1.2) that the efficiency depends on the intrinsic properties of materials used in thermoelectric devices. To maximize the electrical power output, both electrical losses (Joule heating) and thermal losses must be minimized. Therefore, a thermoelectric material should feature a high electrical conductivity σ, but low thermal conductivity κ. However, it is challenging to increase electrical conductivity without effecting thermal conductivity, since the thermal conductance has a lattice and an electronic contribution. For metals thermal and electrical conductivity are correlated via the Wiedemann-Franz Law (see Eq. (1.3)) and cannot be tuned independently[18].

$$\frac{\kappa}{\sigma} = L \cdot T \,, \tag{1.3}$$

where L is Lorenz number ($L = 2.44 \cdot 10^{-8}\ \mathrm{W \cdot \Omega \cdot K^{-2}}$), and T is the temperature.

The Seebeck coefficient is associated with the density of states (DOS) and can be increased by modulation of the DOS, as discussed in Chapter 2.

Undoped semiconductors have a Seebeck coefficient on the order of mV/K. Doped semiconductor materials show a decrease in the Seebeck coefficient, leading to values of a few μV/K for highly doped materials[19–22]. In contrast to the Seebeck coefficient, the electrical conductivity increases with doping because it is proportional to the number of charge carriers and their mobility[23]. In Figure 1.4, the dependence of the electrical conductivity, the Seebeck coefficient, and the thermal conductivity are given as a function of carrier concentration, illustrating the complexity of material optimization.

Among materials, semiconductors have high charge carrier mobility, medium range of carrier concentration, and a smaller number of electrons, which improve their ZT[24]. More precisely, a high range of carrier concentration increases the electrical

conductivity and the thermal conductivity and decreases the Seebeck coefficient, which results in an optimum carrier concentration distinctive for semiconductors.

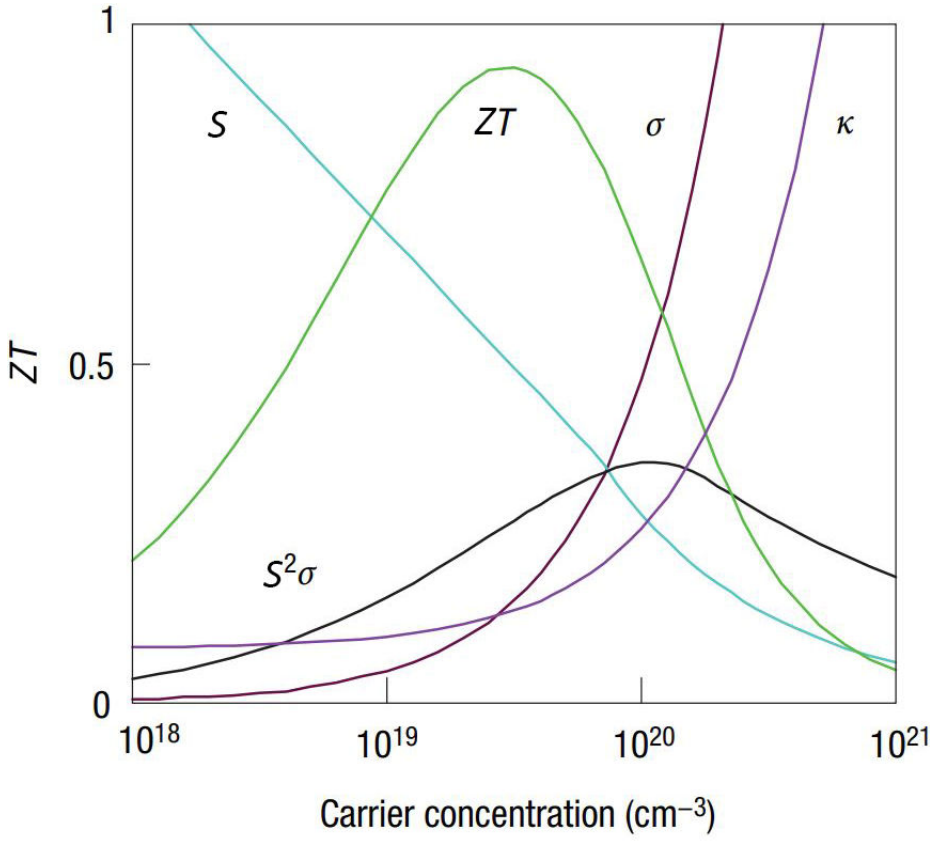

Figure 1.4. – The Seebeck coefficient (S), electrical (σ), and thermal (κ) conductivities, the figure of merit ZT and the power factor $S^2\sigma$ plotted as a function of the carrier concentration n. The Seebeck coefficient decreases as n increases, which is expected[12]. Adapted from reference 25.

In the same manner as in all engines, the maximum thermoelectric efficiency is limited by the Carnot efficiency as[26]:

$$\eta = \eta_c \frac{\sqrt{1 + ZT_{\max}} - 1}{\sqrt{1 + ZT_{\max}} + \frac{T_C}{T_H}}, \tag{1.4}$$

where η_c is the Carnot efficiency, ZT_{max} the maximum figure of merit, and T_H and T_C the temperatures of the hot and cold sources, respectively. Here $T_H > T_C$. The higher the value of ZT_{max}, the closer the efficiency of the thermoelectric generator approaches the Carnot efficiency (Figure 1.5).

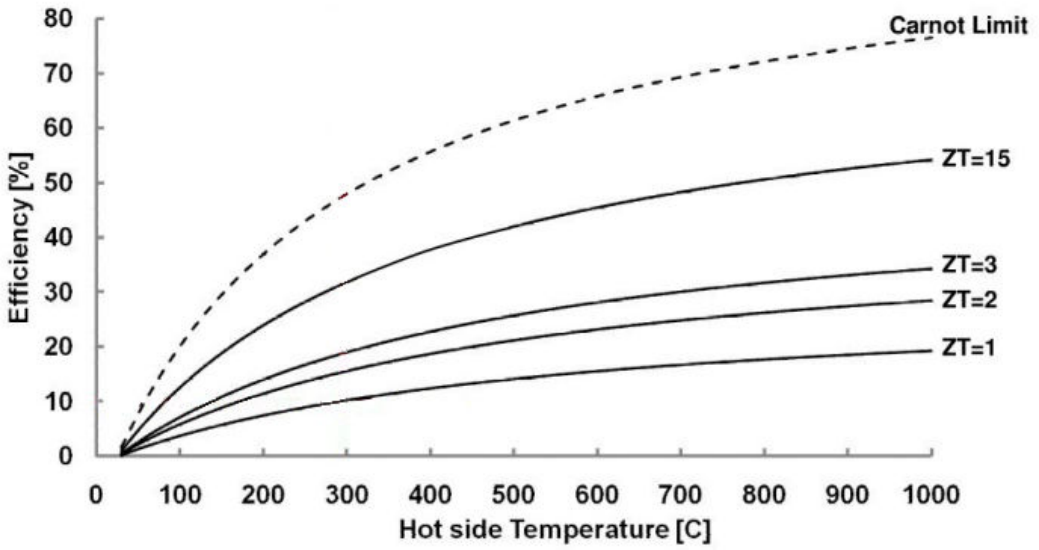

Figure 1.5. – The thermoelectric efficiency (ZT) as a function of temperature. The Carnot efficiency limit is plotted for comparison[27].

Given this, a thermoelectric device with a figure of merit of $ZT = 3$ can convert around 25-30% of waste heat to useful electrical energy at the range of high temperatures (T>500 °C).

Recently, many attempts have been made to reach high ZT values[28–31]. A summary of thermoelectric materials is presented in the next section.

1.4. State-of-the-art thermoelectric materials.

Semiconductor materials are used widely in thermoelectric applications [32–34]. Tremendous efforts have been undertaken to engineer materials to reach higher ZT values[35,36]. Figure 1.6 reviews the historical development of thermoelectric materials over the last 50 years[35]. The first generation of thermoelectric materials with ZT ~ 0.5 is represented by Bi_2Te_3, PbTe, and SiGe, as shown in the left part of the figure (1960-1990s). The second generation was based on utilizing size effects[37–39], as shown in the middle part of the figure. In this part the thermoelectric efficiency was enhanced to about 1.7 by nanostructuring ($AgPb_mSbTe_{m+2}$ [40], nano-Bi_2Te_3 [41], nanoamorphous-Bi_2Te_3 [42], nano-SiGe [43], nanostructural PbS [44]) and electronic structure engineering (Tl doped PbTe [45], $PbTe_{1-x}Se_x$ [46]), and modulation doping (SiGe)[47,48]. The third generation of bulk thermoelectric materials has established new concepts, and new technologies has pushed ZT to 1.8 [46] and even higher, as shown in the right part of Figure 1.6. The right part of the plot shows the high performance realized in hierarchical PbTe and promising thermoelectric materials, including PbSe [48,49], band alignment PbS [50,51], BiCuSeO [52], Cu_2S systems [53,54], SnS [55,56], Cu_2Se systems [57–60], Half-Heusler systems [61,62], and SnSe [63].

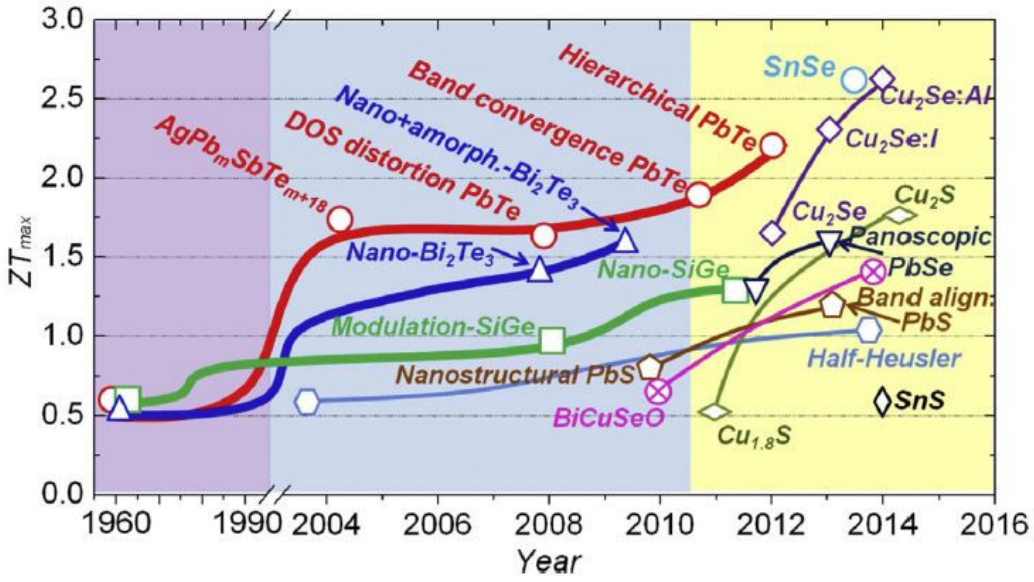

Figure 1.6. – *ZT* of bulk thermoelectric materials as a function of time. The graph is adapted from reference 35.

Even though some materials show *ZT*s higher than 2.0, it is still challenging to use these materials in thermoelectric generators due to their toxicity and high cost. There have been several essential milestones in increasing the *ZT* of thermoelectric materials, as summarized in Table 1.1[47,50, 53, 63-83]. The *ZT* enhancement originates either from the increase of the power factor ($S^2\sigma$) [45,46,71] or decrease of the lattice thermal conductivity κ_{lat} through microstructure engineering[40–44]. Several materials have now been reported to display high *ZT* values (>2.0) at relatively high temperatures[53,64,73,77,84–90]. However, these materials do not have high efficiency at temperatures around 300 – 400 K, which limits their application.

Table 1.1. – Record ZTs of some thermoelectric materials.

Ref.	Material	ZT_{max}	Temperature (K)	p/n
78	$Bi_{83.5}Sb_{16.5}$	0.52	80	n
79	$CsBi_4Te_6$	0.8	225	p
80	$Bi_2Te_{2.79}Se_{0.21}$	1.2	375	n
81	$Bi_{0.5}Sb_{1.5}Te_3$+x%Te	1.86	320	p
82	$MgAg_{0.97}Sb_{0.99}$	1.3	533	p
83	$PbTe_{0.998}I_{0.002}$-3%Sb	1.8	773	n
64	$Pb_{0.98}Na_{0.02}Te$-8%SrTe	2.5	923	p
65	$PbSe_{0.998}Br_{0.002}$-2%Cu2Se	1.8	723	n
66	$Pb_{0.98}Na_{0.02}Se$-2%HgSe	1.7	973	p
67	PbS-4.4%Ag	1.7	850	n
50	$Pb_{0.975}Na_{0.025}S$-3%CdS	1.3	923	p
68	β-Zn_4Sb_3	1.4	750	p
69	$Ba_{0.08}La_{0.05}Yb_{0.04}Co_4Sb_{12}$	1.7	850	n
70	$DD_{0.7}Fe_{2.7}Co_{1.3}Sb_{11.8}Sn_{0.2}$	1.45	823	p
71	$Mg_{2.15}Sb_{0.006}Si_{0.28}Sn_{0.71}$	1.3	700	n
72	$Mg_2Li_{0.025}Si_{0.4}Sn_{0.6}$	0.7	650	p
73	$SnSe_{1-x}Br_x$	2.8	773	n
63	SnSe	2.6	923	p
47	$(Si_{95}Ge_5)_{0.65}(Si_{70}Ge_{30}P_3)_{0.35}$	1.3	1173	n
74	$Si_{80}Ge_{20}B_x$	0.6	1100	p
75	$Zr_{0.2}Hf_{0.8}NiSn_{0.985}Sb_{0.015}$	1.1	1000	n
76	$Nb_{0.88}Hf_{0.12}FeSb$	1.5	1200	p
77	$Cu_2Se_{-x\%}CNT$	2.4	1000	p
53	$Cu_{1.97}S$	1.7	1000	p

Nonetheless, according to some proposals[37,39], when the material system dimensions are reduced to the nanoscale (e.g., nanowires), carrier confinement can be achieved, leading to an increase of ZT at relatively low temperatures. The effect of nanostructuring is addressed in the next section.

1.5. Nanowires for thermoelectric energy conversion.

Nanostructuring plays a crucial role in optimizing the thermoelectric properties of materials. It has been shown that the properties of materials change when the size of the system is scaled down to the nanoscale[91]. It has been stated that the thermoelectric properties of materials at the nanoscale can be adjusted separately from the electrical properties to some extent, improving the figure of merit. For instance, the thermal conductivity can be decreased by using smaller crystals (due to increased scattering of phonons at the boundaries), and, simultaneously, the power factor can be increased due to quantum confinement[38]. Based on theoretical predictions by Hicks &

Dresselhaus, nanowires are promising for thermoelectric energy conversion, since the modified density of states leads to an increase in the Seebeck coefficient (see Chapter 2)[39]. In NWs, the power factor can be increased due to a low effective electron band mass, which allows for a high mobility of the carriers[92,93]. Besides, the conduction of heat by the lattice is significantly reduced due to boundary scattering effects and a lower phonon group velocity. See Figure 1.7a, where lattice thermal conductivity (κ_{lat}) as a function diameter (L) is plotted for different III-V semiconductors. Nevertheless, the expected increase in the power factor in nanostructures has not yet been shown experimentally[94].

Among III-V materials, InSb is predicted to be the most promising material for thermoelectric devices because of its high electrical conductivity and relatively small thermal conductivity[95]. However, to create highly efficient thermoelectric generators ($ZT = 6$), the nanowires should have a diameter of around 10 nm (Figure 1.7b).

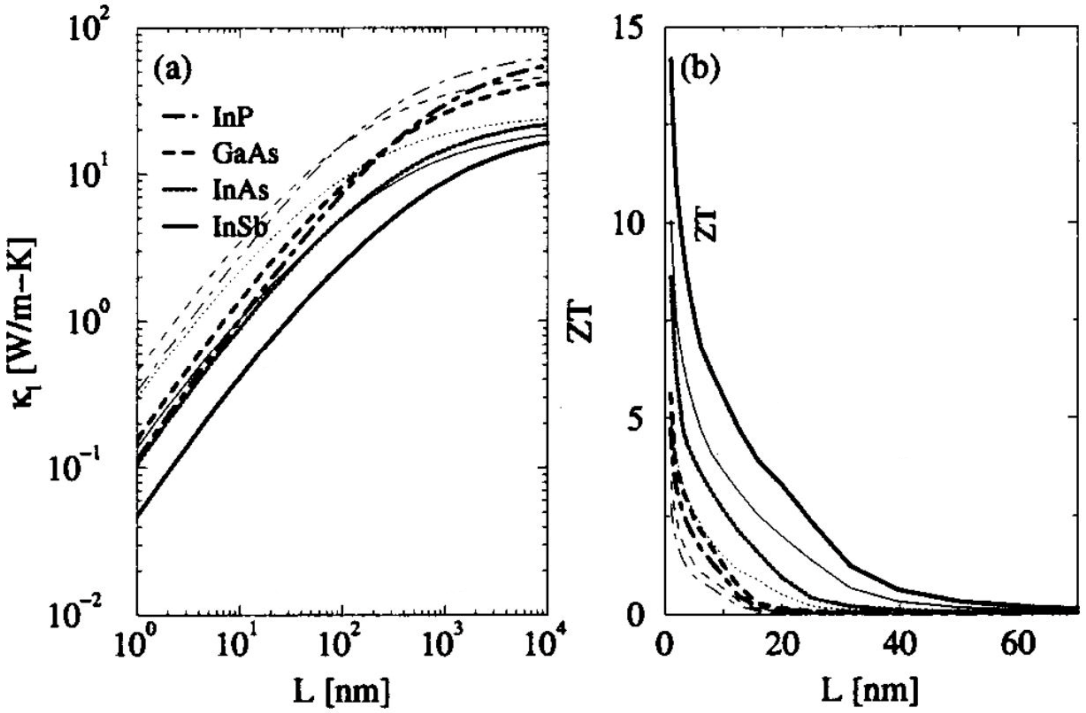

Figure 1.7. – **a,** Lattice thermal conductivity as a function of the thickness, for InSb, InAs, GaAs, and InP nanowires, for diffusive (thick lines) and partially specular (thin lines) phonon boundary scattering. **b,** Calculated ZT as a function of the thickness (Thick: Diffusive boundary scattering; Thin: Partially specular). Adapted from reference 95.

Concluding, it is essential not only from the application point of view but also fundamentally, to study the aspects of phonon and electron transport in nanowires for thermoelectric energy conversion.

1.6. Scope of this thesis.

In this thesis, phonon and electron transport in semiconductor nanowires is studied in detail to provide a fundamental understanding of the possibilities to enhance the efficiency of nanowire-based thermoelectric generators. This thesis is composed of seven chapters, including the introductory one.

Chapter 2 introduces the theoretical background relevant to the work discussed in this thesis.

In Chapter 3, the processing of the microdevices, as well as the preparation of the samples for measurements, are addressed.

In Chapter 4, the experimental setups and measurement techniques are discussed.

In Chapter 5, we demonstrate ballistic transport in ultrathin and ultraclean, GaP nanowires at room temperature over unexpectedly long distances of more than 15 micrometers.

In Chapter 6, we study the thermoelectric properties of InSb nanowires and estimate their thermoelectric efficiency.

In Chapter 7, we develop the prospective nanowire-based thermoelectric generator, which has potential advantages compared to conventional thermoelectric generators.

1.7. References.

1. Singh, B. R. & Singh, O. Study of Impacts of Global Warming on Climate Change: Rise in Sea Level and Disaster Frequency. (2012) doi:10.5772/50464.
2. Pro & Con Quotes: Is Human Activity Primarily Responsible for Global Climate Change? - ProCon.org. https://climatechange.procon.org/is-human-activity-primarily-responsible-for-global-climate-change-pro-con-quotes/.
3. Economic growth, population growth and climate change – Feasta. https://www.feasta.org/2013/08/26/economic-growth-population-growth-and-climate-change/.
4. Climate Change: Global Temperature | NOAA Climate.gov. https://www.climate.gov/news-features/understanding-climate/climate-change-global-temperature.
5. What the World Would Look Like if All the Ice Melted. https://www.nationalgeographic.com/magazine/2013/09/rising-seas-ice-melt-new-shoreline-maps/.
6. LLNL Flow Charts. https://flowcharts.llnl.gov/.
7. Beeby, S. P., White, N. M., Beeby, S. & White, N. *Energy Harvesting for Autonomous Systems.* https://www.researchgate.net/publication/264873114 (2010).
8. Howells, C. A. Piezoelectric energy harvesting Piezoelectric energy harvesting. *Energy Convers. Manag.* **50**, 1847–1850 (2018).
9. Cansiz, M., *et al.* Efficiency in RF energy harvesting systems: A comprehensive

review. *Energy* 174, 292-309 (2019).
10. Do, X., Jeong, C., Nguyen, H., Han, S. & Lee, S. A high efficiency piezoelectric energy harvesting system. 2011 International SoC Design Conference (2011).
11. Kiziroglou, M. E. & Yeatman, E. M. *Materials and techniques for energy harvesting*.
12. Solar Panel Efficiency: What Panels Are Most Efficient? | EnergySage. https://news.energysage.com/what-are-the-most-efficient-solar-panels-on-the-market/.
13. Developing the next generation technologies of renewable electricity and heating/cooling | Programme | H2020 | CORDIS | European Commission. https://cordis.europa.eu/programme/rcn/700351/en.
14. Enescu, D. Thermoelectric Energy Harvesting: Basic Principles and Applications. *Green Energy Advances* (2019).
15. Seebeck, T. J. Ueber die magnetische Polarisation der Metalle und Erze durch Temperaturdifferenz. *Ann. Phys.* **82**, 253–286 (1826).
16. Zheng, X., Liu, C., Yan, Y., Wang Q. A review of thermoelectrics research–Recent developments and potentials for sustainable and renewable energy applications. *Renewable and Sustainable Energy Reviews*. **32,** 486–503 (2014).
17. Rosa, A. Da. Fundamentals of renewable energy processes. (2012).
18. Yadav, A., Deshmukh, P., Roberts, K., Jisrawi, N. & Valluri, S. An analytic study of the Wiedemann–Franz law and the thermoelectric figure of merit. Journal of Physics Communications 3, 105001 (2019).
19. Han, M.-K., Id, J., Lee, D.-H. & Kim, S.-J. materials Thermoelectric Properties of Bi 2 Te 3 : CuI and the Effect of Its Doping with Pb Atoms. doi:10.3390/ma10111235.
20. Guo, Q., Chan, M., Kuropatwa, B. A. & Kleinke, H. Thermoelectric properties of Sn- and Pb-doped Tl 9 BiTe 6 and Tl 9 SbTe 6. *J. Appl. Phys.* **116**, (2014).
21. Ren, Z. F. *et al.* Enhancement of thermoelectric figure-of-merit by a nanostructure approach. 83–93 (2009).
22. Hofmann, A., Kroon, R., Muller, C. *Doping and processing of organic semiconductors for plastic thermoelectrics*. Handbook of Organic Materials for Electronic and Photonic Devices. 429–449, (2019).
23. Kittel, C. & Wiley, J. *Introduction to Solid State Physics*. 8th edition.
24. Nolas, G. S. (George S. ., Sharp, J. (Jeffrey) & Goldsmid, H. J. *Thermoelectrics : basic principles and new materials developments*. (Springer, 2001).
25. Snyder, G. J. & Toberer, E. S. Complex thermoelectric materials. in *Materials for Sustainable Energy: A Collection of Peer-Reviewed Research and Review Articles from Nature Publishing Group* 101–110 (World Scientific Publishing Co., 2010). doi:10.1142/9789814317665_0016.
26. Goldsmid, J. The Physics of Thermoelectric Energy Conversion. (2017).
27. ACTTR Inc. - The Research of Thermoelectric Materials and Applications. http://www.acttr.com/en/en-report/en-report-technology/240-en-tech-thermoelectric-research-application.html.
28. Peng, B. *et al.* High thermoelectric efficiency in monolayer PbI 2 from 300 K to

900 K. *Inorganic Chemistry Frontiers*. **6,** 920-928 (2019).

29. Peng, Y. *et al.* Realizing High Thermoelectric Performance at Ambient Temperature by Ternary Alloying in Polycrystalline Si 1-xy Ge x Sn y Thin Films with Boron Ion. *Scientific Reports,* **9**, 14342 (2019).
30. Chen, Y., Hou, X., Ma, C., Dou, Y. & Wu, W. Review of Development Status of Bi 2 Te 3-Based Semiconductor Thermoelectric Power Generation. (2018) doi:10.1155/2018/1210562.
31. Zide, J. M. O. *et al.* High efficiency semimetal/semiconductor nanocomposite thermoelectric materials. *J. Appl. Phys.* **108**, (2010).
32. Liang, W. *et al.* Field-effect modulation of seebeck coefficient in single PbSe nanowires. *Nano Lett.* **9**, 1689–1693 (2009).
33. Shakouri, A. Recent Developments in Semiconductor Thermoelectric Physics and Materials. *Annu. Rev. Mater. Res.* **41**, 399–431 (2011).
34. Majumdar, A. Thermoelectricity in Semiconductor Nanostructures. *Science* vol. 303 777–778 (2004).
35. Zhang, X., Materiomics, L. Z.-J. of & 2015, undefined. Thermoelectric materials: Energy conversion between heat and electricity. *Elsevier*.
36. Pineda, D., Rezaniakolaei, A., Brand, O. & Fedder, G. Thermoelectric Energy Conversion: Basic Concepts and Device Applications. (2017).
37. Heremans, J., Dresselhaus, M. When thermoelectrics reached the nanoscale. *Nature Nanotechnology* **8**, 471-473 (2013).
38. Sun, X., Dresselhaus, M., Wang, K., & Tanner, M. Effect of Quantum-Well Structures on the Thermoelectric Figure of Merit in the Si/Si1-x Ge x System. *MRS Proceedings*, **452**, 261. (1996).
39. Hicks, L. D. & Dresselhaus, M. S. Thermoelectric figure of merit of a one-dimensional conductor. *Phys. Rev. B* **47**, 16631–16634 (1993).
40. Fang Hsu, K. *et al. Cubic AgPb m SbTe 2m : Bulk Thermoelectric Materials with High Figure of Merit Downloaded from. J. Vac. Sci. Technol. B* vol. 50 http://science.sciencemag.org/ (1997).
41. Poudel, B. *et al.* High-thermoelectric performance of nanostructured bismuth antimony telluride bulk alloys. *Science (80-.).* **320**, 634–638 (2008).
42. Xie, W., Tang, X., Yan, Y., Zhang, Q. & Tritt, T. M. Unique nanostructures and enhanced thermoelectric performance of melt-spun BiSbTe alloys. *Appl. Phys. Lett.* **94**, (2009).
43. Bathula, S. *et al.* Enhanced thermoelectric figure-of-merit in spark plasma sintered nanostructured n-type SiGe alloys. *Appl. Phys. Lett.* **101**, (2012).
44. Zhao, L. D. *et al.* High performance thermoelectrics from earth-abundant materials: Enhanced figure of merit in PbS by second phase nanostructures. *J. Am. Chem. Soc.* **133**, 20476–20487 (2011).
45. Heremans, J. P. *et al.* Enhancement of thermoelectric efficiency in PbTe by distortion of the electronic density of states. *Science.* **321**, 554–557 (2008).
46. Pei, Y. *et al.* Convergence of electronic bands for high performance bulk thermoelectrics. *Nature.* **473**, 66–69 (2011).
47. Yu, B. *et al.* Enhancement of thermoelectric properties by modulation-doping in

silicon germanium alloy nanocomposites. *Nano Lett.* **12**, 2077–2082 (2012).

48. Zhao, L. D. *et al.* High thermoelectric performance via hierarchical compositionally alloyed nanostructures. *J. Am. Chem. Soc.* **135**, 7364–7370 (2013).
49. Wang, H., *et al.* Weak electron–phonon coupling contributing to high thermoelectric performance in n-type PbSe. *PNAS.* **109 (25)**, 9705-9709 (2012).
50. Zhao, L. D. *et al.* Raising the thermoelectric performance of p-type Pbs with endotaxial nanostructuring and valence-band offset engineering using CdS and ZnS. *J. Am. Chem. Soc.* **134**, 16327–16336 (2012).
51. Pei, Y., LaLonde, A. D., Heinz, N. A. & Snyder, G. J. High thermoelectric figure of merit in PbTe alloys demonstrated in PbTe-CdTe. *Adv. Energy Mater.* **2**, 670–675 (2012).
52. Zhao, L. *et al.* BiCuSeO oxyselenides: new promising thermoelectric materials. *Energy and Environmental Science* **7**, 2900-2924 (2014).
53. He, Y. *et al.* High thermoelectric performance in non-toxic earth-abundant copper sulfide. *Adv. Mater.* **26**, 3974–3978 (2014).
54. Ge, Z. *et al.* Synthesis and transport property of Cu 1.8 S as a promising thermoelectric compound. *Chemical Communications.* **47**, 12697-12699 (2011).
55. Tan, Q. *et al.* Thermoelectrics with Earth Abundant Elements: Low thermal conductivity and high thermopower in doped SnS. *J. Mater. Mater. A* **00**, 1–3 (2014).
56. Tan, Q. & Li, J.-F. Thermoelectric Properties of Sn-S Bulk Materials Prepared by Mechanical Alloying and Spark Plasma Sintering. doi:10.1007/s11664-014-3127-0.
57. Liu, H. *et al.* Ultrahigh thermoelectric performance by electron and phonon critical scattering in Cu2Se1-xIx. *Adv. Mater.* **25**, 6607–6612 (2013).
58. Zhong, B. *et al.* High superionic conduction arising from aligned large lamellae and large figure of merit in bulk Cu1.94Al0.02Se. *Appl. Phys. Lett.* **105**, (2014).
59. Liu, H. *et al.* Copper ion liquid-like thermoelectrics. *Nat Mater.* **11(5)**, 422-425 (2012).
60. Yu, B. *et al.* Thermoelectric properties of copper selenide with ordered selenium layer and disordered copper layer. *Nano Energy.* **1(3)**, (2012).
61. Xie, H. *et al.* The intrinsic disorder related alloy scattering in ZrNiSn half-Heusler thermoelectric materials. *Scientific Reports* **4**, 6888 (2014).
62. Xie, H. *et al.* Beneficial contribution of alloy disorder to electron and phonon transport in half-heusler thermoelectric materials. *Adv. Funct. Mater.* **23**, 5123–5130 (2013).
63. Zhao, L. *et al.* Ultralow thermal conductivity and high thermoelectric figure of merit in SnSe crystals. *Nature.* **508**. 373-377 (2014).
64. Tan, G. *et al.* Non-equilibrium processing leads to record high thermoelectric figure of merit in PbTe–SrTe. *Nature Communications* **7**, 12167 (2016).
65. Zhou, C. *et al.* High-Performance n-Type PbSe-Cu2Se Thermoelectrics through Conduction Band Engineering and Phonon Softening. *J. Am. Chem. Soc.* **140**, 15535–15545 (2018).

66. Hodges, J. M. *et al.* Chemical Insights into PbSe- x%HgSe: High Power Factor and Improved Thermoelectric Performance by Alloying with Discordant Atoms. *J. Am. Chem. Soc.* **140**, 18115–18123 (2018).
67. Ibánez, M. *et al.* High-performance thermoelectric nanocomposites from nanocrystal building blocks. *Nature Communications* **7**, 10766 (2016).
68. Lin, J. *et al.* Unexpected high-temperature stability of β-Zn4Sb 3 opens the door to enhanced thermoelectric performance. *J. Am. Chem. Soc.* **136**, 1497–1504 (2014).
69. Shi, X. *et al.* Multiple-filled skutterudites: High thermoelectric figure of merit through separately optimizing electrical and thermal transports. *J. Am. Chem. Soc.* **133**, 7837–7846 (2011).
70. Rogl, G. *et al.* New bulk p-type skutterudites DD0. 7Fe2. 7Co1. 3Sb12− xXx (X= Ge, Sn) reaching ZT> 1.3. *Acta Materialia*, **91**, 227-238 (2015).
71. Liu, W. *et al.* Convergence of conduction bands as a means of enhancing thermoelectric performance of n-type Mg 2Si 1-xSn x solid solutions. *Phys. Rev. Lett.* **108**, (2012).
72. Gao, P. *et al.*The p-type Mg 2 Li x Si 0.4 Sn 0.6 thermoelectric materials synthesized by a B 2 O 3 encapsulation method using Li 2 CO 3 as the doping agent. *J.Mater. Chem. C.* **4**, 929-934 (2016).
73. Chang, C. *et al.* 3D charge and 2D phonon transports leading to high out-of-plane ZT in n-type SnSe crystals. *Science* **360 (6390)**, 778-783 (2018).
74. Vining, C. B., Laskow, W., Hanson, J. O., Van Der Beck, R. R. & Gorsuch, P. D. Thermoelectric properties of pressure-sintered Si 0.8 Ge 0.2 thermoelectric alloys. *J. Appl. Phys.* **69**, 4333 (1991).
75. Liu, Y. *et al.* Demonstration of phonon-glass electron-crystal strategy in (Hf,Zr)NiSn half-Heusler thermoelectric materials by alloying. *J. Name* 1 (2013) doi:10.1039/x0xx00000x.
76. Fu, C. *et al.* Realizing high figure of merit in heavy-band p-type half-Heusler thermoelectric materials. *Nature Communications* **6**, 8144 (2015).
77. Nunna, R. *et al.* Ultrahigh thermoelectric performance in Cu 2 Se-based hybrid materials with highly dispersed molecular CNTs. *pubs.rsc.org.*
78. Lenoir, B. *et al.* Effect of antimony content on the thermoelectric figure of merit of Bi1− xSbx alloys. *Journal of Physics and Chemistry of Solids* 59 (1), 129-134 (1998).
79. Chung, D.-Y. *et al. CsBi 4 Te 6 :* A High-Performance Thermoelectric Material for Low-Temperature Applications. *Science* **287** (5455), 1024-7 (2000).
80. Hu, L. *et al.* Tuning Multiscale Microstructures to Enhance Thermoelectric Performance of n-Type Bismuth-Telluride-Based Solid Solutions. *Adv. Energy Mater.* **5**, (2015).
81. Kim, S. Il *et al.* Dense dislocation arrays embedded in grain boundaries for high-performance bulk thermoelectrics. *Science (80-.).* **348**, 109–114 (2015).
82. Liu, Z. *et al.* Understanding and manipulating the intrinsic point defect in α-MgAgSb for higher thermoelectric performance. *Journal of Materials Chemistry A.* **4,** 16834-16840 (2016).

83. Fu, L. *et al.* Large enhancement of thermoelectric properties in n-type PbTe via dual-site point defects. *Energy and Environmental Science*. **10**, 2030-2040 (2017).
84. Chen, Z. *et al.* Lattice Dislocations Enhancing Thermoelectric PbTe in Addition to Band Convergence. *Adv. Mater.* **29**, (2017).
85. Biswas, K. *et al.* High-performance bulk thermoelectrics with all-scale hierarchical architectures. *Nature* **489**, 414-418 (2012).
86. Korkosz, R. J. *et al.* High ZT in p-type (PbTe)1-2x(PbSe)x(PbS)x thermoelectric materials. *J. Am. Chem. Soc.* **136**, 3225–3227 (2014).
87. Sarkar, S. *et al.* Dual Alloying Strategy to Achieve a High Thermoelectric Figure of Merit and Lattice Hardening in p-Type Nanostructured PbTe. (2018) doi:10.1021/acsenergylett.8b01684.
88. Wu, H. *et al.* Broad temperature plateau for thermoelectric figure of merit ZT>2 in phase-separated PbTe0.7S0.3. *Nature Communications* **5**, 4515 (2014).
89. Zhao, L.-D. *et al.* Ultrahigh power factor and thermoelectric performance in hole-doped single-crystal SnSe. *Science* **351** (6269), (2015).
90. Zhang, X. *et al.* Vacancy Manipulation for Thermoelectric Enhancements in GeTe Alloys. *J. Am. Chem. Soc.* **140**, 15883–15888 (2018).
91. Mohammad S.N. Understanding quantum confinement in nanowires: basics, applications and possible laws. *J. Phys Condens Matter*. 26 (42), (2014).
92. Pei, Y. *et al.* Low effective mass leading to high thermoelectric performance. *Energy and Environmental Science* **5**, 7963-7969 (2012).
93. Jeong, C., Kim, R. & Lundstrom, M. S. On the best bandstructure for thermoelectric performance: A Landauer perspective. in *Journal of Applied Physics* vol. 111 (2012).
94. Mensch, P. *et al.* One-dimensional behavior and high thermoelectric power factor in thin indium arsenide nanowires. *Appl. Phys. Lett.* **106**, (2015).
95. Mingo, N. Thermoelectric figure of merit and maximum power factor in III-V semiconductor nanowires. *Appl. Phys. Lett.* **84**, 2652–2654 (2004).

Chapter 2. Theoretical background.

In this chapter, the theoretical aspects of thermal and electrical transport phenomena are addressed. The theoretical foundation of this thesis covers the topics of heat transfer and the effects of boundaries in nanowire systems, including specular and diffusive scattering. The Seebeck effect as a thermoelectric phenomenon is discussed. Additionally, the influence of field-effect gating on the thermoelectric power factor of a material is addressed. Lastly, the Landauer formalism is explained for the estimation of thermal transport in nanowires.

2.1. Thermoelectric energy conversion.

It has been shown in the previous chapter that semiconductors are promising candidates for efficient thermoelectric conversion[1–3]. According to the theoretical predictions by Hicks & Dresselhaus, nanowires are interesting for thermoelectric applications, because decreasing the dimension of a bulk 3D material to a 1D system increases the figure of merit[4].

Generally, the efficiency of thermoelectric generation[5] can be defined as:

$$\eta = \frac{(T_1 - T_2)\left(\sqrt{1+ZT_m}-1\right)}{T_1\left(\sqrt{1+ZT_m}+\frac{T_2}{T_1}\right)} = \eta_c \frac{\sqrt{1+ZT_m}-1}{\sqrt{1+ZT_m}+\frac{T_2}{T_1}}, \tag{2.1}$$

where η_c is the Carnot efficiency, Z the figure of merit, T_m the mean temperature, and T_1 and T_2 the temperatures of the hot and cold sides, respectively. It is assumed that $T_1 > T_2$ in this case. The higher the value of Z, the closer the thermoelectric efficiency approaches the Carnot efficiency. Thus, a large value of Z is desired for efficient thermoelectric energy conversion.

The figure of merit is defined as:

$$Z = \frac{S^2}{G_{th} \cdot R}, \tag{2.2}$$

where S is the Seebeck coefficient, and G_{th} and R are the thermal conductance and electrical resistance of a thermocouple, respectively[6]. Eq (2.2) can be simplified to (2.3) by taking into account material properties:

$$Z = \frac{S^2}{G_{th} \cdot R} = S^2 \frac{\sigma \cdot A}{l} \frac{l}{\kappa \cdot A} = S^2 \frac{\sigma}{\kappa}, \tag{2.3}$$

where A and l are the cross-sectional area and length of the wire, and κ and σ are the thermal and electrical conductivity, respectively. The SI unit of Z is [K^{-1}], thus to get

a dimensionless number it is often multiplied by the temperature T. ZT is commonly referred to as the figure of merit:

$$ZT = \frac{S^2 \cdot \sigma}{\kappa} \cdot T \tag{2.4}$$

Therefore, it can be concluded that it is essential to characterize the thermal and electron transport in order to calculate the thermoelectric figure of merit (ZT).

2.2. Thermal transport.

In semiconductors, the main heat carriers are phonons, the quasiparticles of atomic vibrations[7]. The concept of a phonon was introduced by the Soviet physicist Igor Tamm in 1932 [8]. Phonons can be considered as particles with a velocity v, a heat capacity C_v and a relaxation time τ, which is the average time it takes for a phonon to undergo a scattering event that changes its momentum. The phonon mean free path $l_{mfp} = v \cdot \tau$ is the average distance that a phonon travels before it changes its direction. The scattering events reduce l_{mfp}. Next to scattering in the bulk, phonons in a finite-sized system can scatter at the boundaries, which is addressed in detail in the next section. The lattice thermal conductivity κ_{lat} can be written as:

$$\kappa_{lat} = \sum C_v \cdot v \cdot l_{mfp}, \tag{2.5}$$

where the sum is over all phonon modes.

In the same way as for electrons, different transport regimes can be identified for phonons. Diffusive heat transport results from multiple scattering events. Structural imperfections and interactions of a phonon with other phonons and with electrons lead to scattering and reduction of the phonon mean free path[9]. However, when the size L of the structure through which the phonons travels becomes much smaller than the mean free path, phonons can travel without scattering, *i.e.*, ballistically, similar to classical ballistic particles[10]. Classical ballistic particles propagate while transferring a hundred percent of their energy. Since a phonon travels ballistically for $L << l_{mfp}$ the thermal resistance is independent of L for ballistic phonons, and, thus, the thermal conductivity is linearly proportional to the length: $\kappa \propto L$. In the ballistic regime the value of the thermal conductivity depends linearly on the system size. The diffusive and ballistic phonon transport regimes are sketched in Figure 2.1.

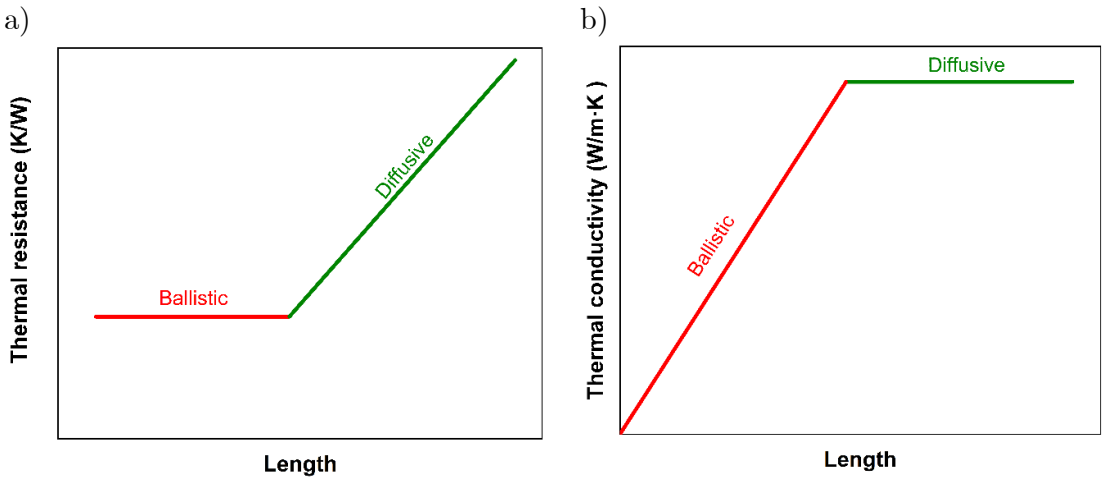

Figure 2.1. – Sketches of ballistic and diffusive transport regimes: **a,** the thermal resistance remains constant in the ballistic regime and is linearly proportional to the system length in the diffusive regime; **b,** for the thermal conductivity the opposite holds.

Since the scattering rate is often frequency-dependent, thermal transport is typically governed by a combination of ballistic and diffusive phonons. Low-frequency phonons tend to be ballistic due to their relatively high group velocities, long mean free paths, and weak scattering rates[11]. At room temperature, low-frequency phonons usually do not significantly contribute to thermal transport because of their low energy density[12–14]. Therefore, to experimentally observe ballistic phonon transport, measurements must be performed for short channel lengths and/or low temperatures. Experimental studies have demonstrated the breakdown of diffusive thermal transport[15–17]. Deviations from diffusive heat flow can occur due to hydrodynamic effects[18–25], but also due to ballistic behavior[16,17,26–31]. The experimental observation of ballistic and diffusive phonon transport in nanowires is discussed in detail in Chapter 5.

2.2.2. Boundary scattering.

In a finite-sized system, additionally to bulk scattering mechanisms, boundary phonon scattering should be considered. More specifically, to include boundary scattering, the scattering time must be adjusted. For simplicity, it is assumed that the reduction of size does not affect the phonon density of states. Below, two approaches are discussed to consider boundary scattering. They are applicable to diffusive and specular scattering.

2.2.2.1. Diffusive scattering.

Diffusive scattering is the reflection of a wave at a surface where the reflected wave is distributed over many angles. For ideal diffusive scattering, the reflected

intensity distribution is independent of the reflection angle. The phonon mean free path l_{mfp} resulting from different scattering mechanisms can be approximated by Matthiessen's rule.

Matthiessen's rule is empirically derived from work by Augustus Matthiessen in 1864 [32]. It is identical to adding the thermal resistances as parallel resistances. In the case of phonon scattering, this can be done by adding the inverses of the phonon mean free paths. The contributions of different scattering mechanisms are included in Matthiessen's rule as follows:

$$\frac{1}{l_{mfp(total)}} = \sum_{N} \frac{1}{l_{mfp(N)}}, \tag{2.6}$$

where $l_{mfp(total)}$ is the total mean free path, and $l_{mfp(N)}$ is the mean free path for a specific scattering mechanism N. In order to take into consideration the boundary scattering in a nanowire, the mean free path resulting from boundary scattering is assumed to be equal to the diameter of the wire, while the bulk scattering is assumed to be unaffected[33]. Applying Matthiessen's rule, the following equation for the mean free path holds:

$$\frac{1}{l_{mfp}} = \frac{1}{l_{mfp(impurities)}} + \frac{1}{l_{mfp(boundanies)}} + \frac{1}{l_{mfp(phonon-phonon)}}. \tag{2.7}$$

The phonon mean free path due to boundary scattering is dependent on the diffusive and specular scattering. It can be estimated by Eq (2.8):

$$l_{mfp(boundaries)} = \frac{1+p}{1-p} d, \tag{2.8}$$

where d is the diameter of the nanowire. The parameter p varies in the range from 0 to 1, where $p = 0$ represents ideal specular scattering and $p = 1$ fully diffusive scattering[34]. Hence, ideal diffusively scattered phonons will travel over a length d, and perfectly specularly scattering phonons will propagate with an infinite mean free path. The latter will not happen in practice, but for high values of p, phonons will propagate along the whole length of the nanowire. Such a propagation phenomenon is known as ballistic transport[34].

Eq. (2.7) has been used in many different nanoscale systems[35,36] to estimate the influence of scattering on thermal and electronic transport. However, the assumption that scattering mechanisms can be considered independently has been challenged[37,38]. Additionally, since the phonons are scattered more frequently near the boundary, the phonon density is locally enhanced[39]. The enhanced phonon density results in increased phonon-phonon scattering near the boundary[40]. This effect comes in addition to the scattering at the boundary itself. This enhancement is not taken into consideration in

Matthiessen's rule. Hence, it is expected that the influence of the boundary is underestimated.

Another approach that addresses boundary scattering has been proposed by Ziman[35]. This approach leads to the following equation:

$$l_{mfp(total)} = l_{mfp(bulk)} \left\{ 1 - \exp\left(-\frac{d}{l_{mfp(bulk)}} \right) \right\}. \tag{2.9}$$

This approach assumes that the phonon mean free path is limited to the diameter of the wire. Typically, in a nanowire, the phonon modes that have a large component of their momentum along the wire propagate much further before meeting the boundary than phonons that have a small such component. Thus, the approximation that the mean free path is limited to the diameter overrates the effect of the boundary. The real solution is expected to be in between the results obtained using Matthiessen's rule and the expression of Ziman's approach.

Both approximate results Eq. (2.8) and (2.9) behave analogously in the limit of small diameter, where they are both linear in *d*. In case of a large diameter, both results become equal to the bulk mean free path. The result of Eq. (2.8) based on Matthiessen's rule approaches bulk behavior much slower than the result of Eq. (2.9) based on Ziman's approach. This comes from the fact that Matthiesen's rule is an underestimation, while the equation based on Ziman's approach is an overestimation of the mean free path[35,41]. Both approximations are sufficient to model the data obtained in this thesis.

2.2.2.2. Specular scattering.

The absence of a disorder may result in specular scattering in the case of a thin, smooth, and single-crystalline nanowire. Specular scattering occurs when the phonons are reflected at the boundaries under a single angle. The edges of the boundaries might have a disordered region with thickness *h,* as shown in Figure 2.2, leading to surface roughness.

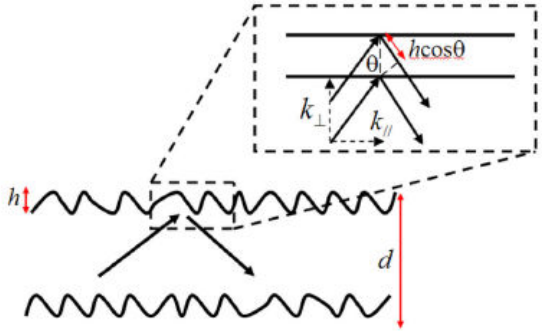

Figure 2.2. – Schematic illustration of a nanowire boundary. *k* is the phonon wave vector, *h* is the thickness of the disordered region, *d* is the diameter of the nanowire, and θ the angle of incidence. Shown is the relation $k_{\perp} = k \cdot cos(\theta)$ – adapted from reference 42.

Specular scattering occurs when the phase difference of the reflected wave $\Delta\varphi << 1$. The reflected wave undergoes destructive interference when $\Delta\varphi \approx 1$. The phase difference can be expressed as[42]:

$$\Delta\phi = 2\pi\frac{2h\sin(\theta)}{\lambda} = 2hk_{\perp}, \tag{2.10}$$

where λ is the wavelength of the phonon, and $k_{\perp}$ is the component of the wave vector perpendicular to the surface:

$$k_{\perp} = \sqrt{k^2 - k_z^2} = k\cos(\theta). \tag{2.11}$$

In the case of specular scattering, the mean free path depends on the frequency and can be obtained from[44]:

$$l_{mfp}^{-1} = B\left(\frac{h}{d}\right)^2\frac{1}{d}\cdot\left(\frac{\omega}{\omega_D}\right)^2 N(\omega), \tag{2.12}$$

where B is a dimensionless constant depending on the details of the disorder, ω is the frequency of the phonon mode, ω_D is the Debye frequency, and $N(\omega)$ is the number of modes with frequency ω [42].

The experiments on the influence of specular scattering on phonon transport are presented in Chapter 5.

2.4. Electronic transport.

2.4.1. The Seebeck effect.

The Seebeck effect describes the phenomenon of the establishment of an electric field inside a material in the presence of an applied temperature gradient. Thomas Johann Seebeck discovered in 1821 [43] that a voltage appears at the junction of two materials when a temperature difference is applied. Figure 2.3 shows the effect in the case of a semiconductor nanowire.

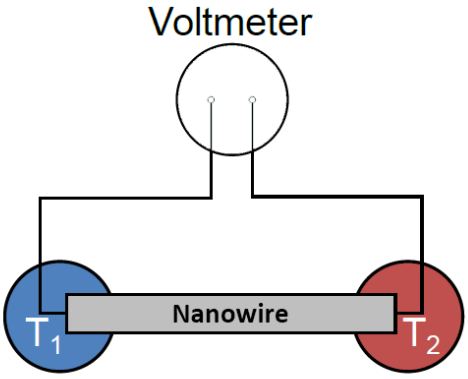

Figure 2.3. – A schematic illustration of the Seebeck effect, where two ends of a semiconductor nanowire are kept at different temperatures T_1 and T_2. The established temperature gradient creates a thermoelectric voltage measured by a voltmeter.

The Seebeck coefficient S can be obtained from the current density j flowing as the result of the applied temperature gradient ∇T and the electric field E:

$$j = \sigma(E - S\nabla T), \tag{2.13}$$

where σ the electrical conductivity. By interrupting the circuit, the current density drops to zero, and the equation simplifies to:

$$E = S\nabla T. \tag{2.14}$$

To obtain the value of the Seebeck coefficient, the electric field should be measured indirectly through the Seebeck voltage (V_S) (see Figure 2.3). The Seebeck voltage can be written as:

$$V_{\mathrm{S}} = \int E(r,T)\mathrm{d}r = \int S(r,T)\cdot\nabla T\mathrm{d}r, \tag{2.15}$$

or

$$V_{\mathrm{S}} = S\cdot(T_2 - T_1). \tag{2.16}$$

The created Seebeck voltage is equal to the difference of the Fermi levels of both metal contacts. As a result, the Fermi level changes within the semiconductor. In the case of an n-type semiconductor, the change in the Fermi level leads to an electron density that is higher at the hot end than at the cold end. This creates a diffusion current from the hot to the cold end. As a result, the negative potential on the cold side is enhanced. The created electric field inside the semiconductor (caused by the potential gradient) activates a drift current, which is flowing opposite to the diffusion current. When drift and diffusion currents cancel each other, the Seebeck voltage (V_S) can be defined as the potential difference between two ends of the semiconductor[44]. For

a p-type semiconductor with holes as the charge carriers, the explanation is similar (the sign in Eq. (2.16) changes).

The energy diagram of an n-type semiconductor with metal contacts at each end is shown in figure 2.4.

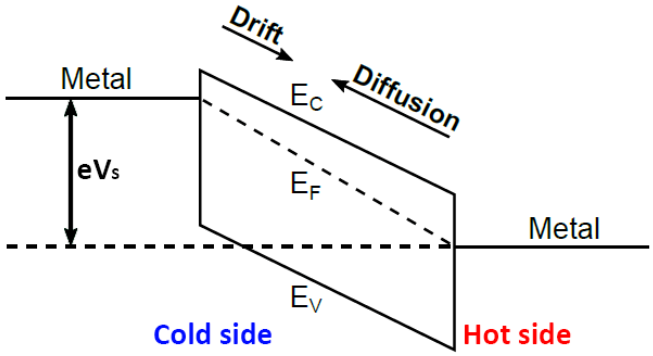

Figure 2.4. – A schematic band diagram of an n-type semiconductor, where a Seebeck voltage (V_S) arises as a result of diffusion and drift currents due to a change of the Fermi level at both ends, induced by an applied temperature gradient.

2.4.2. Quantum confinement effect.

Generally, the electrical conductivity σ is obtained as:

$$\sigma = n \cdot e \cdot \mu, \tag{2.17}$$

where e the charge of the carriers, n the carrier concentration, and μ the carrier mobility. Assuming a constant mobility, a maximum in the power factor ($S^2\sigma$) will be reached when S^2n is maximized. Based on the Boltzmann transport equation within the relaxation time approximation, the factor S^2n can be written as[45]:

$$S^2 n = \frac{1}{(e \cdot T)^2} \left(\frac{\langle \tau \cdot E \rangle}{\langle \tau \rangle} - E_F \right)^2 n, \tag{2.18}$$

where E_F is the Fermi level, and $<\tau E>/<\tau>$ is the average energy of the electrons with relaxation time τ. T is the time that an electron of energy E propagates before being scattered. When the relaxation time (τ) is independent of energy $<\tau E>/<\tau>=<E>$, the power factor ($S^2\sigma$) increases with increasing difference between $<E>$ and E_F. These two quantities depend on the filling of the energy levels in a semiconductor, which is affected by quantum confinement.

The density of filled levels in an energy interval dE is equal to DOS$(E)\cdot f(E)\ dE$, where DOS(E) is the density of states (DOS) and $f(E)$ the Fermi-Dirac distribution function[46]. The DOS changes with energy as shown in Figure 2.5a.

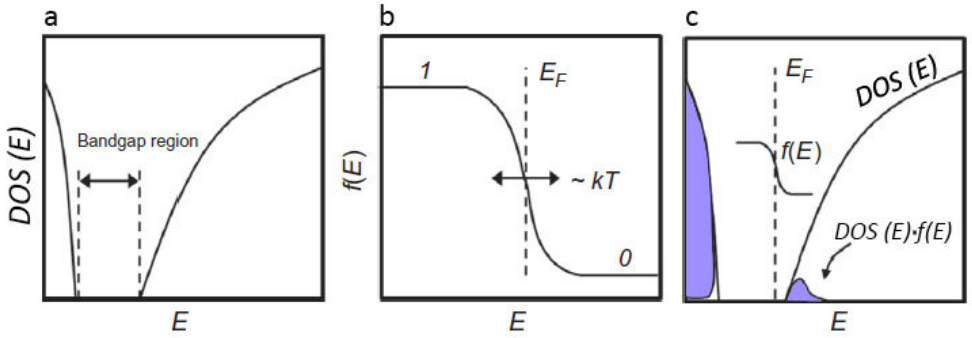

Figure 2.5. – **a,** Density of states (DOS) of a semiconductor as a function of electron energy. **b,** Fermi–Dirac distribution as a function of energy. **c,** Filling of the energy states in a semiconductor material. Colored areas represent levels filled with electrons. – Adapted from reference 47.

The Fermi-Dirac distribution function *f(E)* is the probability that an electron level with an energy E is occupied. The distribution is centered around the Fermi level E_F. The probability changes from 1 to 0 in a range of a few kT energy units (Figure 2.5b). The distribution of filled electron levels in a semiconductor is shown in Figure 2.5c.

The DOS*(E)* is the number of allowed energy levels per unit volume per unit energy range. If any dimension is sufficiently reduced, the *DOS* starts to show a sawtooth-like pattern because of the formation of subbands, as illustrated in Figure 2.6a. Pronounced subbands appear when the diameter is further reduced. In this case, the DOS has a higher magnitude, and the lowest energy E_0 is increased[46,49]. The magnitude of the DOS increases as $1/d^2$ for nanowires, which boosts S^2n [50,51]. Figure 2.6b and c show the filling of the energy levels in a semiconductor with a carrier concentration n, for the bulk and a thin nanowire with $d = 1$ nm, respectively.

It has been theoretically predicted that the diameters required for quantum confinement effects for some semiconductors are in the range of 4–8 nm[50,51]. Theoretically, at smaller diameters, the $1/d^2$ dependence of the *DOS* can enhance the thermoelectric power factor. So far, experimental evidence of the increase in power factor has only been observed in the work of Wu et al. (2013), where the rise of the power factor was measured for comparably thick (20–70 nm) InAs nanowires[52].

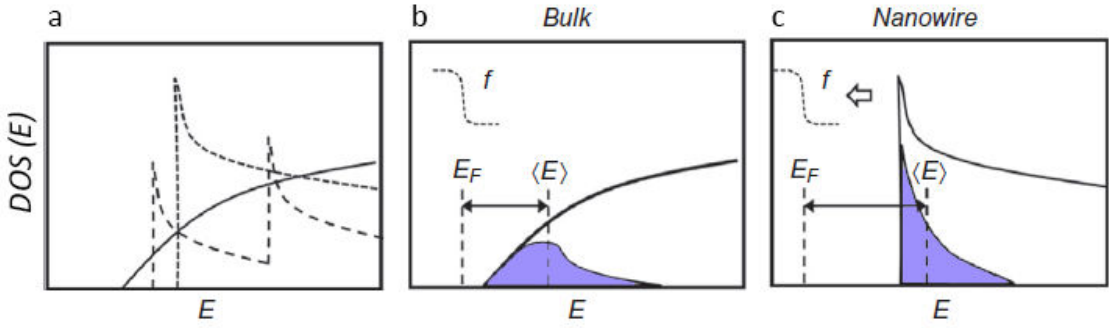

Figure 2.6. – **a,** Density of states of a bulk semiconductor (continuous line), of a semiconductor nanowire with $d = 50$ nm (dashed line) and of a nanowire with $d = 1$ nm (dotted line). **b,** Energy filling distribution for a bulk semiconductor. **c,** Energy filling distribution for a semiconductor nanowire with $d = 1$ nm. The Fermi level (E_F) and the average energy $<E>$ are indicated. Colored areas show levels occupied by electrons. – Adapted from reference 47.

2.4.3. Field-effect gate structures.

2.4.3.1. Field-effect conductivity, charge carrier density, and mobility.

The electrical conductivity σ is defined as the inverse of the electrical resistivity and is related to the geometrical properties of the wire[53]:

$$\sigma = \frac{1}{\rho} = \frac{l}{R \cdot A}, \tag{2.19}$$

where R is the resistance of the wire, ρ the electrical resistivity of the material, l the length, and A the cross-section of the wire.

In a traditional field-effect transistor (FET), the conductivity of the channel is controlled by a gate voltage, which can either deplete or enrich the channel, as shown in Figure 2.7[54]. A source-drain voltage (V_{SD}) induces a current through the device, for an open gate.

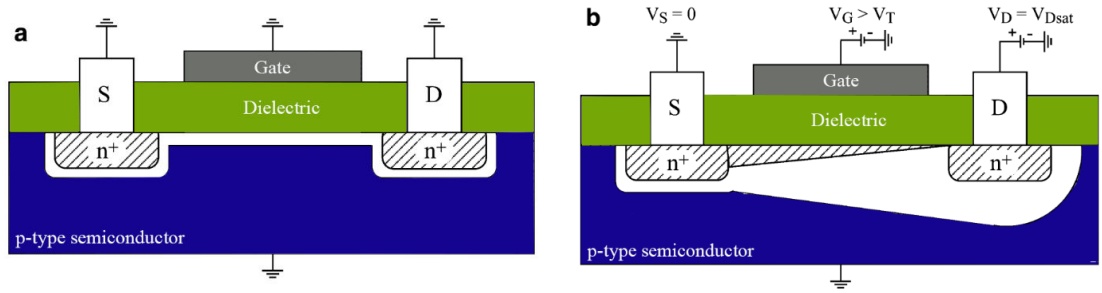

Figure 2.7. – Schematic illustration of a traditional FET with an n-channel: **a,** the enrichment regime. **b,** the pinching off (depleting) regime – Adapted from reference 55.

The charge carrier density of the conducting channel can be extracted from the dependence of a source-drain current I_{SD} versus the gate voltage V_G.

In this thesis, the geometry of the traditional FET is modified to a nanowire field-effect transistor (NW-FET). The field-effect mobility and the carrier density are derived from the field-effect measurements, following the standard square-law model, which is commonly used for nanowire field-effect devices[56–58]. The mobility (μ) of a nanowire with a length L is estimated using Eq. (2.20).

$$\mu = \frac{L^2}{C_{ox} \cdot V_{SD}} \left(\frac{dI_D}{dV_G} \right)_{\max,} \tag{2.20}$$

where V_{SD} is the applied source-drain voltage. The transconductance (dI_{SD}/dV_G) is determined as the slope of a drain current vs back-gate voltage sweep[59]. C_{ox} is the gate-nanowire capacitance. The approximation of a metallic cylinder of diameter d and length L on an infinite plate embedded in an insulating layer with the thickness of t_{ox} and dielectric constant ε is made for the global-gate capacitance calculation[60]. The thickness of the insulating layer is defined as t_{ox}. The capacitance can be calculated using Eq. (2.21)

$$C_{ox} = \frac{2\pi \cdot \varepsilon \cdot \varepsilon_0 \cdot L}{\operatorname{acosh}\left(\frac{d+2 \cdot t_{ox}}{d}\right),} \tag{2.21}$$

where ε is the dielectric constant of the embedding medium, ε_0 is the vacuum permitivity, d is the diameter of the wire, and t_{ox} is the thickness of the dielectric layer.

The effective charge carrier density n of the nanowire can be obtained from the back-gate sweep dependence by extracting the threshold voltage V_{th} of the FET as follows[61]:

$$n = \frac{4 \cdot C_{ox} \cdot V_{th}}{e \cdot \pi \cdot d^2 \cdot L,} \tag{2.22}$$

where e is the electron charge[62]. V_{th} is the threshold voltage, which is equal to the gate voltage where the tangent $(dI_{SD}/dV_G)_{max}$ intersects the horizontal axis. This extrapolation in the linear region technique is widely used in different works[63–65].

2.5. Landauer formalism for the thermal conductance.

The Landauer formalism is originally formulated for electrical conduction, but it can also be applied to phonon conduction[66–70]. The formalism determines the conductance as the integral of the conductances of all quantum channels in the wire. The Landauer formalism assumes that there is no coupling between the channels[71]. The conduction of an individual channel is modeled via a throughput function. The Landauer model for thermal conductance can be written as[41,42]:

$$G_{th} = \frac{1}{2\pi\hbar}\int_0^\infty T(\omega)\frac{\hbar^3\omega^2}{k_B T^2}\frac{e^{h\omega/k_B T}}{\left(e^{h\omega/k_B T}-1\right)^2}d\omega, \tag{2.23}$$

where $T(\omega)$ is the throughput function, which contains the channel density at frequency ω with their transmission probability; the last factor is the derivative of the Bose-Einstein distribution for phonons[42].

Here, the scattering processes are included in the throughput function. The formalism does not consider dephasing processes like Umklapp scattering[42]. Scattering at an interface can take place both specularly and diffusively; however, only the diffusive scattering reduces the thermal conduction. In case of specular scattering, the energy and the momentum of the phonons along the direction of the wire are conserved, while for diffusive scattering the energy is conserved but the momentum along the direction of the wire is not. The surface roughness determines the separation between specular and diffusive scattering. Specular scattering happens if the wavelength component of a phonon perpendicular to the surface is larger than the surface roughness. In this case, a cut-off frequency can be determined, which is the frequency of the modes that still undergo specular scattering at the surface. This frequency is defined as:

$$\omega_0 = \frac{\vartheta}{h}, \tag{2.24}$$

where ϑ is the speed of sound, and h is the thickness of the surface roughness.

The throughput can be expressed as follows[41]:

$$T(\omega) = \frac{N(\omega)}{1 + L/l_{mfp(avg)}(\omega)}, \tag{2.25}$$

where $N(\omega)$ is the number of modes, L is the length of the system, and $l_{mfp(avg)}$ is the average mean free path at frequency ω. When $l_{mfp(avg)} >> L$, the throughput becomes independent of the length, implying ballistic transport. When $l_{mfp(avg)} << L$, the throughput is proportional to $l_{mfp(avg)}/L$, characterizing diffusive transport.

The application of the Landauer formalism to phonon transport in GaP nanowires is discussed in detail in Chapter 5.

2.6. Summary.

The theoretical aspects of thermal and electrical transport in semiconductor nanowires have been discussed in this chapter. It has been shown that to estimate the effect of boundary scattering on heat transport, several techniques can be used. Aspects of electrical transport, conditions for establishing a high Seebeck coefficient in 1D systems and the influence of the field effect on the thermoelectric power factor of

nanowires have been addressed. The Landauer formalism was reviewed, which provides an estimation of the thermal conductance in nanowire systems.

2.7. References.

1. Li, Z., Sun, Q., Yao, X. D., Zhu, Z. H. & Lu, G. Q. Semiconductor nanowires for thermoelectrics. *Journal of Materials Chemistry* vol. 22 22821–22831 (2012).
2. Lee, S. H., Jang, S. Y., Roh, J. W., Park, J. & Lee, W. Thermoelectric properties of individual single-crystalline PbTe nanowires. in *INEC 2010 - 2010 3rd International Nanoelectronics Conference, Proceedings* 1203–1204 (2010). doi:10.1109/INEC.2010.5424953.
3. Lee, S., Kim, K., Kang, D.-H., Meyyappan, M. & Baek, C.-K. Vertical Silicon Nanowire Thermoelectric Modules with Enhanced Thermoelectric Properties. *Nano Lett.* **19**, 747–755 (2019).
4. Hicks, L. D. & Dresselhaus, M. S. Effect of quantum-well structures on the thermoelectric figure of merit. *Phys. Rev. B* **47**, 12727–12731 (1993).
5. Goldsmid, H. J. *The physics of thermoelectric energy conversion. The Physics of Thermoelectric Energy Conversion* (Morgan and Claypool Publishers, 2017). doi:10.1088/978-1-6817-4641-8.
6. da Rosa, A. V. *Fundamentals of Renewable Energy Processes. Fundamentals of Renewable Energy Processes* (Elsevier Inc., 2013). doi:10.1016/C2011-0-06913-2.
7. Cochran, W. *The dynamics of atoms in crystals.* (Edward Arnold, 1973).
8. Chaichian, M. (Masud), Perez Rojas, H. & Tureanu, A. *Basic concepts in physics : from the cosmos to quarks.*
9. Bourgeois, O. *et al.* Reduction of phonon mean free path: From low-temperature physics to room temperature applications in thermoelectricity. *Comptes Rendus Physique* vol. 17 1154–1160 (2016).
10. Tran, J. T. V., Fontaine, G. (Gérard), Hinds, E. (Edward) & Rencontre de Moriond (28th : 1993 : Villars-sur-Ollon, S. *Particle astrophysics, atomic physics and gravitation : proceedings of the XXIXth Rencontre de Moriond, series: Moriond Workshops : Villars sur Ollon, Switzerland, January 22-29, 1994.* (Editions Frontières, 1994).
11. Barbosa, F. R. & Srivastava, R. Low-frequency optical phonons in silica. *Solid State Commun.* **34**, 305–308 (1980).
12. Larkin, J. M., Turney, J. E., Massicotte, A. D., Amon, C. H. & McGaughey, A. J. H. Comparison and evaluation of spectral energy methods for predicting phonon properties. *J. Comput. Theor. Nanosci.* **11**, 249–256 (2014).
13. Fan, D. D. *et al.* Understanding the electronic and phonon transport properties of a thermoelectric material BiCuSeO: A first-principles study. *Phys. Chem. Chem. Phys.* **19**, 12913–12920 (2017).
14. Gold-Parker, A. *et al.* Acoustic phonon lifetimes limit thermal transport in methylammonium lead iodide. *Proc. Natl. Acad. Sci. U. S. A.* **115**, 11905–11910 (2018).
15. Koh, Y. K. & Cahill, D. G. Frequency dependence of the thermal conductivity

of semiconductor alloys. *Phys. Rev. B - Condens. Matter Mater. Phys.* **76**, (2007).

16. Anufriev, R., Gluchko, S., Volz, S. & Nomura, M. Quasi-Ballistic Heat Conduction due to Lévy Phonon Flights in Silicon Nanowires. *ACS Nano* **12**, 11928–11935 (2018).
17. Hu, Y., Zeng, L., Minnich, A. J., Dresselhaus, M. S. & Chen, G. Spectral mapping of thermal conductivity through nanoscale ballistic transport. *Nat. Nanotechnol.* **10**, 701–706 (2015).
18. Alvarez, F. X., Jou, D. & Sellitto, A. Phonon hydrodynamics and phonon-boundary scattering in nanosystems. *J. Appl. Phys.* **105**, (2009).
19. Cepellotti, A. *et al.* Phonon hydrodynamics in two-dimensional materials. *Nat. Commun.* **6**, (2015).
20. Lee, S., Broido, D., Esfarjani, K. & Chen, G. Hydrodynamic phonon transport in suspended graphene. *Nat. Commun.* **6**, 6290 (2015).
21. Ding, Z. *et al.* Phonon hydrodynamic heat conduction and Knudsen minimum in graphite. *Nano Lett.* **18**, 638–649 (2017).
22. Torres, P. *et al.* First principles kinetic-collective thermal conductivity of semiconductors. *Phys. Rev. B* **95**, (2017).
23. Ziabari, A. *et al.* Full-field thermal imaging of quasiballistic crosstalk reduction in nanoscale devices. *Nat. Commun.* **9**, (2018).
24. Martelli, V., Jiménez, J. L., Continentino, M., Baggio-Saitovitch, E. & Behnia, K. Thermal Transport and Phonon Hydrodynamics in Strontium Titanate. *Phys. Rev. Lett.* **120**, (2018).
25. Beardo, A. *et al.* Hydrodynamic Heat Transport in Compact and Holey Silicon Thin Films. *Phys. Rev. Appl.* **11**, (2019).
26. Siemens, M. E. *et al.* Quasi-ballistic thermal transport from nanoscale interfaces observed using ultrafast coherent soft X-ray beams. *Nat. Mater.* **9**, 26–30 (2010).
27. Bae, M. H. *et al.* Ballistic to diffusive crossover of heat flow in graphene ribbons. *Nat. Commun.* **4**, (2013).
28. Hsiao, T. K. *et al.* Observation of room erature ballistic thermal conduction persisting over 8.3 μm in SiGe nanowires. *Nat. Nanotechnol.* **8**, 534–538 (2013).
29. Wilson, R. B. & Cahill, D. G. Anisotropic failure of Fourier theory in time-domain thermoreflectance experiments. *Nat. Commun.* **5**, (2014).
30. Lee, J., Lim, J. & Yang, P. Ballistic Phonon Transport in Holey Silicon. *Nano Lett.* **15**, 3273–3279 (2015).
31. Anufriev, R., Ramiere, A., Maire, J. & Nomura, M. Heat guiding and focusing using ballistic phonon transport in phononic nanostructures. *Nat. Commun.* **8**, (2017).
32. Matthiessen, A., Vogt, C., Matthiessen, A. & Vogt, C. On the Influence of Temperature on the Electric Conducting-Power of Alloys. *RSPT* **154**, 167–200 (1864).
33. Swinkels, M. Y. *et al.* Diameter dependence of the thermal conductivity of InAs nanowires. *Nanotechnology* **26**, 385401 (2015).
34. Srivastava, G. P. *The physics of phonons.* (A. Hilger, 1990).

35. Ziman, J. M. *Electrons and Phonons : The Theory of Transport Phenomena in Solids Abstract and Keywords*. (2001). doi:10.1093/acprof.
36. Ibach, H. & Lüth, H. *Solid-State Physics*. (Springer Berlin Heidelberg, 1991). doi:10.1007/978-3-642-97230-0.
37. Jumper, W. D. & Lawrence, W. E. Low-temperature electrical and thermal resistivities of potassium: Deviations from Matthiessen's rule. *Phys. Rev. B* **16**, 3314–3321 (1977).
38. Karamargin, M. C., Reynolds, C. A., Lipschultz, F. P. & Klemens, P. G. Lattice thermal conductivity and deviations from Matthiessen's rule for dilute alloys of tin with cadmium. *Phys. Rev. B* **6**, 3624–3633 (1972).
39. Rashid, Z., Zhu, L. & Li, W. Effect of confinement on anharmonic phonon scattering and thermal conductivity in pristine silicon nanowires. *Phys. Rev. B* **97**, 75441 (2018).
40. Hicks, L. D. & Dresselhaus, M. S. Thermoelectric figure of merit of a one-dimensional conductor. *Phys. Rev. B* **47**, 16631–16634 (1993).
41. Chen, R. *et al.* Thermal Conductance of Thin Silicon Nanowires. *Phys. Rev. Lett.* **101**, (2008).
42. Murphy, P. G. & Moore, J. E. Coherent phonon scattering effects on thermal transport in thin semiconductor nanowires. *Phys. Rev. B - Condens. Matter Mater. Phys.* **76**, (2007).
43. Seebeck, T. J. Ueber die magnetische Polarisation der Metalle und Erze durch Temperatur-Differenz. *Ann. Phys.* **82**, 1–20 (1826).
44. Pichanusakorn, P. & Bandaru, P. R. Minimum length scales for enhancement of the power factor in thermoelectric nanostructures. *J. Appl. Phys.* **107**, (2010).
45. G. S. Nolas, J. Sharp, J. G. *Thermoelectrics, Basic principle and new materials development*. (Springer-Verlag Berlin Heidelberg, 2001). doi:70.1007/978-3-662-04569-5.
46. Gadea, G., Morata, A. & Tarancon, A. Semiconductor Nanowires for Thermoelectric Generation. in 321–407 (2018). doi:10.1016/bs.semsem.2018.01.001.
47. Krane, K. S. *Introductory Nuclear Physics, 3rd Edition*. (1987).
48. Koumoto, K. Thermoelectric nanomaterials. (Springer, 2015).
49. Pichanusakorn, P. & Bandaru, P. Nanostructured thermoelectrics. doi:10.1016/j.mser.2009.10.001.
50. Goldsmid, H. J. *Introduction to thermoelectricity*. (Springer, 2010).
51. Cornett, J. E. & Rabin, O. Thermoelectric figure of merit calculations for semiconducting nanowires. *Appl. Phys. Lett.* **98**, (2011).
52. Wu, P. M. *et al.* Large thermoelectric power factor enhancement observed in InAs nanowires. *Nano Lett.* **13**, 4080–4086 (2013).
53. Young, H. University physics with modern physics. (Addison-Wesley, 2015).
54. Huang, C., Marshall, M. & White, B. H. Field effect transistor applications. *Trans. Am. Inst. Electr. Eng. Part I Commun. Electron.* **75**, 323–329 (2013).
55. Bouvet, M. Phthalocyanine-based field-effect transistors as gas sensors. *Anal. Bioanal. Chem.* **384**, 366–373 (2006).

56. Shen, L. F. *et al.* High-Performance Wrap-Gated InGaAs Nanowire Field-Effect Transistors with Sputtered Dielectrics. *Sci. Rep.* **5**, (2015).
57. Gül, Ö. *et al.* Towards high mobility InSb nanowire devices. *Nanotechnology* **26**, (2015).
58. Ford, A. C. *et al.* Diameter-dependent electron mobility of lnas nanowires. *Nano Lett.* **9**, 360–365 (2009).
59. S. M. Sze . Kwok K. Ng. *Physics of Semiconducting Devices.* (John Wiley & Sons, Inc., Hoboken, New Jersey, 2007).
60. Ramo, S., Whinnery, J. . & Van Duzer, T. Maxwell's Equation: Penetration of Electromagnetic fields into a good conductor. in *Fields and waves in communication electronics* 149–153 (John Wiley & Sons, Inc., 1994).
61. Van Weperen, I., Plissard, S. R., Bakkers, E. P. A. M., Frolov, S. M. & Kouwenhoven, L. P. Quantized conductance in an InSb nanowire. *Nano Lett.* **13**, 387–391 (2013).
62. Scheffler, M., Nadj-Perge, S., Kouwenhoven, L. P., Borgström, M. T. & Bakkers, E. P. A. M. Diameter-dependent conductance of InAs nanowires. *J. Appl. Phys.* **106**, (2009).
63. Ortiz-Conde, A. *et al.* A review of recent MOSFET threshold voltage extraction methods. *Microelectron. Reliab.* **42**, 583–596 (2002).
64. Jang, S. Y. *et al.* Transport properties of single-crystalline n-type semiconducting PbTe nanowires. *Nanotechnology* **20**, (2009).
65. Heedt, S. *et al.* Electronic Properties of Complex Self-Assembled InAs Nanowire Networks. *Adv. Electron. Mater.* **2**, 1500460 (2016).
66. Yazji, S. *et al.* Complete thermoelectric benchmarking of individual InSb nanowires using combined micro-Raman and electric transport analysis. *Nano Res.* **8**, 4048–4060 (2015).
67. Shi, L. *et al.* Measuring thermal and thermoelectric properties of one-dimensional nanostructures using a microfabricated device. *J. Heat Transfer* **125**, 881–888 (2003).
68. Wingert, M. C. *et al.* Sub-amorphous Thermal Conductivity in Ultrathin Crystalline Silicon Nanotubes. *Nano Lett.* **15**, 2605–2611 (2015).
69. Chen, J., Zhang, G. & Li, B. Remarkable reduction of thermal conductivity in silicon nanotubes. *Nano Lett.* **10**, 3978–3983 (2010).
70. Cahill, D. G. *et al.* Nanoscale thermal transport. *Journal of Applied Physics* vol. 93 793–818 (2003).
71. Nazarov, Y. & Blanter, Y. Quantum transport. (Cambridge University Press, 2009).

Chapter 3. Device fabrication.

In this chapter, the growth of the nanowires, the processing of the microdevices, and the preparation of the samples for measurements are described. Since the growth optimization is not part of this research, the nanowire growth is discussed only briefly in Section 3.1. In Section 3.2, the fabrication process of the thermal conductivity microdevice is described in detail. Section 3.3 addresses the fabrication process and technological parameters of thermopower device fabrication. All additional information is given in Appendix A3.

3.1. Nanowire growth.

Nanowires can be made using a wide variety of methods. In general, growth methods can be divided into two groups: top-down and bottom-up techniques. In the top-down techniques, a layer of material is grown, and after that, the layer is locally etched away to form nanowires[1]. In bottom-up methods, the nanowires are grown on selective parts of the substrate[2]. Bottom-up approaches contain catalyzed and non-catalyzed growth techniques. In catalyzed growth, catalyst particles are used to boost the growth and, hence, form nanowires. Nanowires studied in this thesis were grown using the catalyzed bottom-up method called Vapor-Liquid-Solid (VLS) growth[2], which is described in the next section.

3.1.1. VLS growth.

Small catalytic particles are formed on a substrate to grow nanowires. Electron Beam Lithography (EBL)[3], nanoimprint lithography[4], or dispersed colloidal particles over the substrate[5] can be used for this purpose. In a chemical vapor deposition (CVD) growth reactor, gas precursors are introduced into the chamber. After decomposition, the precursors are absorbed in the catalytic particle, forming a liquid alloy. The crystal growth nucleates at the liquid/solid interface when the alloy is supersaturated[6]. A schematic overview of the VLS technique is shown in Figure 3.1.

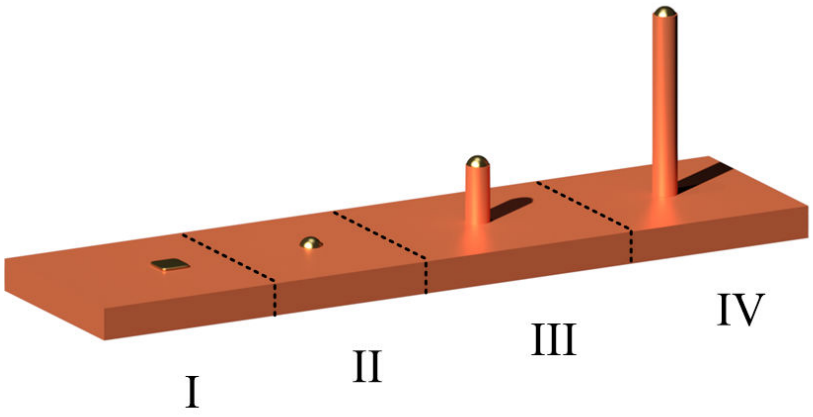

Figure 3.1. – Stages of catalyzed VLS growth: I) A catalytic particle (in our case Au) is placed on the sample; II) The sample is heated under a gas flow with the group V constituents of the final nanowire; III) VLS growth of the nanowire is initiated by switching on the group III flow; IV) Axial and radial NW growth.

In the VLS method, the diameter of the nanowire depends on the dimensions of the liquid alloy[2]. The growth process can be tuned by changing the substrate temperature, gas flows, and chamber pressure. Additionally, selective-area epitaxy (SAE), involving a patterned mask substrate that directs one-dimensional growth, has emerged as a natural candidate to provide highly regular arrays of NWs with perfect vertical yield[7]. SAE is highly successful in producing uniform arrays of III−V nanowires without the necessity to use catalytic metal particles. The benefits of the VLS and SAE techniques can be combined, resulting in high yield and better control of the NW diameter[8,9]. The SAE-VLS growth technique is schematically illustrated in Figure 3.2. This technique has been applied to grow InSb nanowires. The detailed growth description can be found in Section 3.1.4.

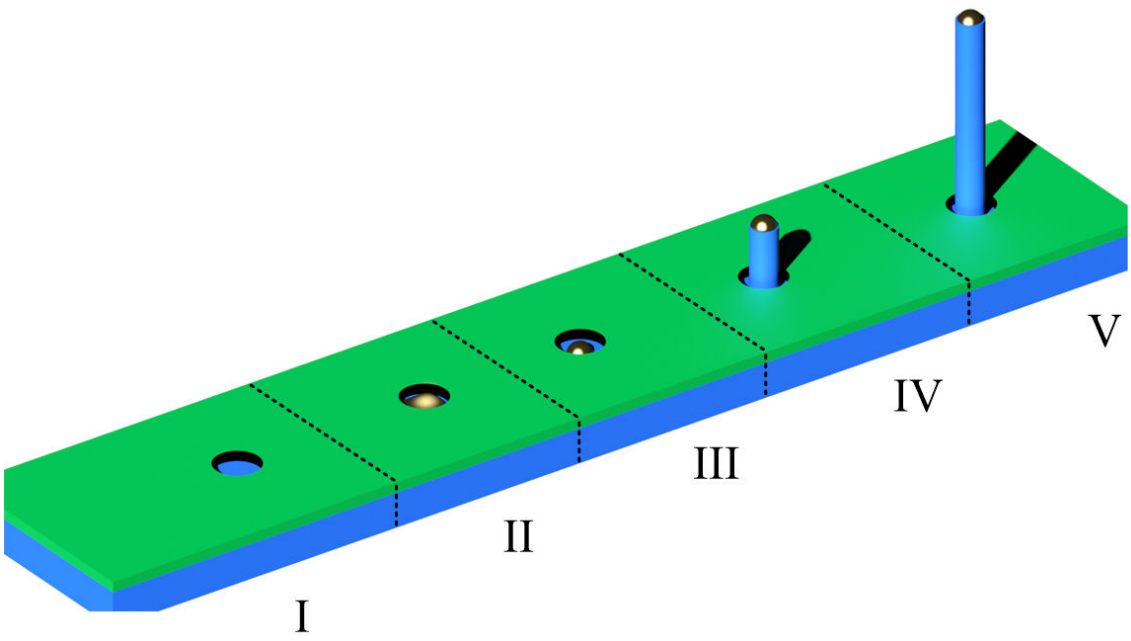

Figure 3.2. – Stages of SAE VLS growth technique: I) a Si_3N_4 layer (colored in green) is deposited using plasma-enhanced chemical vapor deposition, and holes are etched with a buffered oxide etchant; II) 8 nm gold particles are deposited using electron beam lithography (EBL) and a lift-off process; III) The sample is heated under a gas flow with the group V constituent of the final nanowire and forms an alloy; IV) VLS growth of the nanowire underneath the catalytic particle; V) Axial and radial NW growth.

3.1.2. Sample growth.

This section provides a short overview of the growth processes used for the different nanowire samples. More detailed information on the substrate preparation, and growth parameters presented in Appendixes A3.1 and A3.2.

3.1.2.1. GaP nanowires.

GaP nanowires (NWs) are grown by the VLS method, using an array of gold catalyst droplets on a (111)B GaP substrate inside a metal-organic vapor-phase epitaxy (MOVPE) reactor. A schematic illustration of the growth technique is shown in figure 4.1. The patterns for NW growth are fabricated by EBL, followed by a lift-off process of the 4 nm thick gold layer to achieve NWs with small diameters. The NWs were grown at 750 °C using Tri-Methyl Gallium (TMG) and Phosphine (PH_3) as precursors[10]. In order to obtain nucleation of NWs with diameters smaller than 40 nm, the V/III ratio has to be increased by a factor of five during the nucleation step (the absolute values are given in Appendix A3.1) and by a factor of two during the growth of the NWs, as compared to the V/III ratio used for NWs with a larger diameter. This

effect can be attributed to the Gibbs-Thomson effect[11,12], where the high surface tension of small-diameter catalyst droplets leads to a lower supersaturation than for large-diameter droplets. By increasing the V/III ratio, the supersaturation is brought to an optimal level for the NW growth. In this way, it is possible to create NWs with a diameter in the range 25-140 nm on the same substrate. Figure 3.3 shows a SEM image of nanowire arrays.

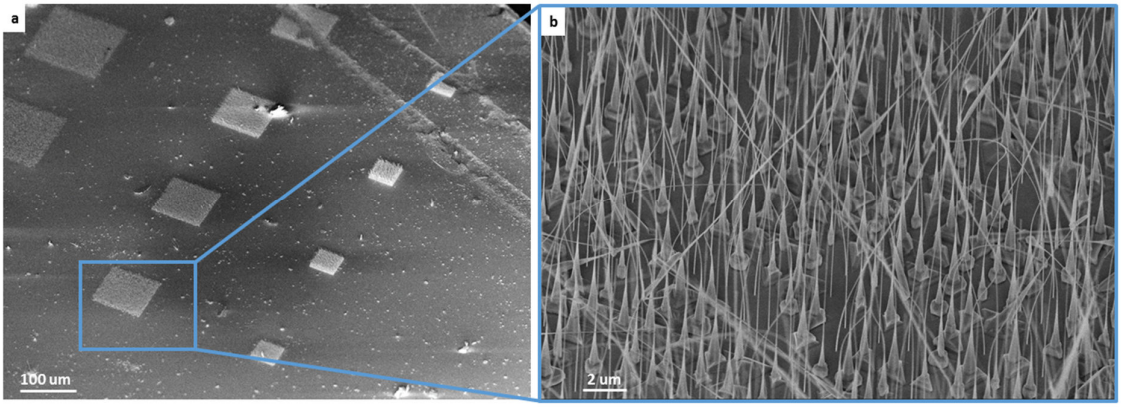

Figure 3.3. – **a,** SEM image of GaP NW arrays. **b**, The zoomed-in image of 25 nm thin GaP nanowires. The images are taken with 5 kV acceleration voltage and under 45^{o} tilt.

A high-resolution transmission electron microscopy (TEM) image, shown in Figure 3.4, indicates that the NWs have a uniform diameter along their length and a defect-free wurtzite (WZ) crystal structure, although the bulk crystal structure of GaP is zinc blende[10]. A native gallium oxide layer of about 2 nm thick is present on the surface of each NW.

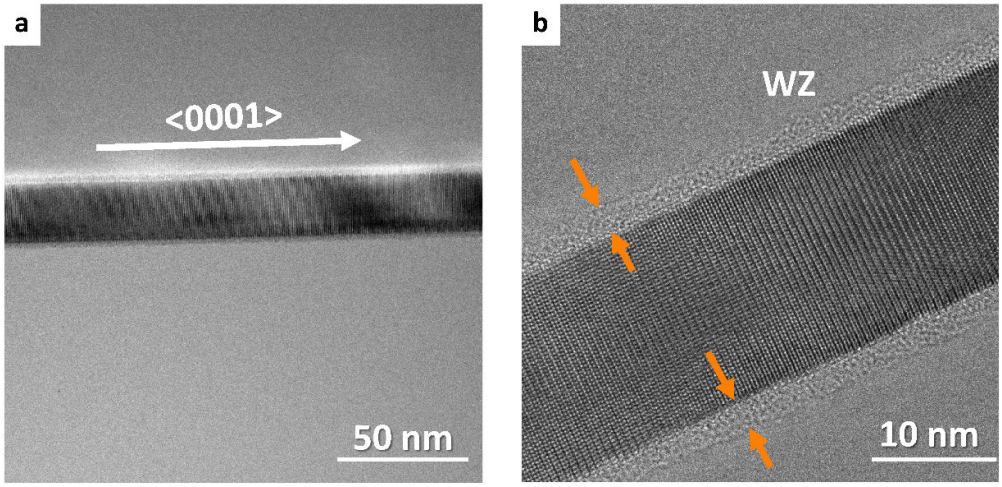

Figure 3.4. – **a**, TEM image of a 25 nm diameter GaP nanowire (NW), grown along the <0001> direction. **b**, A high-resolution TEM image was taken along the <11$\bar{2}$0> direction showing defect-free wurtzite (WZ) crystal structure and a layer of gallium oxide (orange arrows).

3.1.2.2. InSb nanowires.

The InSb nanowires are grown on InSb (111)B substrates using the SAE VLS growth technique stated in the previous section (see Figure 3.2). The nanowires are grown in a horizontal Aixtron 200 MOVPE reactor. A schematic illustration of the growth process is shown in Figure 3.2. In this process, a Si_3N_4 mask is used to decrease the parasitic growth[13]. The sample is heated to 495 °C. The precursors, trimethyl indium, and trimethyl antimony are introduced in the gas phase, and In, and Sb atoms dissolve in the Au particle, resulting in a liquid catalyst droplet. InSb growth nucleates below the droplet when the catalyst is supersaturated. A detailed description of the fabrication process is presented in Appendix A3.2. A typical SEM image of the InSb nanowires used in the thesis is shown in Figure 3.5.

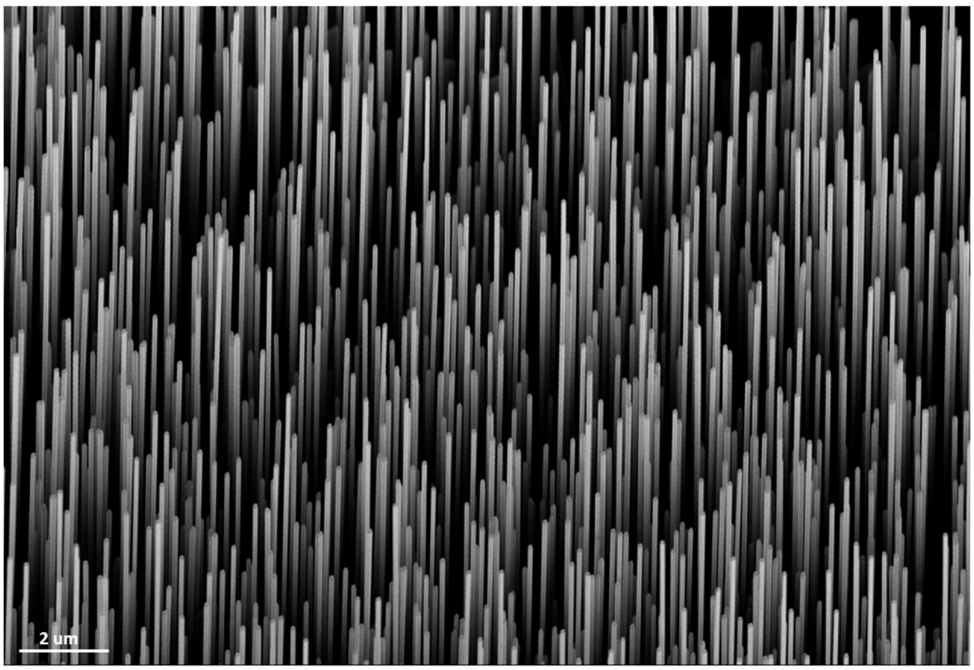

Figure 3.5. – SEM image of the InSb nanowires grown by the VLS technique. The picture is taken at 5 kV acceleration voltage and under 30° tilt.

TEM images, shown in Figure 3.6, indicate that the NWs have a uniform diameter along their length and a defect-free zinc blende (ZB) crystal structure, the same crystal structure as bulk InSb[13].

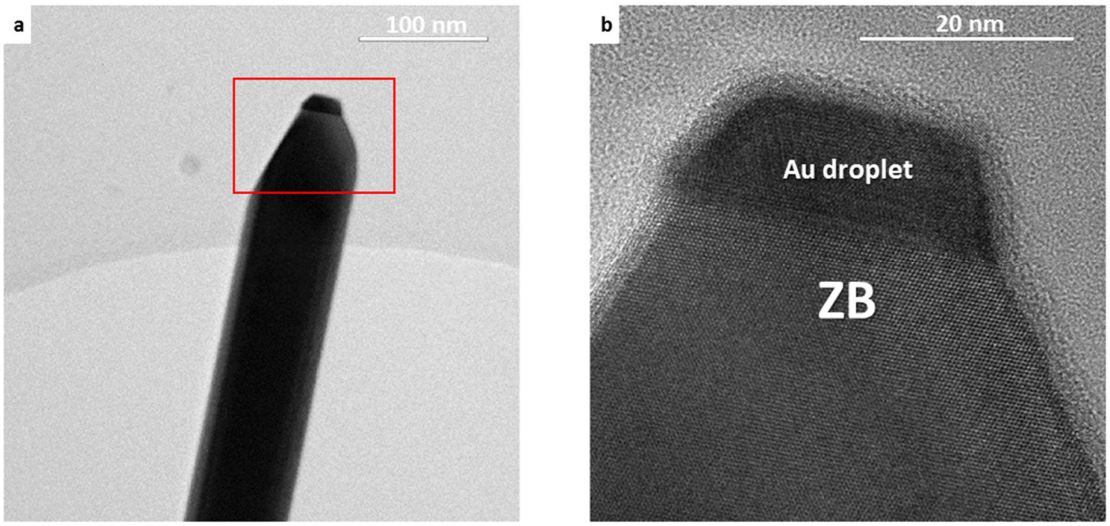

Figure 3.6. – **a**, Transmission electron microscope micrograph of an InSb nanowire. **b**, High-resolution TEM of the marked area showing the zinc blende crystal structure of the nanowires.

3.2. Fabrication of microdevice to measure thermal conductivity.

In order to study the thermal properties of nanowires (NWs), microdevices are fabricated, which allow measuring the thermal conductance of nanowires (see Chapter 4 for more details). In this section, the processing steps of the device fabrication are discussed. All the processing took place in the cleanroom facilities of Nanolab@TUe at the Eindhoven University of Technology. The chapter will follow the order of the manufacturing technology.

An overview of the processing steps is presented in Figure 3.7.

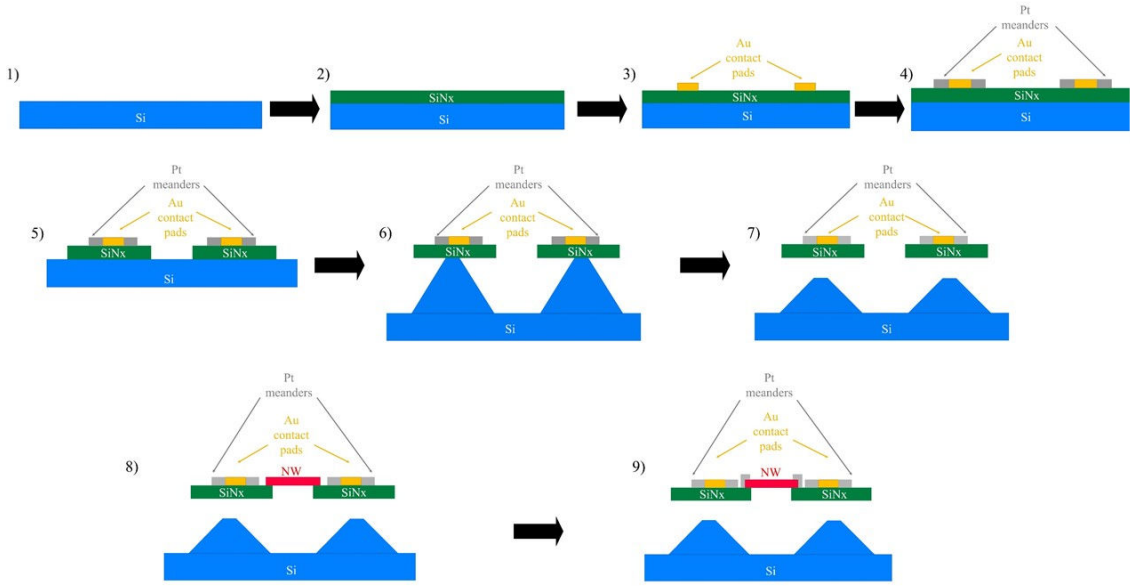

Figure 3.7. – Schematic overview of the microdevice fabrication steps: 1) i-Si (100) wafer used as a substrate; 2) Si_3N_4 layer grown by plasma-enhanced chemical vapor deposition (PECVD); 3) Au contact pads are defined using electron beam lithography (EBL) and lift-off process; 4) Pt lines and meanders are created by EBL and lift-off process; 5) Si_3N_4 membranes are defined using EBL and reacting-ion etching (RIE) process; 6) Si wet etching with Tetramethylammonium hydroxide (TMAH); 7) Si down-etch with KOH; 8) NW placed between the membranes; 9) Pt/C top contacts are deposited by electron beam-induced deposition (EBID).

3.2.1. Si_3N_4 film growth.

The growth of the Si_3N_4 film is performed on the Si [100] using a Plasma Enhanced Chemical Vapour Deposition (PECVD) process. PECVD is a Chemical Vapour Deposition process where a plasma is used to break the chemical bonds of the precursor material. Because a plasma is used to break these bonds, the growth can take place at lower temperatures, 300 °C in our case. The PECVD reactor used for this growth has a parallel plate reactor. Therefore, the plasma is created between two

parallel plates. One of them acts as a sample holder. In order to form the plasma, a high AC voltage between the plates was applied. A combination of two different frequencies of the AC voltage was used to fabricate a stress-free Si_3N_4 film in the PECVD reactor[14]. It is essential to have a stress-free layer, to avoid damaging the suspended membranes. If the tensile stress in the layer is too high, it will break the membranes once they are released from the substrate, while a compressive strain would cause buckling of the membranes. Thus, during the growth, the frequency is repetitively changed from high to low frequency and back, which helps to reduce the stress in the growing layer[14].

A high frequency will mainly accelerate the electrons since the ions are unable to follow such higher frequency[15]. Contrary, a low frequency activates the ions, and, therefore, they will be accelerated towards the surface and bombard it[14]. This process creates two effects. First, the ions can be implanted into the film, resulting in a higher packing density and, thus, inducing compressive strain in the film. Second, the ions deliver energy to the surface, enhancing surface migration and reactions, reducing the tensile stress in the film. Hence, high frequency gives tensile strain; contrary, low frequency gives compressive strain. Stress-free film formation can be achieved by choosing a proper combination of the frequencies[15]. SiH_4, N_2, and NH_3 precursors were used to grow the Si_3N_4 film. The composition of the film depends strongly on the ratio between these precursors. A combination of high and low frequency of 13.56 MHz and 50 kHz, respectively, was used. The exact ratio between the high (HF) and the low-frequency (LF) pulse time was varied. The used pulse times were consistently 5-7 s and 13-15 s for the LF and the HF pulses, respectively. This set of parameters allows keeping the tensile strain small enough. The determined growth rate is around 11 nm/min depending on the machine condition. A growth time of 60 min was used, giving a thickness of the Si_3N_4 layer around 650 nm.

3.2.2. Au contact pads.

It is crucial to make contact pads, that are mechanically stable when contacted with the measurement probes. Thus, Au has been chosen for this purpose. The contact pads are created using EBL and lift off. In order to prepare the sample for EBL, the sample is cleaned using a 300 W oxygen plasma for 10 minutes. Right after that, a 950 K PMMA A11 resist is spun at 6000 RPM in an open-air spinner for 30 s. Afterward, the resist is baked in an oven at 175 °C for 30 min. Baking removes all the solvents from the resist, forming a stable layer with a thickness of about 1.3 μm. After that, the sample is loaded in the EBL chamber. The 950K PMMA A11 is a positive resist, meaning that electron exposed parts will disappear after development. The higher the electron dose, the more material will be removed. A higher dose will also result in steeper slopes of the exposed resist sidewalls due to the backscattering of electrons on the surface, which might affect the lift-off process. Therefore, the appropriate dose must be chosen carefully. In order to estimate the right dose, Monte Carlo simulations have been done[17]. The results of the simulations are shown in figure A3.1. Based on the

obtained results, the proper dose is chosen for every EBL step. The detailed parameters of the EBL exposure can be found in Appendix A3.4.

After the exposure, the photoresist is developed using the PMMA developer Methyl-iso-butyl ketone (MIBK: IPA solution with the ratio of 1:3) for 80 s followed by IPA cleaning for 80 s. Once the resist is developed, the sample is placed inside an evaporator. A flux of metal atoms towards the surface is created by evaporation using heating from accelerated electrons. The process is controlled using a crystal monitor to ensure reproducible thicknesses. A stack of 14/140 nm Ti/Au layers is deposited for the contact pads in this way. The Ti layer is used as an adhesive layer[18]. The sample is placed in a closed beaker above the acetone for the lift-off process of the Ti/Au layer. The sample is kept in the acetone vapor for 15 min. During that time, small cracks appear at the metallization layer, which helps to access the polymer layer in the next step. After that, the sample is directly placed inside acetone for 5 minutes, followed by an ultrasonic bath for 5 minutes until all undesired metal is gone. As a result, all the resist is removed, and the designed contacts are left. As a final step, the sample is placed inside Isopropyl alcohol (IPA) for 2 min to remove acetone leftovers.

3.2.3. Pt meanders and lines.

In a next step, the Pt meanders and lines are manufactured in a similar way as the Au contact pads. Samples are cleaned using a 300 W Oxygen plasma for 10 minutes. After that, the resist, 950 K PMMA A4, is spun at 8000 RPM in an open-air spinner for 30 s. The sample is placed inside the oven at 175 °C for 30 min removing the solvents and creating a stable resist layer with a thickness of 140 nm. The sample is then directly placed in the EBL chamber. For the development process, an MIBK: IPA solution was used with a ratio of 1:3 and a development time of 80 s, after which the sample was rinsed in IPA for 80 s. After the development, the sample is cleaned by a 100 W O_2 plasma for 10 s to remove residues from the surface. After the oxygen plasma, the sample is placed in the chamber of the Pt evaporator for metal deposition, and a 30 nm thick Pt layer is deposited. The thickness has been chosen based on COMSOL Multiphysics simulation results presented in Chapter 4.

In this process, the Pt layer has been deposited without any sticking layer (commonly used are Ti or Ni to enhance the adhesive properties of a noble metal to the substrate). It is essential to reduce the thermal conduction and improve the temperature dependence of the meanders' resistance. Even a thin adhesive layer would have a significant effect on these parameters. Nevertheless, without an adhesive layer, the Pt is less likely to stick to the Si_3N_4 layer. Thus, special care has to be taken during processing. After 15 min inside the acetone, vapor cracks appear, and the sample is placed vertically inside the acetone and left in the solution overnight. After that, the lifted Pt layer is gently blown away using a pipette. The sample is placed inside IPA for 20 min to remove acetone leftovers and in a 300 W O_2 plasma for 10 minutes to remove organic leftovers.

3.2.4. Si_3N_4 dry etching.

Once the Pt meanders and lines are created, a protective Si_3N_4 layer is deposited on top. Without this layer, the Pt structures would be slightly under-etched, and as a result, the entire structure could be removed. Therefore, the sample is placed inside a PECVD reactor for 31 minutes in order to grow a 350 nm stress-free Si_3N_4 layer on top of the metals. After deposition of the protection layer, the shapes of the membranes and supporting beams are defined using EBL. The process is similar to the process for the Au pads definition. However, in this case, a thicker layer of 950 K PMMA A11 resist is used. The resist spun at 2000 RPM for 30 s results in a thickness of 1.3 μm. In order to remove all the solvents after spinning, the sample is baked inside an oven for 30 minutes at 175 °C. The parameters of the EBL exposure can be found in Appendix A3.4.

The exposure is followed by a developed step using an MIBK: IPA 1:3 solution for 80 s and IPA cleaning for 80 s. After the development, the sample is placed inside a Reactive Ion Etching (RIE) reactor. The machine etches materials using a combination of physical ion bombardment to increase the energy at the surface and reactive ions, which induces selectivity for different materials. The Si_3N_4 is etched using a mixture of a CHF_3 and an O_2 plasma. In this way, all the components are etched. However, the etch rate for Si_3N_4 (110 nm/min) is much higher than for PMMA (65 nm/min). Thus, according to estimations, about 1.2 μm of Si_3N_4 could be etched. Hence, an etching time of 11 min is more than required. However, a longer etching time could compensate for fluctuations in the etch rate and the thickness variation. After the Si_3N_4 is etched all the way through, the Si might be etched but with a lower etching rate than the Si_3N_4. A thin layer of reaction products of the etching process is created on the etched surfaces after the RIE process. This layer has to be removed before the next etching step. Thus, a 300 W O_2 plasma cleaning and 5 s HF (1%) dip is used to eliminate the unwanted layer. After this step, the sample is ready for the Si wet etching steps.

3.2.5. Si wet etching.

In order to suspend the Si_3N_4 membranes, the underlying Si layer is etched. The Si etching step is performed using an AZ 826 MIF developer solution, a mixture of a 2.38% Tetramethylammonium hydroxide (TMAH) solution with certain surfactants, at a temperature of 80 °C[19]. It has been found that a low concentration of TMAH etches isotropically[19].

The chemical reaction mechanism of the Si wet etching can be written as Eq. (3.1). This reaction is based on the basic character of the substances, which causes the OH^- group to bind to the silicon.

$$2\left[(CH_3)_4\,N\right]^+\left[OH\right]^- + Si + 2H_2O \rightarrow 2\left[(CH_3)_4\,N\right]^+ + Si(OH)_2O_2^{2-} + 2H_2. \tag{3.1}$$

The orthosilicic acid formed by the chemical reaction will be dissolved in the etching solution. The etching rate of Si is about 2 μm/hr. In order to make the 10 μm undercut, the sample has been placed in the solution for 5 hours. The TMAH slightly etches Si_3N_4 (around 40 nm/hour) and, thus, will marginally change the dimensions of the membrane structure and partly remove the protective Si_3N_4 layer.

3.2.6. Si down etching.

After the undercut etching step, the membrane structures are almost suspended. However, anisotropic etching of Si will result in the pyramid-like structure formation under the membranes (Figure 3.7 step 6). Therefore, an extra etching step must be implemented to make the structures fully suspended. KOH serves as an anisotropic etching agent with the [111] stop plane[20]; thus, it can be used to remove the pyramid-like structures underneath the membranes. Directly after the previous fabrication step, the sample is rinsed in ultra-pure-water (UPW) and then placed inside a 33% KOH water-based solution at 80°C for 5 minutes. It is crucial to keep the sample wet at all wet etching steps to prevent collapsing of the membranes by capillary forces. The simplified chemical reaction of the KOH etching can be written as:

$$Si + 2OH^- + 2H_2O \rightarrow SiO_2(OH)_2^{2-} + 2H_2. \tag{3.2}$$

The KOH solution has a highly anisotropic etching, preferably etching in the [100] direction with an etching rate of about 1.4 μm/min. KOH has a negligible etching rate of Si_3N_4 and also does not attack Pt, which might be exposed because the protective Si_3N_4 layer could be partially open during the first wet etching step. After etching for 5 min, the membranes are fully suspended and ready for the drying step.

3.2.7. IPA vapor drying.

After the Si down etching step, the sample is rinsed in (UPW). In order to prevent collapsing of the membranes from the drying water, the sample is placed in IPA at 80 °C, in which the water will dissolve. The sample is kept above heated IPA. IPA vapor has a smaller surface tension than water. Thus, this reduces capillary forces, preventing pulling down of the membranes, which would cause collapsing.

3.2.8. Si_3N_4 layer elimination.

Finally, the leftovers of the protection Si_3N_4 layer are removed by RIE etching using a similar method as applied to define the membranes and beams discussed in Section 3.2.4. A recipe with an etching rate of about 15 nm/min was used. Typically, the etching time for this process is in the range from 3 to 4 min. An SEM picture of the manufactured device is shown in Figure 3.8.

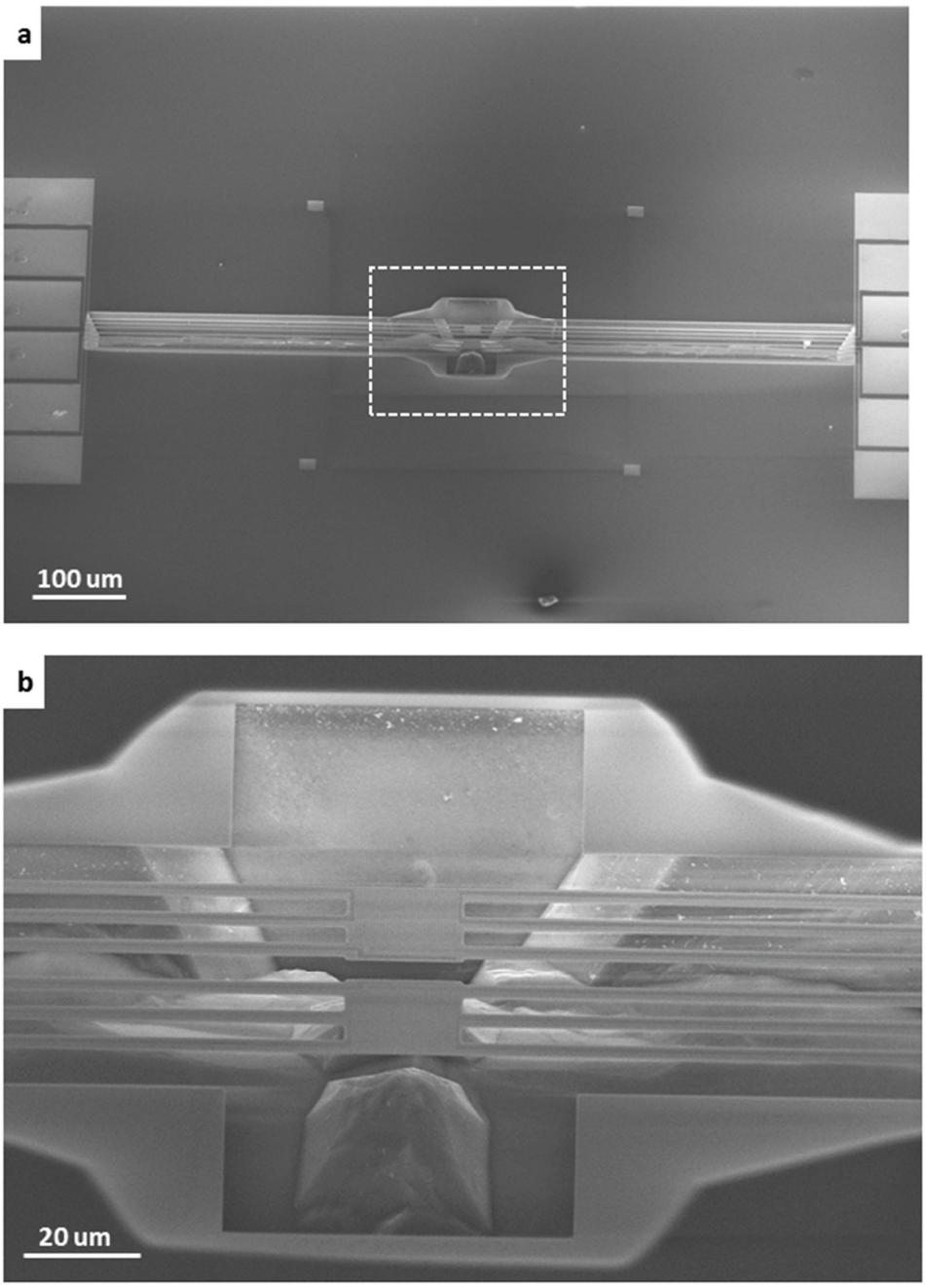

Figure 3.8. – **a,** An overview SEM image of Si_3N_4 membranes. **b,** Zoomed-in SEM image of the marked area of the suspended Si_3N_4 membranes. Pictures are taking under a 45° tilt with a 20 kV acceleration voltage.

3.2.8. Nanowire manipulation.

Once the fabrication process is completed, a nanowire has to be placed between the membranes. Nanowires are transferred using a Kleindiek micromanipulator under an optical microscope, as shown in Figure 3.9.

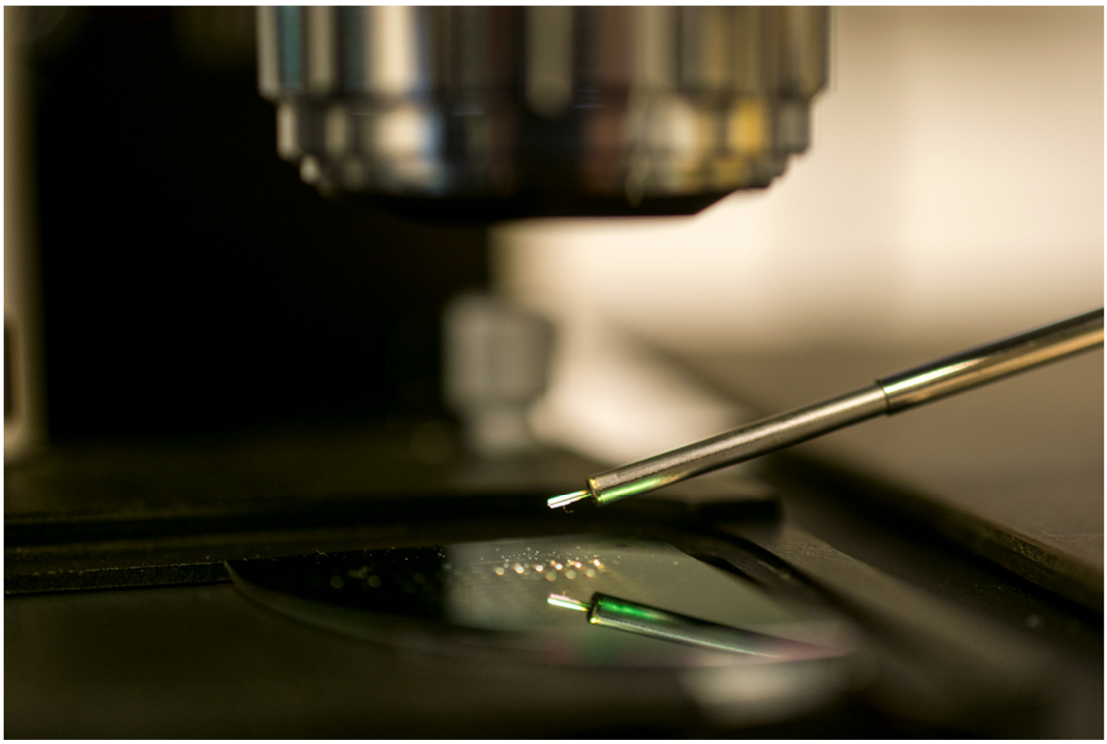

Figure 3.9. –Photo of the micromanipulator used for the nanowire transferring.

A small tungsten tip with a diameter of 100 nm is attached to the manipulator and used for picking up the nanowires. Van der Waals' forces cause the nanowire to stick to the tungsten tip, allowing lifting the nanowire from its substrate so that it can be placed on the device. The micromanipulator has a piezo-controlled tip, which helps to move the tip with high accuracy (down to nm)[21]. The manipulator can be used both in a vacuum environment inside an SEM chamber, for instance, and under an optical microscope. However, nanowires will be contaminated with some C-based materials after electron beam exposure, which can significantly influence the thermal properties of the nanowires[22]. Thus, it is crucial to perform the transfer under an optical microscope. Although the nanowires have a diameter smaller than the wavelength of visible light, they can be transferred optically. The nanowires cause an optical distortion on a large and thin area, which makes them visible under the microscope. The sample is arranged in such a way that the wire is located perpendicular to the sides of the membranes. The manipulator tip is brought down in the such a way that the wire touches either or both of the membranes. Then, the manipulator is pushed down a bit more, and the membranes will be slightly bent. Thanks to their geometry and flexibility, no permanent deformation is made. When the Van der Waals forces are

high enough, the nanowire is landed on the first membrane, can be released from the tip, and is landed on the second membrane. A transferred nanowire bridging between the membranes is shown in Figure 3.10.

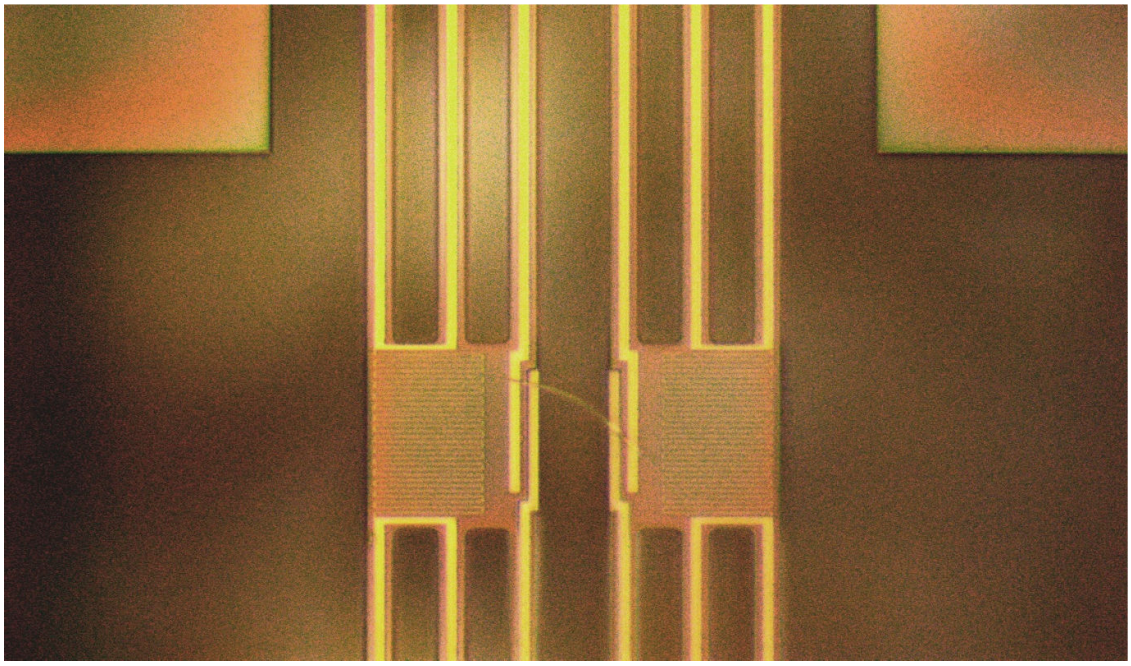

Figure 3.10. – An optical image (top view) of a nanowire placed between the membranes.

3.2.9. Top Pt/C contacts.

In case the thermal contact between the nanowire and membrane is insufficient, additional Pt/C top contacts are deposited on top of the NW by electron beam induced deposition (EBID) of Pt inside an FEI Strata dual-beam DB235 FIB system. The sample is placed inside the chamber, and top contacts can be defined using a gas injection system. The precursor molecules are cracked due to the influence of the electron beam[23]. This technique allows local deposition and prevents nanowires to be exposed to the electron beam.

An SEM image of the fabricated device with top Pt/C contacts is shown in Figure 4.11. The effect of the Pt/C contacts on the thermal measurement is addressed in Chapters 5 and 6. Once Pt/C contacts are made, the device is ready for the thermal transport measurements described in Chapter 4.

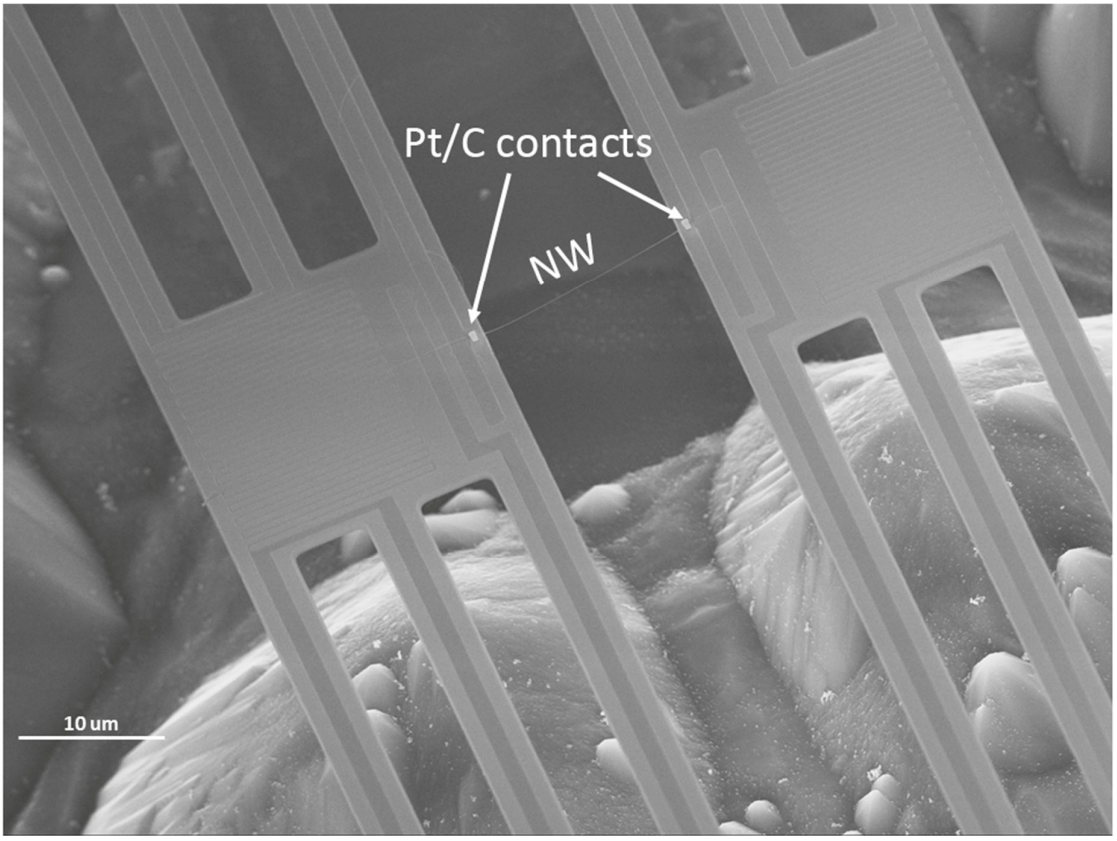

Figure 3.11. – SEM image of the fabricated device with Pt/C top contacts. The picture is taken at 20 kV under a 45^{o} tilt.

3.3. Power factor microdevice fabrication process.

In order to measure the Seebeck coefficient of the InSb nanowires, the device shown in Figure 3.12 has been fabricated. The schematic illustration of the fabrication process of the microdevice to measure the power factor is shown in Figure 3.12.

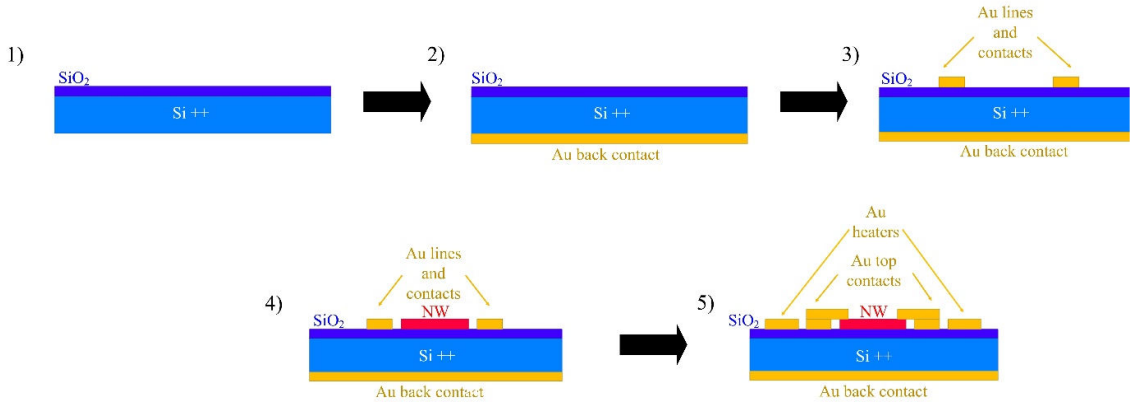

Figure 3.12. – Schematic illustration of fabrication process of the microdevice to measure the power factor: 1) SiO_2/Si ++ wafer used a substrate; 2) Au back contact deposited on the backside to provide sufficient gate response; 3) Au contact lines and pads created on the top side; 4) NW transferred to a prefabricated device; 5) Top contacts and heaters are defined.

3.3.1. Back contact.

First, a Ti/Au back contact is made to the highly doped Si substrate, which is used as a back gate. An RIE step is required to remove the native oxide on the backside. The protective 950 K PMMA A11 is spun at 2000 RPM in an open-air spinner for 30 s on the top side of the sample to protect the thermal oxide on the front side. Afterward, the sample is placed on a hot plate at 180 °C for 4 min. The resulting thickness of the PMMA is around 1.3 μm. The SiO_2 etching is performed using dry etching. The etching rate of SiO_2 in CHF_3 plasma is around 50 nm/min. Thus, the layer is etched for 2 min 15 s in order to remove the native oxide. Right after this step, the sample is loaded into the evaporator, and Ti/Au 15/150 nm layers are deposited. The Ti layer is used as an adhesive layer. After deposition, the sample is cleaned by a 300 W oxygen plasma for 10 min, which removes the protective PMMA layer.

3.3.2. EBL contact pads and lines.

Au contact pads are created using EBL and a lift-off process, as described in Section 3.2.2. The 950 K PMMA A6 resist spun at 3000 RPM in an open-air spinner for 30 s. Afterward, the resist is baked on a hot plate at 180 °C for 3 min and 30 s. The baking removes all the solvents from the resist creating a stable layer with a thickness of about 520 nm. After that, the sample is loaded in the EBL chamber. The parameters of the EBL exposure can be found in Appendix A3.4. After the exposure, the photoresist is developed using MIBK:IPA solution with a ratio of 1:3 for 80 s followed by IPA cleaning for 80 s. Once the resist is developed, the sample is placed inside an evaporator. A 15/150 nm Cr/Au layer is deposited for the contact pads in this way. Cr is used as an adhesive layer in this case. After deposition, the sample is placed in a closed beaker

above the acetone for the lift-off process of the Cr/Au layer. The process is the same as described in Section 3.2.2.

3.3.3. Nanowire manipulation.

Samples are cleaned using a 300 W oxygen plasma for 10 min. At this point, the nanowires can be transferred from the as-grown sample to the prefabricated device. The transferring technique is similar to the process described in Section 3.2.8. The only difference is that the nanowires have to be placed in a particular position on the flat SiO_2 substrate. Ideally, the nanowires are positioned horizontally in the center of every device. An SEM image of a transferred nanowire is shown in Figure 3.13.

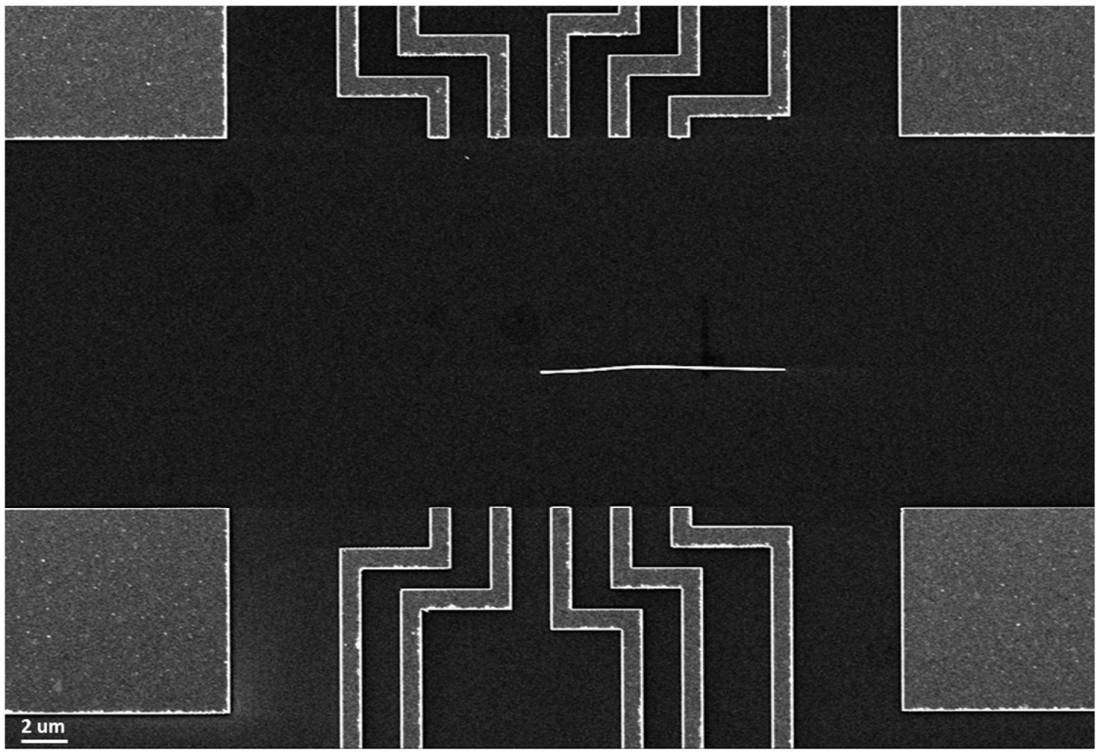

Figure 3.13. – SEM image of the nanowire transferred to the prefabricated device. This image is imported to AutoCAD to define individual contacts and heaters.

3.3.4. EBL top contacts.

After wire transfer, individual top contacts are designed using AutoCAD software. The sample is covered with two layers of PMMA: 1) 495 K PMMA A6 spun at 2000 rpm for 30 s; 2) 950 K PMMA A2 spun at 2000 rpm for 30 s. The measured total thickness of the layer is around 470 nm. The structure is defined using EBL. The parameters of the EBL exposure can be found in Appendix A3.4. The sample is developed using an MIBK:IPA solution with a ratio of 1:3 for 80 s followed by IPA cleaning for 80 s. After development, the resist residues are removed by a 10 W O_2

plasma for 10 s. The InSb nanowire surface is passivated with sulphur in an ammonium sulfide solution[4,25]. Finally, the electrodes and resistive lines of Cr/Au 10/150 nm are deposited by electron beam evaporation. Cr is used as an adhesive layer but also provides an ohmic contact to the InSb nanowires[24]. An SEM image of the manufactured device is shown in Figure 3.14.

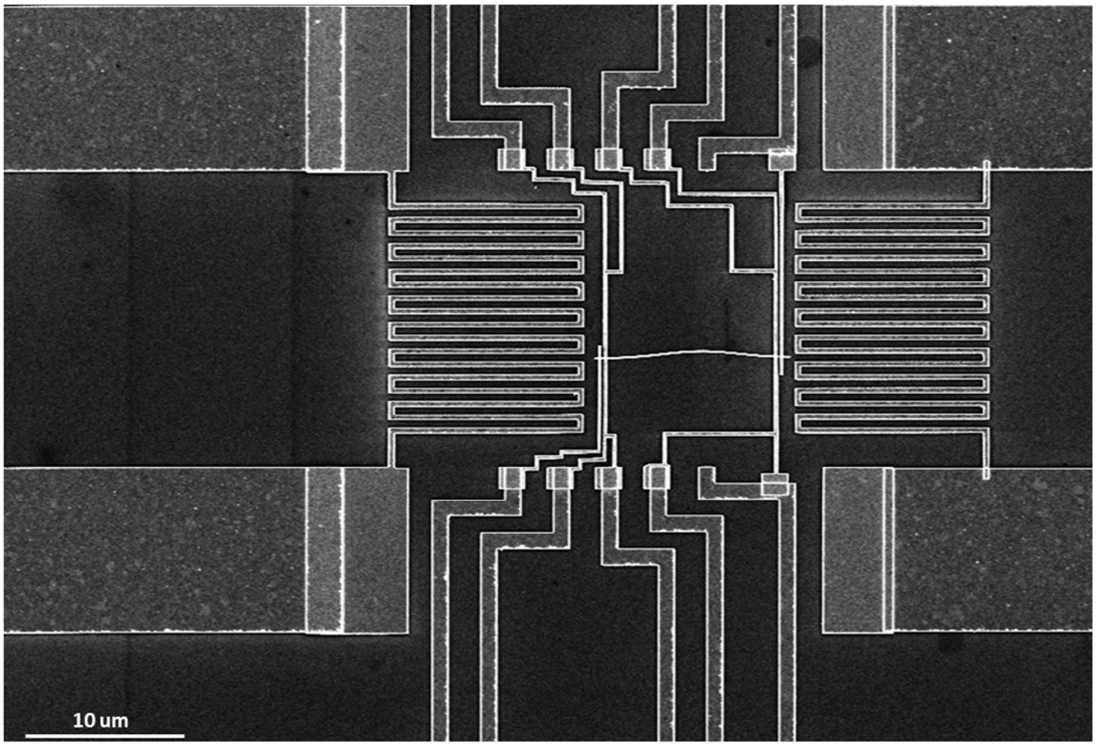

Figure 3.14. – SEM image of the microdevice to measure power factor.

It is essential to keep the nanowires clean[22]. Therefore, the SEM image, as shown in Figure 3.14, has been taken after all desired measurements have been made.

Appendix A3.1. GaP nanowires growth parameters.

#	Step name	Parameters	Time
1	Cleaning GaP substrate	H_3PO_4 UPW O_2 Plasma (300 W)	2 min 5 min 10 min
2	950K PMMA A2 spinning	8000 rpm	30 s
3	Resist baking	Hot plate 180 °C	3 min
4	EBL exposure	Appendix A4.4.1	60 min
5	Development	MIBK:IPA IPA	80 s 80 s
6	Descum	O_2 Plasma (100W)	10 s
7	Catalytic particles formation	Au 4 nm	10 min
8	Lift-off	Acetone vapor Acetone IPA	15 min 30 min 5 min
9	Cleaning	H_2SO_4: H_2O_2 4:1	10 s
10	Nanowire growth	750°C X_i (TMG) = 1.9×10^{-5}, X_i (PH_3) = 3.4×10^{-2}, the reactor pressure was 30 mbar, with a total flow of 4000 sccm, and H_2 was used as a carrier gas.	160 min

Appendix A3.2. InSb nanowires growth parameters.

#	Step name	Parameters	Time
1	Cleaning InSb substrate	NH_4F:HF = 7:1 IPA UPW	5 min 5 min 10 min
2	Si_3N_4 mask growth	PECVD 25 nm Si_3N_4	3 min
3	Cleaning	O_2 Plasma (40W)	1 min
4	ZEP spinning	4000 rpm	30 s
5	Resist baking	Hot plate 180 °C	3 min
6	EBL exposure	Appendix A4.4	60 min
7	Development	MIBK:IPA (1:1) IPA	80 s 80 s
8	Descum	O_2 Plasma (100 W)	10 s
9	Si_3N_4 etching	BHF (20:1)	20 s
10	Catalytic particles formation	Au 10 nm	25 min
11		PRS 3000 at 80°C	30 min

	Lift-off	IPA	10 min
12	Cleaning	O_2 Plasma (300 W)	10 s
13	Nanowire growth[23]	495°C X_i (TMI) = 2.8×10^{-7}, X_i (TMSb) = 5.1×10^{-5}, the reactor pressure was 50 mbar, with a total flow of 6000 sccm, and H_2 was used as a carrier gas.	60 min

Appendix A3.3. Thermal properties microdevice fabrication.

#	**Step name**	**Parameters**	**Time**
1	Cleaning	O_2 Plasma (300 W)	10 min
2	Deoxidation	HF (1%)	1 min
3	PECVD Si_3N_4 growth 650 nm	Si_3N_4 LF+HF	60 min
4	Cleaning	O_2 Plasma (300 W)	5 min
5	950K PMMA A11 Spinning	6000 rpm	30 s
6	Resist baking	Oven 175 °C	30 min
7	EBL exposure	Appendix A4.4.3	120 min
8	Development	MIBK: IPA IPA	80 s 80 s
9	Descum	O_2 Plasma (100 W)	10 s
10	Contact pads formation	Ti/Au 14 nm/140 nm	60 min
11	Lift-off	Acetone vapor Acetone IPA	15 min 480 min 5 min
12	Cleaning	O_2 Plasma (300 W)	10 min
13	950K PMMA A4 spinning	8000 rpm	30 s
14	Resist baking	Oven 175 °C	30 min
15	EBL exposure		60 min
16	Development	MIBK:IPA IPA	80 s 80 s
17	Descum	O_2 Plasma (100 W)	10 s
18	Pt lines and meanders formation	Pt 30 nm	30 min
19	Lift-off	Acetone vapor Acetone IPA	15 min 480 min 5 min
20	Cleaning	O_2 Plasma (300 W)	10 min
21	Protection Si_3N_4 layer (350 nm)	PECVD Si_3N_4 LF+HF	30 min
22	Cleaning	O_2 Plasma (300 W)	10 min
23	950K PMMA A11 spinning	2000 rpm	30 s
24	Resist baking	Oven 175 °C	40 min

25	EBL exposure	Appendix A4.4.4	180 min
26	Development	MIBK:IPA IPA	80 s 80 s
27	Dry Si_3N_4 etching	RIE O_2+CHF	12 min
28	Cleaning	O_2 Plasma (300 W)	10 min
29	Deoxidation	HF (1%)	5 s
30	Si underetch	TMAH at 80°C	360 min
31	Cleaning	UPW	5 min
32	Si downetch	KOH (33%) at 80°C	5 min
33	Cleaning	UPW	5 min
34	Drying	IPA at 80°C	10 min
35	Protection layer removing	RIE O_2+CHF_3	90 s
36	Cleaving		5 min
37	Nanowire transferring	–	–
38	EBID Pt top contacts		45 min per NW

Appendix A3.4. Electron beam lithography parameters.

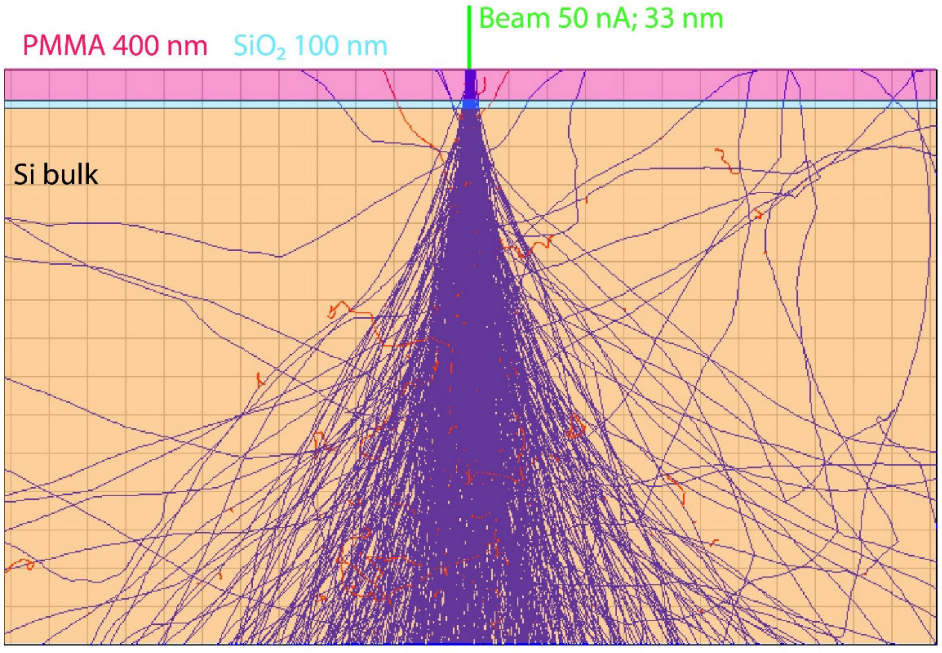

Figure A3.1. – The results of the Monte-Carlo simulation of 500 electron trajectories (33 nm beam size) with the energy 100 kV incident on a PMMA resist-SiO_2-Si structure (#7 in the table below).

#	**Step**	**EBL parameters**	**Section**
1	GaP catalytic particles	Beam current: 1 nA; Beam size: 21 nm; Apperture: 300 μm; Dose:1500 μC/cm^2.	4.1.3
2	InSb opening SAE mask	Beam current: 1 nA; Beam size: 21 nm; Apperture: 300 μm; Dose:1800 μC/cm^2.	4.1.4
3	InSb catalytic particles	Beam current: 1 nA; Beam size: 21 nm; Apperture: 300 μm; Dose:2000 μC/cm^2.	4.1.4
4	Membranes contact pads	Beam current: 50 nA; Beam size: 33 nm; Apperture: 300 μm; Dose:1340 μC/cm^2.	4.2.2
5	Membranes Pt metallization	**Pt lines:** Beam current: 80 nA; Beam size: 44 nm; Apperture: 300 μm; Dose:2000 μC/cm^2. **Pt meanders:** Beam current: 4 nA; Beam size: 19 nm; Apperture: 300 μm; Dose:1800 μC/cm^2.	4.2.3
6	Membranes etching pattern	Beam current: 30 nA; Beam size: 29 nm; Apperture: 300 μm; Dose:1340 μC/cm^2.	4.2.4
7	Power factor device contact metallization	**Contact pads:** Beam current: 50 nA; Beam size: 33 nm; Apperture: 300 μm; Dose:1500 μC/cm^2. **Contact lines:** Beam current: 20 nA; Beam size: 24 nm; Apperture: 300 μm; Dose:1500 μC/cm^2.	4.3.2
		Top contact lines: Beam current: 1.5 nA; Beam size: 19 nm;	

8	Power factor top contact metallization	Apperture: 300 μm; Dose:1900 μC/cm^2. **Top contact lines (fine):** Beam current: 1.5 nA; Beam size: 19 nm; Apperture: 300 μm; Dose:2000 μC/cm^2. **Heaters:** Beam current: 8 nA; Beam size: 20 nm; Apperture: 300 μm; Dose:1900 μC/cm^2.	4.3.4

Appendix A3.5. Power factor microdevice fabrication.

#	**Step name**	**Parameters**	**Time**
1	Cleaning	O_2 Plasma (300 W)	10 min
2	Protection sacrificial layer (950K PMMA A11 spinning)	2000 rpm	30 s
3	SiO_2 removing	RIE O_2 +CHF_3	2 min 15 s
4	Back contact formation	Ti/Au 15 nm/150 nm	30 min
5	Protection layer removing and cleaning	O_2 Plasma (300 W)	15 min
6	950K PMMA A6 Spinning	3000 rpm	30 s
7	Resist baking	Hot plate 180 ^{o}C	3 min 30 s
7	EBL exposure	Appendix A4.4.5	60 min
8	Development	MIBK:IPA IPA	80 s 80 s
9	Descum	O_2 Plasma (100 W)	10 s
10	Contact pads and lines formation	Cr/Au 10 nm/120 nm	40 min
11	Lift-off	Acetone vapor Acetone IPA	15 min 480 min 5 min
12	Cleaning	O_2 Plasma (300 W)	10 min
13	Nanowire transferring	–	–
13	495K PMMA A6 spinning	2000 rpm	30 s
14	Resist baking	Hot plate 180 ^{o}C	3 min
15	950K PMMA A2 spinning	2000 rpm	30 s
16	Resist baking	Hot plate 180 ^{o}C	3 min
17	EBL exposure	Appendix A4.4.6	60 min
18	Development	MIBK:IPA IPA	80 s 80 s

19	Descum	O_2 Plasma (100 W)	10 s
20	Sulfur passivation		180 min
21	Top contacts and heaters formation	Cr/Au 10/120 nm	40 min
22	Lift-off	Acetone vapor Acetone IPA	15 min 480 min 5 min
23	Drying	N_2 flow	10 s

3.4. References.

1. Solanki, A. & Um, H. Top-Down Etching of Si Nanowires. Semiconductors and Semimetals 71-149 (2018).
2. Wagner, R. & Ellis, W. Vapor-liquid-solid mechanism of single crystal growth. Applied Physics Letters 4, 89-90 (1964).
3. Wang, J. et al. Reversible Switching of InP Nanowire Growth Direction by Catalyst Engineering. Nano Letters 13, 3802-3806 (2013).
4. Mårtensson, T. et al. Nanowire Arrays Defined by Nanoimprint Lithography. Nano Letters 4, 699-702 (2004).
5. Lumsdon, S. & Scott, D. Assembly of Colloidal Particles into Microwires Using an Alternating Electric Field. Langmuir 21, 4874-4880 (2005).
6. Glas, F., et al. Why Does Wurtzite Form in Nanowires of III-V Zinc Blende Semiconductors? Physical Review Letters 99, (2007).
7. Gao, Q. et al. Simultaneous Selective-Area and Vapor–Liquid–Solid Growth of InP Nanowire Arrays. Nano Letters 16, 4361-4367 (2016).
8. Kakko, J. et al. Fabrication of Dual-Type Nanowire Arrays on a Single Substrate. Nano Letters 15, 1679-1683 (2015).
9. Hertenberger, S. et al. Growth kinetics in position-controlled and catalyst-free InAs nanowire arrays on Si(111) grown by selective area molecular beam epitaxy. Journal of Applied Physics 108, 114316 (2010).
10. Assali, S. et al. Direct Band Gap Wurtzite Gallium Phosphide Nanowires. Nano Letters 13, 1559-1563 (2013).
11. Ely, D., et al. Ostwald–Freundlich diffusion-limited dissolution kinetics of nanoparticles. Powder Technology 257, 120-123 (2014).
12. Perez, M. Gibbs-Thomson effects in phase transformations. Scripta Materialia 52, 709-712 (2005). 10. doi: 10.1186/s11671-016-1370-4.
13. Gazibegovic, S. et al. Epitaxy of advanced nanowire quantum devices. Nature 548, 434-438 (2017).
14. Wan, Y., et al. Characterisation and optimisation of PECVD SiNx as an antireflection coating and passivation layer for silicon solar cells. AIP Advances 3, 032113 (2013).
15. Cianci, E., et al. Dual frequency PECVD silicon nitride for fabrication of CMUTs' membranes. Sensors and Actuators A: Physical 127, 80-87 (2006).

16. Liang, J., et al. Improved bi-layer lift-off process for MEMS applications. Microelectronic Engineering 85, 1000-1003 (2008).
17. Rommel, M. & Nilsson, B. Estimating the optimum dose for arbitrary substrate materials based on Monte Carlo simulated point spread functions. Microelectronic Engineering 155, 29-32 (2016).
18. Nagata, H., et al. Improvement of bonding strength between Au/Ti and SiO_2 films by Si layer insertion. Journal of Vacuum Science & Technology A: Vacuum, Surfaces, and Films 17, 1018-1023 (1999).
19. Thong, J., et al. TMAH etching of silicon and the interaction of etching parameters. Sensors and Actuators A: Physical 63, 243-249 (1997).
20. Kim, B. & Cho, D.D. Aqueous KOH Etching of Silicon (110). Journal of The Electrochemical Society 145, 2499 (1998).
21. GmbH, K. Kleindiek Nanotechnik: Electron Microscopy. Nanotechnik.com (2019). at <https://www.nanotechnik.com/mm3a-em.html>
22. Blömers, C. et al. Hall effect measurements on InAs nanowires. Applied Physics Letters 101, 152106 (2012).
23. Córdoba, R. et al. Comparison of ion- and electron-beam-induced Pt nanodeposits: composition, volume per dose, microstructure, and in-situ resistance. EMC 2008 14^{th} European Microscopy Congress 1–5 September 2008, Aachen, Germany 657-658 (2008).
24. Gül, Ö. et al. Towards high mobility InSb nanowire devices. Nanotechnology 26, 215202 (2015).
25. Lvova, T. et al. Chemical passivation of InSb (100) substrates in aqueous solutions of sodium sulfide. Semiconductors 47, 721-727 (2013).

Chapter 4. Experimental methods.

In this chapter, the experimental methods used to measure the thermoelectric properties of nanowires are described. In order to determine the thermoelectric efficiency of a device, both the thermal conductivity and power factor have to be obtained, as explained in Chapter 1. The measurements have been performed using two different measurement platforms: 1) In order to measure the thermal transport of a nanowire, high sensitivity and thermal isolation are required because the thermal conductivity of a single nanowire is relatively low. The fabrication of the microdevice to perform the measurements has been discussed in Chapter 3. Section 4.1 describes the principles of operation of the thermal transport microdevice. 2) The thermopower measurements platform should provide the temperature gradient along the nanowire and at the same time allow to measure the current-voltage characteristic of the nanowire. The fabrication of the devices is discussed in Chapter 3. In Section 4.2, the device for the power factor measurements described. In Section 4.3, the probe station in which the sample is placed and the electronics are described. In Section 4.4, several limitations of the measurement technique and errors are addressed. Finally, Section 4.5 describes alternative measurement techniques applied in this thesis, which help to overcome some of the limitations.

4.1 Thermal transport microdevice.

The microdevice used to explore the thermal transport of nanowires is based on the devices described by Swinkels *et al*[3-5]. The device consists of two suspended Si_3N_4 membranes with platinum meander structures on top of each membrane that act as heaters and thermometers. The fully suspended membranes are supported by 0.5 mm long Si_3N_4 beams to provide thermal isolation. A schematic illustration of the device is shown in Figure 4.1.

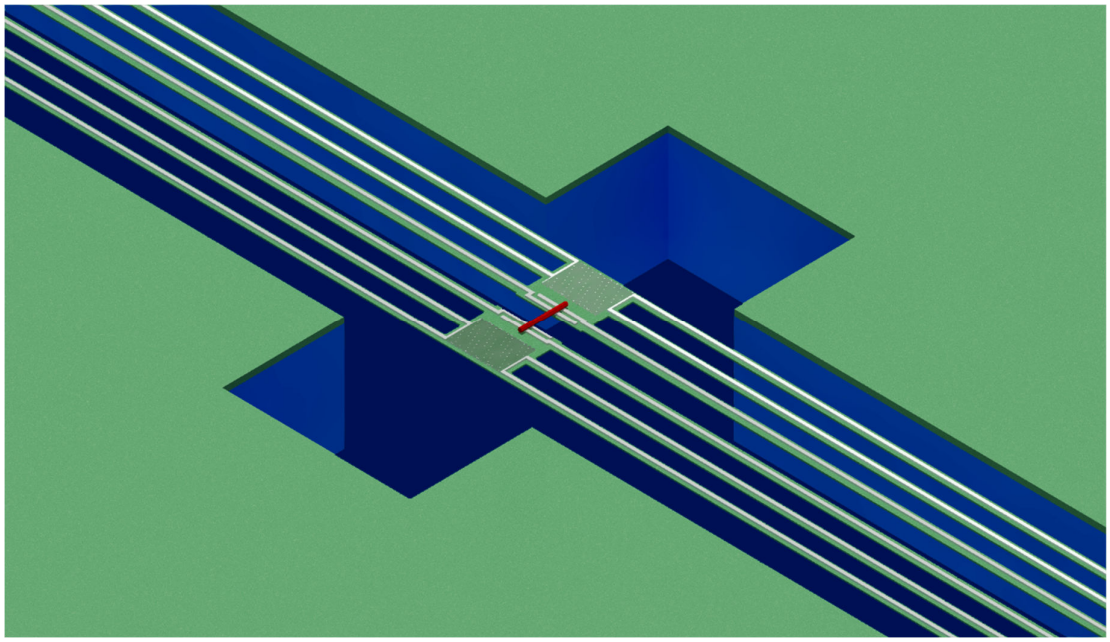

Figure 4.1. – Illustration of the microdevice for thermal transport characterization. The nanowire (colored in red) is bridging between the suspended membranes.

A single nanowire is placed on top of the membranes, such that it is bridging the platforms. The temperature on both sides of the nanowire can be measured using the Pt resistance-thermometers. To eliminate the influence of the contact lines, a four-point probe technique (4W) is applied to measure the resistance of each meander thermometer. Platinum has been chosen because it has a linear resistance-temperature dependence down to 50 – 70 K, depending on the film quality. The sensitivity of the measurement depends on α, ($\alpha = 1/R \cdot dR/dT$) and the film quality. A typical Pt thermometer resistance – temperature dependence is shown in Figure 4.2.

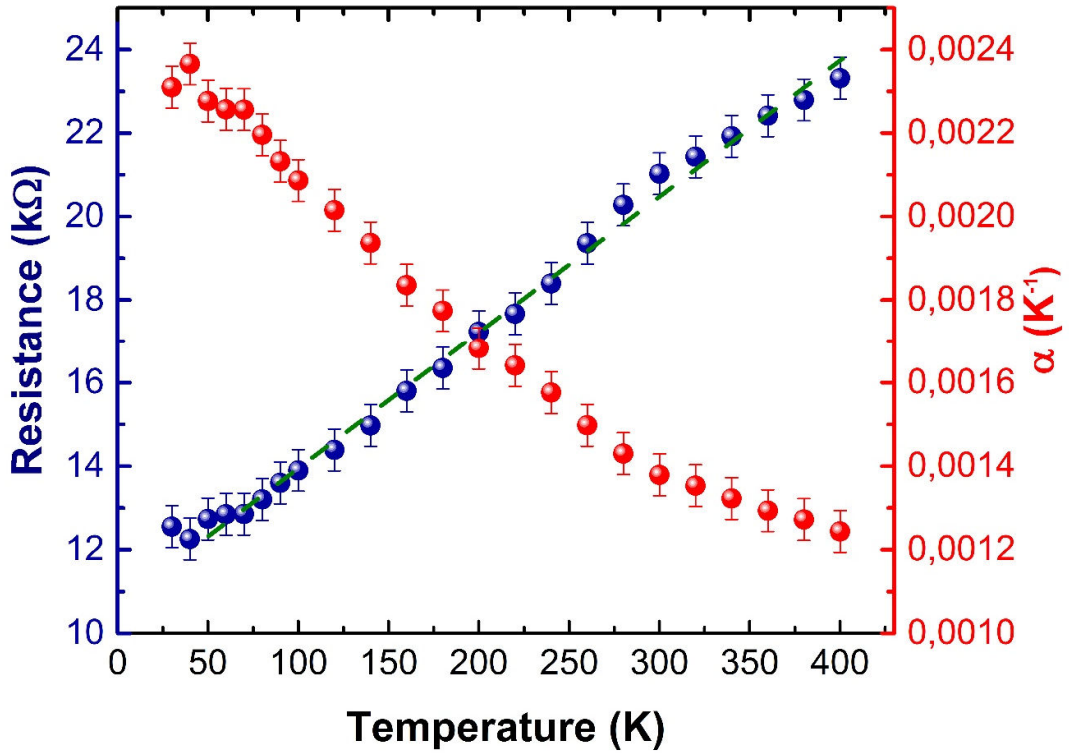

Figure 4.2. – Resistance and α coefficient as a function of temperature dependences for a Pt meander thermometer, used in the measurements. Blue data points are experimental measurement results and the green dotted line is fit to determine the α coefficient.

The specific resistance is calibrated for each meander structure. This is done by ramping a small sensing current from -20 nA to 20 nA with a step of 2 nA at each temperature step. The low current prevents the sample from Joule heating during the calibration step. Additionally, the power dissipated in the meander thermometer is measured to determine the heat flowing through the nanowire. Part of the dissipated heat will be conducted to the meander structure. Additionally, the dissipated power in the contact leads will be partly heating the membrane and hence the wire. It is assumed that the temperature of one platform, determined by the background temperature and heating by the Pt meander structure, is uniform throughout the membrane. This implies that the temperature completely drops over the suspended nanowire. In order to confirm this assumption, the temperature distribution across the membrane has been measured using thermoreflectance (Figure 4.3a) and simulated using COMSOL Multiphysics (Figure 4.3b). A finite element analysis in COMSOL of the simplified device confirms the heat distribution in the device, as shown in Figure 4.3.

Due to the limitation of the thermal imaging measurement technique, it is not possible to precisely measure heat the distribution along the Si_3N_4 [30]. Nevertheless, the shape of the measured temperature distribution on the membrane is in good agreement

with the simulated temperature map. A high temperature of the edges corresponds to the vibrations of the membranes over time and the edge effects of the measurement technique.

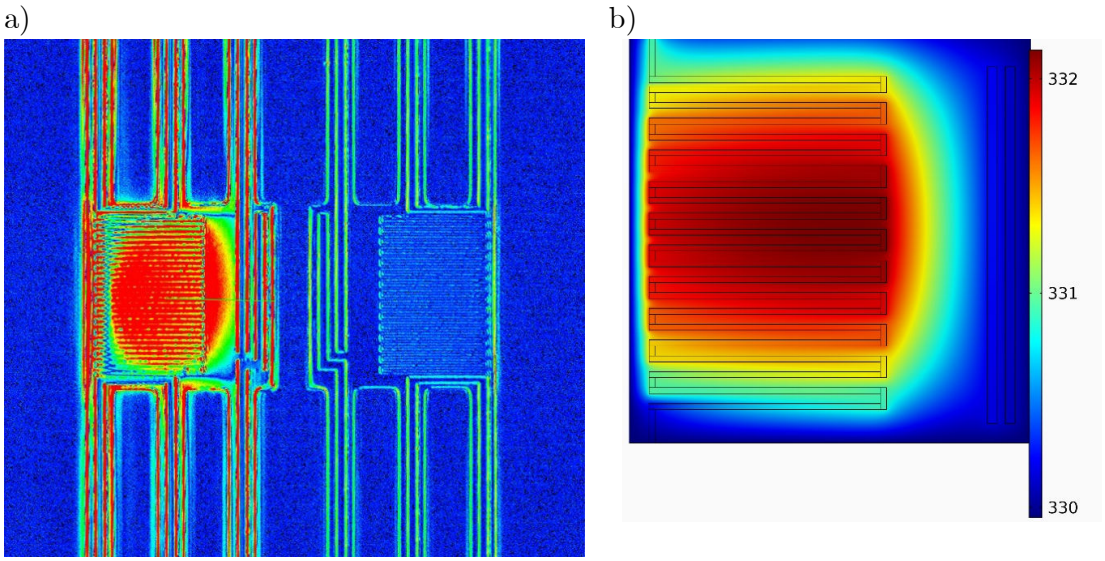

Figure 4.3. – **a,** Thermal image of the temperature distribution in the suspended membranes device. **b,** Simulated temperature distribution in the suspended membranes device. The heat dissipates from the meander heating structure via the beams.

The total resistance of the lines and meander structure is measured using a two-point measurement, to correct for heating in the contact leads. The dissipated power is proportional to the resistance. Thus, the total heating power can be calculated using Eq. (4.1)[4]:

$$P_{\mathrm{Total}} = P_{\mathrm{M}} + 0.5P_{\mathrm{L}} = \left(1 + 0.5\frac{R_{\mathrm{L}}}{R_{\mathrm{M}}}\right) P_{\mathrm{M}} = \frac{R_{\mathrm{M}} + 0.5R_{\mathrm{L}}}{R_{\mathrm{M}}} P_{\mathrm{M}}, \tag{4.1}$$

where P_M and P_L are the power dissipated in the meanders and lines, respectively.

Part of the total dissipated power is going through the nanowire. An overview of the power dissipations and heat flows involved is shown in Figure 4.4.

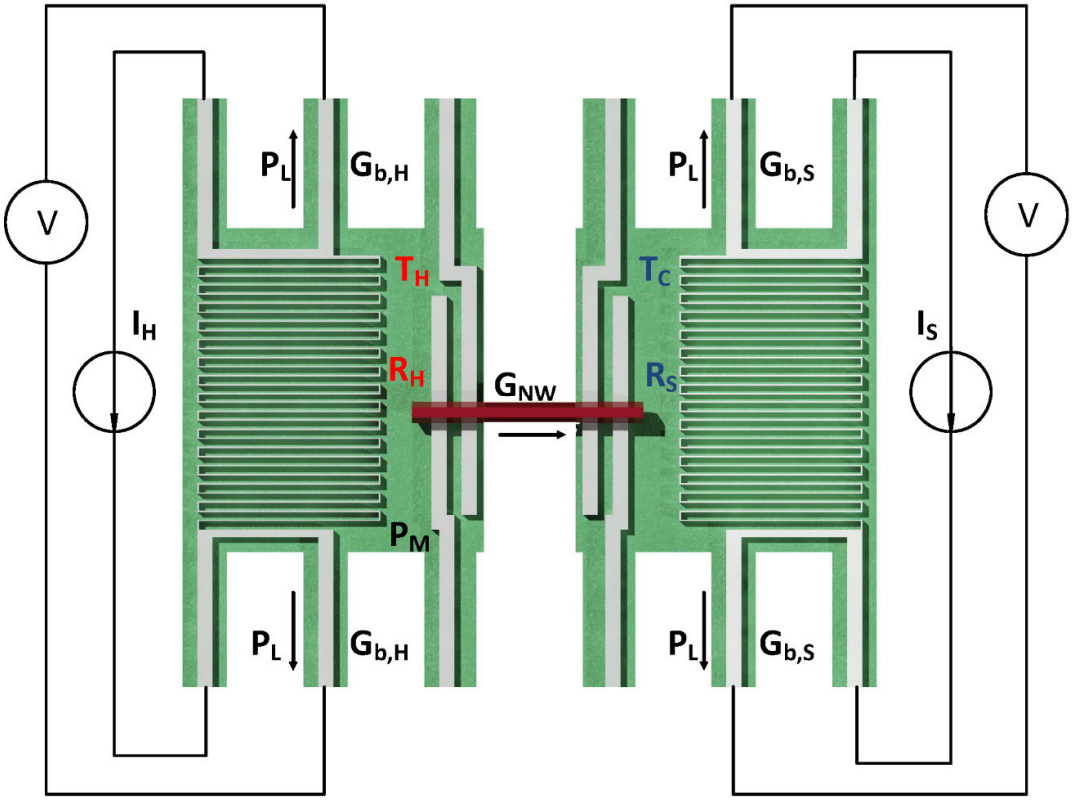

Figure 4.4. – Schematic illustration of the microdevice with nanowire used for the thermal conductance measurements. The indicated quantities are explained in the text. The arrows represent heat flows.

Part of the power flows from the heating membrane via conduction through the supporting beams to the chip (environment), which acts as a heat sink (Figure 4.3). Hence, the energy balance for the whole system can be written as[4]:

$$P_H + P_S = G_{b,H}\Delta T_H + G_{b,S}\Delta T_S \rightarrow G_{b,S} = \frac{P_H + P_S}{\frac{G_{b,H}}{G_{b,S}}\Delta T_H + \Delta T_S}, \tag{4.2}$$

where P_H, P_S is the power dissipated in the heating/sensing meander, respectively, $G_{b,H}$ and $G_{b,S}$ are the thermal conductances of the suspension beams, and ΔT_H and ΔT_S are the temperature differences between the heater and sensor, respectively, and the environment. The subscript H stands for the heating side, whereas subscript S stands for the sensing side. Assuming that the beam conductance $G_{b,H} = G_{b,S} = G_b$ we obtain[4]:

$$G_b = \frac{P_H + P_S}{\Delta T_H + \Delta T_S}. \tag{4.3}$$

In order to calculate the nanowire thermal conductance, a heat balance for the sensing membrane is given in Eq. (4.4). It is assumed that the heat transported through the wire is also transported to the heat sink through the Si_3N_4 beams.

$$G_{b,S}\Delta T_S = G_{NW}\left(\Delta T_H - \Delta T_S\right) \rightarrow G_{NW} = G_{b,S}\frac{\Delta T_S}{\Delta T_H - \Delta T_S,} \tag{4.4}$$

where G_{NW} is the thermal conductance of the nanowire.

Actually, the dissipated power will increase with the heating current, and thus the slope of the temperature-power relation with power can be determined. Hence, Eq.'s (4.3) and (4.4) can be adapted by applying:

$$\frac{d\Delta T_x}{dP} = \frac{\Delta T_x}{P_H + P_S.} \tag{4.5}$$

Additionally, a linear relationship between power and temperature is assumed in the case of a small temperature difference and the absence of temperature-dependent effects. Therefore, inserting Eq. (4.5) into Eq.'s (4.3) and (4.4) gives:

$$G_b = \left(\frac{d\Delta T_H}{dP} + \frac{d\Delta T_S}{dP}\right)^{-1}, \tag{4.6}$$

$$G_{NW} = G_b\frac{d\Delta T_S}{dP}\left(\frac{d\Delta T_H}{dP} - \frac{d\Delta T_S}{dP}\right)^{-1}. \tag{4.7}$$

The assumption that the two beams have equal conduction is not always valid[6]. In order to correct for different beam conductions, it is assumed that the nanowire conduction G_{NW} is symmetric, following this assumption,we have.

$$G_{NW} = G'_{NW} \rightarrow \frac{\left(P_H + P_S\right)\Delta T_S}{\left(\frac{G_{b,H}}{G_{b,S}}\Delta T_H + \Delta T_S\right)\left(\Delta T_H - \Delta T_S\right)} = \frac{\left(P'_H + P'_S\right)\Delta T'_S}{\left(\frac{G_{b,S}}{G_{b,H}}\Delta T'_H + \Delta T'_S\right)\left(\Delta T'_H - \Delta T'_S\right)}. \tag{4.8}$$

All parameters in Eq. (4.8) can be measured. Therefore, the equation can be used to determine the ratio of the beam conductions. This is then used in equation (4.2) to obtain the nanowire conduction. Solving Eq. (4.8) gives two solutions; at which only one is physical. Writing down the solution of Eq. (4.8) provides the following equation:

$$\frac{G_{b,H}}{G_{b,S}} = \frac{-ABD + B^2D + BCD - BD^2 + \sqrt{BD\left[4AC(A-B)(C-D) + BD(A-B-C+D)^2\right]}}{2AD(A-B)}. \tag{4.9}$$

Where

$$A = \frac{dT_H}{dP}, \tag{4.10}$$

$$B = \frac{dT_S}{dP}, \tag{4.11}$$

$$C = \frac{dT'_H}{dP'}, \tag{4.12}$$

$$D = \frac{dT'_S}{dP'}. \tag{4.13}$$

The applied Joule heating power (P) dissipated by the heater (P_L) raises its temperature by ΔT_H while the remaining part of the power (P_2) goes through the NW and raises the temperature of the sensor by ΔT_S:

$$\begin{cases} P = P_L + P_2 \\ P_L = G_{\mathrm{b,H}} \Delta T_{\mathrm{H}} \\ P_2 = G_{\mathrm{b,S}} \Delta T_{\mathrm{s}} = G_{NW} \left(\Delta T_{\mathrm{H}} - \Delta T_{\mathrm{S}} \right) \end{cases}. \tag{4.14}$$

Solving Eq. (4.14) for G yields for the case of identical Si_3N_4 beams ($G_{b,H} = G_{b,S}$):

$$G_{NW} = \frac{P}{\Delta T_{\mathrm{H}} - \Delta T_{\mathrm{S}}} \frac{\Delta T_{\mathrm{S}}}{\Delta T_{\mathrm{H}} + \Delta T_{\mathrm{S}}}. \tag{4.15}$$

Thanks to the linear relation between the Pt film resistance and temperature, as shown in Figure 4.2, the temperature changes ΔT_H and ΔT_S of the heating and sensing membranes can be found by accurately measuring the resistance changes. Since the applied heating power P is known, G_{NW} can be calculated from Eq. (4.15).

The obtained thermal conductance can be converted into thermal conductivity, κ, by using the geometrical properties of the nanowire (diameter and length)[7]:

$$\kappa = \frac{4 \cdot G_{\mathrm{NW}} \cdot L}{\pi \cdot D^2}, \tag{4.16}$$

where L is the nanowires length, and D is the diameter.

4.2 Power factor microdevice.

A device to measure the power factor of the nanowires, shown in Figure 4.5, has been designed and fabricated. The microdevice consists of a nanowire, two heaters, two thermometers, and top contacts. The nanowire is placed on a Si/SiO_2 chip, and top contacts and thermometers/heaters are defined by electron beam lithography (EBL)

and lift-off processes (see Chapter 3). Importantly, the Si++ substrate can be used as a back gate such that the nanowire is the channel in a field-effect device. With this device we want to measure the power factor, which is determined by the following parameters: 1) carrier mobility; this is measured from the slope of the transconductance as defined by Eq. (2.20). 2) carrier concentration in the nanowire can be determined from the threshold potential according to Eq. (2.22). 3) the Seebeck coefficient is measured from the resulting voltage at open circuit when a temperature gradient is induced as described in Eq. (2.16). The nanowire has four top contacts, two of which are used to provide the current, and the others are shared for both voltage measurements and temperature measurements via resistor thermometers. Each heater is operated by a heating current (12 mA in our case). A schematic illustration of the device is shown in Figure 4.5. In order to induce a thermal gradient across the wire, it is important that the heat is dissipated in the direct surrounding of the meandering heating structure and not in the contact leads.

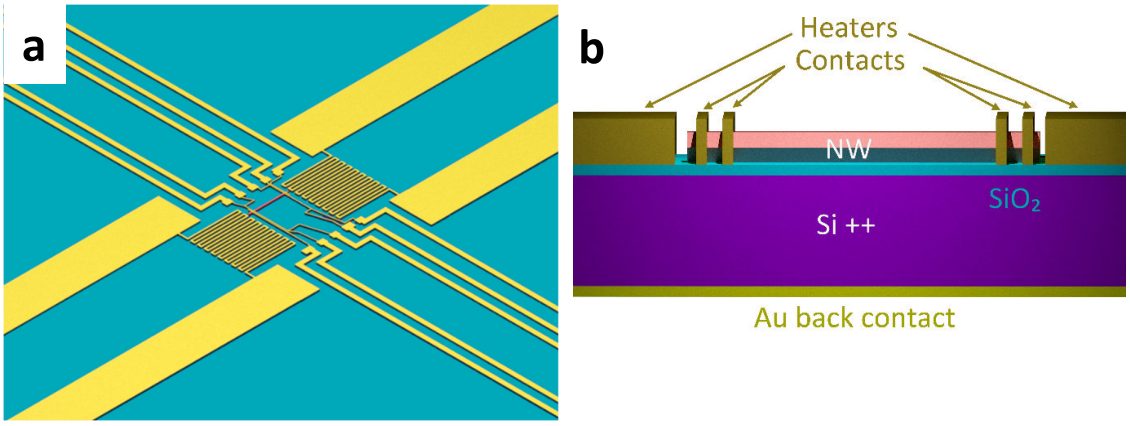

Figure 4.5. – **a,** Schematic illustration of the microdevice, and **b,** its cross-section. The device consists of a nanowire, two heaters, two thermometers, and top contacts.

The electrical equivalent circuit of the microdevice is shown in Figure 4.6.

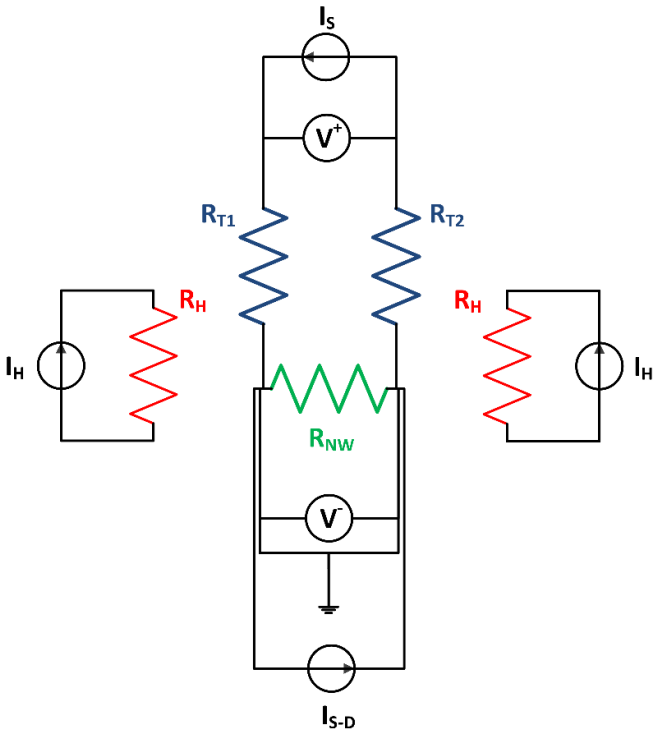

Figure 4.6. – An equivalent circuit of the microdevice for the power factor measurements. The indicated quantities are explained in the text.

In order to dissipate the majority of the heat around the meandering heating element, the resistance of the heating element (R_H) should be much higher than the resistance of the contact lines connected to the heating element (R_L)[8]. A calculation of the ratio of R_H and R_L can be found in Appendix A4.1. The heat dissipation of the structure is modeled in a simplified COMSOL Multiphysics simulation. As an input parameter, the heating current of 12 mA is used. The model assumes that the temperature of the backside is equal to $T = 300$ K, not taking into account cooling via convection. The modeling results confirm that most of the heat is generated in the meandering structure, inducing a thermal gradient across the nanowire, as shown in Figure 4.7.

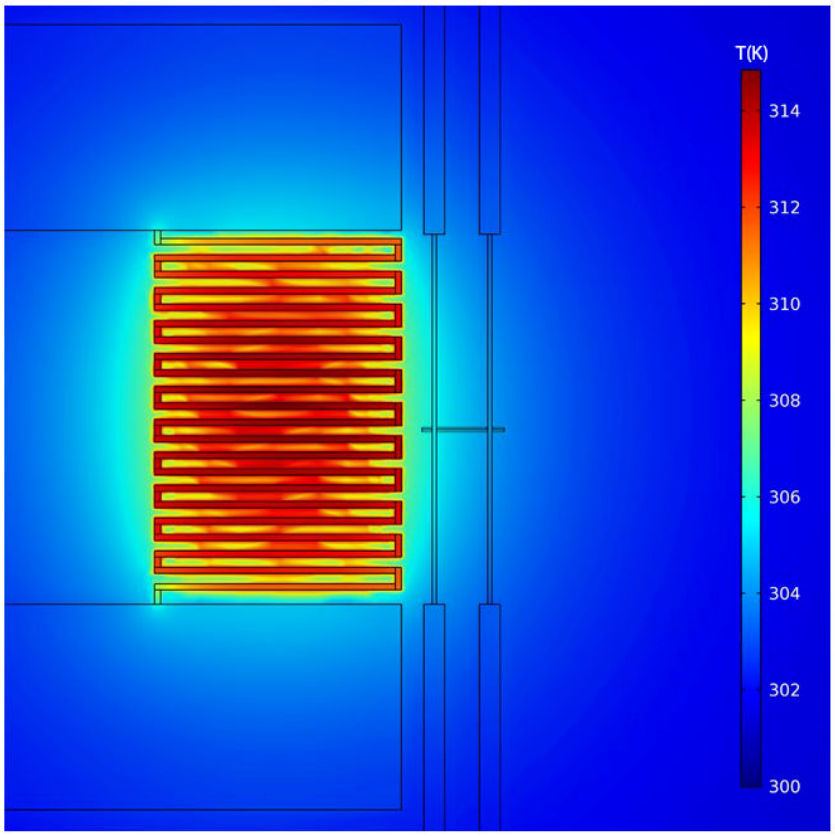

Figure 4.7. – Simulation results of the temperature distribution in the simplified power factor microdevice. The nanowire is located next to the center of the heating device.

In order to calculate the Seebeck coefficient, the temperature difference ΔT between the two ends of the nanowire must be measured. This is done by using resistive thermometers, as shown in Figure 4.5a. The electrical contact to the nanowire must be ohmic. As discussed in Chapter 3 for InSb nanowires, Pt is not suitable for this. Instead Au has been used[9]. The resistance of the Au lines increases with the temperature. In an acceptable approximation, this relation is linear in the range from 300 K to 400 K, as shown in Figure 4.8.

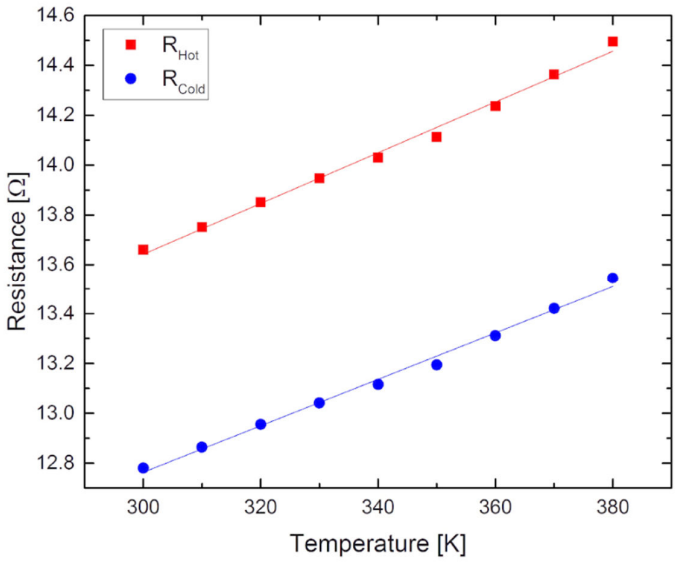

Figure 4.8. – Typical resistance of Au lines as a function of temperature, which is used in the Seebeck coefficient measurements. Data points represent experimental measurement results, lines are fits, which are used to determine the α coefficient.

The resistance–temperature curve is used to calibrate the thermometers before each measurement. As explained in Chapter 2, the Seebeck coefficient is determined from the open-circuit voltage (V_{OC}) induced by the applied temperature difference (ΔT). The power factor microdevice can be operated in two directions since it is symmetric. Moreover, the device configuration is suitable for traditional four-probe measurements, which allows determining the electrical conductivity of the nanowire.

In this device, the Seebeck coefficient can be studied as a function of the carrier concentration (by using the back gate), and as a function of the temperature. Furthermore, the device configuration allows estimating the charge carrier mobility in the nanowire, by sweeping the gate voltage at a given source-drain voltage. An example of a back-gate sweep is shown in Figure 4.9.

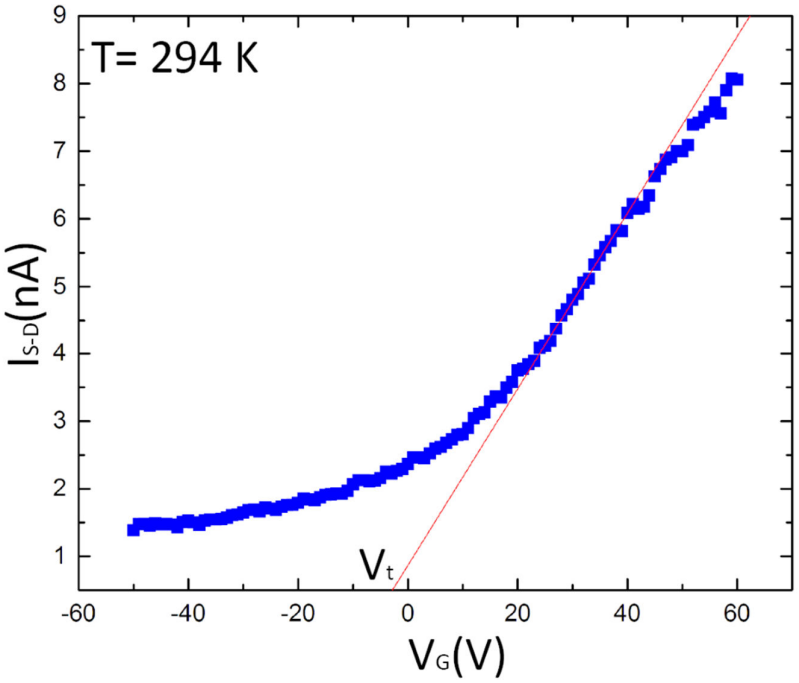

Figure 4.9. – Typical source-drain current (I_{S-D}) back gate (V_G) sweep dependence of a nanowire. $V_{S-D} = 0.01$ mV.

The carrier mobility can be derived from the slope. A tangent of the maximum slope can be calculated. Then, using Eq. (2.20), the mobility can be estimated. Eq. (2.20) assumes constant carrier mobility. However, in reality, this is not the case. Typically, as a benchmark for a nanowire performance, the maximum value of dG/dV_G is taken, and the quantity determined in this way is called 'field-effect mobility'[11, 12]. We follow this convention in this thesis. The specific capacitance C_{spec} for the nanowire is given by Eq. (2.21)[10]. For the sample used in this thesis, $t_{ox} = 100$ nm and $\varepsilon = 3.9$. The carrier density is extracted from the threshold voltage (V_t).

4.3 Probe station and measurement configurations.

It is crucial to perform the measurements described above in a low-pressure atmosphere in order to prevent thermal transport between the membranes through convection and conduction in the gas phase. Thus, all the measurements described above are performed inside a Janis ST-500 probe station. A schematic drawing of the probe station chamber is shown in Figure 4.10. The probe station's chamber is pumped down to a pressure of around $1 \cdot 10^{-6}$ mbar (at room- temperature) with a pump set containing an Edwards backing pump and a turbopump. All room- temperature measurements have been performed at this pressure. The vacuum chamber is equipped with a thermocouple and an internal heater to measure and control the temperature at the sample chuck, respectively. The probe station allows a wide range of working temperatures (2.5 K – 400 K). The combination of the temperature controller and

heater allows keeping the desired temperature within 0.1 K accuracy. The sample is placed on top of the sample chuck using thermal paste, which provides a proper thermal contact. We assume that the sample has the same temperature as the chuck. For the electrical measurements, the sample is glued to the chuck by electrically conductive Ag paste to provide an acceptable gate response.

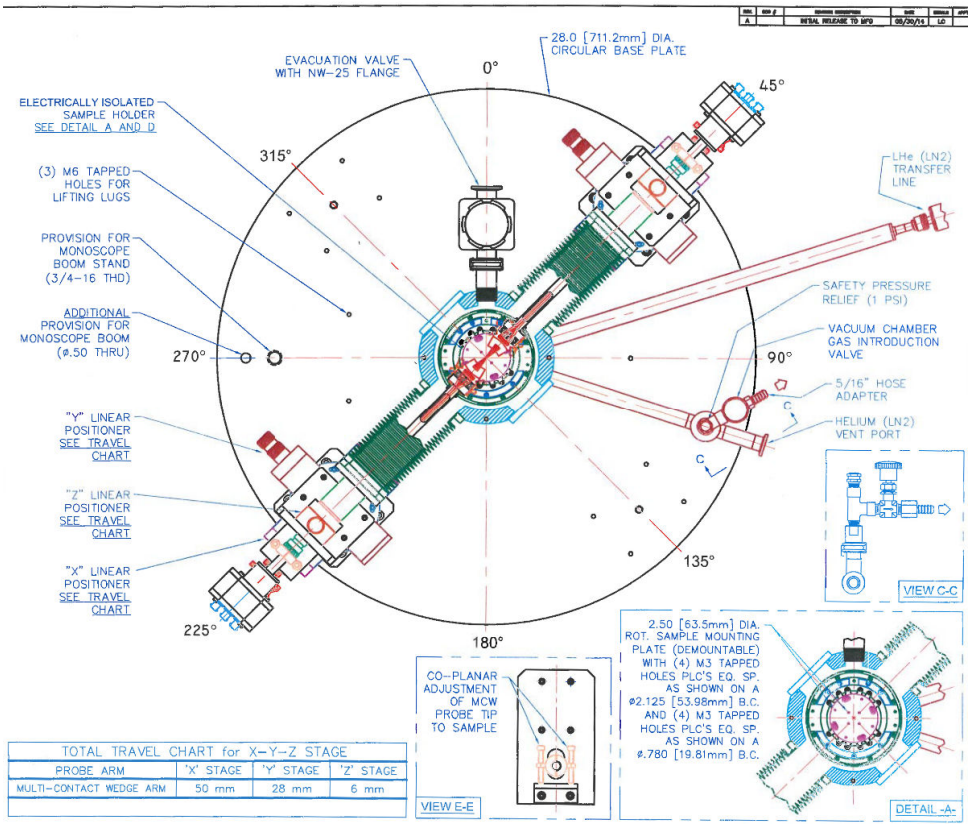

Figure 4.10. – Drawing (top view) of the Janis ST-500 probe station (image courtesy of Janis Research Company, LLC). The essential components and some of their dimensions are indicated in the drawing.

Two moveable arms are connected to the probe station. As shown in Figure 4.11, six BeCu probe tips are connected to each arm, providing the twelve connections needed to perform thermal and electrical measurements as described in Sections 4.1 and 4.2. A standard optical microscope is used to accurately place the probes on the contact pads. Four outer tips of each probe are used for the four-point measurement of the meandering structures to perform the thermal analyses. In the case of electrical measurements, all twelve probes are used.

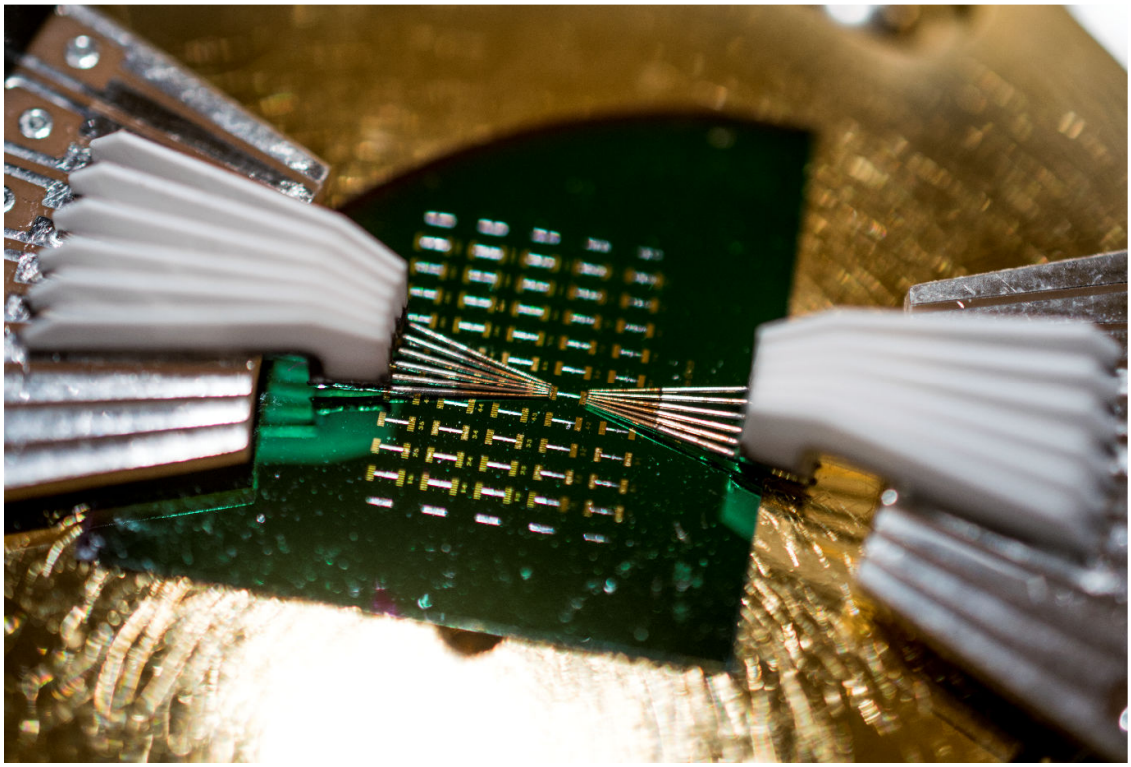

Figure 4.11. – Image of the sample inside the cryostat. BeCu probe tips are placed on the sample's contact pads.

The probe tips are wired to a Keithley 4200 Semiconductor Characterization System (SCS) via current amplifiers and a switching board, as shown in Figure 4.12. The Keithley 4200 SCS is a system with four source measure units (SMUs) combined in a single device. These SMU's can be employed as current/voltage sources or meters. All SMUs have two connections: 'force' and 'sense'. The force unit has a low input impedance, and it is thus used as a current/voltage source, or as a current meter. The sensing unit has a high input impedance and therefore it is suitable for measuring voltages. In order to perform a four-point measurement, the 'force' SMU is connected as a current source, and the 'sense' part of the same SMU is connected to measure the voltage. The National Instruments (NI) NI USB-3625 switching board allows measuring heat transport in two directions, by applying heating current to one of the membranes and sensing to another one, and vice versa. The high input impedance of the sensing units protects current to flow to the voltage meter. Therefore, there is no voltage drop across the leads from the probe station and the platinum lines to the voltage measuring unit. When the sensing unit is disconnected, the voltage is measured in the force unit (2W measurements).

The Keithley 4200 system has a low current noise level ($5{\cdot}10^{-12}$ A) due to the preamplifiers connected close to the sample. However, the system has limited sensitivity to low voltages; therefore, another Keithley configuration, described below, has been used for the power factor measurements.

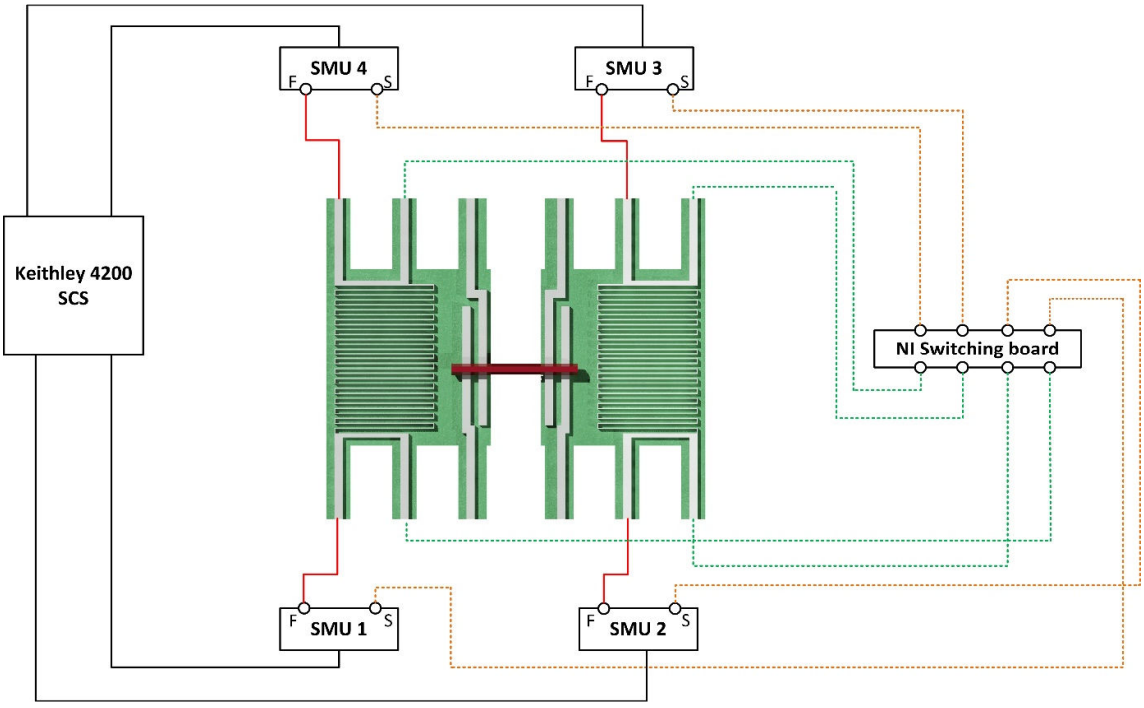

Figure 4.12. – Schematic configuration of the wiring for thermal properties measurements.

An external Keithley 2182A nano voltmeter and Keithley 6220 low noise precision current source have been added to the configuration. The NI USB-3625 switching board is used to share the nano voltmeter between the two device thermometers. The combination of external equipment, together with the Keithley 4200 SCS, allows reaching acceptable measurement sensitivity. Figure 4.13 shows the configuration; essential components are mentioned in the picture.

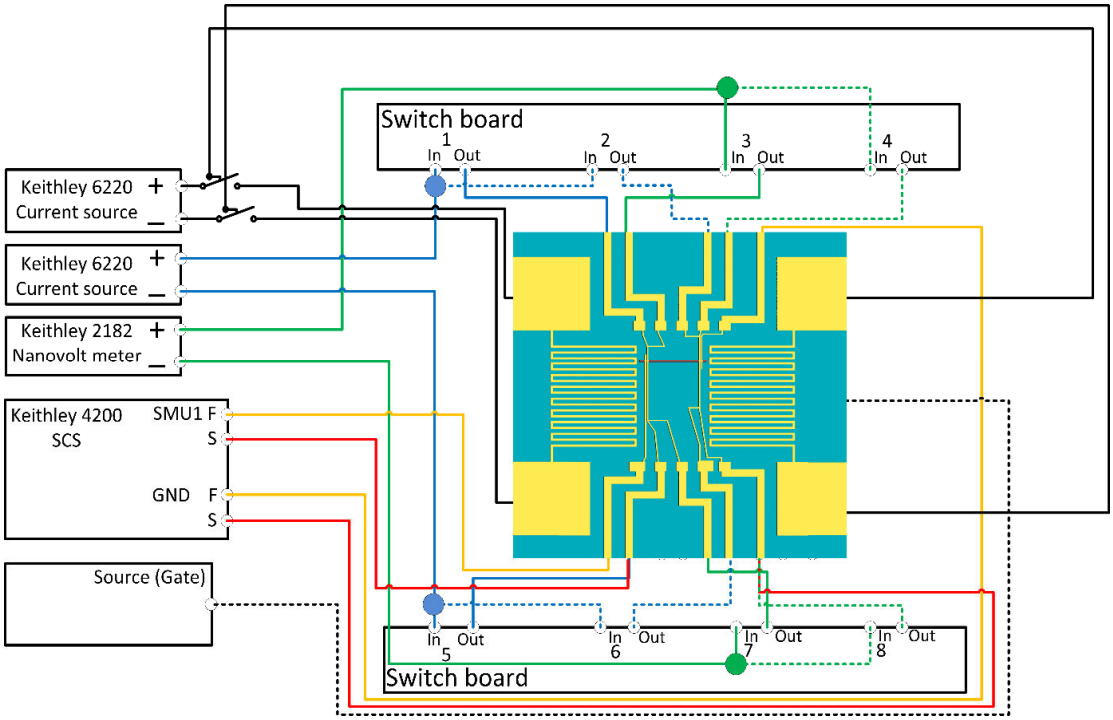

Figure 4.13 – The wiring scheme of the setup used for power factor measurements. When the switch on the board is flipped, the lines and dashed lines of a specific color are swapped. Both switches are switched at the same time. The switches of the Keithley 6220 current source allow applying a heating gradient in two directions separately. The source of the gate voltage is shown in the figure with a black dashed line.

After all measurements have been completed, the sample is inspected with a Scanning Electron Microscope (SEM) to estimate the geometrical properties of the nanowire. It is essential to perform these measurements at the final step since there have been reports on the influence of carbon and other contaminations inside the SEM chamber affecting the transport properties of the nanowire[13]. After finding the nanowire dimensions, the power factor is calculated using the following equations[14]:

$$PF = \frac{S^2}{R_{NW} \cdot A}, \tag{4.17}$$

$$A = \frac{\pi}{4} D^2, \tag{4.18}$$

where R_{NW} is the nanowire resistance and D the diameter of the nanowire. As an approximation, a circular wire is assumed because it is impossible to determine the exact faceting of the nanowire in the SEM.

4.4. Limitations of the measurement technique.
4.4.1. Sensitivity.

As explained in the previous section, the main limitation of the thermal conductance measurement technique is the sensitivity of the temperature measured on the sensing side. It lies in the precision of the determination of the resistance difference, and thus the temperature difference. A large part of the measurement error is due to the small resistance change (several Ohms ,which correspond to ΔT=1 K), on a resistance exceeding 10 kOhm. Thus, a high accuracy is required. Moreover, the resistance change needs to be measured at very low power to prevent Joule heating effects, which would lead to a reduction of accuracy. One way to overcome this issue is to use a Wheatstone bridge setup configuration[15]. This technique allows measuring the change in the desired resistance and not the total resistance. A Wheatstone bridge is based on resistors with two parallel lines of resistors in series, as shown in Figure 4.15[20].

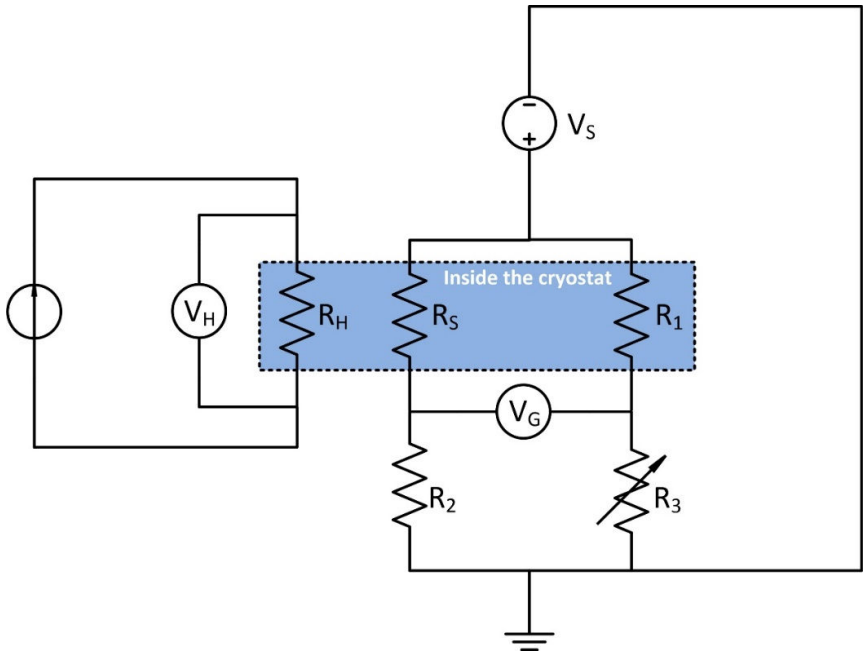

Figure 4.15. – Schematic illustration of the Wheatstone bridge setup. The unknown resistance R_s is to be measured. The resistances R_1, R_2, and R_3, are known, and R_3 is adjustable.

The setup is arranged in such a way that the voltage measured across the bridge is zero when the bridge is balanced. Therefore, a voltage will be created over the bridge when one resistance changes. The established voltage is related to the resistance changes via Eq. (4.19):

$$V_{Br} = \left(\frac{R_2}{R_S + R_2} - \frac{R_3}{R_1 + R_3} \right) V_S \rightarrow R_S = \frac{R_2}{\frac{V_{BF}}{V_S} + \frac{R_3}{R_1 + R_3}} - R_2 \quad , \tag{4.19}$$

where Vs is the voltage applied by the source, V_{Br} the voltage over the bridge, and R_X the resistances as shown in Figure 4.15. In this work, the Wheatstone bridge is used to measure a small resistance change on the sensing side. The resistance change on the heating side is measured using the standard four-probe technique described in Section 4.1. A neighboring meander structure, which is not part of the measurement, is used as paired resistance. Resistance fluctuations, caused by temperature fluctuations, are balanced out since the meanders are in the cryostat and relatively close to each other. Nevertheless, in this scheme, the sensing meander is measured through a two-point measurement. Thus, platinum contact lines will contribute to the measurement results. The platinum contact lines connected to the meander heat up during the measurements, changing their resistance. Assuming a linear temperature profile along the Si_3N_4 beams[21], the total change of the sensing resistance can be given as:

$$\begin{aligned} R_S + \Delta R_S &= 2\left[R_B + \frac{dR_B}{dT}\left(\frac{T_S - T_0}{2}\right)\right] + R_M + \frac{dR_M}{dT}\left(T_S - T_0\right) \rightarrow \\ \Delta R_S &= \left(\frac{dR_B}{dT} + \frac{dR_M}{dT}\right)\Delta T \end{aligned} \quad , \tag{4.20}$$

where R_B is the resistance of the Si_3N_4 beams, and R_M the resistance of the meander. The first factor 2 in Eq. (4.20) comes from the fact that current is going via two Si_3N_4 beams, and the second factor 2 comes from the linear temperature profile. Determine derivative of R_M is crucial since it has been used in the previous analysis. The derivative can be extracted using the equation:

$$\begin{aligned} \frac{dR_B}{dT} &= \alpha_B R_B = \frac{\alpha_B}{\alpha_S}\frac{1}{R_s}\frac{\Delta R_s}{\Delta T}R_B \rightarrow \\ \frac{dR_M}{dT} &= \frac{\Delta R_s}{\Delta T} - \frac{dR_B}{dT} = \left(1 - \frac{\alpha_B}{\alpha_S}\frac{R_B}{R_S}\right)\cdot\frac{\Delta R_s}{\Delta T} = \frac{R_M + \left(2 - \frac{\alpha_B}{\alpha_S}\right)R_B}{R_M + 2R_B}\cdot\frac{\Delta R_s}{\Delta T} \end{aligned} \quad . \tag{4.21}$$

It is assumed that $\alpha_B = \alpha_S$, thus the correction factor will be [15]:

$$\frac{dR_M}{dT} = \frac{R_M + R_B}{R_M + 2R_B}\cdot\frac{\Delta R_S}{\Delta T}. \tag{4.22}$$

Usually, α_B will be larger than α_S because the meanders are thinner and have more scattering on the sidewalls. In fact, by assumption, the correction factor is overestimated and with this also the temperature changes of the meanders. Nevertheless, using values obtained from the measurements described in Section 4.1, the deviation due to the difference in values of α is $\leq$5%.

It was experimentally found that the bridge voltage V_{Br} could never be reduced to zero by changing the variable resistance. This effect is attributed to a parasitic frequency-dependent impedance of the variable resistance. The effect increases with

frequency. Hence, an optimal frequency was found, which results in low impedance and reduced noise[21]. Furthermore, this value is still below the measurement accuracy of the standard technique by two orders of magnitude. The experiment shows that the bridge method can be used to measure thermal conductance below 10^{-11} W/K. Results using the standard and the Wheatstone bridge technique are compared in Figure 4.16.

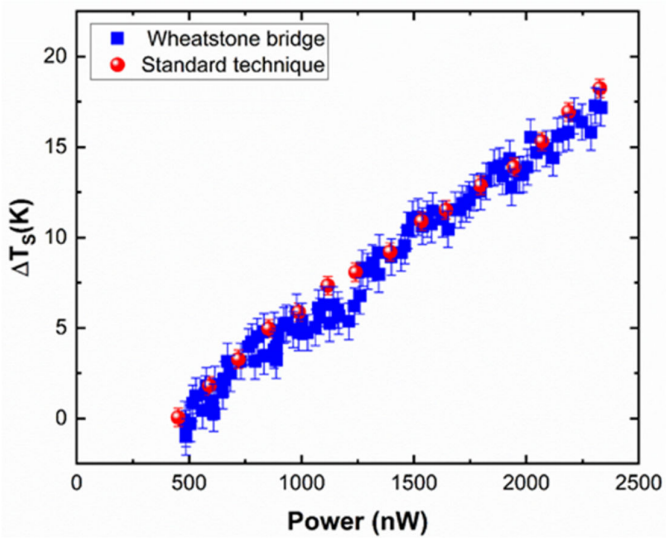

Figure 4.16. – Comparison of the obtained data between the standard technique and Wheatstone bridge technique.

The sensitivity obtained from both methods is comparable. However, the standard technique is much faster and more convenient than the Wheatstone bridge method. Therefore, most of the thermal conductance measurements were done using the conventional technique. The Wheatstone bridge method was only used to validate the measurement results in which the conductance was close to the resolution provided by the standard procedure.

4.4.2. Thermal contact resistance.

Another essential limitation of the measurement technique is the thermal contact resistance[4], which is the resistance between the nanowire and the Si_3N_4 membrane. This resistance fundamentally arises due to a mismatch in phonon wavevector of the different materials, but in practice it is determined by the poor mechanical contact. The thermal contact resistance can never be obviated entirely since the thermal mismatch between two materials is a fundamental issue. Therefore, it is essential to estimate the influence of the thermal contact resistance, especially at the nanoscale[16]. The resistance can be determined by measuring the difference in voltage for a known current through the nanowire or contact lead, following Ohm's Law: $R=\delta U/\delta I$. In order to determine the influence of the contact resistance, the measurements have been performed using both a two-probe (2W) and four-probe measurement (4W). For the

2W measurement technique, a current is sent through two contacts and the voltage is measured via the same contacts. However, a 4W measurement allows probing the voltage difference by the other two contacts, which are placed in between the current contacts. Thus, it will fully avoid contact resistance. In order to determine the influence of the contact resistance in both cases (thermal measurements and power factor measurements), two and four-probe measurements are compared in Figure 4.14.

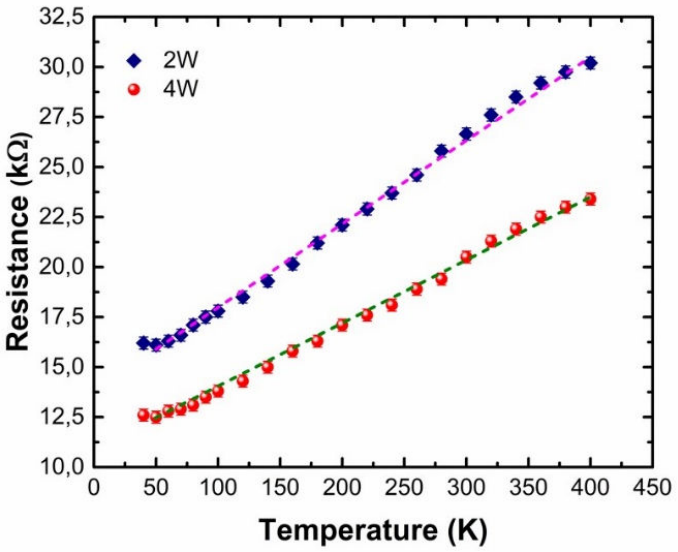

Figure 4.14. – Comparison between 2W and 4W measurements: Resistance-temperature dependence of Pt thermometers.

Based on the obtained results, it can be concluded that the contact resistance is significant (5 kOhm) and that the thermometer measurements thus require the 4W technique, which has been used in all experiments[19].

4.5. Alternative measurement techniques.

4.5.1. Thermal imaging.

A thermal imaging (TI) technique has been applied to validate the temperature distributions in the designed measurement devices. TI is a thermography technique that detects small changes in the light reflectance from a surface due to a change in temperature through the following equation[22]:

$$\frac{\Delta R'}{R'} = C_{TR} \cdot \Delta T, \tag{4.23}$$

where R' is reflectance, and C_{TR} is the thermoreflectance coefficient. C_{TR} depends on the wavelength and the material[22]. A photo of the TI setup is shown in figure 4.17. A microscope and a CCD camera are used to obtain a 2D temperature distribution with a spatial resolution of a few hundred nanometers, determined by the Rayleigh

criterion[23]. The main limitation of this technique is the restricted number of materials which can be measured[24].

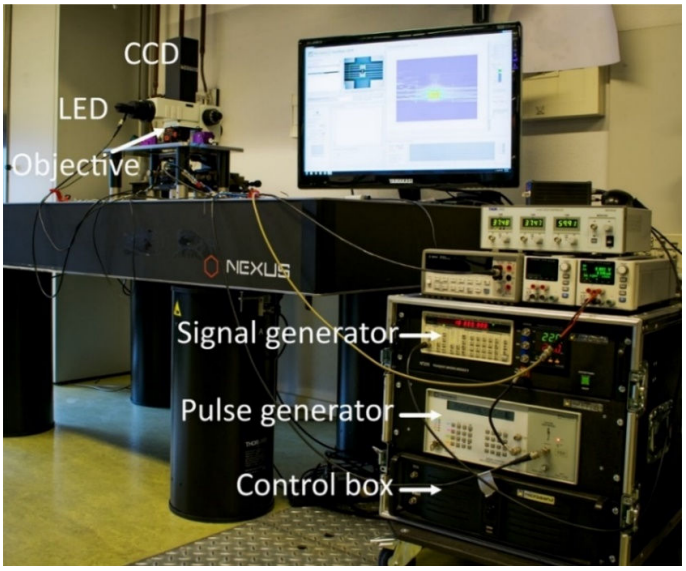

Figure 4.17. – Photo of the thermal imagine setup. Essential components are indicated in the picture.

For example, the temperature of SiO_2 cannot be measured using thermoreflectance since SiO_2 (as well as Si_3N_4) is mostly transparent to visible light (530 nm light was used)[25]. On the other hand, the temperature of the Au leads and contacts can be accurately measured using this technique. TI has been used to verify some of the assumptions made in the previous sections. For example, a thermal image of one of the fabricated power factor devices has been made and is shown in Figure 4.18, which shows that indeed it is not possible to capture temperature distribution along the SiO_2 layer.

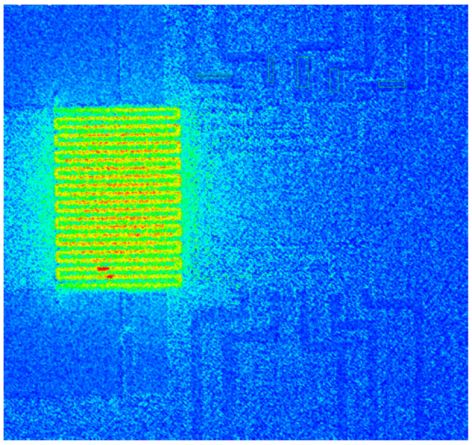

Figure 4.18. – 2D temperature map of the fabricated power factor device, confirming that the heat is dissipated in the meandering structure and not in the contact lines. The dissipation of the heat in SiO_2 cannot be captured by TI, due to the limitations of the method.

However, the obtained results confirm that the simulated (Figure 4.7) and the measured (Figure 4.18) temperature profiles are similar.

4.5.2. Raman thermography.

Another measurement technique, which is used in the thesis to verify thermal conductivity measurement results, is Raman thermography. Raman thermography is a laser-based microscopy measurement technique[26-28]. Laser light is focused through the objective of a microscope onto the nanowire, as shown in Figure 4.19.

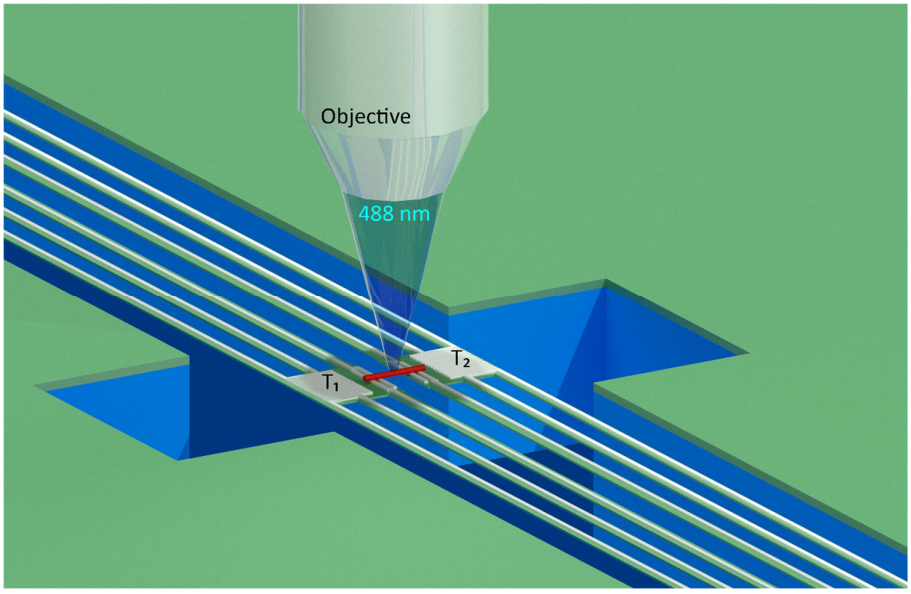

Figure 4.19. – Schematic illustration of the Raman thermography technique: a laser spot is moved along the wire, and Raman spectra are acquired with and without applied temperature gradient across the nanowire.

By moving the laser spot over the suspended nanowire, temperature maps can be obtained by measuring each point. At each position, a Raman spectrum is taken with and without applying a temperature gradient (for both directions of the applied temperature gradient). Then every spectrum is deconvoluted with Lorentzian functions, and since $d\omega \propto dT$ the shift of the TO mode as a function of position along the nanowire for the different applied temperature gradient provides a value of the lattice temperature[29].

Raman thermography was performed by exciting the samples with a 488 nm Coherent Sapphire laser. The measurements were performed in a backscattering geometry using a 100x (NA=0.5) objective, which provides a spatial resolution of about 700 nm[29]. The polarization of the laser light and the outcoming scattered beam can be controlled and selected by polarization optics. In order to maximize the absorption and thus the Raman scattering intensity, the polarization of the excitation light is set parallel to the nanowire axis. The scattered light is collected by a 750 mm focal length

monochromator equipped with a 1.800 g/mm, providing a spectral resolution of < 1 cm^{-1}. The temperature resolution is defined by the system's spectral resolution and the material temperature-dependent Raman shift of the optical phonon modes. In the system used in this thesis, a temperature resolution of a few K can be reached. Typical Raman spectra obtained from a nanowire are presented in Figure 4.19.

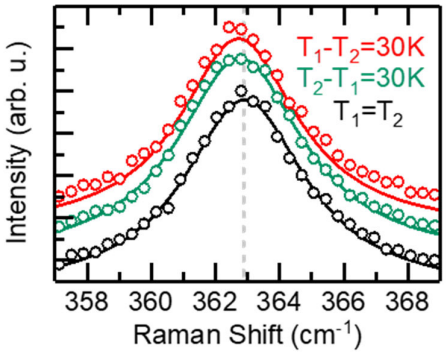

Figure 4.20. – Typical Raman spectra obtained from a nanowire: black represents the spectrum without a temperature gradient, red and green with a temperature gradient applied in both directions, respectively. Data points represent experimental data, and lines are fitted spectra.

Appendix A4.1. Seebeck device architecture.

The heating element should work such that most of the heat will dissipate in the heating structure and not in the contact lines connecting the heating structure. The proposed design must meet this requirement. In order to check that a relation exist between R_h and R_l has to be calculated. Using Eq. (A4.1)

$$\sigma = \frac{1}{\rho} = \frac{l}{R \cdot A}. \tag{A4.1}$$

The relation can be estimated by the formula (A4.2.):

$$\frac{R_h}{R_l} = \frac{L_h \cdot A_l}{L_l \cdot A_h}, \tag{A4.2}$$

where L and A are the length and cross-sectional area of the lines, respectively.

The subscripts h and l refer to the meandering heating structure and the lines connecting the heater, respectively. The higher the R_h/R_l ratio the more heat will be dissipated in the meandering heater. It can be concluded that the ratio depends only on the geometrical properties of the contact lines. Figure A4.1 shows the proposed design with some of the dimensions.

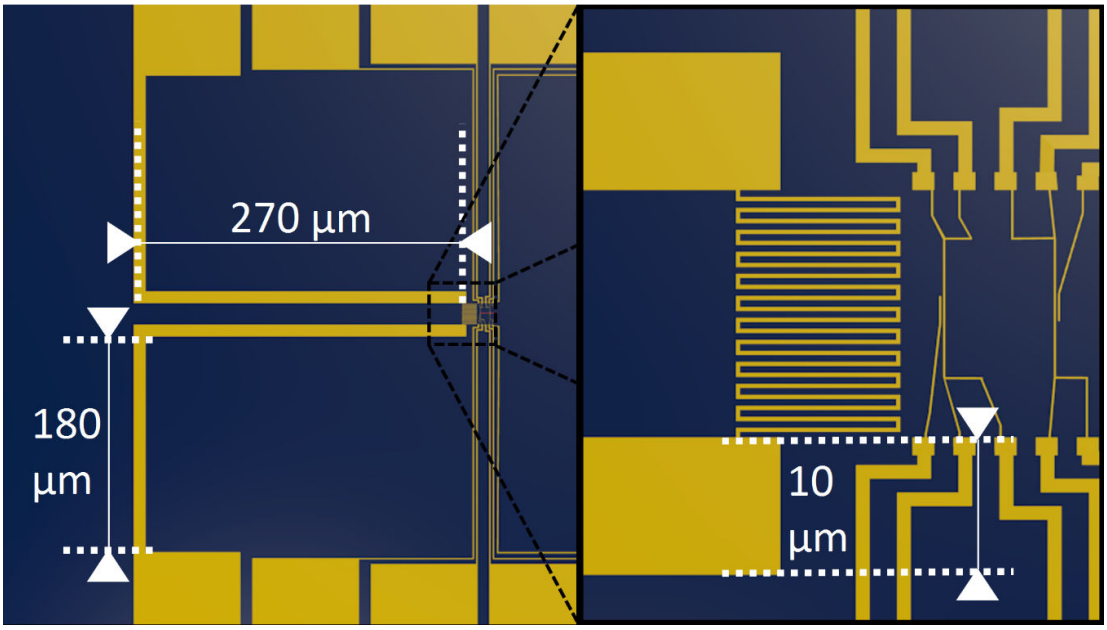

Figure A4.1. – The dimensions of the wires connecting the meandering structure to the contact pads.

The total length of the gold lines is 2 x (270 + 180) μm. The thickness of the gold lines is 800 nm, and their width is 10 μm. The dimentions of the meandering structure are around 270 µm long and 300 nm wide. The thickness of the meandering structure and lines are 150 nm. Putting the parameters into Eq. (A4.2) gives the calculated value $R_h/R_l = 53.333$. Therefore, most of the heat will dissipate in the meandering structure, which is further confirmed by the TI heat distribution map (Figure 4.18).

4.6. References.

1. Li, D. et al. Thermal conductivity of individual silicon nanowires. Applied Physics Letters 83, 2934-2936 (2003).
2. Hernandez, J. et al. Thermoelectric properties of SnSe nanowires with different diameters. Scientific Reports 8, (2018).
3. Swinkels, M. Y. et al. Diameter dependence of the thermal conductivity of InAs nanowires. Nanotechnology 26, 385401 (2015).
4. Shi, L. et al. Measuring Thermal and Thermoelectric Properties of One-Dimensional Nanostructures Using a Microfabricated Device. Journal of Heat Transfer 125, 881 (2003).
5. Wang, X. et al. Measuring nanowire thermal conductivity at high temperatures. Measurement Science and Technology 29, 025001 (2018).
6. Weathers, A. et al. Reexamination of thermal transport measurements of a low-thermal conductance nanowire with a suspended micro-device. Review of Scientific Instruments 84, 084903 (2013).

7. Chen, R. et al. Thermal Conductance of Thin Silicon Nanowires. Physical Review Letters 101, (2008).
8. Akdemir, B. & Reisoğlu, B. A Novel Glow Plug Design to Improve Heating Capability via Induction Heating. International Journal of Automotive Engineering and Technologies 6, 85-94 (2017).
9. Gül, Ö. et al. Towards high mobility InSb nanowire devices. Nanotechnology 26, 215202 (2015).
10. Ford, A. et al. Diameter-Dependent Electron Mobility of InAs Nanowires. Nano Letters 9, 360-365 (2009).
11. Scheffler, M. et al. Diameter-dependent conductance of InAs nanowires. Journal of Applied Physics 106, 124303 (2009).
12. Conesa-Boj, S. et al. Boosting Hole Mobility in Coherently Strained [110]-Oriented Ge–Si Core-Shell Nanowires. Nano Letters 17, 2259-2264 (2017).
13. Blömers, C. et al. Hall effect measurements on InAs nanowires. Applied Physics Letters 101, 152106 (2012).
14. Bergman, T., Lavine, A. & Incropera, F. Fundamentals of heat and mass transfer. (Wiley, 2007).
15. Wingert, M. et al. Ultra-sensitive thermal conductance measurement of one-dimensional nanostructures enhanced by differential bridge. Review of Scientific Instruments 83, 024901 (2012).
16. Shi, L. Thermal and Thermoelectric Transport in Nanostructures and Low-Dimensional Systems. Nanoscale and Microscale Thermophysical Engineering 16, 79-116 (2012).
17. Heedt, S. et al. Electronic Properties of Complex Self-Assembled InAs Nanowire Networks. Advanced Electronic Materials 2, 1500460 (2016).
18. Chiu, S. et al. Four-probe electrical-transport measurements on single indium tin oxide nanowires between 1.5 and 300 K. Nanotechnology 20, 105203 (2009).
19. van Weperen, I. et al. Quantized Conductance in an InSb Nanowire. Nano Letters 13, 387-391 (2012).
20. Wheatstone, C. An Account of Several New Instruments and Processes for Determining the Constants of a Voltaic Circuit. Proceedings of the Royal Society of London 4, 469-471 (1837).
21. Wenner, F. & Smith, A. Measurement of low resistance by means of the Wheatstone bridge. (U.S. Govt. Print. Off., 1924).
22. Jiang, P. et al. Tutorial: Time-domain thermoreflectance (TDTR) for thermal property characterization of bulk and thin film materials. Journal of Applied Physics 124, 161103 (2018).
23. Chavez, R. et al. Thermopower characterization of InSb nanowires using thermoreflectance. 23rd International Workshop on Thermal Investigations of ICs and Systems (THERMINIC) (2017).
24. Ziabari, A. et al. Sub-diffraction-limit thermal imaging for HEMT devices. 31st Thermal Measurement, Modeling & Management Symposium (SEMI-THERM) (2015).
25. Wang, L., Cheaito, R., Braun, J., Giri, A. & Hopkins, P. Thermal conductivity measurements of non-metals via combined time- and frequency-domain

thermoreflectance without a metal film transducer. Review of Scientific Instruments 87, 094902 (2016).
26. Kuball, M. & Pomeroy, J. A Review of Raman Thermography for Electronic and Opto-Electronic Device Measurement with Submicron Spatial and Nanosecond Temporal Resolution. IEEE Transactions on Device and Materials Reliability 16, 667-684 (2016).
27. Faqir, M. et al. New GaN Power-Electronics Packaging Solutions: A Thermal Analysis Using Raman Thermography. Journal of Microelectronics and Electronic Packaging 8, 110-113 (2011).
28. Zardo, I. et al. Raman spectroscopy of wurtzite and zinc-blende GaAs nanowires: Polarization dependence, selection rules, and strain effects. Physical Review B 80, (2009).
29. Yazji, S. et al. Complete thermoelectric benchmarking of individual InSb nanowires using combined micro-Raman and electric transport analysis. Nano Research 8, 4048-4060 (2015).
30. Torres, J., Springer, T., Welch, A. & Pearce, J. Limitations of a thermal camera in measuring surface temperature of laser-irradiated tissues. Lasers in Surgery and Medicine 10, 510-523 (1990).

Chapter 5. Ballistic phonons in ultrathin nanowires.

According to Fourier's law, a temperature difference across a material results in a linear temperature profile and a thermal conductance that decreases inversely proportional to the system length. These are the hallmarks of diffusive heat flow. Here, we report heat flow in ultrathin (25 nm) GaP nanowires in the absence of a temperature gradient within the wire and find that the heat conductance is independent of wire length. These observations deviate from Fourier's law and are direct proof of ballistic heat flow, persisting for wire lengths up to at least 15 μm at room temperature. When doubling the wire diameter, a remarkably sudden transition to diffusive heat flow is observed. The ballistic heat flow in the ultrathin wires can be modeled within Landauer's formalism by ballistic phonons with extraordinary long mean free path.

5.1. Introduction.

Heat flow in macroscopic systems is traditionally described by Fourier's law for diffusive heat flow[1]. The advancement of micro and nanotechnology has led in the last few years to observations of non-diffusive heat flow. Deviations from diffusive heat flow can occur due to the wave nature of phonons[2], hydrodynamic effects[3–10] but also due to ballistic behavior[11–18]. In nanowires (NWs), the scattering of phonons at the NW surface reduces the thermal conductivity as compared to the bulk[19]. However, when the surface is atomically flat, phonons may reflect specularly from the surface[20, 21] and ballistic heat flow in the axial direction may occur. Realizing ballistic flow over large distances at room temperature requires a long phonon mean free path (MFP), which is challenging due to different scattering mechanisms.

In this chapter, we demonstrate room-temperature axial ballistic heat flow in ultrathin, 25 nm diameter, GaP NWs up to wire lengths of at least 15 μm, and a sharp transition to diffusive heat flow when the diameter is doubled to 50 nm. The temperature profile along the NWs is obtained by Raman thermometry, confirming the presence of a temperature gradient in the diffusive flow regime and its absence in the ballistic regime.

5.2. Nanowire devices.

We grow GaP NWs with 25-140 nm diameters by metal-organic vapor phase epitaxy using the vapor-liquid-solid growth technique (see Appendix A5.1). The NWs are grown in arrays by substrate/catalyst patterning. Within an array, the NWs have a uniform diameter along their length with a <5 nm diameter spread. We analyze the structural properties of the NWs by transmission electron microscopy (TEM). TEM images show stacking-fault-free NWs, grown along the <0001> direction; see Figure 5.1a. The NWs have atomically flat {11-00} side facets covered by an approximately 2 nm thick amorphous oxide layer; see Figure 5.1b. Electron diffraction patterns taken

in the TEM further show that NWs with different diameters used in our study all have the wurtzite (WZ) crystal structure (see Figure A5.1). Atom-probe tomography (APT) demonstrates the chemical purity of the NWs and the absence of heavy element impurities; see Figure 5.1c and Appendix A5.2.

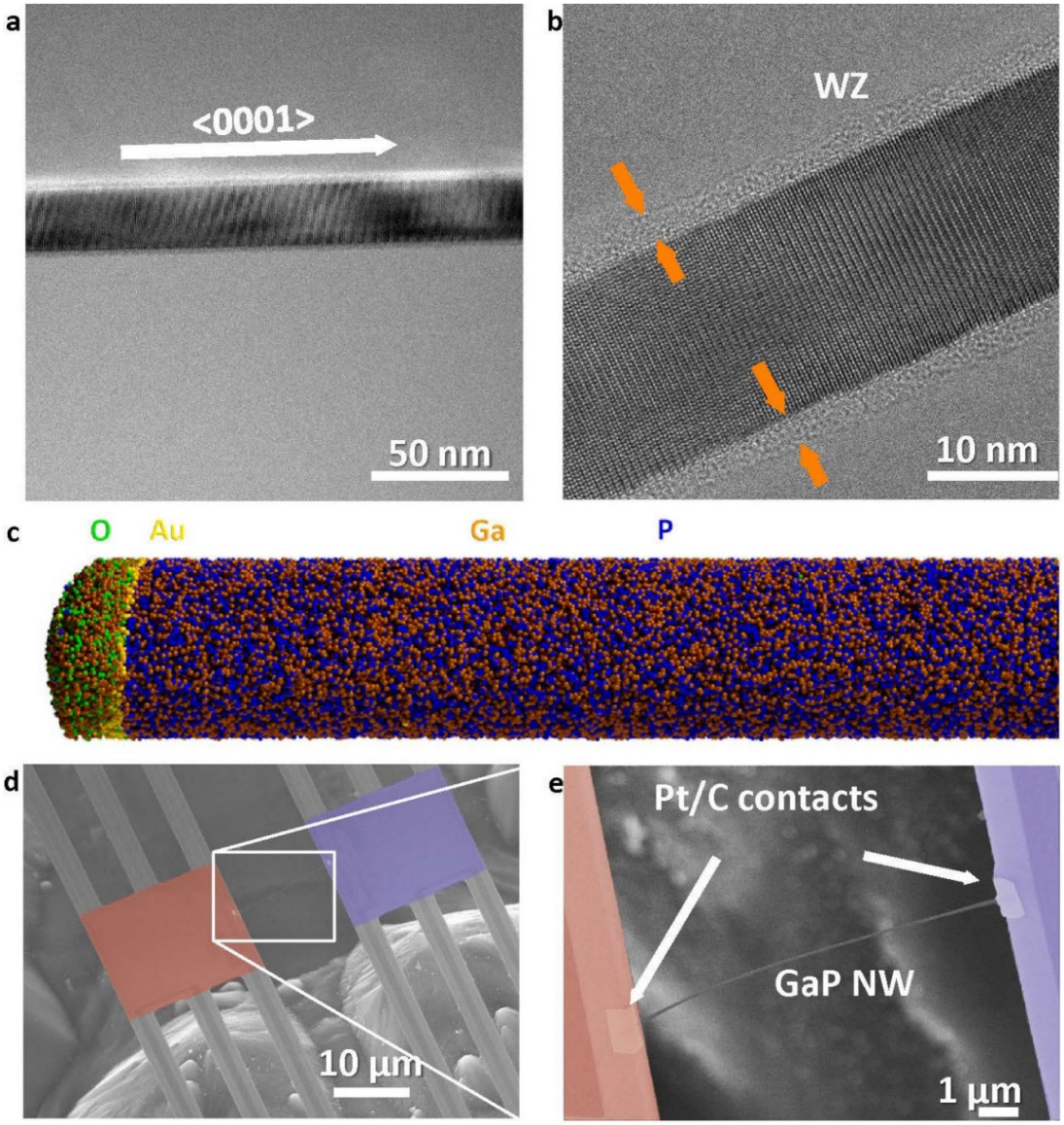

Figure 5.1. – GaP nanowire properties and device for thermal conductance measurements. **a**, TEM image of a 25 nm diameter GaP nanowire (NW), grown along the <0001> direction. **b**, High-resolution TEM image taken along the $<11\bar{2}0>$ direction of an NW showing defect-free wurtzite (WZ) crystal structure and a layer of oxide (orange arrows). **c**, APT analysis of a 25 nm diameter NW showing its high chemical purity. **d**, 45°-tilted SEM image of the thermal conductance measuring device, with suspended heating (red) and sensing (blue) membranes. **e**, Zoom-in of the NW bridging the suspended membranes. Electron beam-induced deposited Pt/C improves the thermal contact.

The NWs are therefore atomically clean and defect-free. Limitations of the APT technique prevent the detection of the oxide layer[22]. We fabricate microdevices[23, 24] to study the thermal conductivity of individual NWs (see Appendix A5.3). The devices consist of two suspended membranes with Pt meander structures on top, which can be used as heater and thermometer; see the scanning electron microscopy (SEM) picture in Figure 5.1d. Different spacings between the membranes allow measuring NWs of different lengths. Using a micromanipulator under an optical microscope, we place as-grown single NWs with selected diameter between the membranes. Pt/C contacts are deposited on top of the NWs to improve the thermal contact; see Figure 5.1e. We determine the thermal conductivity κ from the measured thermal conductance G and the NW dimensions.

5.3. Diffusive to ballistic heat flow transition.

The extracted κ at room temperature $T = 300$ K is plotted in Figure 5.2a as a function of diameter d for NWs with approximately the same length $L = 6.7 \pm 0.1$ μm, with d ranging from 25 to 140 nm. These results were fitted to expose the influence of the thermal contact resistance, R_c [24]. In an NW with heat flow dominated by diffuse scattering at the NW surface, κ increases with d according to Mathiessen's rule $\kappa \propto (1+l_{bulk}/d)^{-1}$, where l_{bulk} is the bulk MFP, as indicated by the dashed line. A reduced κ with respect to this line, which is observed for $d \geq 75$ nm, indicates that R_c is no longer negligible compared to the NW resistance[24]. For thin wires ($d < 50$ nm), on the contrary, an enhanced κ is observed, indicating that a non-diffusive transport mechanism, not dominated by contact resistance, becomes progressively important with decreasing diameter. To investigate the transport mechanism in the thin wires, the thermal resistance $R = 1/G$ has been plotted as a function of NW length L for diameters $d = 25$ and 50 nm in Figure 5.2b (main panel). For the 50 nm NWs R is linearly dependent on L, in accordance with diffusive heat flow. For the 25 nm NWs, however, R is independent of L for all measured NWs, up to $L = 15$ μm, which is proof of ballistic transport. We attribute this resistance to a small number of ballistic modes contributing to transport (see below). We note that the extrapolation of the 50 nm data goes through the origin, corroborating a negligible R_c, in agreement with a model where R_c is taken inversely proportional to the contact area between contact and NW (solid curve in Figure 5.2a). Although we cannot estimate R_c for the 25 nm NWs directly from the measurements, a negligible contact resistance follows from this model. The measured linear dependence of the device conduction with the number of NWs for $d = 25$ nm and $L = 6.7 \pm 0.1$ μm (inset in Figure 5.2b) excludes the influence of a possible background conduction. The data therefore unequivocally point at a transition from diffusive to length-independent ballistic heat flow in 25 nm NWs over unprecedented distances.

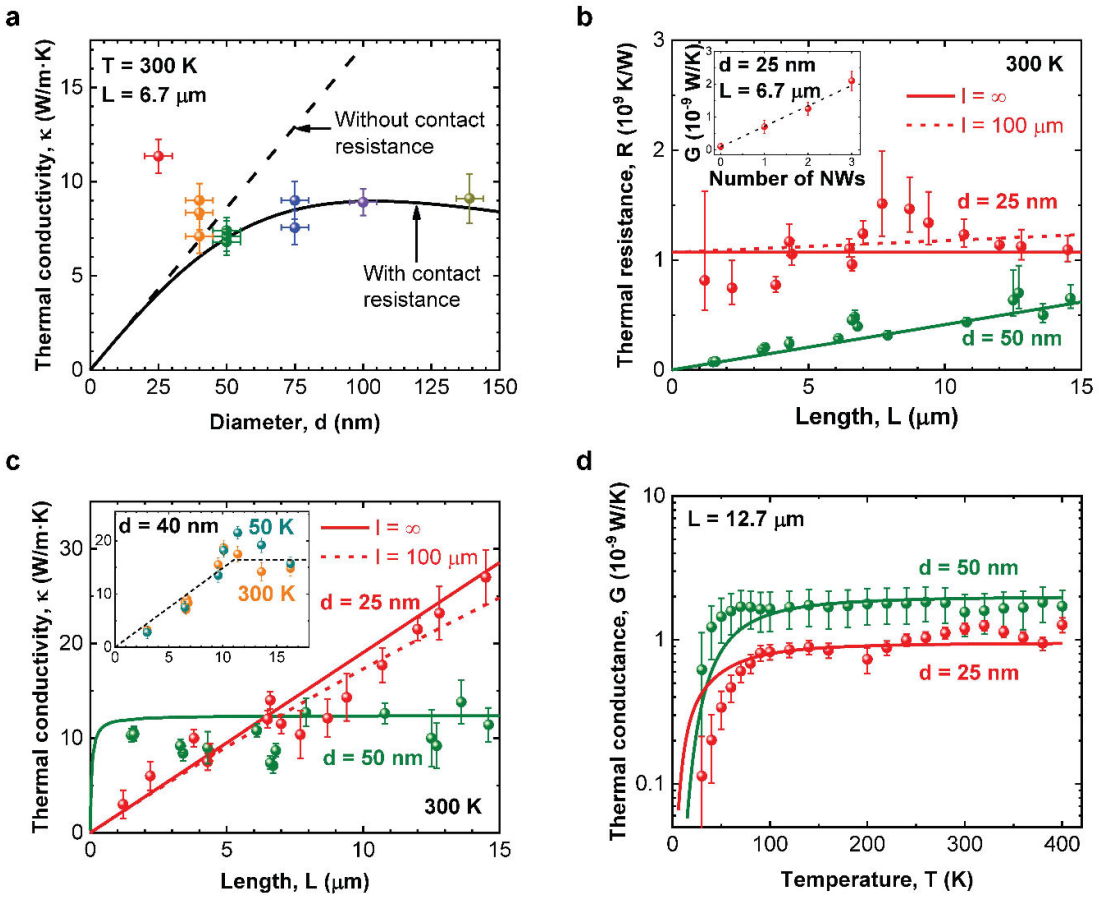

Figure 5.2. – Transition from diffusive to ballistic heat flow. a, Room-temperature (300 K) thermal conductivity κ of GaP NWs of length $L = 6.7 \pm 0.1$ μm as function of diameter d. Full curve: fit of results for $d \geq 50$ nm to $\kappa = (1/c_1 d + c_2 \pi d/4L)^{-1}$ (diffusive heat flow with MFP $l = d << l_{bulk}$ and contact resistance $R_c = c_2/d$, with $c_1 = 1.7 \times 10^8$ W/m^2·K and $c_2 = 4.6$ m·K/W). Dashed line: $\kappa = c_1 d$ (diffusive heat flow without contact resistance and $d << l_{bulk}$). **b,** Symbols: measured length dependence of resistance R of NWs with $d = 25$ and 50 nm. Lines: modeling results based on Landauer's formalism, using the numbers of specular phonon modes N_s ($d = 25$ nm, solid line: MFP $l = \infty$, dashed line: $l = 100$ μm) and diffusive phonon modes N_d ($d = 50$ nm, MFP $l = d$) from Figure A5.10. For $d = 25$ nm, the curve for $l = 100$ μm is obtained by dividing the result for $l = \infty$ by the transmission coefficient $l/(l+L)$ [28]. Inset: conductance G of a device without an NW (see Appendix A5.3) and with 1, 2 and 3 NWs with $d = 25$ nm and $L = 6.7 \pm 0.1$ μm. Dashed line: linear fit. **c,** Same results as in the main panel of B, but for the conductivity κ. Inset: results for $d = 40$ nm NWs measured at 300 and 50 K. Dashed line: a guide to the eye. **d,** Measured (symbols) and modeled (curves) T-dependent thermal conductance G of $d = 25$ and 50 nm NWs with length $L = 12.7 \pm 0.2$ μm.

To further investigate the features of the diffusive-to-ballistic transition we plot in Figure 5.2c (main panel) κ vs L for $d = 25$ and 50 nm NWs at 300 K, clearly showing the remarkable fact that for long wires the thermal conductivity of the ultrathin 25 nm NWs exceeds that of the thicker 50 nm NWs. The inset displays results for 40 nm NWs at 300 and 50 K, showing that at both room and low temperature this is a transition case: the heat flow is ballistic up to $L \approx 11$ μm and then becomes diffusive. Figure 5.2d shows a very weak T-dependence of the thermal conductance G for both 25 and 50 nm NWs of 12.7 ± 0.2 μm length down to about 100 K (below this temperature, G steeply decreases due to phonon freeze-out). Results for 75 nm NWs are comparable to those for 50 nm NWs, showing also a very weakly T-dependent diffusive heat flow (see Figure A5.4). The T-insensitivity rules out explanations for the diffusive-to-ballistic transition based on phonon-phonon interactions, which are strongly T-dependent. In particular, Umklapp scattering, which leads to a strong decrease of κ in bulk GaP above 50 K[25], appears to play no significant role. Also, the involvement of phonon-polaritons as heat-conducting species is unlikely, because they would yield a contribution to G that is linear in T [26].

5.4. Diffusive and ballistic thermal profiles.

To substantiate the ballistic transport in the thin NWs, we probe the thermal profile of 25 and 50 nm NWs with Raman thermometry, which is a contactless method, in the same devices as used for the thermal conductivity measurements; see Figure 5.3a. Here, the local average lattice temperature is measured using the Raman shift of the transverse optical (TO) mode[27] (see Appendix A5.5 for experimental details). We keep the system temperature at $T = 300$ K and heat the hot contact by $\Delta T = 30$ K. Swapping the contacts yields the same results (see Figure A5.5). The frequency shift, $\delta\omega$, of the TO mode (at about 363 cm^{-1} in GaP) with respect to the case without applying a temperature difference provides an estimate of the local lattice temperature increase, δT, since $\delta\omega \propto \delta T$; see Figures 5.3b and d. This differential measurement cancels out changes in the TO mode frequency along the wire caused by other effects than the temperature difference, such as small laser heating effects and local strains. The temperature profile along the 50 nm NW (Figure 5.3c) is linear, in agreement with diffusive transport. Importantly, the Raman thermometry measurements on the 50 nm NW further confirm the absence of significant contact resistance, since the measured temperature gradient agrees with the applied temperature difference, which was calibrated in an independent manner.

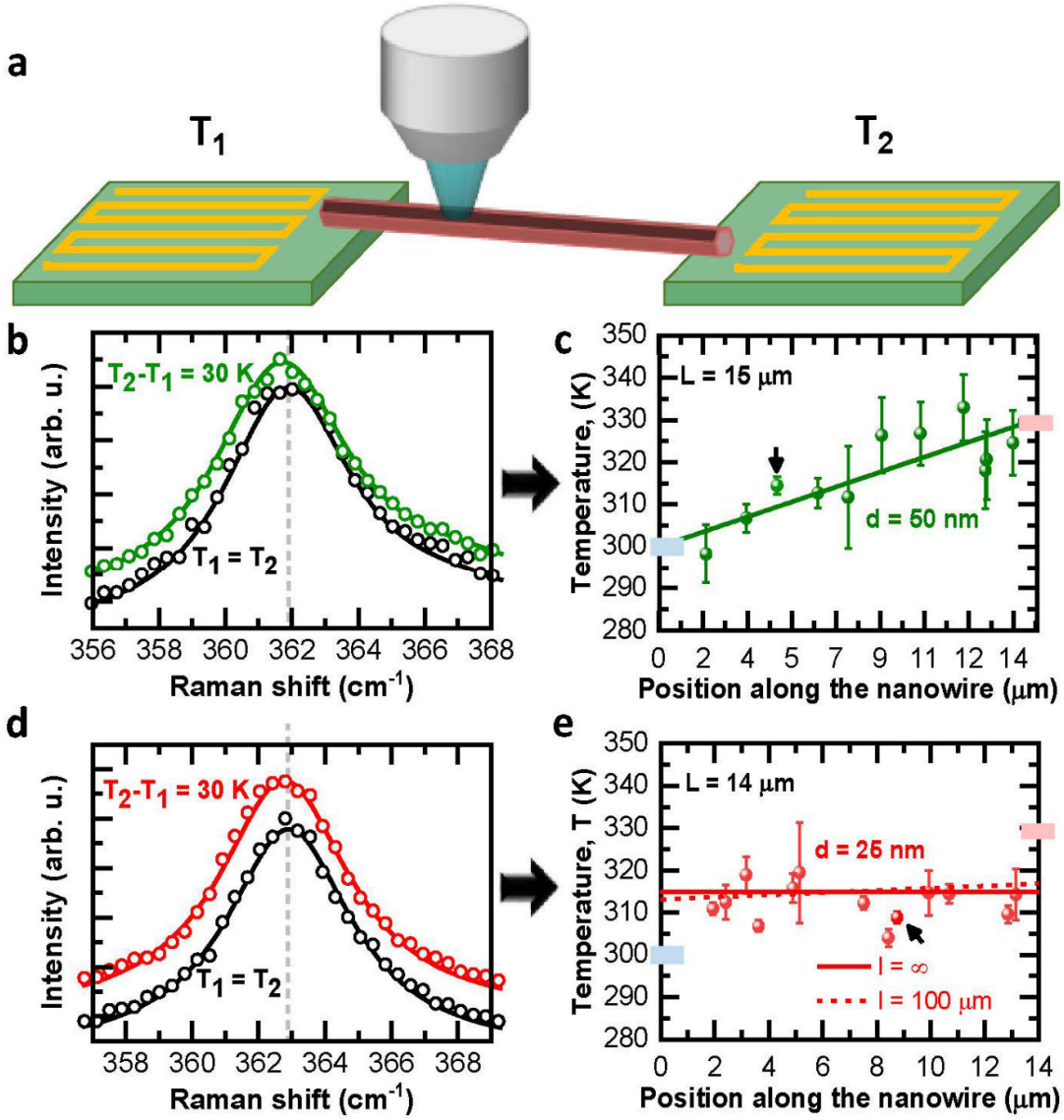

Figure 5.3. – Temperature profiles in the diffusive and ballistic regimes. **a,** Illustration of the microdevice with NW used for the measurements of the thermal profile. A laser spot is moved along the wire, and Raman spectra are acquired for $T_1 = T_2 = 300$ K and $T_1 = 300$ K, $T_2 = 300$ K + ΔT. **b,** Spectra measured at the position indicated by the arrow in c for an NW with $d = 50$ nm and $L = 14.7 \pm 0.3$ μm. Solid lines: Lorentzian fits to the spectra. **c,** Resulting temperature profile along the NW while applying $\Delta T = 30$ K using the Pt meander heaters. Solid line: modeled profile for purely diffusive heat flow. **d** and **e**, The same as b and c but for an NW with $d = 25$ nm and $L = 14.0 \pm 0.3$ μm. Solid line in e: modeled profile for purely ballistic transport with MFP $l = \infty$. Dashed line: profile for $l = 100$ μm with a transmission coefficient $l/(l+L)$, having a slope $[1-l/(l+L)]\Delta T/L$ [28]. The bars at the left and right y-axis in c and e show the temperature of the contacts.

In the 25 nm NW (Figure 5.3e), however, we observe symmetric temperature jumps at the contacts and a constant temperature along the whole wire with δT close to 15 K, exactly as predicted by ballistic heat transport theory[28]. We note that the TO mode itself contributes negligibly to the heat flow because of its very short MFP, but probes the average temperature of the heat-carrying phonons. In ballistic heat flow, heat-carrying phonons traveling in either direction through the NW have the temperature of the contact from which they were injected. The lattice thermalizes equally with the 'hot' and 'cold' phonons and therefore the TO mode probes the average of the contact temperatures, *i.e.*, $\delta T = 15$ K. These results demonstrate the analogy with electrical transport through a ballistic quantum wire, where the electrical potential along the wire is constant and equal to the average of the potentials applied at the contacts[29]. To the best of our knowledge, this is the first measurement of the theoretically predicted temperature profile for ballistic heat transport. Together with the heat transport measurements of Figure 5.2, this provides strong experimental proof for ballistic heat flow.

5.5. Modelling within Landauer's formalism.

We are not aware of an existing model in the literature that can capture a diffusive-to-ballistic transition for decreasing dimensions with the features discussed in this work. To give a tentative explanation, we apply a model based on Landauer's formalism for phonon transport. It neglects anharmonic effects that lead to phonon-phonon scattering, in accordance with the weak T-dependence of our experimental data (see inset of Figure 5.2c and Figure 5.2d). The model we apply has been developed by Murphy and Moore[20] and Chen *et al.*[30]. (see Appendix A5.6) and was successfully used to describe heat flow in silicon NWs[30] and holey silicon[15]. It distinguishes between two different types of phonon scattering at the NW surface: the surface appears sharp (diffuse) to phonons with an inverse perpendicular wave vector component longer (shorter) than the surface oxide layer thickness, leading to mostly specular (diffuse) scattering with long (short) MFP[20, 30]. This description is also consistent with Lévy walk dynamics[18]. We obtain the numbers of modes N_s and N_d of the 'specular' and 'diffusive' phonons at each frequency from *ab-initio* calculations of the phonon band structure of WZ GaP and phonon subband formation in the NW (see Appendix A5.7). In Figure A5.10 these numbers are plotted for $d = 25$ and 50 nm, and an oxide layer thickness $h = 2.45$ nm (fitted to obtain agreement with the $d = 25$ nm thermal transport data, see below). This value of h is close to the measured thickness, see Figure 5.1b. We note that the number of specular phonon modes N_s is only a small fraction (~ 1%) of the number of diffusive modes N_d. We only consider phonons with a frequency below the Debye frequency. Higher-frequency phonons are hardly excited at the considered temperatures and have too short MFPs to significantly contribute to the heat flow.

A model where both contributions of specular phonons with a strongly increased MFP and of diffusive phonons with an MPF $l = d$ are considered equally does not agree with our data (see Figure A5.11). The contribution of diffusive phonons in the 25 nm NWs would lead to an offset in the thermal conductivity κ and the contribution of

specular phonons in the 50 nm NWs would lead to a linear increase in κ, both of which are not observed. Suppression of the contribution to the heat flow of diffusive phonons in the 25 nm NWs accompanied by an enhancement of the contribution of specular phonons is in our model a necessary ingredient to explain the experimental data. As shown by the solid lines in Figures 5.2b-d, we obtain agreement with experiment both for 25 and 50 nm NWs if we 1) neglect for the 50 nm NWs the heat flow carried by specular phonons in Landauer's expression for G (Eq. A5.1 in Appendix A5.6.) and 2) disregard for the 25 nm NWs the contribution of diffusive phonons, taking only into account the heat flow carried by specular phonons with strongly increased MFP. A finite but strongly increased MFP l up to 100 μm would still agree with the heat transport data (dashed lines in Figures 5.2b and c) and would result in a small temperature gradient in the 25 nm NW that is within the experimental uncertainty of the Raman measurements (dashed line in Figure 5.3e). Phonons in the 25 nm NWs therefore travel practically unimpeded and can truly be called ballistic. The weak T-dependence of the heat transport shown in Figure 5.2d is explained by the fact that the main features in both N_s and N_d appear at phonon energies significantly below the thermal energy (see Figure A5.10).

5.6. Discussion and conclusion.

A possible cause for the suppression of the heat flow carried by diffusive phonons is Anderson localization[31] of these phonons in the 25 nm NWs. Recent works show that in NWs with rough or amorphous surfaces, Anderson localization could take place[32, 33]. The effect was shown to be increasingly important for thinner wires[20]. Another cause could be the coupling of the localized modes in the amorphous oxide layer to propagating modes in the crystalline core[34, 35]. Such coupling could result in an effective layer near the boundary of the wire where the thermal conductivity is greatly reduced, an effect that can be much stronger for thinner wires. Finally, within the hydrodynamic framework[3–5, 10], the so-called no-slip condition could also lead to a strong reduction of the thermal conductivity near the boundary of the nanowire, quenching the contribution to the heat flow of diffusive phonons. A possible origin for the enhancement of the contribution of specular phonons is a strongly reduced scattering of these phonons into diffusive modes caused by localization-induced decoupling of specular and diffusive phonons. This scenario, which would agree with the observed weak T-dependence of the transition, is explained in Appendix A5.9.

These qualitative explanations of the reduction of the contribution of diffusive phonons to the heat flow and the enhancement of the contribution of specular phonons should be quantified, such that they can be experimentally verified. Ballistic phonon transport may find application in phonon transistors[36, 37], phonon waveguides[38], and in novel cooling solutions for computer chips, which require rapid removal of heat from ever-decreasing volumes. Ballistic heat flow could possibly be realized more easily in other compound semiconductors composed of lighter elements than Ga and P, such as Al and N, because of even longer MFPs.

Appendix A5.1. Nanowire growth.

GaP nanowires (NWs) are grown by the vapor-liquid-solid (VLS) method, using an array of gold catalyst droplets. In order to achieve small diameters, the patterns for NW growth are fabricated by electron beam lithography (EBL). To obtain nucleation of NWs with diameters smaller than 40 nm, the V/III element ratio has to be increased by a factor of five during the nucleation step and by a factor of two during the growth of the NWs, as compared to the V/III ratio used for NWs with a larger diameter. This can be attributed to the Gibbs-Thomson effect[39, 40], where the high surface tension of small-diameter catalyst droplets leads to a lower supersaturation than for large-diameter droplets. By increasing the V/III ratio, the supersaturation is again brought to an optimal level for the NW growth. In this way, we obtain NWs with diameters in the range 25-140 nm needed for the diameter-dependent study of the thermal transport. Figure A5.1 show SEM images of GaP nanowire arrays together with TEM analysis. Based on the SEM images it can be concluded that the nanowire arrays are homogeneous (Figures A5.1a, e, i, m). TEM images further validate that the NWs have a uniform diameter along their length and defect-free wurtzite (WZ) crystal structure (Figures A5.1b, f, j, n). A native gallium oxide layer of about 2 nm thick is present on the surface of each NW (Figures A5.1c, g, k, o). Electron diffraction patterns additionally confirm the WZ crystal structure of the NWs with different diameters (Figures A5.1d, h, l, p).

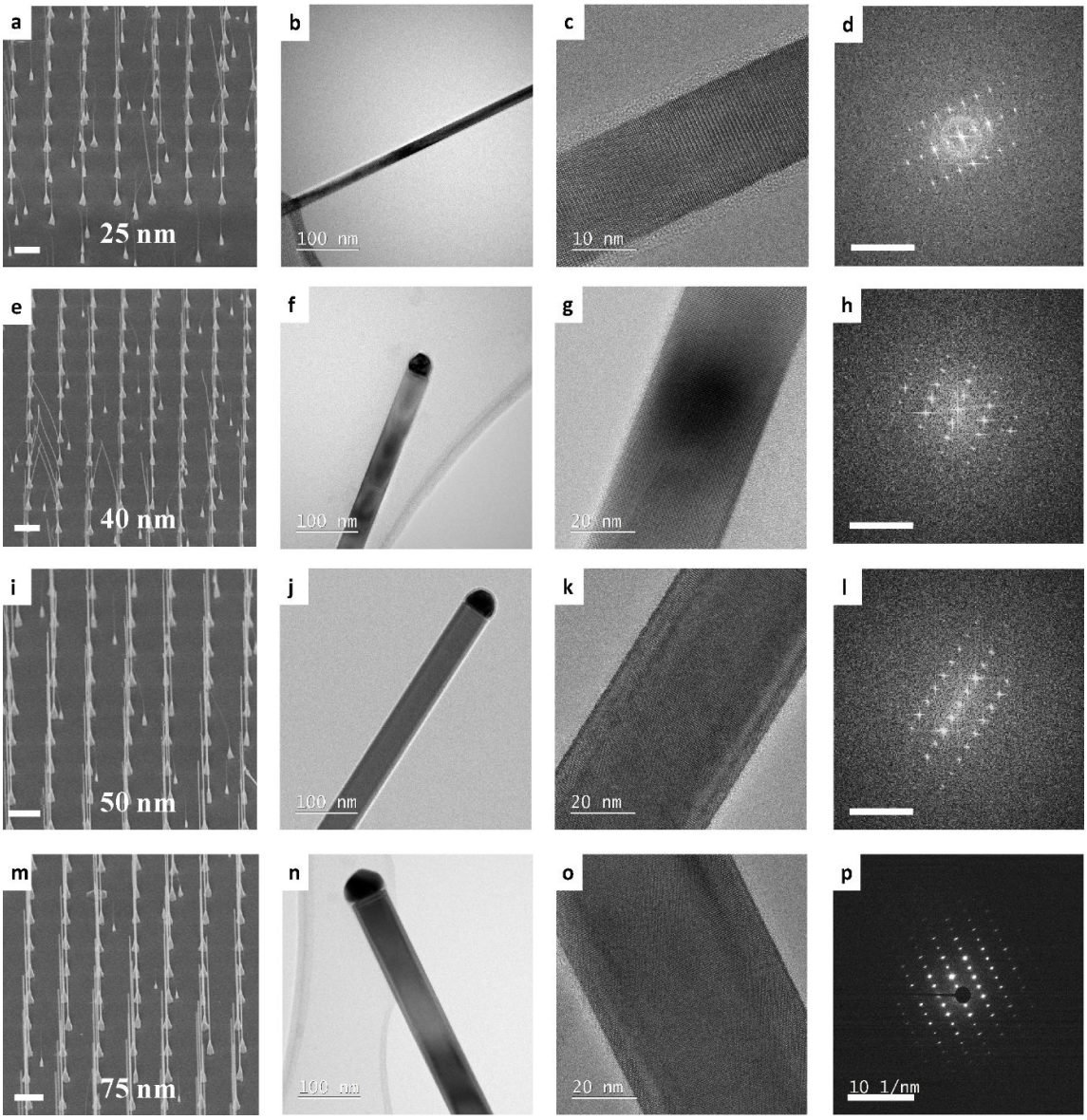

Figure A5.1. – **a, e, i, m,** SEM images of arrays of GaP NWs with increasing diameter. Scale bars: 2 μm. **b, f, j, n,** Representative TEM images of the NWs. Scale bars: 100 nm. **c, g, k, o,** Enlarged high-resolution TEM images of NWs with different diameters. **d, h, l, p,** Electron diffraction patterns of the NWs. Scale bars: 10 nm^{-1}.

Appendix A5.2. Elemental analysis.

Atom Probe Tomography (APT) is used to determine the elemental purity of the NWs. Samples are prepared in an FEI Nova Nanolab 600i based on the method described by S. Koelling *et al*[41]. The APT is performed in a LEAP 4000X HR using laser powers in the range 0.3-0.7 pJ and a base temperature of 20 K. The data are analyzed using IVAS 3.8.0.

We analyze five NWs with diameters ranging from 25 to 70 nm and check for contaminants that we expect to be present in the reactor. The results are shown in Table A5.1. An exemplary mass spectrum is shown in Figure A5.2c. For all elements heavier than Si, the concentrations estimated by APT coincide with the noise level[41], showing variations between measurements that are comparable to or larger than the average; see Table A5.1.

Signals above the noise level are only observed for H, C, O, and Si/N. Si has nearly exactly twice the mass of N, and hence the two elements cannot be distinguished from their mass-to-charge ratio. Apart from Si, all these species are known to be present in the vacuum chamber. It is, therefore, not possible to determine whether the signals result from contamination of the NWs or from the absorption of atoms from the vacuum on the NW surface during the analysis. Hence, the measured values are upper limits for potential contaminations. All potential contaminations are well below levels for which we expect any influence on the thermal properties.

In addition, the APT analyses can be used to check whether the two Ga isotopes ^{69}Ga and ^{71}Ga are distributed homogeneously throughout the NW. As shown in Figures A5.2a and b both isotopes are present at the expected natural abundance along both the radial and axial directions.

Table A5.1. Average concentration and standard deviation of elements that are potential contaminants in the GaP NW, based on APT measurements on 5 NWs. Only elements are known to be present in the vacuum chamber of the APT show a significant signal.

Element	**H**	**C**	**O**	**N/Si**	**Au**	**In**	**Al**	**Ge**	**As**	**Zn**	**Sn**
Conc. (%)	0.0286	0.0023	0.0210	0.0013	0.0002	0.0001	0.0001	0.0012	0.0002	0.0004	0.0003
SD (%)	0.0117	0.0003	0.0069	0.0006	0.0004	0.0001	0.0001	0.0017	0.0004	0.0034	0.0008

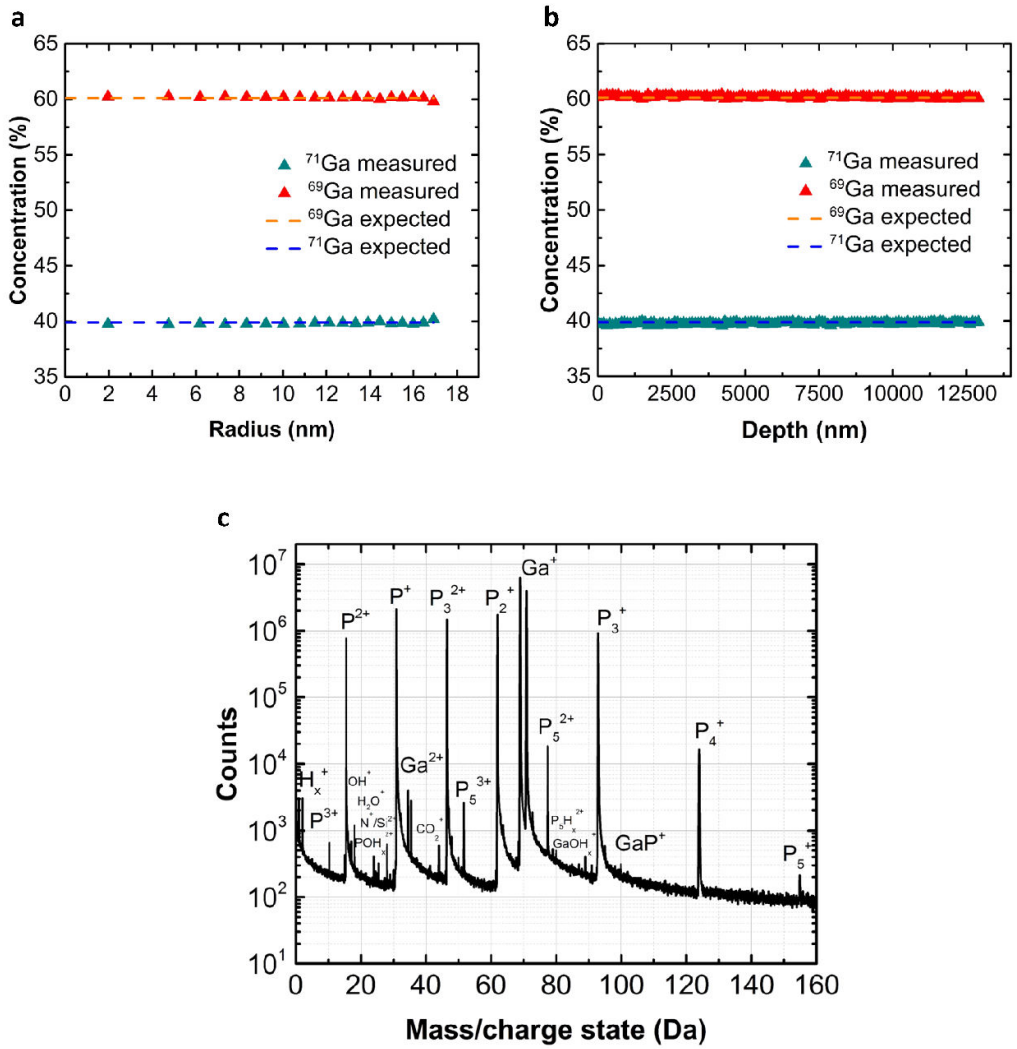

Figure A5.2. – **a**, Radial and **b**, axial distribution of ^{69}Ga and ^{71}Ga inside a GaP NW. The isotopes are present in the expected abundance and homogeneously distributed in the NW. **c**, Mass spectrum of an NW, showing only peaks resulting from Ga ions, P ions and elements known to be present in the vacuum chamber (H, C, O, N).

Appendix A5.3. Background conductance.

To obtain an estimate of the background conductance (caused, for example, by radiative heat transport) we show in Figure A5.3 results for ΔT_{H} and ΔT_{S} as a function of the applied power P, measured without an NW bridging the heater and sensor. This measurement has been done using a Wheatstone bridge technique, which has a high sensitivity. Using Eq. (4.15), the background conductance is estimated to be $G_{\mathrm{background}}$ = (1.4 ± 0.1) ×10^{-10} W/K, which is at least one order of magnitude lower than the conductances reported in the main text.

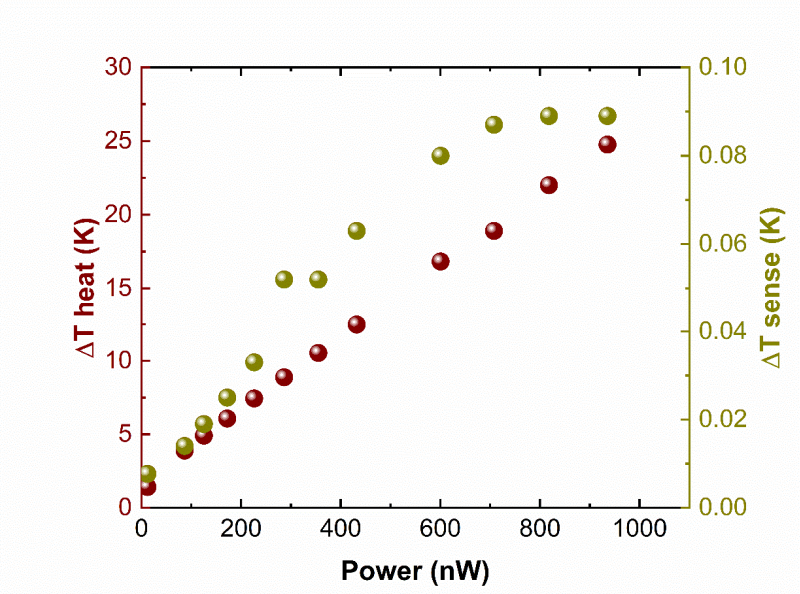

Figure A5.3. – Temperature difference ΔT_H of the heater (dark red, left axis) and ΔT_S of the sensor (dark yellow, right axis) as a function of applied power P, measured without an NW bridging heater and sensor.

Appendix A5.4. Diffusive heat flow in 75 nm diameter nanowires.

Figure A5.4 shows room-temperature values of κ for $d = 75$ nm as a function of NW length L. The results for $d = 50$ nm NWs are shown for comparison. Just like for $d = 50$ nm, the $d = 75$ nm results show diffusive heat flow. The sizes of κ for $d = 75$ nm are not very different from those for $d = 50$ nm because of the non-negligible contact resistance for $d = 75$ nm (see Figure 5.2a). The inset of Figure A5.4 compares the T-dependences of G of NWs of about equal length for $d = 75$ nm ($L = 12.5 \pm 0.2$ μm) and 50 nm ($L = 12.7 \pm 0.2$ μm), showing a weak T-dependence above 100 K for both diameters.

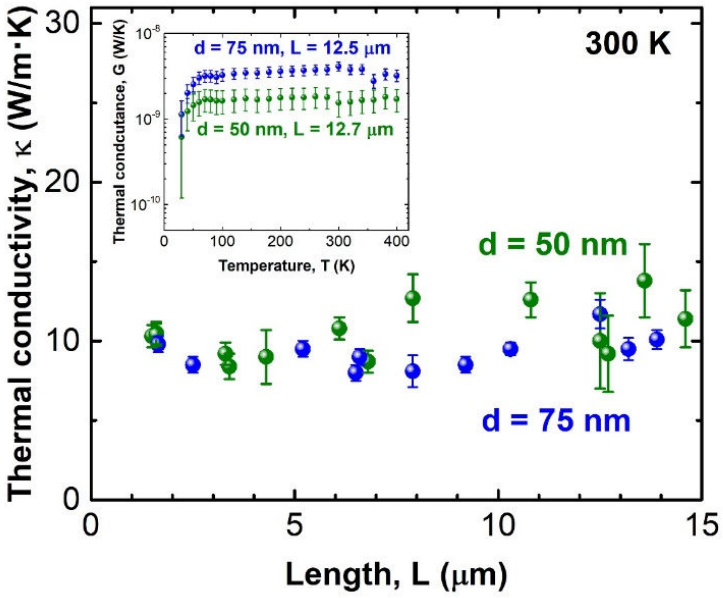

Figure A5.4. – Room-temperature thermal conductivity as a function of length L for $d = 50$ and 75 nm diameter NWs. Inset: temperature dependence of the thermal conductance of $d = 75$ nm ($L = 12.5 \pm 0.2$ μm) and $d = 50$ nm ($L = 12.7 \pm 0.2$ μm) diameter NWs.

Appendix A5.5. Raman thermometry.

The temperature profile along the NW length is probed using the Raman shift of the transverse optical (TO) phonon mode of the NW[43,44]. The excitation laser spot employed for the Raman spectroscopy is moved along the wire, while a temperature difference ΔT is applied between the ends of the wire using the resistive elements designed on the suspended Si_3N_4 membranes. A schematic of the method employed for our measurements is presented in Figure 5.3a in the main text. At each position along the nanowire, we collect a Raman spectrum without applying a temperature gradient and Raman spectra for both directions of the applied temperature difference to check for the symmetry of the response. Each spectrum is then fitted with Lorentzian functions. The frequency shift $\delta\omega$ of the TO mode (at about 363 cm^{-1} in GaP) with respect to the case without applying a temperature gradient provides an estimate of the local lattice temperature, since $\delta\omega \propto \delta T$. Local variations in the Raman shift due to other factors than the temperature gradient, such as small laser heating effects and locally varying strains, are canceled out by this technique. Figure A5.5 shows the results of the measurements for an NW with $d = 25$ nm and $L = 14.0 \pm 0.3$ μm.

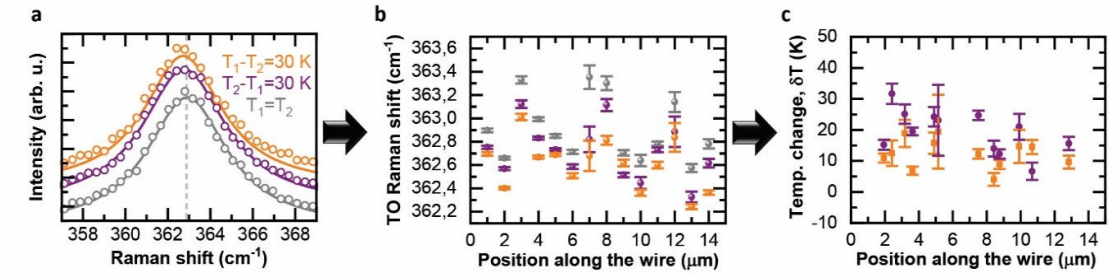

Figure A5.5. – **a,** Raman spectra for the case $T_1 = T_2 = 300$ K, the case $T_1 = 300$ K, $T_2 = 330$ K and the case $T_1 = 330$ K, $T_2 = 300$ K, acquired at about 9 μm from contact 1 along an NW with $d = 25$ nm and $L = 14.0 \pm 0.3$ μm. **b,** Extracted Raman shifts of the TO mode along the NW. **c,** Temperature profile determined from the Raman shifts in B for both directions of the applied temperature difference.

We have measured the temperature profiles along $d = 25$ and 50 nm NWs with $L = 14.0 \pm 0.3$ and 14.7 ± 0.3 μm, respectively, displayed in Figures 5.3c and e, for $\Delta T = 30$ K, which is also the temperature difference used in the thermal conductance measurements. In order to improve the signal-to-noise ratio, each Raman spectrum is integrated over 300 s and is the result of the average of 2 spectra in the case of the $d = 25$ nm NW and 3 spectra in the case of the $d = 50$ nm NW. In the Raman experiments, the samples are excited with the 488 nm line of a coherent Sapphire (SF) laser. The measurements are performed in a backscattering geometry using a 100× (NA = 0.5) objective, which allows a spatial resolution of about 700 nm. The polarization of the incident laser light and the outgoing scattered light can be controlled and selected by means of polarization optics. In these measurements, the polarization of the excitation light is set parallel to the NW axis in order to maximize the absorption and, thus, the Raman scattering intensity. The scattered light is collected by a 750 mm focal length monochromator equipped with an 1800 g/mm grating and a thermoelectrically cooled back-illuminated deep-depletion CCD detector, providing a spectral resolution better than 1 cm^{-1}.

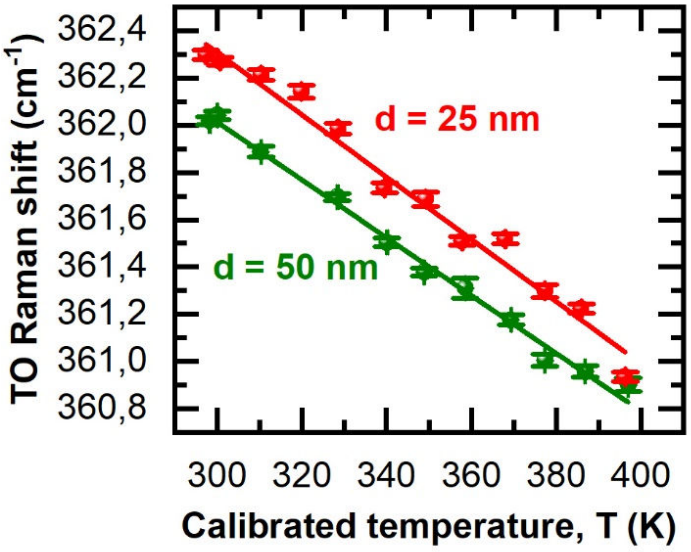

Figure A5.6. – Calibration of the shift of the TO mode for $d = 25$ and 50 nm NWs. The lines are linear fits to the data.

The spatial resolution of the Raman thermometry is determined by the size of the laser spot size, which is diffraction-limited. The temperature resolution is a few K and is limited by the spectral resolution of the system and the material-characteristic temperature-dependent Raman shift of the TO mode. In order to account for size effects in the dependence of the TO mode frequency on temperature, we have calibrated the frequency shift of this mode as a function of temperature for the $d = 25$ and 50 nm NWs before the measurement; see Figure A5.6. To this end, the nanowires were transferred onto a Si substrate, with a temperature defined by the temperature controller inside the sample holder of the probe station. The actual temperature was determined using the shift of the degenerate TO/LO mode of the Si substrate as a thermometer.

Finally, we checked the effect of the laser power on the measurements of the temperature profile. We want to avoid local heating by the excitation laser, which would alter the measured lattice temperature. To exclude this effect, we performed spatially resolved Raman measurements along the NWs without applying an external temperature gradient but using different laser powers (10 and 25 μW). The results for a $d = 25$ nm wire with $L = 14.0 \pm 0.3$ μm are shown in Figure A5.7. No significant dependence of the TO frequency on laser power is observed. We performed the measurements of the temperature profile along the NWs using a laser power below 25 μW for the $d = 25$ nm wire and below 50 μW for the $d = 50$ nm wire, avoiding heating effects.

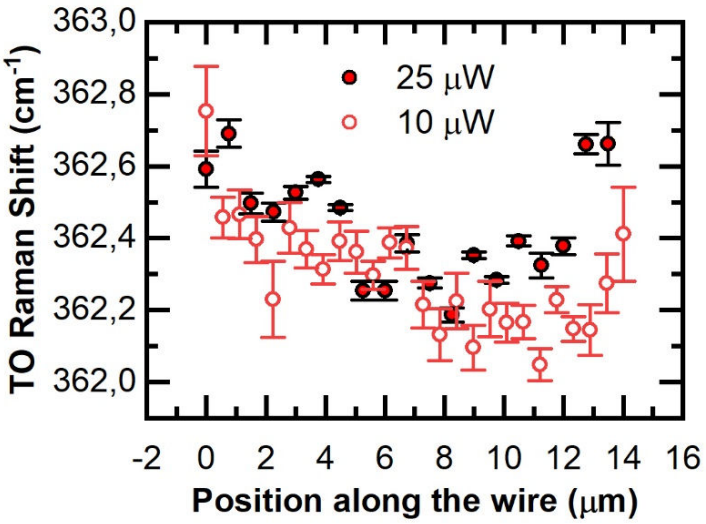

Figure A5.7. – Raman shift of the TO mode measured along a $d = 25$ nm diameter NW with length $L = 15$ μm for two different laser powers, 25 and 10 μW.

Appendix A5.6. Application of Landauer's formalism for heat flow.

We model the heat flow in the NWs with Landauer's formalism, as formulated by Murphy and Moore[20] and Chen *et al.*[30]. In this formulation, the thermal conductance G of an NW is given by

$$G = \frac{1}{2\pi\hbar}\int_0^\infty \left(\frac{N_s(\omega)}{1+L/l(\omega)} + \frac{N_d(\omega)}{1+L/d}\right)\frac{\hbar^3\omega^2}{k_B T^2}\frac{e^{\hbar\omega/k_B T}}{\left(e^{\hbar\omega/k_B T}-1\right)^2}d\omega \quad \text{(A5.1)}$$

where ħ is the reduced Planck constant and k_B Boltzmann's constant. The number of propagating phonon modes in the NW at the frequency ω, $N(\omega)$, is split into a 'specular' part $N_s(\omega)$ and a 'diffusive' part $N_d(\omega)$ ($N_1(\omega)$ and $N_2(\omega)$, respectively, in Ref. 30. 'Specular' phonons have a small wave vector $k_\perp$ (long-wavelength component) perpendicular to the NW surface, $k_\perp < 1/h$, where h should be comparable to the oxide layer thickness. 'Diffusive' phonons have a large perpendicular wave vector (small perpendicular wavelength component) $k_\perp > 1/h$. In the next section (Appendix 5.7), we explain how we obtain N_s and N_d for a given value of h. We perform the integration in Eq. (A5.1) up to the Debye frequency ω_D (58×10^{12} s^{-1}, corresponding to a Debye temperature of 445 K[45]). Phonons with higher frequency are hardly excited at the considered temperatures and have very short MFPs. Such phonons will, therefore, not contribute significantly to the heat flow.

Diffusive phonons reflect diffusely from the NW surface and therefore have an MFP $l = d$, leading to the transmission probability $1/(1+L/d)$ in the diffusive contribution in Eq. (A5.1). Chen *et al.* use an expression for the frequency-dependent MFP $l(\omega)$ of specular phonons that was originally derived by Santamore and Cross[46].

In this derivation, the disorder is treated as a perturbation, giving rise to a probability for incident phonons in forward propagating modes in the NW to be reflected in backward propagating modes. In the diffusive regime ($d \geq 50$ nm), all phonon modes, diffusive and specular, are propagating. Scattering of specular phonons into diffusive phonon modes is then an important process that limits their MFP. Because also $N_s << N_d$ (see Figure A5.10) we can assume that the specular contribution in Eq. (A5.1) is then small compared to the diffusive contribution. We obtain the L-dependent resistance R and conductivity κ, and the T-dependent conductance G for $d = 50$ nm (green curves in Figures 5.22b-d) by taking into account only the second, diffusive, contribution in Eq. (A5.1). Because $d << L$, R is proportional to L and the heat flow is diffusive. Since $N_d \propto d^2$ we have $G \propto d^3$ and, using Eq. (4.16), $\kappa \propto d$ (see the dashed line in Figure 5.2a). We note that since $N_s << N_d$ and $N_s + N_d$ does not depend on h, N_d is almost independent of h.

In our modeling, we assume that the situation is reversed for $d = 25$ nm: the diffusive contribution in Eq. (A5.1) is now negligible and the specular contribution is dominant because of a very long MFP of the specular phonons, which have become ballistic. Possible causes for this are discussed in the main text. We now assume that $l(\omega) >> L$ which leads to the observed ballistic heat flow. In Figure A5.8 we explore various values of h in evaluating the first, specular, contribution in Eq. (A5.1) for $d = 25$ nm at $T = 300$ K, putting $l(\omega) = \infty$. These results show that the calculated conductance (proportional to the slope of the lines) very sensitively depends on h. Taking $h = 2.45$ nm yields results in good agreement with the experiment. These results are reproduced in Figure 5.2c (solid red line). This value of h is close to the experimentally found oxide layer thickness of about 2 nm, which, considering the sensitive h-dependence in Figure 5.8, demonstrates the consistency of our approach. The corresponding T-dependence of G is shown in Figure 5.2d (red curve).

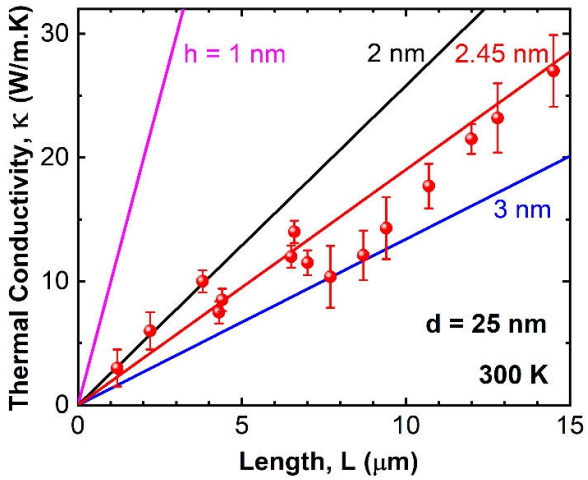

Figure A5.8. – Room-temperature thermal conductivities κ of $d = 25$ nm NWs calculated from the first, specular, term in the Landauer expression Eq. (S4) for $l(\omega) = \infty$ and various values of h, compared to the measurements displayed in Figure 5.2c. The value of h determines the number of specular phonon modes $N_s(\omega)$.

Appendix A5.7. Calculation of the numbers of specular and diffusive phonon modes.

For Si NWs Murphy and Moore[20] and Chen *et al.*[30] used the Debye approximation to calculate the number of modes N and the contributions N_s and N_d. We find, however, that the Debye approximation is too crude to be applied to GaP NWs. Instead, we use the full *ab-initio* calculated the phonon band structure of bulk WZ GaP and a similar method as introduced by Mingo[47] to obtain from the phonon band structure the numbers of modes in the NW.

Figure S11 shows the bulk phonon band structure calculated using the software package Phonopy[48] with force constants obtained from *ab-initio* density functional theory (DFT) calculations within the local density approximation (LDA) of the exchange-correlation potential, as implemented in the VASP package[49]. We use cut-off energy of 282 eV for the plane-wave basis set, a 4×4×4 k-point grid for sampling the hexagonal Brillouin zone, with Gaussian smearing of 0.1 eV width, and a 4×4×3 supercell (192 atoms) for the phonon calculations, using atomic displacements of 0.01 Å. The relaxed hexagonal lattice constants of our *ab-initio* calculations are a = 3.79 Å and c = 6.26 Å.

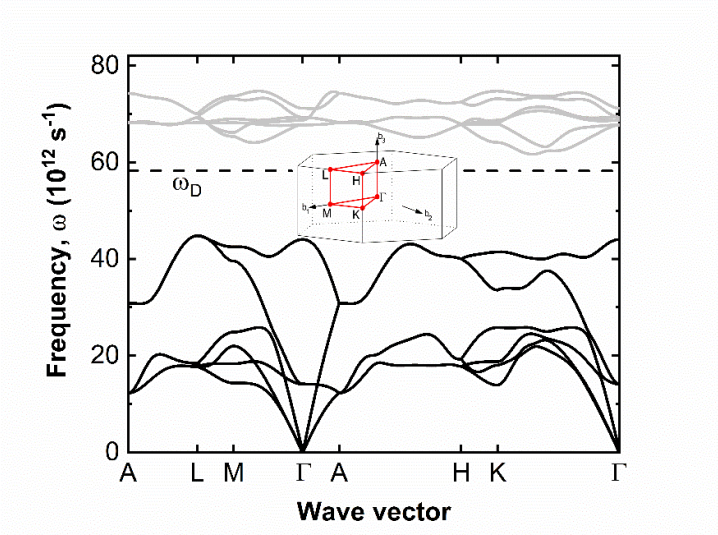

Figure A5.9. – Phonon band structure of bulk WZ GaP. The inset shows the hexagonal Brillouin zone. The dashed line indicates the Debye frequency ω_D. In all our calculations, we take into account only the bands below ω_D.

The boundary conditions at the NW surface lead to the discretization of the allowed wave vectors $\vec{k}_\perp$ perpendicular to the growth direction of the NWs (the c-axis) and to the formation of phonon subbands. The type of boundary conditions (free or frozen) and the shape of the NW cross-section become irrelevant when $d >> a$ [47], which is the case for our NWs. Following Ref. 47, we choose for convenience frozen boundary conditions and a rhomboidal cross-section with a surface area equal to the approximately circular cross-section of the NWs. We obtain the subband dispersion

along within the growth direction from the phonon band structure of Figure A5.9 for each discrete $\vec{k}_{\perp}$ and this the number of modes at each frequency. If $k_{\perp} < 1/h$, the subband contributes to N_s, otherwise to N_d. The results for N_s and N_d for the cases d = 25 and 50 nm are given in Figure A5.10. We note that N_s and N_d are proportional to d^2 when $d >> a$.

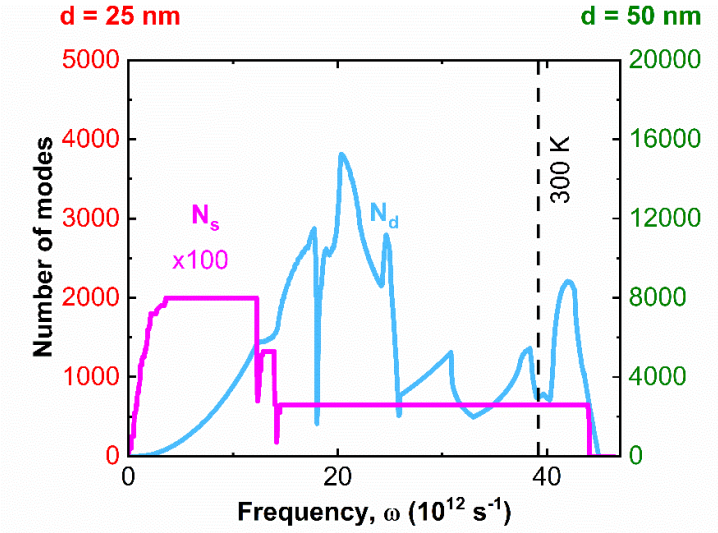

Figure A5.10. – Calculated numbers of specular (N_s, purple) and diffusive (N_d, blue) phonon modes as a function of frequency ω, for an oxide layer thickness h = 2.45 nm. Numbers along left (right) axis: results for d = 25 nm (50 nm). Notice the multiplication factor for N_s. Vertical dashed line: phonon energy equal to thermal energy at 300 K.

Appendix A5.8. Contributions of specular and diffusive phonons to the thermal conductivity.

In Figure A5.11, we show the results from the model considering the specular and diffusive contributions in Eq. (A5.1) for NWs with d = 25 and 50 nm. It is clear that adding a diffusive contribution to d = 25 nm NW would result in an offset in thermal conductivity κ, while adding a specular contribution (with $l = \infty$) to d = 50 nm NW would result in a κ that increases linearly with L (dashed lines). These results clearly do not match what is observed experimentally. We, therefore, assume that the contribution of specular phonons is negligible for d = 50 nm NWs, while the contribution of diffusive phonons is negligible for d = 25 nm NWs (solid lines, same as in Figure 5.2c).

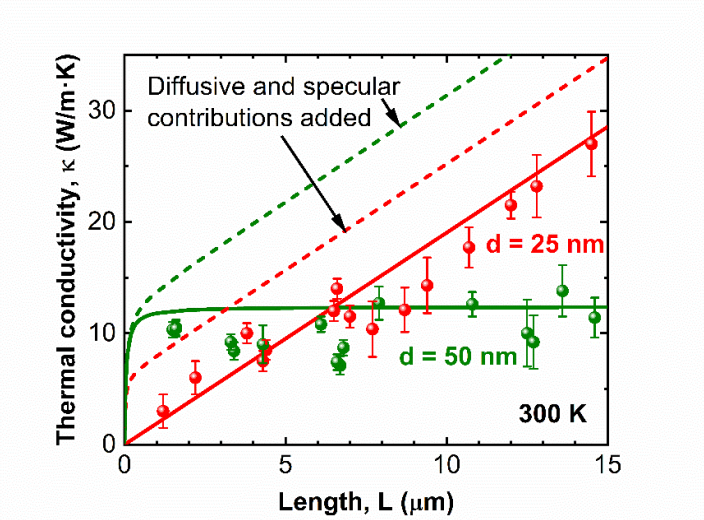

Figure A5.11. – Contributions of specular and diffusive phonons to thermal conductivity κ of $d = 25$ nm and $d = 50$ nm NWs. Symbols: same as in Figure 5.2c. Full lines: model results with the only contribution of specular phonons with MFP $l = \infty$ for $d = 25$ nm and only contribution of diffusive phonons with $l = d$ for $d = 50$ nm (same as in Figure 5.2c). Dashed lines: contributions of diffusive and specular phonons added for both cases $d = 25$ and 50 nm.

Appendix A5.9. Decoupling of specular and localized diffusive phonons.

In the Landauer formalism, the heat conductance is obtained by calculating in the harmonic approximation the transmission coefficients of phonons in all propagating modes impinging on the NW from the contacts. Figure A5.12 shows a specular phonon impinging on the NW from the left contact. Following the usual methodology in solving scattering problems, the phonon is described as a wave packet consisting of a linear combination of normal modes of the complete NW, including the amorphous oxide layer inducing the scattering. The normal frequencies in the wave packet are narrowly distributed around a central frequency. Each normal mode in the linear combination evolves periodically in time with its normal frequency, yielding the time evolution of the wave packet. When time proceeds, the wave packet moves into the NW and gets scattered by the amorphous oxide layer. After the scattering, the wave packet consists of a transmitted and a reflected part, the amplitudes of which determine the transmission and reflection coefficients.

We assume that in the diffusive regime ($d \geq 50$ nm), all normal modes are extended over the whole NW, *i.e.*, all normal modes are propagating. The normal modes are mixtures of specular and diffusive modes because of the coupling between these modes by the amorphous oxide layer. When an impinging specular phonon (built up from specular modes) is expanded as a linear combination of normal modes and propagated in time, it will become a linear combination of transmitted and reflected

specular and diffusive modes after the scattering. This leads to the scattering of specular phonons into diffusive modes, which limits the MFP of specular phonons.

In the localization scenario proposed to occur for $d = 25$ nm, the 'diffusive' normal modes (being composed of predominantly diffusive modes) become localized at specific locations in the NW, showing an exponential spatial decay; see Figure A5.12. Because the impinging phonon wave packet has no spatial overlap with the now localized diffusive normal modes, these modes do not occur in the linear combination constituting the wave packet. This holds for all times: before, during, and after the scattering. Impinging specular phonons can, therefore, no longer scatter into localized diffusive modes and are decoupled from the diffusive phonons. Because the diffusive modes constitute the great majority of modes, the scattering length of specular phonons would strongly increase.

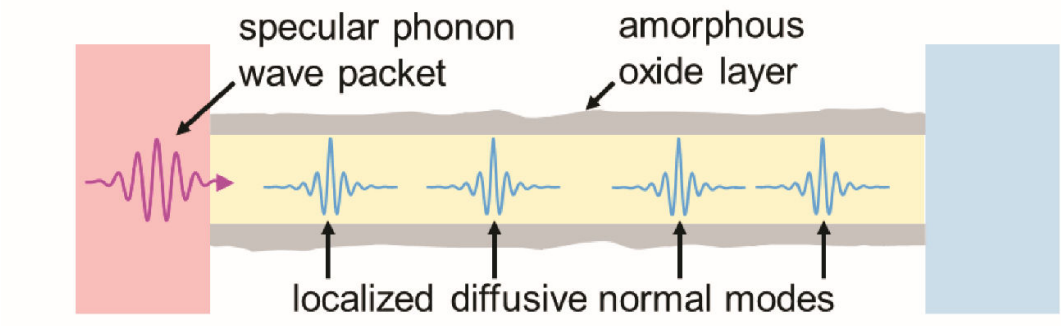

Figure A5.12. – Specular phonon wave packet impinging from the left contact onto a $d = 25$ nm diameter NW. The NW contains diffusive normal modes that are localized because of the disorder induced by the amorphous oxide layer. Since there is initially no spatial overlap, the wave packet will not contain these normal modes as components. The resulting decoupling of specular and localized diffusive phonons would lead to a greatly increased scattering length of specular phonons, making them ballistic.

5.7. References.

1. J. B. J. baron Fourier, *Théorie analytique de la chaleur* (F. Didot, 1822).
2. J. Maire, R. Anufriev, R. Yanagisawa, A. Ramiere, S. Volz, M. Nomura, Heat conduction tuning by wave nature of phonons. *Sci. Adv.* **3**, e1700027 (2017).
3. F. X. Alvarez, D. Jou, A. Sellitto, Phonon hydrodynamics and phonon-boundary scattering in nanosystems. *J. Appl. Phys.* **105**, 14317 (2009).
4. A. Cepellotti, G. Fugallo, L. Paulatto, M. Lazzeri, F. Mauri, N. Marzari, Phonon hydrodynamics in two-dimensional materials. *Nat. Commun.* **6**, 6400 (2015).
5. S. Lee, D. Broido, K. Esfarjani, G. Chen, Hydrodynamic phonon transport in suspended graphene. *Nat. Commun.* **6**, 6290 (2015).
6. Z. Ding, J. Zhou, B. Song, V. Chiloyan, M. Li, T.-H. Liu, G. Chen, Phonon hydrodynamic heat conduction and Knudsen minimum in graphite. *Nano Lett.* **18**, 638–649 (2017).

7. P. Torres, A. Torelló, J. Bafaluy, J. Camacho, X. Cartoixà, F. X. Alvarez, First principles kinetic-collective thermal conductivity of semiconductors. *Phys. Rev. B.* **95**, 165407 (2017).
8. A. Ziabari, P. Torres, B. Vermeersch, Y. Xuan, X. Cartoixà, A. Torelló, J.-H. Bahk, Y. R. Koh, M. Parsa, D. Y. Peide, others, Full-field thermal imaging of quasiballistic crosstalk reduction in nanoscale devices. *Nat. Commun.* **9**, 255 (2018).
9. V. Martelli, J. L. Jiménez, M. Continentino, E. Baggio-Saitovitch, K. Behnia, Thermal transport and phonon hydrodynamics in strontium titanate. *Phys. Rev. Lett.* **120**, 125901 (2018).
10. A. Beardo, M. Calvo-Schwarzwälder, J. Camacho, T. G. Myers, P. Torres, L. Sendra, F. X. Alvarez, J. Bafaluy, Hydrodynamic Heat Transport in Compact and Holey Silicon Thin Films. *Phys. Rev. Appl.* **11**, 34003 (2019).
11. M. E. Siemens, Q. Li, R. Yang, K. A. Nelson, E. H. Anderson, M. M. Murnane, H. C. Kapteyn, Quasi-ballistic thermal transport from nanoscale interfaces observed using ultrafast coherent soft X-ray beams. *Nat. Mater.* **9**, 26–30 (2010).
12. M.-H. Bae, Z. Li, Z. Aksamija, P. N. Martin, F. Xiong, Z.-Y. Ong, I. Knezevic, E. Pop, Ballistic to diffusive crossover of heat flow in graphene ribbons. *Nat. Commun.* **4**, 1734 (2013).
13. T.-K. Hsiao, H.-K. Chang, S.-C. Liou, M.-W. Chu, S.-C. Lee, C.-W. Chang, Observation of room-temperature ballistic thermal conduction persisting over 8.3 μm in SiGe nanowires. *Nat. Nanotechnol.* **8**, 534 (2013).
14. R. B. Wilson, D. G. Cahill, Anisotropic failure of Fourier theory in time-domain thermoreflectance experiments. *Nat. Commun.* **5**, 5075 (2014).
15. J. Lee, J. Lim, P. Yang, Ballistic phonon transport in holey silicon. *Nano Lett.* **15**, 3273–3279 (2015).
16. Y. Hu, L. Zeng, A. J. Minnich, M. S. Dresselhaus, G. Chen, Spectral mapping of thermal conductivity through nanoscale ballistic transport. *Nat. Nanotechnol.* **10**, 701 (2015).
17. R. Anufriev, A. Ramiere, J. Maire, M. Nomura, Heat guiding and focusing using ballistic phonon transport in phononic nanostructures. *Nat. Commun.* **8**, 15505 (2017).
18. R. Anufriev, S. Gluchko, S. Volz, M. Nomura, Quasi-ballistic heat conduction due to Lévy phonon flights in silicon nanowires. *ACS Nano.* **12**, 11928–11935 (2018).
19. L. D. Hicks, M. S. Dresselhaus, Thermoelectric figure of merit of a one-dimensional conductor. *Phys. Rev. B.* **47**, 16631 (1993).
20. P. G. Murphy, J. E. Moore, Coherent phonon scattering effects on thermal transport in thin semiconductor nanowires. *Phys. Rev. B.* **76**, 155313 (2007).
21. Y.-C. Wen, C.-L. Hsieh, K.-H. Lin, H.-P. Chen, S.-C. Chin, C.-L. Hsiao, Y.-T. Lin, C.-S. Chang, Y.-C. Chang, L.-W. Tu, others, Specular scattering probability of acoustic phonons in atomically flat interfaces. *Phys. Rev. Lett.* **103**, 264301 (2009).
22. P. Bas, A. Bostel, B. Deconihout, D. Blavette, A general protocol for the

reconstruction of 3D atom probe data. *Appl. Surf. Sci.* **87**, 298–304 (1995).

23. L. Shi, D. Li, C. Yu, W. Jang, D. Kim, Z. Yao, P. Kim, A. Majumdar, Measuring thermal and thermoelectric properties of one-dimensional nanostructures using a microfabricated device. *J. Heat Transfer.* **125**, 881–888 (2003).
24. M. Y. Swinkels, M. R. Van Delft, D. S. Oliveira, A. Cavalli, I. Zardo, R. W. der Heijden, E. Bakkers, Diameter dependence of the thermal conductivity of InAs nanowires. *Nanotechnology.* **26**, 385401 (2015).
25. M. Levinshtein, S. Rumyantsev, M. Shur, *Handbook Series on Semiconductor Parameters* (World Scientific, 1996; https://www.worldscientific.com/doi/abs/10.1142/2046-vol1).
26. J. Ordonez-Miranda, L. Tranchant, B. Kim, Y. Chalopin, T. Antoni, S. Volz, Quantized thermal conductance of nanowires at room temperature due to Zenneck surface-phonon polaritons. *Phys. Rev. Lett.* **112**, 55901 (2014).
27. K. S. Olsson, K. An, X. Li, Magnon and phonon thermometry with inelastic light scattering. *J. Phys. D. Appl. Phys.* **51**, 133001 (2018).
28. J. Maassen, M. Lundstrom, Steady-state heat transport: Ballistic-to-diffusive with Fourier's law. *J. Appl. Phys.* **117**, 35104 (2015).
29. R. de Picciotto, H. L. Stormer, L. N. Pfeiffer, K. W. Baldwin, K. W. West, Four-terminal resistance of a ballistic quantum wire. *Nature.* **411**, 51 (2001).
30. R. Chen, A. I. Hochbaum, P. Murphy, J. Moore, P. Yang, A. Majumdar, Thermal conductance of thin silicon nanowires. *Phys. Rev. Lett.* **101**, 105501 (2008).
31. P. W. Anderson, Absence of diffusion in certain random lattices. *Phys. Rev.* **109**, 1492 (1958).
32. S. Xiong, K. Sääskilahti, Y. A. Kosevich, H. Han, D. Donadio, S. Volz, Blocking phonon transport by structural resonances in alloy-based nanophononic metamaterials leads to ultralow thermal conductivity. *Phys. Rev. Lett.* **117**, 25503 (2016).
33. P. Markoš, K. A. Muttalib, Phonon localization in nanowires dominated by surface roughness. *Phys. Rev. B.* **99**, 134208 (2019).
34. S. Xiong, D. Selli, S. Neogi, D. Donadio, Native surface oxide turns alloyed silicon membranes into nanophononic metamaterials with ultralow thermal conductivity. *Phys. Rev. B.* **95**, 180301 (2017).
35. M. Verdier, Y. Han, D. Lacroix, P.-O. Chapuis, K. Termentzidis, Radial dependence of thermal transport in silicon nanowires. *J. Phys. Mater.* **2**, 15002 (2018).
36. L. Wang, B. Li, Thermal logic gates: computation with phonons. *Phys. Rev. Lett.* **99**, 177208 (2007).
37. S. R. Sklan, Splash, pop, sizzle: Information processing with phononic computing. *AIP Adv.* **5**, 53302 (2015).
38. D. Hatanaka, I. Mahboob, K. Onomitsu, H. Yamaguchi, Phonon waveguides for electromechanical circuits. *Nat. Nanotechnol.* **9**, 520 (2014).
39. D. R. Ely, R. E. García, M. Thommes, Ostwald--Freundlich diffusion-limited dissolution kinetics of nanoparticles. *Powder Technol.* **257**, 120–123 (2014).
40. M. Perez, Gibbs--Thomson effects in phase transformations. *Scr. Mater.* **52**, 709–

712 (2005).

41. S. Koelling, A. Li, A. Cavalli, S. Assali, D. Car, S. Gazibegovic, E. Bakkers, P. M. Koenraad, Atom-by-atom analysis of semiconductor nanowires with parts per million sensitivity. *Nano Lett.* **17**, 599–605 (2017).
42. M. C. Wingert, Z. C. Y. Chen, S. Kwon, J. Xiang, R. Chen, Ultra-sensitive thermal conductance measurement of one-dimensional nanostructures enhanced by differential bridge. *Rev. Sci. Instrum.* **83**, 24901 (2012).
43. M. Soini, I. Zardo, E. Uccelli, S. Funk, G. Koblmüller, A. i Morral, G. Abstreiter, Thermal conductivity of GaAs nanowires studied by micro-Raman spectroscopy combined with laser heating. *Appl. Phys. Lett.* **97**, 263107 (2010).
44. S. Yazji, E. A. Hoffman, D. Ercolani, F. Rossella, A. Pitanti, A. Cavalli, S. Roddaro, G. Abstreiter, L. Sorba, I. Zardo, Complete thermoelectric benchmarking of individual InSb nanowires using combined micro-Raman and electric transport analysis. *Nano Res.* **8**, 4048–4060 (2015).
45. http://www.ioffe.ru/SVA/NSM/Semicond/GaP/basic.html. This is the value for zincblende GaP, but the difference with the wurtzite GaP of the nanowires should be insignificant.
46. D. H. Santamore, M. C. Cross, Effect of surface roughness on the universal thermal conductance. *Phys. Rev. B.* **63**, 184306 (2001).
47. N. Mingo, Calculation of Si nanowire thermal conductivity using complete phonon dispersion relations. *Phys. Rev. B.* **68**, 113308 (2003).
48. A. Togo, I. Tanaka, First principles phonon calculations in materials science. *Scr. Mater.* **108**, 1–5 (2015).
49. G. Kresse, J. Furthmüller, Efficient iterative schemes for ab initio total-energy calculations using a plane-wave basis set. *Phys. Rev. B.* **54**, 11169 (1996).

Chapter 6. Thermoelectric properties of InSb nanowires.

Introduction.

As has been indicated in Chapter 1, among the group III–V materials InSb is the most promising semiconductor for thermoelectrics[1]. It has been predicted that the thermoelectric efficiency can be enhanced by going towards low-dimensional structures. For instance, the magnitude of the density of states increases as the inverse of the squared diameter of the nanowire ($1/d^2$), leading to enhanced efficiency. Therefore, it is interesting to study the thermoelectric properties of InSb nanowires and estimate their thermoelectric efficiency (ZT). Recent papers have studied the influence of doping on the thermoelectric efficiency and reported ZT values of 0.015 – 0.025 [2] and 0.002 – 0.005 [3] for Se-doped InSb nanowires with diameters 145-195 nm, and 133-171 nm, respectively. Here we focus on enhancing the thermoelectric efficiency by reducing nanowire diameters down to 50 nm[4–6].

In this chapter, an analysis of the thermoelectric properties of relatively thin InSb nanowires is presented. The thermal conductivity of single InSb nanowires has been measured using the suspended membranes technique[7]. The Seebeck coefficient and electrical conductivity, which together determine the power factor, have been studied based on the field-effect nanowire transistor measurements technique[8]. The thermoelectric properties of undoped InSb nanowires have been examined for the first time. We obtain ZT values of around 0.04 for undoped InSb nanowires with a diameter of about 50 nm. We expect that the thermoelectric efficiency can be further increased by impurity doping of InSb nanowires or by a reduction in the nanowire diameter down to 10 nm[1].

6.1. Structural properties of InSb nanowires.

InSb NWs with diameters from 50 to 180 nm are grown by metal-organic vapor phase epitaxy (MOVPE) using the SAE VLS growth technique[9]. Detailed information about NW growth is given in Chapter 4. The structural properties of the NWs have been analyzed by transmission electron microscopy (TEM), as presented in Figure 6.1a. TEM and high angle annular dark-field (HAADF) images (Figure 6.2b) show defect-free NWs with the zinc blende crystal structure and uniform diameter, grown along the <111>B direction. The TEM images show that the NWs have atomically flat {110} side facets covered by a few nanometer-thick amorphous native oxide layer. The electron diffraction pattern of the InSb NW confirms the zinc-blende (ZB) crystal structure (Figure 6.1c).

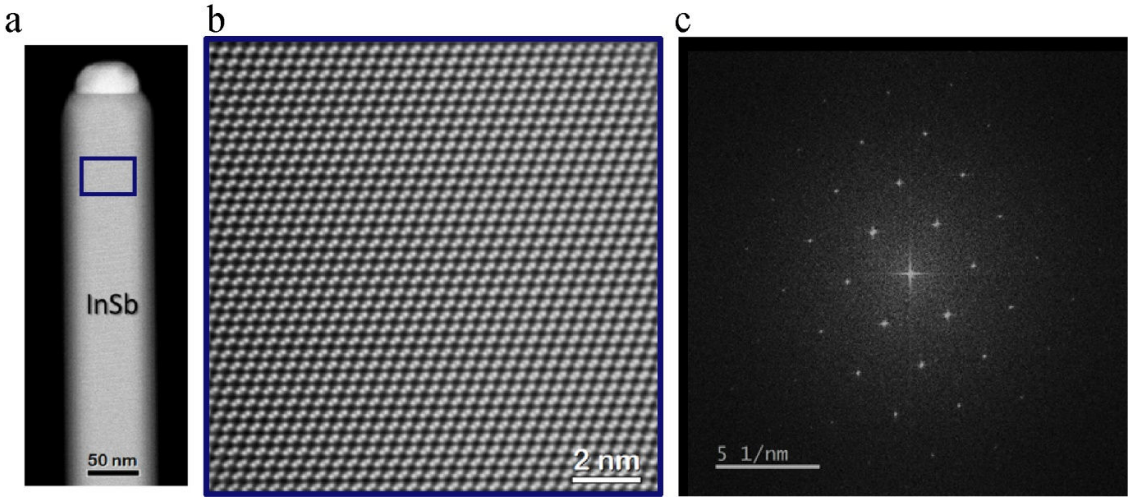

Figure 6.1. – **a,** Overview dark-field TEM image is showing the Au-catalyst particle on the top, and **b,** high-resolution TEM image showing the zincblende (ZB) crystal structure of the InSb nanowire. The wires are defect-free and grow along a <111>B direction. **c,** Fourier Transform pattern of the InSb nanowire showing defect-free ZB crystal structure[9]. These images are taken along the [110] zone axis.

Atom Probe Tomography (APT) has been used to determine the elemental purity of the NWs[10]. The characterization process is similar to the one described in Chapter 5. NWs are analyzed with a particular focus on contaminants that are expected to be present in the growth chamber. The atomic concentration along an InSb NW is shown in Figure 6.2a. Arsenic (As) is incorporated at a level of 0.0006 ± 0.0002%, and phosphorus (P) at 0.0010 ± 0.0005%, which is about an order of magnitude lower than the InSb NWs grown with InP stems[9]. The low concentrations of P and As elements presented in the NWs are likely attributed to the background levels in the growth chamber. All potential contaminations are well below levels for which any influence on the transport properties is expected[11,12]. The atom probe tomography (APT) reconstruction image of an InSb nanowire is shown in Figure 6.2b. The APT analysis demonstrates the chemical purity of the NWs and the absence of heavy element impurities.

a)

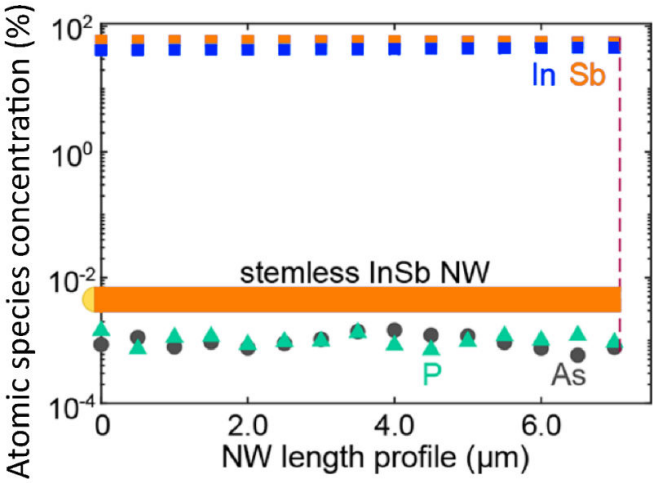

b)

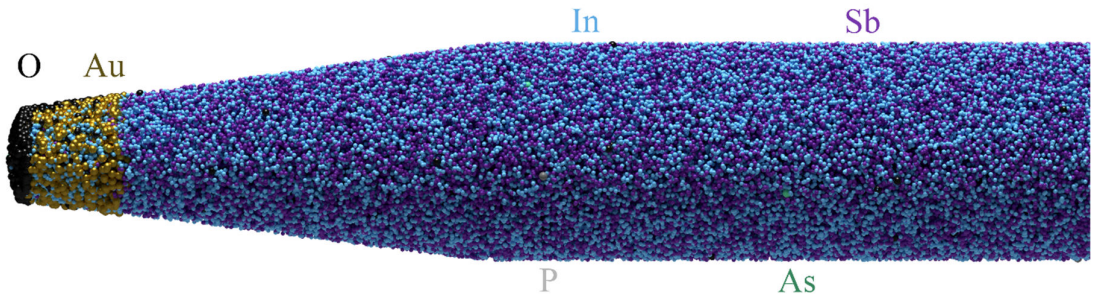

Figure 6.2. – **a,** Concentrations of atomic species along an InSb NW. A 50/50 ratio of In/Sb is found as expected for a III–V compound. **b,** Atom probe tomography reconstruction image of an InSb nanowire. Adapted from reference 9.

6.2. Thermal conductivity of InSb nanowires.

We now continue studying the thermoelectric efficiency. We start by measuring the thermal conductivity using suspended membranes. As explained previously (Chapter 5), it is essential to verify that the thermal contact resistance does not dominate the overall device thermal resistance. The extracted thermal conductivity κ at room temperature ($T = 300$ K) is plotted in Figure 6.3 as a function of diameter d for NWs with approximately the same length $L = 5.5$ μm, with d ranging from 50 to 175 nm. These results were fitted to expose the influence of the thermal contact resistance, R_c [7]. In an NW with heat flow dominated by diffuse scattering at the NW surface, κ increases with d according to Mathiessen's rule $\kappa \propto \left(1 + l_{\text{bulk}} / d\right)^{-1}$, where l_{bulk} is the bulk MFP, as indicated by the dashed line. A reduced κ with respect to this line, which is observed for $d \geq 80$ nm, means that R_c is no longer negligible compared to the NW resistance, R_{NW} [7]. For thin wires ($d < 75$ nm), on the contrary, the data points are following the expected behavior for a diffusive transport mechanism, indicating that the contact resistance is not significant. Therefore, we can measure the thermal

conductivity of InSb nanowires with a diameter ≤ 70 nm using the suspended membranes technique.

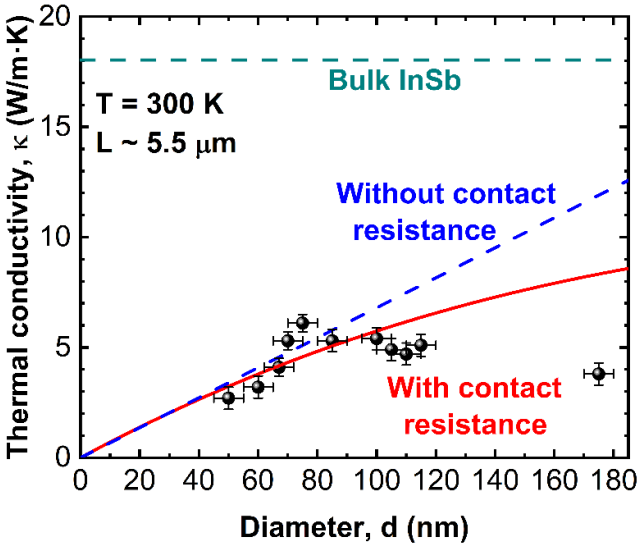

Figure 6.3. – Room-temperature (300 K) thermal conductivity κ of InSb NWs of length $L = 5.5$ μm as function of diameter d. All the nanowires measured have Pt/C top contacts. Full curve: fit of results for $d \geq 50$ nm to $\kappa = (1/c_1 d + c_2 \pi d/4L)^{-1}$ (diffusive heat flow with MFP $l = d << l_{bulk}$ and contact resistance $R_c = c_2/d$, with $c_1 = 1.4\times10^6$ W/m²·K and $c_2 = 2.5$ m·K/W). Dashed line: $\kappa = c_1 d$ (diffusive heat flow without contact resistance and $d << l_{bulk}$).

In Figure 6.4, the thermal conductivity is plotted as a function of the length of NWs with diameters of 50 and 60 nm at 300 K. It can be seen that for NWs with $d =$ 50 nm and 60 nm, κ is independent of L (thermal conductance, G, is inversely proportional to L), following diffusive heat flow, which is expected for these nanowires due to their relatively short phonon mean free path[2] (see Figure 2.1).

Thermal conductivities of (2.75±0.73) W/m·K and (3.62±0.61) W/m·K are found for the 50 nm and 60 nm NWs, respectively. These values are used in the calculation of the ZT of InSb nanowires.

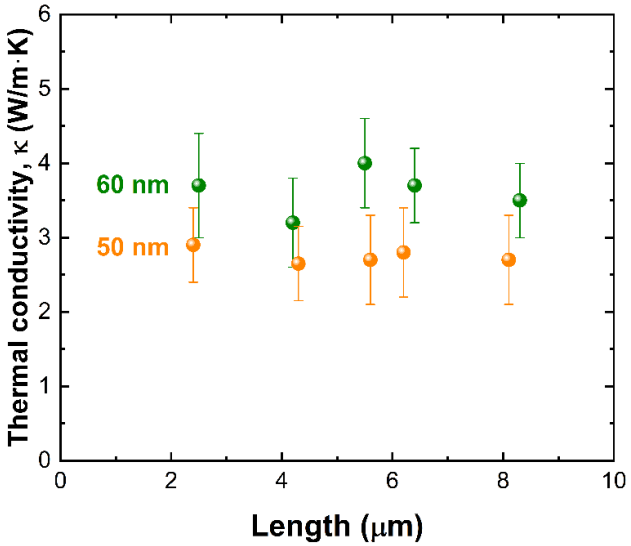

Figure 6.4. – Length-dependence of the thermal conductivity, κ of InSb NWs with diameters $d = 50$ and 60 nm, measured using Pt/C contacts at $T = 300$ K.

6.3. Temperature-dependent thermal conductivity.

Figure 6.5 shows the thermal conductivity of NWs with a diameter of 50, 60, and 70 nm as a function of temperature in the range 50 – 400 K. The temperature dependence of the thermal conductivity is weak in the range of 100 – 400 K. At low temperatures (50 – 100 K), κ sharply decreases due to phonon freeze-out. At relatively high temperatures (100 – 400 K), κ is almost temperature independent due to the diffusive nature of the majority of the phonon spectrum[13]. Umklapp scattering, which leads to a substantial decrease in the thermal conductivity in bulk InSb above 10 K[14], appears to play no significant role in these nanowires.

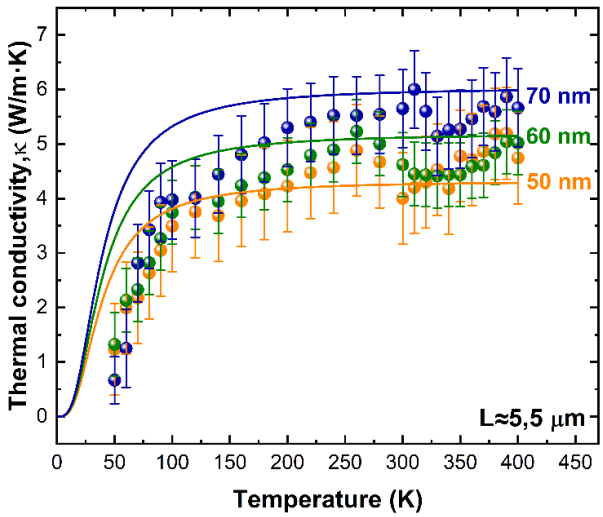

Figure 6.5. – Measured (symbols) and modeled (curves) T-dependent thermal conductivity κ of $d = 50$, 60, and 70 nm NWs with length $L \approx 5.5$ μm.

In order to quantify the obtained experimental results, the Landauer formalism has been used to model the thermal conductivity temperature dependence[15]. This model has previously been applied to explain the results of GaP nanowires in Chapter 5. We model the thermal conductivity of InSb nanowires using the Landauer formalism with the Debye linear dispersion approximation for the number of phonon modes[16]. The Debye approximation is chosen here for simplicity. The total number of phonon modes has been estimated using the following equation[17]:

$$N(\omega) = 4 + A \cdot \left(\frac{d}{a}\right)^2 \cdot \left(\frac{\omega}{\omega_D}\right)^2, \tag{6.1}$$

where a is the lattice constant, and the 4 indicates the four modes (one longitudinal, one torsional, and two flexural) that propagate as $\omega \rightarrow 0$; A is a dimensionless fitting parameter. The total number of modes ($N(\omega)$) can be separated into the number of modes with mean free path l (ballistic), $N_1(\omega)$, and the number with a mean free path of d (diffusive), $N_2(\omega)$. At low frequencies, all modes have $hk_\perp \leq 1$, whereas any modes that begin to propagate at $\omega > c/h$ are assumed to have $hk_\perp > 1$. $N_2(\omega)$ is defined by $N_2(\omega) = N(\omega) - N_1(\omega)$. The thermal conductance is then given by the Landauer formalism as:

$$G = \frac{1}{2\pi\hbar}\int_0^\infty \left(\frac{N_1(\omega)}{1+L/l(\omega)} + \frac{N_2(\omega)}{1+L/d}\right) \cdot \frac{\hbar^3\omega^2}{k_B T^2} \cdot \frac{e^{\frac{\hbar\omega}{\hbar\omega T}}}{\left(e^{\frac{\hbar\omega}{k_B T}} - 1\right)^2} d\omega. \tag{6.2}$$

Here only the diffusive phonon contribution has been estimated since no sign of ballistic behavior has been found in InSb nanowires (see Figure 6.5.). Therefore, Eq. (6.2) can be rewritten as:

$$G = \frac{1}{2\pi\hbar}\int_0^\infty \left(\frac{N_2(\omega)}{1+L/d}\right) \cdot \frac{\hbar^3\omega^2}{k_B T^2} \cdot \frac{e^{\frac{\hbar\omega}{k_B T}}}{\left(e^{\frac{\hbar\omega}{k_B T}} - 1\right)^2} d\omega, \tag{6.3}$$

where L is the nanowire length. It assumed that in the case of diffusive phonon modes, the phonon mean free path ($l(\omega)$) is equal to the nanowire diameter (d). The thermal conductivity κ is calculated considering dimensions of nanowires as following:

$$\kappa = \frac{4 \cdot L}{2(\pi)^2 (D)^2 \hbar}\int_0^\infty \left(\frac{N_{\mathrm{s}}(\omega)}{1+L/l(\omega)} + \frac{N_{\mathrm{d}}(\omega)}{1+L/d}\right) \frac{\hbar^3\omega^2}{k_{\mathrm{B}} T^2} \frac{e^{\hbar\omega/k_B T}}{\left(e^{\hbar\omega/k_B T} - 1\right)^2} d\omega. \tag{6.4}$$

The phonon density of states approximated by the Debye approach is shown in Figure A6.1. A detailed description of the Landauer formalism is presented in Appendix A6.1. The calculated thermal conductivity using the Landauer formalism, as shown in Figure 6.5, is in reasonable agreement with the experimental results, especially at T>100 K. Below 100 K there is quite a discrepancy between the model and the data,

which is ascribed to the approximated PDOS by the Debye model. The Landauer formalism can thus qualitatively reproduce the experimentally observed behavior, and it confirms the diffusive behavior of phonons in this system. For a complete understanding of the system, more in-depth simulations such as molecular dynamics and non-equilibrium Boltzmann equation can be applied[13,18,19].

6.4. The electrical conductivity of InSb nanowires.

In order to estimate the electrical conductivity of InSb nanowires, the resistance of the nanowires has been measured using the four-probe technique at different temperatures (see Figure 6.6a). Based on the obtained results, it can be concluded that the contact resistance is much smaller than the wire resistance and therefore plays an insignificant role (see Appendix A6.2.). In addition, from the temperature-dependent resistance the bandgap energy of the semiconductor can be extracted if the resistance is indeed determined by the nanowire channel. In Figure 6.6b, the natural logarithm of the measured resistance is plotted against $1/T$ for a typical device. Based on Boltzmann relation[20], the slope $dln(R)/d(1/T)$ corresponds to E_g/K_B (where K_B is the Boltzmann constant).

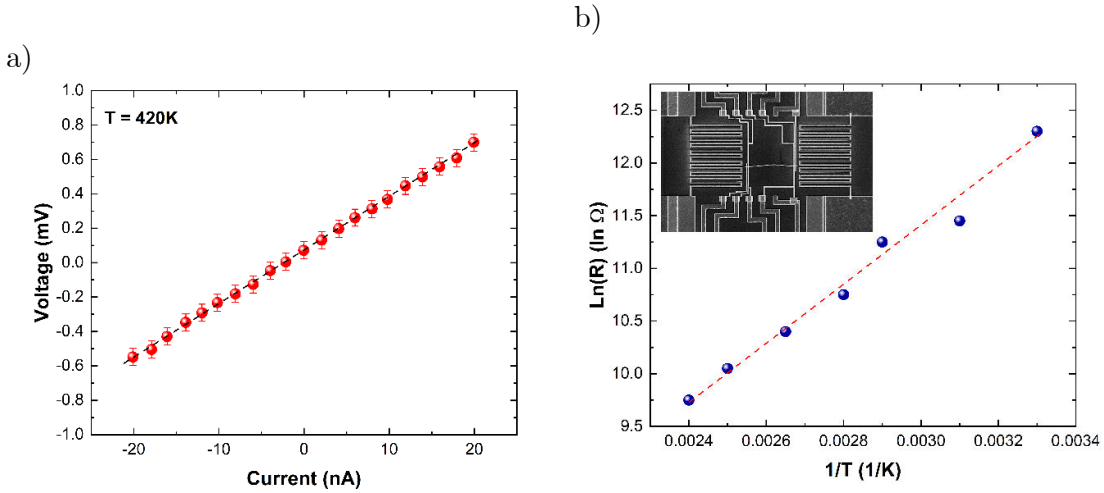

Figure 6.6. – **a,** The natural logarithm of the 85 nm InSb nanowire resistance plotted versus $1/T$. A linear fit (dashed line) is made through the data points. Inset: SEM image of the device. **b,** V-I characteristics of 85 nm InSb nanowire measured using the four-probe technique.

The extracted value of the bandgap energy is (0.22 ± 0.02) eV, which is close to to the values of (0.17 – 0.18) eV reported for bulk InSb at 300 K[21]. The slightly higher observed bandgap energy may be due to confinement effects in these 50-60 nm diameter nanowires since the electron effective mass in InSb is very small, and the Bohr radius of InSb is around 65 nm[22].

The influence of the back-gate voltage on the electrical conductivity has been measured in the temperature range 6 – 420 K. In Figure 6.7a, gate sweeps for 50, 60, 80 nm diameter InSb nanowires are shown at 6 K and 420 K.

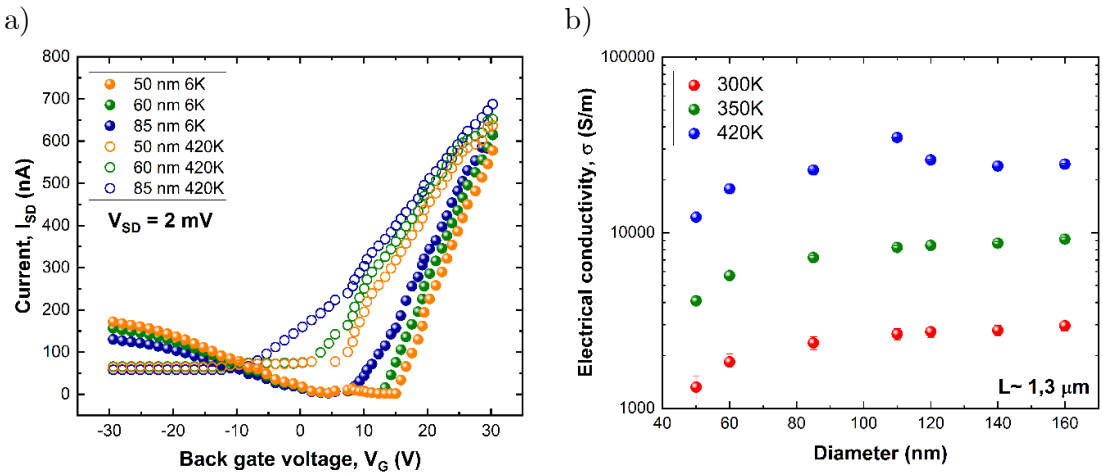

Figure 6.7. – **a,** The electrical conductance plotted as a function of the back-gate voltage for InSb nanowires with 50, 60, and 85 nm diameters at 6 K (closed symbols) and 420 K (open symbols). Source-drain bias (V_{SD}) is equal to 2 mV. **b,** The electrical conductivity of InSb NWs as a function of nanowire diameter at different temperatures. V_G=*0 V*. NWs have the length $L \approx 1.3$ μm.

Typical pinch-off curves are observed at 420 K. The charge carriers get thermally excited over the bandgap *Eg*, (*Eg* (InSb) = 0.17 *eV* at 300 K), resulting in non-zero current (I_{SD}). The threshold voltage (V_{th}) tends to become more positive for decreasing diameter at 6 K and 420 K. The slope (dI_{SD}/dV_G) is steeper with decreasing diameter and temperature due to the decreased number of scattering between charge carriers. From the data shown in Figure 6.7a, it can be concluded that the wires can facilitate ambipolar transport. This effect is observed for a temperature of 6 K, and it is possible to extract the charge carrier concentration and mobility of both holes and electrons from the slope in the linear region of these curves[25,26]. These data are given in Appendix A6.3.

The electrical conductivity of the InSb nanowires is found from V-I measurements. An exemplary V-I curve of InSb NW is shown in Figure 6.6b. The conductivity is calculated using Eq. (2.19). The dimensions of the nanowires are measured using ImageJ software based on the SEM images of the devices (see inset of Figure 6.6b)[23]. We find that the electrical conductivity is constant for wires with d>100 nm but decreases (by a factor of 2) for wires with a diameter of 50 nm, as shown in Figure 6.7b. Recent studies on the conductivity of InSb nanowires show a similar trend, which was explained by electron scattering at the nanowire surface[24]. The obtained values, for the large diameter wires, agree with previously published results on InSb at 300 K[2,3,24].

6.5. Seebeck coefficient of InSb nanowires.

6.5.1. Establishing a thermal gradient.

In order to experimentally determine the Seebeck coefficient, a thermal gradient has to be induced along the InSb nanowire. For this, the devices discussed in Chapter 4 have been used. One side of the devices is heated by applying a heating current of 12 mA to the meandering element, and the temperature difference along the nanowire is measured with calibrated resistive thermometers. Based on the results obtained from these measurements, it can be concluded that the typical ΔT used in our experiments is about 2 – 6 K depending on the position of the nanowire.

In order to verify the obtained results, the temperature profile of the device has been measured by thermoreflectance imaging. Due to the limitations of the thermal imaging, the temperature distribution along the SiO_2 layer cannot be captured[27]. Therefore, a calibration sample has been made, as shown in Figure 6.8.

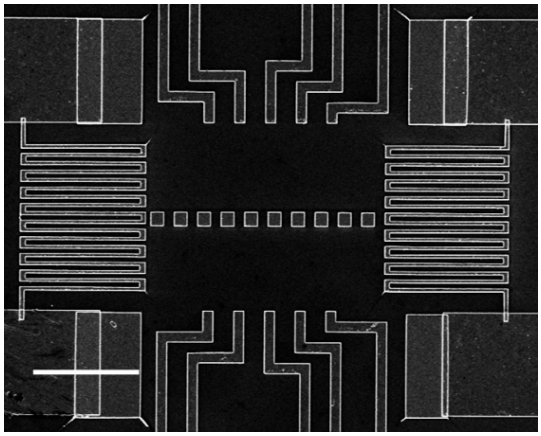

Figure 6.8. – SEM-image of the calibration sample. The scale bar is 10 μm.

The calibration sample consists of two heating elements and small squares placed at the specific positions away from the heaters. The squares are made of Au and provide enough reflectance allowing to measure the temperature profile. The obtained temperature profile and the thermal image are shown in Figure 6.9a. The difference in the reflectance between high reflective and non-reflective surfaces causes the fluctuation of the experimental data.

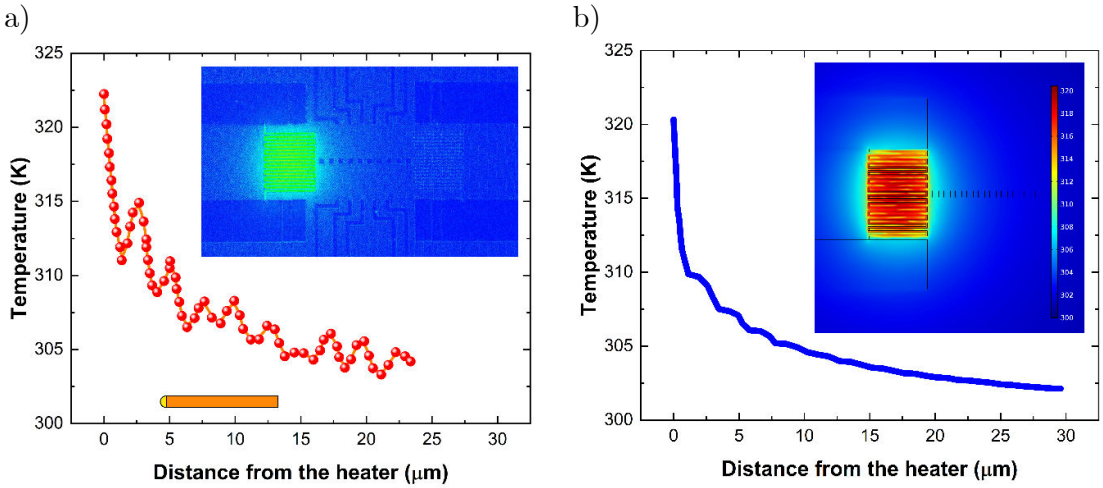

Figure 6.9. – **a,** Temperature profile obtained by thermal imaging of the calibration device. *Inset*: the thermal image of the heat distribution on the calibration device. **b,** Simulated temperature profile acquired by COMSOL Multiphysics simulations. *Inset:* Simulated temperature distribution map. Both profiles are obtained at $T_{ambient} = 300$ K.

The data obtained by thermal imaging contain noise, which is filtered out to make the shape of the profile more visible. The temperature distribution along the calibration sample has been simulated using finite-difference time-domain COMSOL Multiphysics. The results of the modeling are shown in Figure 6.9b. It can be concluded that experimental and modeled data are in quantitative agreement. For the Seebeck coefficient experiments, the same settings have been used.

6.5.2. Seebeck coefficient.

The Seebeck voltage is determined from the voltage shift of the V-I characteristics measured with and without a temperature gradient. The V-I curves, as shown in Figure 6.10, are measured using the four-probe technique, which eliminates the influence of the contact resistance[20].

From the linear fit, the offset ΔV is determined by subtracting the intersect values at zero current. The ΔV values are used to determine the Seebeck coefficient of the nanowires, as defined in Eq. (2.18). The Seebeck voltage as a function of temperature for InSb nanowires is shown in Figure 6.11a. The Seebeck voltage is negative, which is expected since electrons are the majority carriers in the InSb wires. The absolute Seebeck voltage increases significantly (by a factor 4-5) with decreasing nanowire diameter.

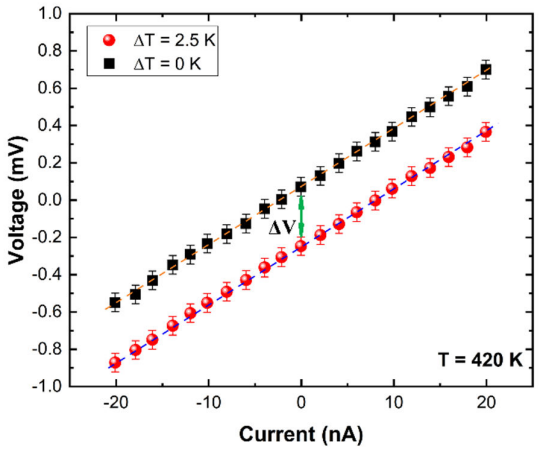

Figure 6.10. – *V-I* characteristics of InSb nanowire measured using the four-probe technique with and without applied temperature gradient of 2.5 K, which corresponds to the position of the NW schematically indicated in Figure 6.9a (d = 85 nm, T = 420 K). Generated Seebeck voltage (ΔV) indicated by the green double arrow.

The Seebeck coefficient is calculated based on the Seebeck voltage and the measured temperature difference. The Seebeck coefficient is plotted as a function of nanowire diameter in Figure 6.11b in the temperatures range 300 – 420 K. It is technically challenging to control the temperature of the heating element of the device at low ambient temperatures (T<300 K); therefore, the Seebeck voltage at low temperatures has not been measured. The highest absolute Seebeck coefficient value of -593.33 ± 30.21 μV/K is obtained for a 50 nm diameter wire at 420 K. This value is almost two times higher than the Seebeck coefficient of bulk InSb which is around -300 μV/K at 300 K[21] and InSb nanowires with a 180 nm diameter, which is around -120 μV/K at 400 K[3]. However, the Seebeck coefficient for thick nanowires (d = 100 – 160 nm) is close to that of bulk InSb.

The increase of the Seebeck coefficient with decreasing diameter agrees qualitatively with theoretical predictions from models based on single-band transport[21]. However, other models that consider multiple-band transport predict absolute increases in the Seebeck coefficient as the diameter of the nanowires decreases below 20 nm[28,29]. The magnitude of the effect depends on the effective DOS and the position of the chemical potential. Such a pronounced effect of the nanowire diameter on the Seebeck coefficient has not been observed before and is very promising for enhancing the thermoelectric efficiency. It has been previously observed that the enhancement of thermoelectric efficiency can be associated with the drastic reduction the of thermal conductivity without significantly affecting the Seebeck coefficient and electrical conductivity in the case of rough etched Si nanowires[5]. Additionally, a power factor enhancement has been observed for thin InAs nanowires[30]. The enhancement effect has been attributed to quantum-dot-like states that form in nanowires as a result of interference between propagating states and 0D resonances.

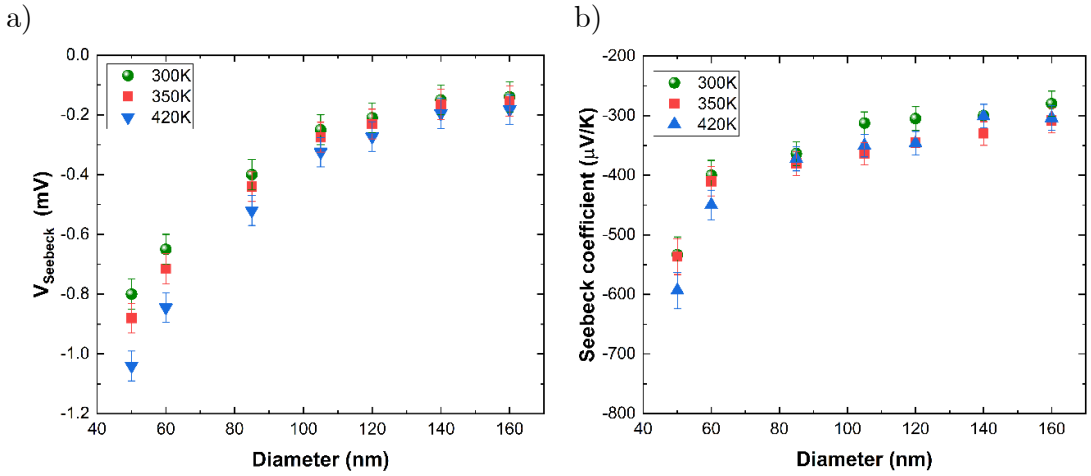

Figure 6.11. – **a,** Seebeck voltage as a function of InSb nanowire diameter at different temperatures. **b,** Seebeck coefficient of InSb NWs as a function of diameter at different temperatures.

6.6. The power factor of InSb nanowires.

The power factor ($S^2\sigma$) can be calculated from the measured electrical conductivity and the Seebeck coefficient. In Figure 6.12, the power factor as a function of nanowire diameter is plotted at different temperatures. The power factor follows the Seebeck coefficient diameter dependence. The highest measured power factor is around (0.47±0.4) mW/(m·K^2) at 420 K for a nanowire with a diameter of 50 nm.

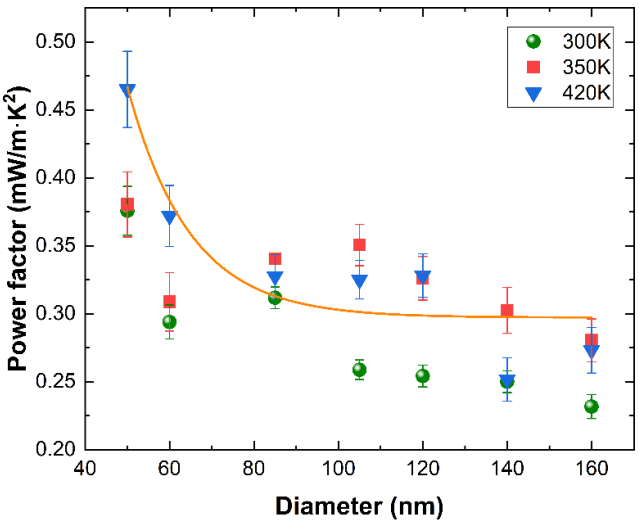

Figure 6.12. – The power factor of InSb NWs as a function of diameter at different temperatures.

The power factors measured here are higher than the highest values found in other studies at similar temperatures[2,3]. Note that the power factors have been determined without a back-gate voltage in these experiments ($V_G = 0$). The influence of the field-effect on the thermoelectric performance is shown in Figure 6.13b.

6.7. Thermoelectric efficiency of InSb nanowires.

Finally, the ZT of InSb nanowires has been estimated using the measured thermal conductivity and power factor. The thermoelectric efficiency as a function of nanowire diameter is given in Figure 6.13a.

The ZT of the measured nanowires is higher than that of bulk InSb (ZT ~ 0.15 at 300 K)[32] because of the increased Seebeck coefficient and lowered thermal conductivity. Recently published data shows that Se-doped nanowires in the range of diameters 145-195 nm possess an estimated ZT of 0.015 – 0.025 [2]. On the other hand, InSb nanowires of diameters 133-171 nm have a ZT around 0.002 – 0.005 [3]. We obtain ZT values between 0.035 and 0.04 at 300 K for undoped InSb nanowires with diameters 50 and 60 nm, respectively. To the best of our knowledge, these values are the highest reported for InSb NWs so far. Moreover, we are expecting that the thermoelectric efficiency can be further increased by tuning the chemical potential by impurity doping of InSb nanowires and/or by decreasing the nanowire diameter down to 10 nm.

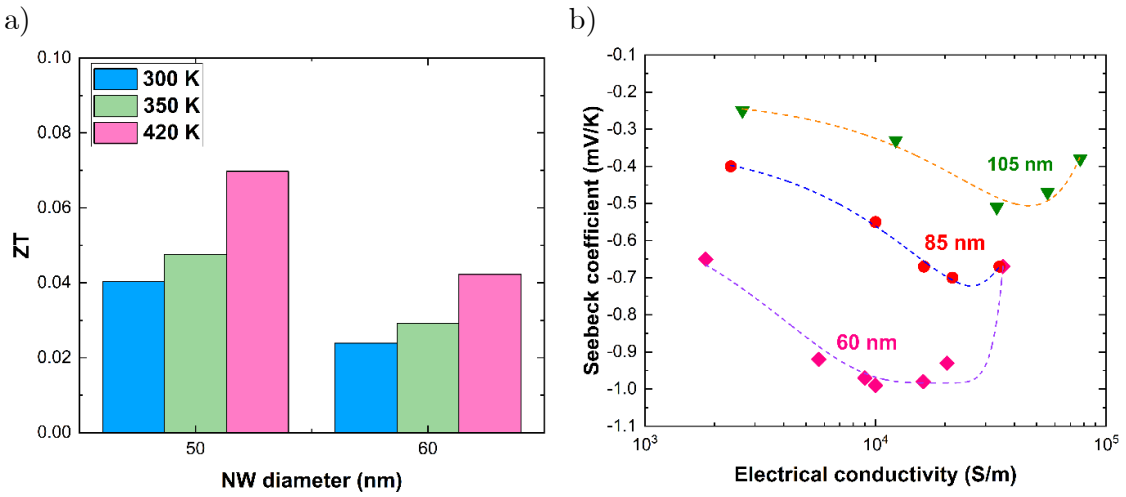

Figure 6.13. – **a,** Estimated thermoelectric efficiency (ZT) of InSb NWs as a function of diameter at different temperatures. Each column corresponds to a different temperature. **b,** Seebeck coefficient as a function of the electrical conductivity of InSb NWs. Symbols are measured data points, and lines are fits to the data following the approach suggested in reference 31.

Additionally, the back-gate voltage can be used to tune the chemical potential through the conduction band states to increase the Seebeck coefficient. The influence of the field-effect on the Seebeck coefficient is shown in Figure 6.13b. It is found that

the Seebeck coefficient can be increased by more than a factor 2. The obtained results are compared with the theoretically predicted Price curve[31]. Such thermoelectric doping curves can be applied to estimate the optimal doping concentration leading to an increase in the Seebeck coefficient. It can be seen that the Seebeck coefficient can be increased for optimal electrical conductivity. It can be concluded that the ZT is enhanced up to 0.83 (assuming a constant thermal conductivity). It requires higher electrical conductivity to change the Seebeck coefficient for thicker nanowires. Nevertheless, to make a definite conclusion, a wide range of diameters and conductivities must be examined[31,33].

6.8. Conclusions.

In conclusion, we presented a complete study of the thermoelectric properties of individual InSb NWs in the range of diameters from 50 nm to 175 nm using combined measurement techniques. Thermal conductivity measurements using suspended membranes and field-effect electrical measurements allowed the estimation of the thermoelectric efficiency of the NWs. It has been found that the thermal conductivity of only relatively thin InSb NWs can be measured reliably using the proposed measurement technique. It is found that the Seebeck coefficient can be increased by more than a factor 2 as compared to the bulk value. The obtained results are compared with the theoretically predicted Price curve[31].

The measurement technique can be applied to other semiconductor nanowires and material systems. The measured ZT values are, to the best of our knowledge, the highest reported values so far for single InSb NWs. Moreover, the thermoelectric efficiency can be further enhanced by reaching quantum confinement. Therefore, thin InSb nanowires are promising candidates as elements of prospective thermoelectric generators[34].

Appendix A6.1. Application of Landauer's formalism for heat flow in InSb nanowires.

Although the ω-k curves for acoustic phonons are nonlinear, often the Debye approximation is used, which assumes a linear and isotropic relation between the frequency ω and the wavevector k [26]. This approximation is valid for low frequencies.

The phonon density of states (PDOS) has been calculated using the Debye approximation. In the Debye model, the dispersion relation is linear, $\omega = \vartheta\,|k|$, and the density of states is quadratic:

$$D(\omega) = \frac{3 \cdot \omega^2}{2 \cdot \vartheta^3 \cdot \pi^2}, \tag{A6.1}$$

where ϑ is the speed of sound. This equation holds up to a maximum frequency called the Debye frequency ω_D ($D(\omega) = 0$). In three dimensions, there are 3 degrees of freedom per atom, so the total number of phonon modes is $3N$.

$$3N = \int_0^{\omega_D} D(\omega)d\omega \,, \tag{A6.2}$$

where N is the atomic density.

For a one-dimensional monatomic chain, the Debye frequency can be defined as follows:

$$\omega_D = \vartheta \cdot \frac{\pi}{a} = \vartheta \cdot \pi \cdot \frac{M}{L} = \vartheta \cdot \pi \cdot \lambda \,, \tag{A6.3}$$

where a is the distance between two neighboring atoms in the chain, M is the total number of atoms in the chain, L is the length of the system, and λ is the linear number density[17].

To calculate the PDOS, it is assumed that the sound velocities of longitudinal (ϑ_L) and transversal (ϑ_T) modes are equal to 3770 m/s, and 1870 m/s, respectively, and the Debye temperature of the InSb is 160 K[35].

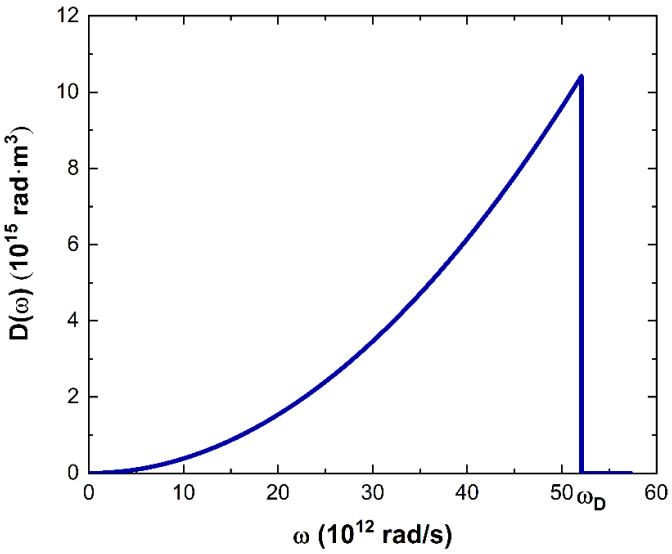

Figure A6.1. – The calculated density of phonon states using the Debye approximation.

Appendix A6.2. Electrical contact resistance.

The electrical contact resistance is estimated by comparing the resistance of an InSb nanowire obtained by two-probe (2W) and four-probe (4W) measurement techniques. These results are plotted in Figure A6.2.

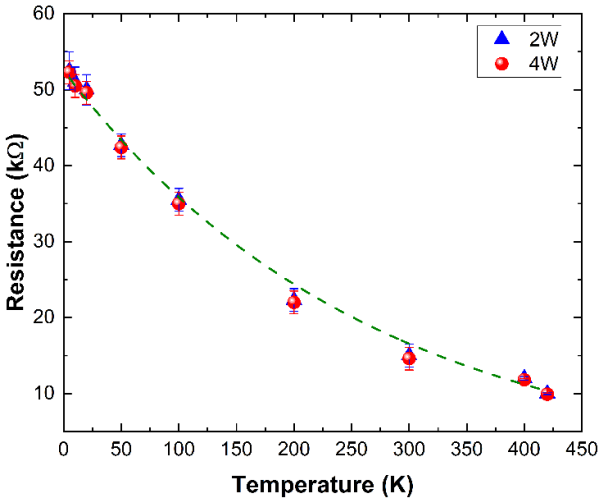

Figure A6.2. – Resistance as a function of the temperature of a typical InSb nanowire measured with 2W and 4W techniques.

Based on the achieved results, it can be concluded that the contact resistance is negligible for the measured temperature range.

Appendix A6.3. Evidence of quantum interference.

Back gate sweeps at 6 K and 10 K are shown in figure A6.3. Oscillatory behavior of the conductance of the nanowire with a length of 220 nm and a diameter of 70 nm is observed.

These oscillations are not found at higher temperatures or longer wires, which might indicate that the electron transport is taking place in the quasi-ballistic regime. Such conductance oscillations have been observed in other studies[36], where this behavior has been attributed to Fabry-Pérot oscillations[37]. It is, therefore, likely to achieve ballistic electron transport in InSb nanowires on devices with a shorter NW length and/or at a lower temperature.

An exemplary plot of electrical conductance as a function of back-gate voltage for the forward and the backward sweeps is shown in figure A6.3b. The presence of a small hysteresis observed between the forward and backward sweeps is possibly caused by heating of the wire during the measurements or due to the presence of water molecules on the silicon dioxide layer, acting as a polar field gate[26].

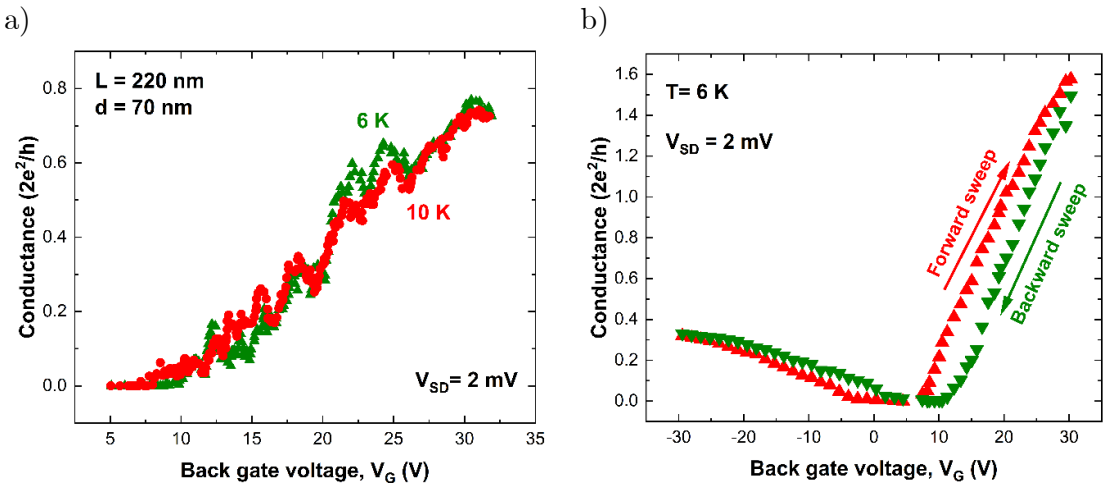

Figure A6.3. – **a,** The conductance of the InSb nanowire of length of about 220 nm and diameter of 70 nm plotted for the forward back-gate voltage sweeps. Data shown in green is measured at 6 K and red at 10 K, respectively. **b,** The electrical conductance plotted as a function of the back-gate voltage for 85 nm InSb NW. The red triangles are the data obtained from the forward sweep direction, and the green triangles are derived from the backward sweep.

Appendix A6.4. Charge carrier concentration and mobility of InSb nanowires.

As explained in Chapter 2, the charge carrier concentration and mobility can be extracted from back-gate dependencies[26]. Since InSb nanowires show bipolar behavior (Figures 6.7a and A6.3b), it is possible to extract the carrier concentration and mobility of both electrons and holes. The electron mobility and concentration of electrons are shown in Figures A6.4a and b, respectively.

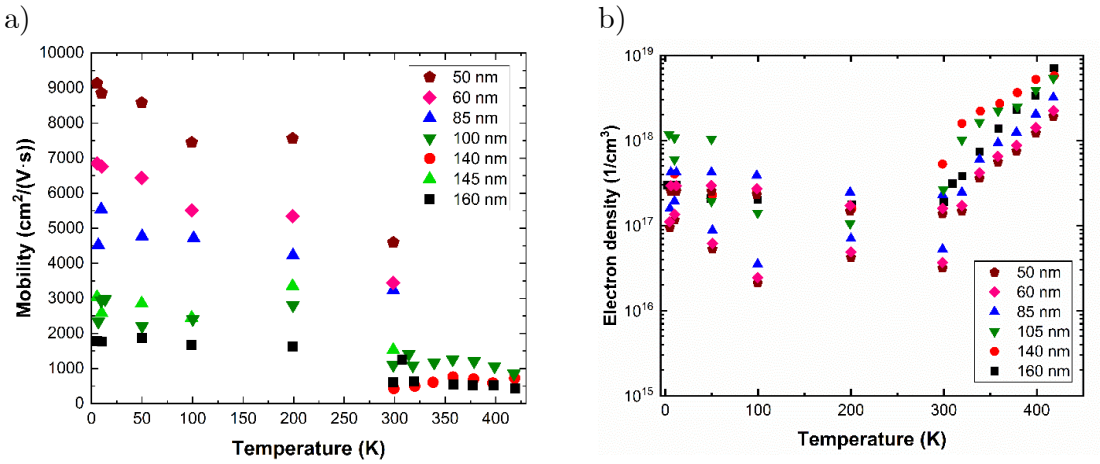

Figure A6.4. – **a,** Electron mobility of InSb NWs as a function of diameter at different temperatures. **b,** Electron density in InSb nanowires as a function of temperature.

At lower temperatures, the mobility is higher due to reduced collisions between charge carriers[38]. Higher values of the mobility can be achived at temperatures below 5 K.

The electron concentration in InSb nanowires can be tuned from degenerate (10^{18}/cm^3) at high temperatures to an intrinsic ($2{\cdot}10^{16}$/cm^3) semiconductor at low temperatures[39]. The holes mobility as a function of temperature is plotted in Figures A6.5.

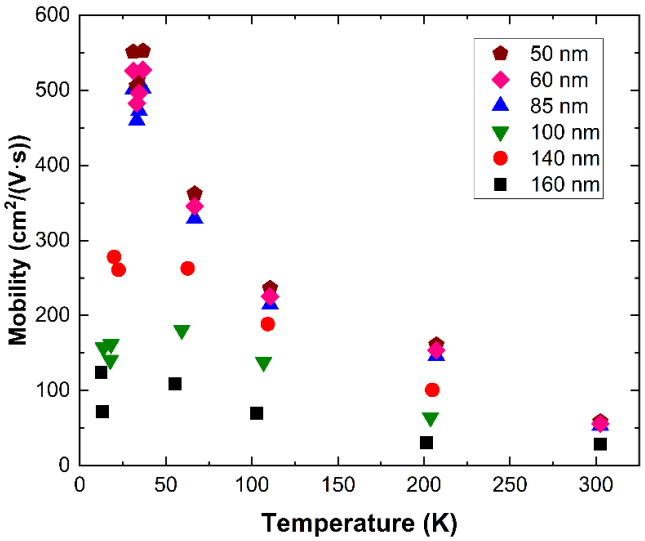

Figure A6.5. – Hole mobility as a function of temperature for InSb nanowires with different diameters.

The obtained results suggest that holes have lower mobility than electrons. The highest measured hole mobility of around 500 cm^2/(V·s) is found for a nanowire with a diameter smaller than 85 nm[39].

6.9. References.

1. Mingo, N. Thermoelectric figure of merit and maximum power factor in III-V semiconductor nanowires. *Appl. Phys. Lett.* **84**, 2652–2654 (2004).
2. Yazji, S. *et al.* Complete thermoelectric benchmarking of individual InSb nanowires using combined micro-Raman and electric transport analysis. *Nano Res.* **8**, 4048–4060 (2015).
3. Zhou, F. *et al.* Effect of growth base pressure on the thermoelectric properties of indium antimonide nanowires. *J. Phys. D. Appl. Phys.* **43**, (2010).
4. Boukai, A. I. *et al.* Silicon nanowires as efficient thermoelectric materials. *Nature* **451**, 168–171 (2008).
5. Hochbaum, A. I. *et al.* Enhanced thermoelectric performance of rough silicon nanowires. *Nature* **451**, 163–167 (2008).
6. Ryu, H. J. *et al.* Quantitative determination of contributions to the

thermoelectric power factor in si nanostructures. *Phys. Rev. Lett.* **105**, (2010).
7. Swinkels, M. Y. *et al.* Diameter dependence of the thermal conductivity of InAs nanowires. *Nanotechnology* **26**, 385401 (2015).
8. Venkateshvaran, D., Kronemeijer, A. J., Moriarty, J., Emin, D. & Sirringhaus, H. Field-effect modulated Seebeck coefficient measurements in an organic polymer using a microfabricated on-chip architecture. *APL Mater.* **2**, (2014).
9. Badawy, G. *et al.* High Mobility Stemless InSb Nanowires. *Nano Lett.* **19**, 3575–3582 (2019).
10. Koelling, S. *et al.* Characteristics of cross-sectional atom probe analysis on semiconductor structures. *Ultramicroscopy* **111**, 540–545 (2011).
11. Klamchuen, A. *et al.* Dopant homogeneity and transport properties of impurity-doped oxide nanowires. *Appl. Phys. Lett.* **98**, 053107 (2011).
12. Fernandez-Serra, M.-V. & Blase, X. *Electronic and transport properties of doped silicon nanowires*. vol. 1 (Oxford University Press, 2017).
13. Donadio, D. & Galli, G. Temperature dependence of the thermal conductivity of thin silicon nanowires. *Nano Lett.* **10**, 847–851 (2010).
14. Thermal properties of Indium Antimonide (InSb). http://www.ioffe.ru/SVA/NSM/Semicond/InSb/thermal.html.
15. Das, S. G. & Dhar, A. Landauer formula for phonon heat conduction: relation between energy transmittance and transmission coefficient. *Eur. Phys. J. B* **85**, (2012).
16. Jeong, C., Datta, S. & Lundstrom, M. Full dispersion versus Debye model evaluation of lattice thermal conductivity with a Landauer approach. in *Journal of Applied Physics* vol. 109 (2011).
17. Chen, R. *et al.* Thermal Conductance of Thin Silicon Nanowires. *Phys. Rev. Lett.* **101**, (2008).
18. Carolina Sparavigna, A. Some Notes on Boltzmann and Landauer Phonon Thermal Transport at Nanoscale. *Int. J. Sci.* **0**, 24–27 (2014).
19. Mcgaughey, A. J. H. & Kaviany, M. Phonon Transport in Molecular Dynamics Simulations: Formulation and Thermal Conductivity Prediction. (2006) doi:10.1016/S0065-2717(06)39002-8.
20. Kittel, C. Introduction to solid state physics. (Wiley, 2005).
21. Madelung, O. & Meyerhofer, D. Physics of III-V compounds. (Wiley, 1964).
22. Pandya, S. G. & Kordesch, M. E. Characterization of InSb Nanoparticles Synthesized Using Inert Gas Condensation. *Nanoscale Res. Lett.* **10**, (2015).
23. ImageJ. https://imagej.nih.gov/ij/.
24. Thelander, C., Caroff, P., Plissard, S. & Dick, K. A. Electrical properties of InAs 1-xSb x and InSb nanowires grown by molecular beam epitaxy. *Appl. Phys. Lett.* **100**, (2012).
25. Pribiag, V. S. *et al.* Electrical control of single hole spins in nanowire quantum dots. *Nat. Nanotechnol.* **8**, 170–174 (2013).
26. Gül, Ö. *et al.* Towards high mobility InSb nanowire devices. *Nanotechnology* **26**, (2015).

27. Shakouri, A. *et al.* Stable thermoreflectance thermal imaging microscopy with piezoelectric position control. 2016 32nd Thermal Measurement, Modeling & Management Symposium (SEMI-THERM) (2016).
28. Chen, I. J., Burke, A., Svilans, A., Linke, H. & Thelander, C. Thermoelectric Power Factor Limit of a 1D Nanowire. *Phys. Rev. Lett.* **120**, (2018).
29. Hung, N. T., Hasdeo, E. H., Nugraha, A. R. T., Dresselhaus, M. S. & Saito, R. Quantum Effects in the Thermoelectric Power Factor of Low-Dimensional Semiconductors. *Phys. Rev. Lett.* **117**, (2016).
30. Wu, P. M. *et al.* Large thermoelectric power factor enhancement observed in InAs nanowires. *Nano Lett.* **13**, 4080–4086 (2013).
31. Price, P. J. Theory of transport effects in semiconductors: Thermoelectricity. *Phys. Rev.* **104**, 1223–1239 (1956).
32. Bowers, R., Ure, R. W., Bauerle, J. E. & Cornish, A. J. InAs and InSb as thermoelectric materials. *J. Appl. Phys.* **30**, 930–934 (1959).
33. Tan, G., Zhao, L. D. & Kanatzidis, M. G. Rationally Designing High-Performance Bulk Thermoelectric Materials. *Chemical Reviews* vol. 116 12123–12149 (2016).
34. Cheng, Y. *et al.* New insight into InSb-based thermoelectric materials: from a divorced eutectic design to a remarkably high thermoelectric performance. *J. Mater. Chem. A* **5**, 5163–5170 (2017).
35. Helme, B. G. & King, P. J. The phonon viscosity tensor of Si, Ge, GaAs, and InSb. *Phys. Status Solidi* **45**, K33–K37 (1978).
36. Li, S. *et al.* Ballistic transport and quantum interference in InSb nanowire devices. *Chinese Phys. B* **26**, (2017).
37. Kretinin, A. V., Popovitz-Biro, R., Mahalu, D. & Shtrikman, H. Multimode Fabry-Pérot Conductance Oscillations in Suspended Stacking-Faults-Free InAs Nanowires. *Nano Lett.* **10**, 3439–3445 (2010).
38. Konar, A. *et al.* Carrier Transport in High Mobility InAs Nanowire Junctionless Transistors. *Nano Lett.* **15**, 1684–1690 (2015).
39. Seol, J. H. *et al.* Measurement and analysis of thermopower and electrical conductivity of an indium antimonide nanowire from a vapor-liquid-solid method. *J. Appl. Phys.* **101**, (2007).

Chapter 7. Nanowire-based thermoelectric generator.

7.1. Introduction. Architectures of thermoelectric generators.

As been stated in Chapter 1, the efficiency of commercially available thermoelectric devices is relatively low[1]. Nevertheless, even low-efficicent thermoelectric devices can find applications in wearable electronics and Internet of Things (IoT) devices[2,3]. Thermoelectric generators available on the market are quite large, and it is very challenging to scale them down for use in small-scale autonomous devices. Different attempts have been made to scale down and increase the efficiency of thermoelectric generators[4–9].

Nanowires are predicted to increase the Seebeck effect due to confinement of charge carriers, and can lead to a decrease in thermal conductivity due to boundary scattering of phonons leading to enhanced thermoelectric efficiency[10]. When scaling down, not only the active thermoelectric material but also other characteristics like device architecture, including the planarization layer and contacts, are essential. Various materials and designs of nanowire-based thermoelectric generators have been proposed[4–8,11,12], as summarized in Table 7.1.

In this chapter, the architecture of a nanowire-based thermoelectric generator as well as the fabrication process are proposed. The proof of concept prototype is built based on InSb nanowires and its performance has been measured.

A review of the literature shows that Si nanowires are widely used[4,6–8,11] due to the abundance of Si. However, the bulk thermoelectric efficiency (ZT) of Si is only around 0.01. In order to make Si nanowires thermoelectrically efficcient, wires have been etched such that their side facets become rough[13]. In addition, diameter modulation[14], and superlattice[15] nanowire structures have been implemented, which all have the purpose to reduce the lattice thermal conductivity, but are not the best solutions in terms of power factor. As a planarization (filling) layer, which typically has a volume fraction of about 95 %, in many cases SiO_2 is used[4,8,16]. Since it can be fabricated by different techniques, it introduces flexibility in the fabrication process. However, the thermal conductivity of SiO_2 is about 1.4 W/m·K[17], which means that the planarization layer will conduct a significant amount of heat and therefore decreases the temperature difference across the structure. Polymers are more promising for use as a planarization layer since they possess a lower thermal conductivity and thus sustain the temperature difference[18]. In some of the proposed devices[5,6,11] an airgap has been left, which has a thermal conductivity of around 0.03 W/m K[19]. However, in this case, the nanowires are suspended, resulting in a fragile construction, which makes the structure less reliable and more difficult to scale. Typically, the thermoelectric output of the devices is in the range from nW to a few μW. Such thermoelectric microgenerators (μTEGs) are potential candidates as energy harvesters for IoT sensors[20].

Table 7.1 – Overview of nanowire-based thermoelectric generators.

#	Ref.	Material	Device architecture	Filling material	Performance
1	4	Top-down Si NWs	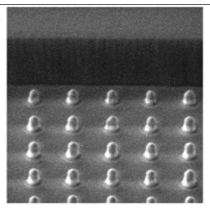	SiO_2	4.6nW/cm^2 $\Delta T = 95^oC$ Scalable
2	5	SiGe CVD grown NWs	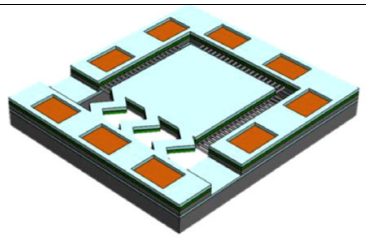	Air	7.1μW/cm^2 $T_{HOT} = 200^oC$ Not scalable
3	6	Si VLS grown NWs	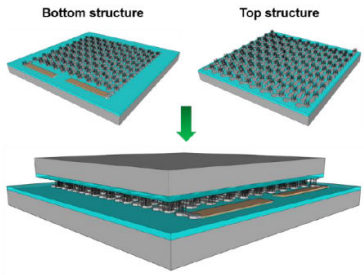	Air	Unknown Not scalable
4	7	Top-down etched Si NWs	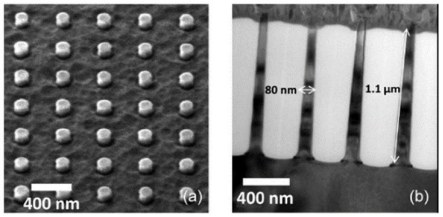	Polyimide	0.47μW/cm^2 $\Delta T = 70K$ Scalable
5	8	Si NWs	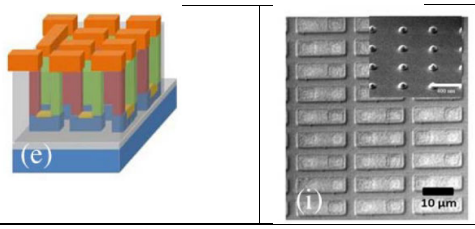	SiO_2	0.228 μW/cm^2 $\Delta T = 0.12K$ Scalable
6	9	Horizontal Si etched NWs	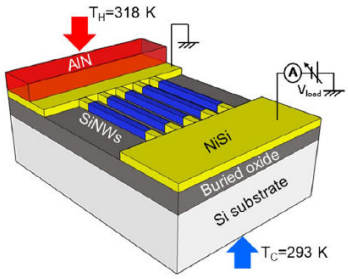	Air	27.9nW/cm^2 $\Delta T = 25K$ Not scalable

7.2. Novel nanowire-based thermoelectric generator.

Here we present a novel architecture of a nanowire-based thermoelectric generator [21]. The proposed thermoelectric generator consists of nanowire arrays of different charge carrier types (n- and p-type, like in a conventional TEGs, Appendix A7.1.) connected electrically in series and thermally in parallel. The schematic architecture of the proposed thermoelectric generator is shown in Figure 7.1a. Compared to other generators, our thermoelectric generator is envisioned to feature unique properties like flexibility and scalability. All these properties make the proposed generator suitable for a wide variety of applications, including self-charging electronic wearables and on-body devices, IoT sensors, sensors for self-driving cars, etc[20].

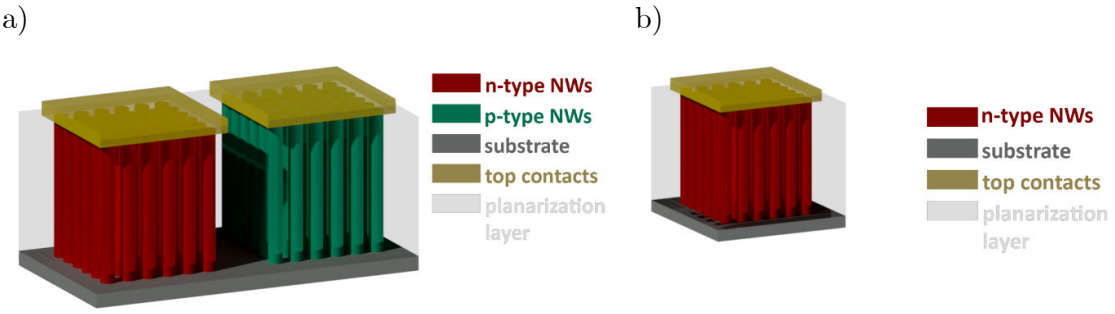

Figure 7.1. – **a,** Schematic illustration of the proposed nanowire-based thermoelectric generator. **b,** Schematic illustration of the simplified n-type nanowire-based thermoelectric generator. Essential components are indicated in the image.

Due to the technological challenges of growing differently doped nanowires simultaneously on the same substrate, we focus on one part of the device, *i.e.,* an n-type doped nanowire array (see Figure 7.1b).

7.3. Fabrication process of nanowire-based thermoelectric device.

To create the nanowire-based thermoelectric generator, the following fabrication steps are carried out: 1) nanowire growth; 2) polymer planarization; 3) polymer etching; 4) top contact metallization; 5) bottom contact deposition. The schematic overview of the fabrication process is shown in Figure 7.2.

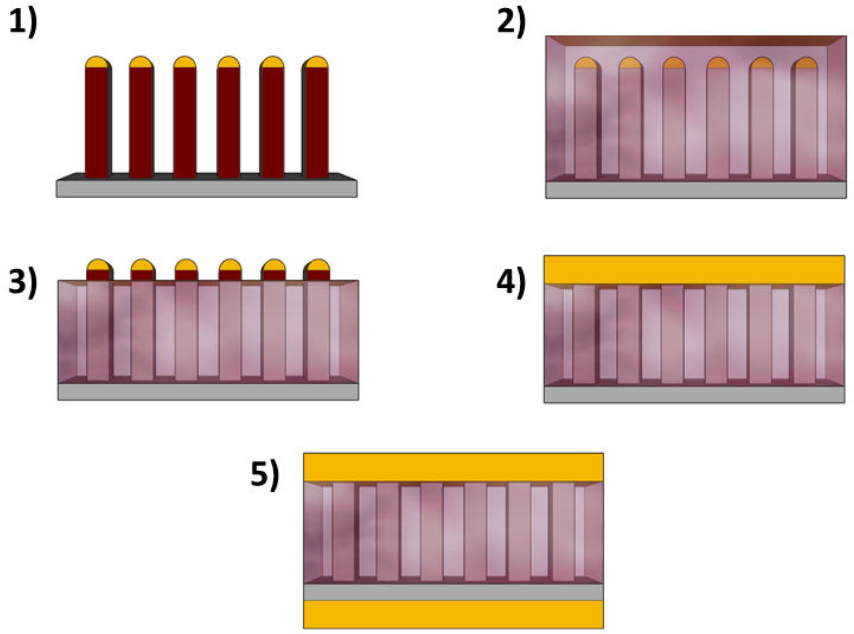

Figure 7.2. – Schematic overview of fabrication steps: 1) Nanowires are created by the metal-organic vapor phase epitaxy growth technique; 2) The polymer Bisbenzocyclobutene (BCB) spun on the nanowire sample; 3) Reactive ion etching (RIE) of the polymer layer to access the top part of the nanowire array; 4) Deposition of the top contact; 5) Bottom contact formation.

The fabrication steps are presented in detail in the corresponding sections below.

7.3.1. Nanowire growth.

The proof-of-concept prototype has been built based on InSb nanowires since, according to the theoretical predictions, this material is the best among the group III-V materials[22]. The nanowires have been grown by the SAE VLS technique[23], as described in a paper by G. Badawy *et al* [24].

Arrays of InSb nanowires with diameters of about 100 nm, length of 4 μm, and pitch of 500 nm have been formed as an active element of the proposed TEG.

7.3.2. Planarization.

In order to make a top contact to the nanowire array, a planarization step is required. For this purpose, the polymer Bisbenzocyclobutene (BCB) has been chosen. BCB is widely used in the semiconductor industry for electrical isolation and planarization[25] and is found to be the best option due to its low thermal (κ =0.29 W/m·K), and electrical conductivity (leakage current around 10^{-10}A/cm^2) and mechanical properties (tensile strength = 87 ± 9 MPa), which make this material suitable for application as planarization layer in our thermoelectric generators[26]. Before the BCB spinning, the adhesion promoter (AP 3000) is spun on top of the nanowire surface to increase the adhesion between the BCB and the nanowires. The BCB (3022-57) layer is applied via spin-coating. For the wires used in this thesis, 5 μm-thick layers have been made (see Appendix A7.2). The sample with the BCB layer is cured inside a vacuum oven at 250 ^{o}C for 1 hour with a ramping rate of 5 ^{o}C/min to avoid the formation of air pockets. After curing, the sample is placed in the RIE chamber to etch down the top BCB layer above the tips of the nanowires. A mixture of CHF_3 and O_2 gases is used to create the plasma. The etching rate of BCB using the recipe is around 110 nm/min. The resulting thickness of the BCB layer is measured using the reflectometer Filmetrics LS-DT2 with the F20-UV source. The main advantage of this measurement technique is that it does not damage the surface of the sample. The ideal height of the opened nanowire tips is around 100 nm, which can be controlled by the timing of the RIE process.

7.3.3. Top and bottom contacts.

Optical lithography is used to define a top contact layer. A negative resist ma-N440 is spun onto the sample surface at 2000 rpm for 30 s. The sample is baked at 90 ^{o}C for 5 min. The sample is exposed to UV light for 400 s in 4 cycles, using the mask of an array of squares 500 μm by 500 μm. The sample is developed using ma-D 330S for 1 min and 45 s. Before the contact deposition, the nanowires are passivated with sulphur following the process described in Chapter 4. The sample is mounted inside the evaporator and the top Cr/Au contacts are formed. An SEM image of the fabricated thermoelectric generator is shown in Figure 7.3 (see also Appendix A7.3.).

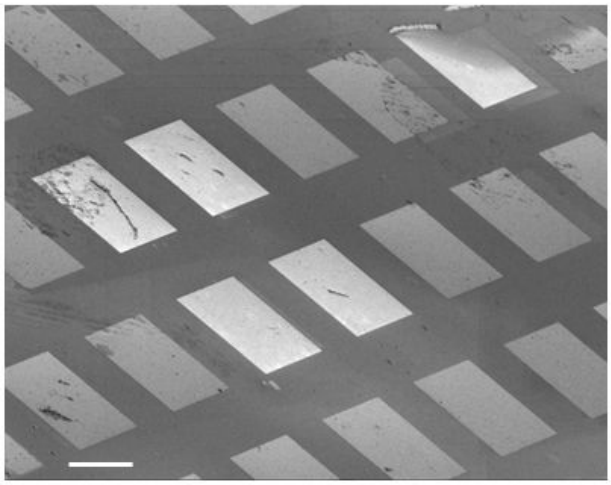

Figure 7.3. – 45°-tilted SEM image of the nanowire-based thermoelectric generator, showing the top contacts of fabricated devices. The scale bar is 500 μm.

7.4. Measurement technique.

In order to measure the performance of the nanowire-based thermoelectric generators (output voltage and Seebeck coefficient), the measurement setup shown in Figure 7.4a has been built. The setup consists of an optical microscope used for positioning the sample and the contact probes. The sample is placed on top of a Peltier element, which acts as a heater in this case. The probes are positioned in such a way that the electrical contact between top contact and the substrate (bottom contact) is established, as shown in Figure 7.4b.

Due to the leakage current that can influence the thermal and the voltage measurements, the Seebeck coefficient measurements have been split into two steps. A voltage measurement was performed using an Agilent 34401A digital multimeter. The resistance between the two probes is measured to check whether the proper electrical connection is made. Typical values of the resistance of the nanowire array are in the kOhm range.

The temperature measurements have been performed using the set of thermocouples, as schematically illustrated in Figure 7.4c. The operating principle of the thermocouple is based on the Peltier effect[27].

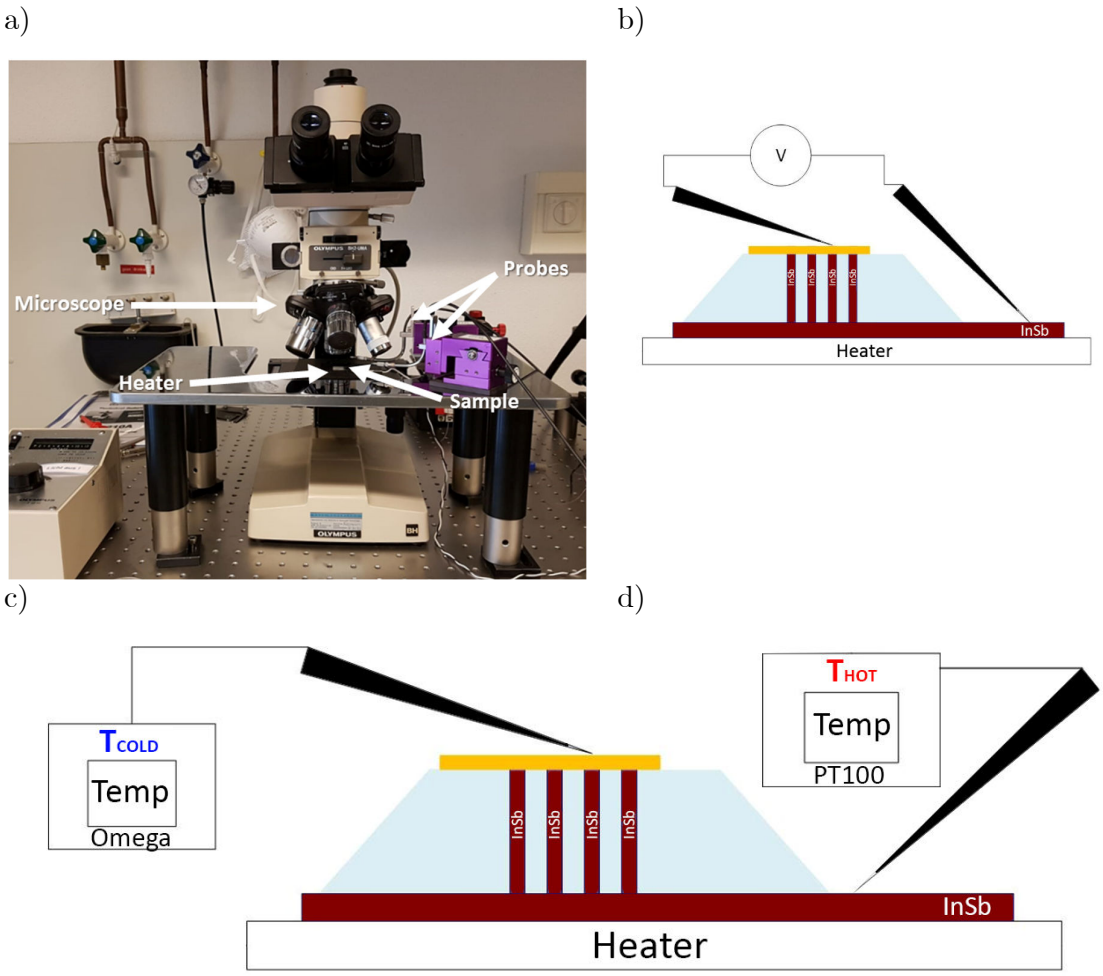

Figure 7.4. – **a,** Photo of the Seebeck characterization measurement setup of nanowire arrays. **b,** Schematic illustration of the Seebeck voltage measurements across the nanowire-based thermoelectric generator. **c,** Schematic illustration of the temperature measurements of the hot side (PT100) and the cold side (Omega) of the nanowire-based thermoelectric generator.

First, the InSb substrate without the arrays of nanowires is placed on top of the heating element to measure the temperature on the substrate, which will be the temperature of the hot side (T_{HOT}). Thermal paste is used to establish a proper thermal contact between the sample and the heating element as well as between the thermocouples and the sample. The temperature on top of the substrate is measured using the PT100 thermocouple. Then, the Omega micro thermocouple is placed on the top contact of the nanowire-based thermoelectric generator (Figure 7.4c). The temperature of the top contact is referred to as the cold side (T_{COLD}). The measurement accuracy of the PT100 and Omega thermocouples is about 1 ^{o}C for the range of 100 ^{o}C. The established ΔT across the device can be calculated as $\Delta T = T_{HOT} - T_{COLD}$.

7.5. Results and discussion.

7.5.1. The temperature difference across the thermoelectric device.

First of all, the temperature across the fabricated device is measured following the procedure described in Section 7.4. The calibrated measurements of the temperature as a function of applied heating power are shown in Appendix A7.4. Based on the results of these measurements, the temperature difference across the device is obtained. In Figure 7.5a, the temperature difference across the thermoelectric device as a function of the temperature of the Peltier element is plotted. The temperature difference is linearly proportional to the T_{HOT}, as can be seen from the plot. The average temperature difference across the nanowire-based thermoelectric device is around ΔT = 2.65 K at T_{HOT} = 57 °C. The established ΔT is changing in time since the cold side is heating up. To verify this, the temperature has been measured over 60 min, and the generated voltage is stable in this time window (Figure 7.6a).

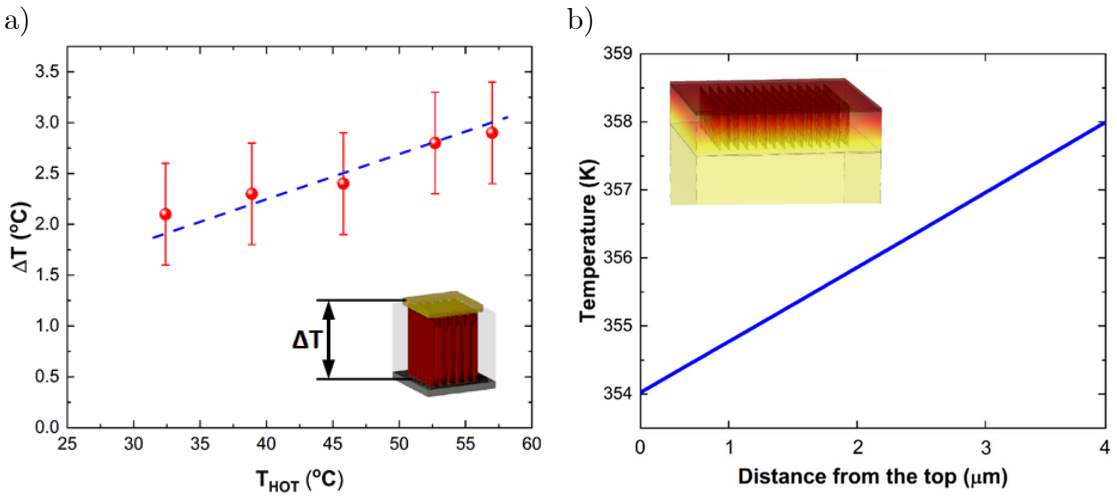

Figure 7.5. – **a,** The measured temperature difference across the nanowire-based thermoelectric generator as a function of applied temperature. **b,** The calculated temperature difference across the nanowire-based thermoelectric generator. *Inset:* simulated temperature distribution map across the thermoelectric device.

The temperature profile across the thermoelectric device has been simulated using finite element modeling in COMSOL Multiphysics. An array of 15 by 15 nanowires with 100 nm diameter and 4 μm length has been used to simplify the simulations. The model does not take into consideration convection and it is assumed here that the established temperature difference is constant over time. The calculated temperature profile is shown in Figure 7.5b.

It can be derived that the modeled temperature difference between the top side and the bottom side of the nanowire arrays is equal to 4 K at T_{HOT} = 57 °C, which is

higher than the measured value (Appendix A7.4). The simulated value is overestimated since the thermal conductivity the InSb nanowires is assumed to be equal to the bulk InSb thermal conductivity (κ_{bulk} = 18 W/m·K) and other effects like convection are not taken into account in the modeling. The measured temperature difference is probably underestimated, since there may be a thermal contact resistance between the thermocouple and the surface. The real temperature difference is, in the range 2.6 – 4.0 K. To enhance the accuracy of the measurements, the temperature measurements should be improved by using more sensitive thermocouples or making thermal images. Besides, the sample should be placed inside a vacuum chamber to avoid the effect of heat convection. Finally, the contact pads should be wirebonded to establish more reliable electrical contacts.

7.5.2. Seebeck coefficient.

The established Seebeck voltage has been measured multiple times on one of the manufactured thermoelectric devices to study the voltage output time dependence. Figure 7.6a shows the generated voltage output as a function of the number of measurements. The level of the voltage output is slightly fluctuating, and the fluctuations increase with applied heating temperature. The fluctuations of the measured temperature are coming from the heat convection. The generated voltage has been obtained from averaging over the data set (100 data points). The averaged voltage as a function of applied temperature for three devices is shown in Figure 7.6b. It is shown that the generated voltage increases linearly with T_{HOT}, which is a sign of the thermoelectric effect[28]. Three measured devices show similar behavior: the generated voltage is increasing with the applied temperature. A maximum Seebeck voltage of around -1.8 mV is measured for the applied temperature difference of around 2.95 K (Figure 7.6c). The sign of the generated voltage is negative, which agrees with the expected n-type nature of the InSb nanowires (see Chapter 6). It is found that the voltage output is similar to recently reported nanowire-based thermoelectric generators based on horizontal SiGe nanowires[5]. Nevertheless, our thermoelectric device works with a relatively small temperature difference and has a simpler architecture.

The Seebeck coefficient can be estimated from the slope of $\Delta V/\Delta T$, as shown in Figure 7.6c. These data are used to calculate the Seebeck coefficient of InSb nanowires based thermoelectric device. The measured Seebeck coefficient versus the device number is shown in Figure 7.6d. The temperature measurements give a significant uncertainty in the Seebeck coefficient, mostly due to the poor thermal contact between the thermocouple and the sample.

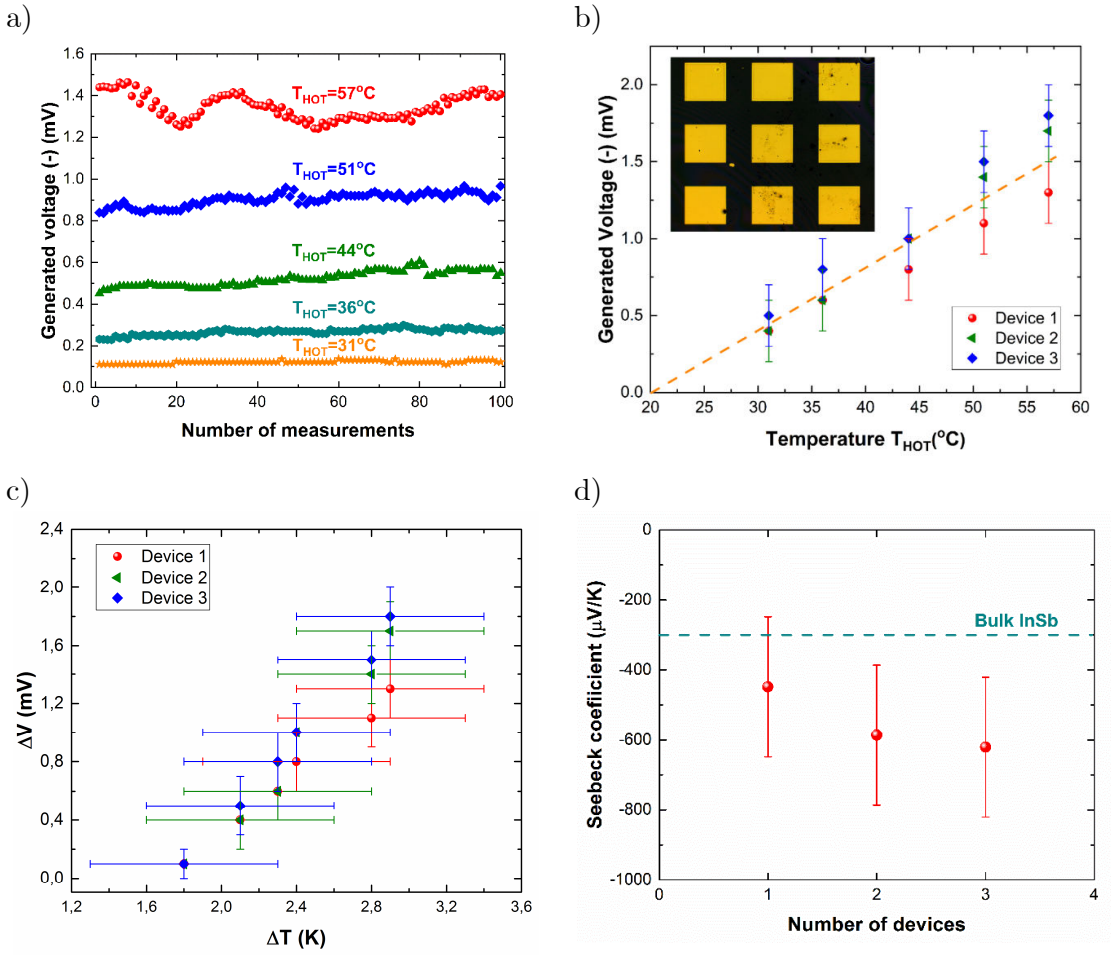

Figure 7.6. – **a,** Measured generated voltage as a function of the number of measurements. **b,** Measured generated voltage as a function of applied temperature (T_{HOT}); *Inset*: top view optical image of manufactured thermoelectric devices. **c,** Generated voltage (ΔV) as a function of the temperature difference across the thermoelectric generator. **d,** Seebeck coefficient of three measured thermoelectric devices ($\Delta T \approx 2.65$ K, $T_{HOT} = 57$ °C).

It is found that the measured Seebeck coefficient of these InSb nanowire arrays is higher than the measured Seebeck coefficient of the individual 100 nm diameter InSb nanowires (see Chapter 6). Most likely, the high Seebeck coefficient values are coming from the underestimated temperature difference across the thermoelectric device. Consequently, if the temperature difference is taken equal to the simulated one, the values of the Seebeck coefficient are closer to the values obtained for the single InSb NWs (see Appendix A7.5, A7.6, and Chapter 6).

7.6. Conclusion and outlook.

A nanowire-based thermoelectric generator has been designed and fabricated. The suggested fabrication process is relatively easy and allows scalability since all the proposed processes are well established in the semiconductor industry. Fabricated thermoelectric devices have been characterized in terms of the electrical output and the Seebeck coefficient. The voltage output has been measured and found to be stable over time. Additionally, for the first time, the Seebeck coefficient of an InSb nanowire array has been measured. However, the measured values are higher than for the single InSb NWs. This effect is probably coming from the fact that the measured temperature difference is underestimated. To establish more accurate results, the temperature measurements should be improved. The sample has to be placed inside a vacuum chamber to overcome the effect of the heat convection, and the contacts have to be wirebonded to provide sufficient electrical contact to enhance the accuracy of the measurements. Moreover, to estimate the thermoelectric efficiency (ZT) of the nanowire-based thermoelectric devices, it is essential to measure the thermal conductivity of the nanowire array, which remains challenging.

In conclusion, the proposed design and fabrication process of the nanowire-based thermoelectric device is promising for IoT sensors. Nevertheless, further optimization of the design and measurement technique is required to estimate the efficiency (ZT) of the thermoelectric energy conversion.

Appendix A7.1. Working principles of thermoelectric generation.

Generally, thermoelectric generators consist of a so-called thermoelectric unit. The thermoelectric unit is made of one n-type and one p-type semiconductor. The semiconductors are connected by a metal strip that connects them electrically in series and thermally in parallel, as shown in Figure A7.1.

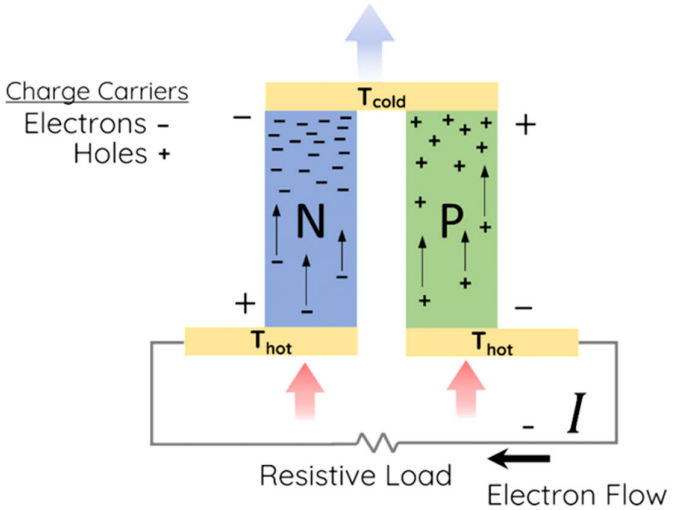

Figure A7.1. – Working principles of thermoelectric generators Apadted from reference [29].

The Seebeck effect is established due to the motion of charge carriers inside the semiconductors. Charge carriers diffuse away from the hot side of the semiconductor (electrons in case of an n-type semiconductor, and holes for a p-type semiconductor). The diffusion builds regions on the cold side where electrons and holes are concentrated. This effect generates a voltage that is proportional to the temperature difference across the semiconductors.

Appendix A7.2. BCB spinning.

Test samples have been made with different spinning speeds to get the right thickness of the BCB layer. The BCB thickness as a function of the spinning speed is shown in Figure A7.2.

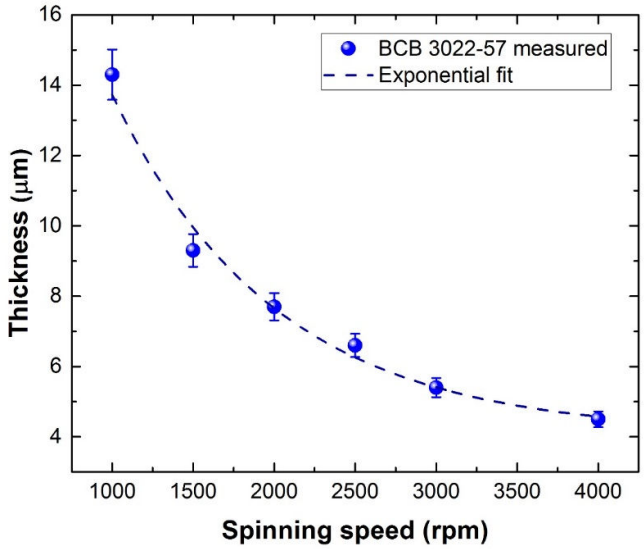

Figure A7.2. – BCB 3022-57 spinning curve and exponential fit.

Appendix A7.3. Fabricated thermoelectric device.

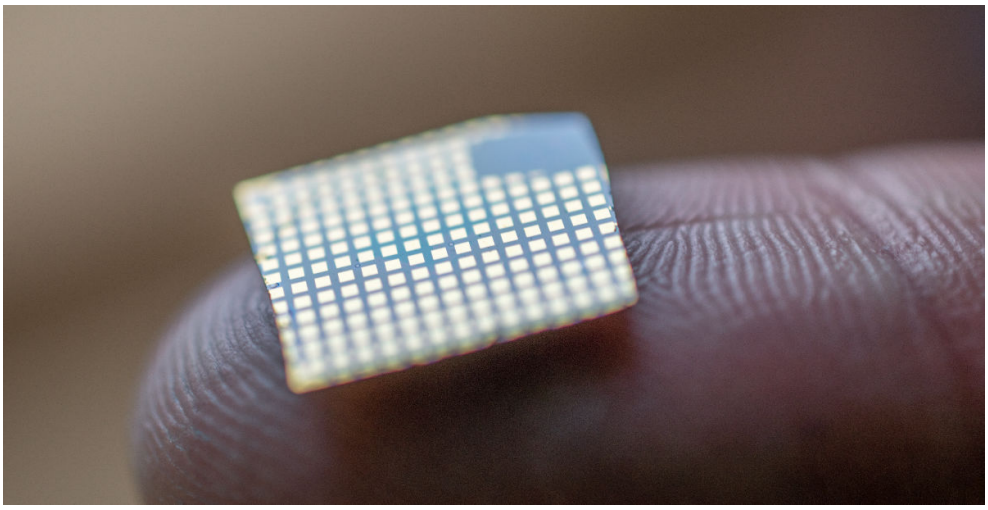

Figure A7.3. – Photo of fabricated thermoelectric devices.

Appendix A7.4. Calibration measurements of the Peltier heating element.

The calibration measurements are made to define the temperature on the hot and cold sides. The voltage as a function of applied Peltier voltage is shown in Figure A7.4.

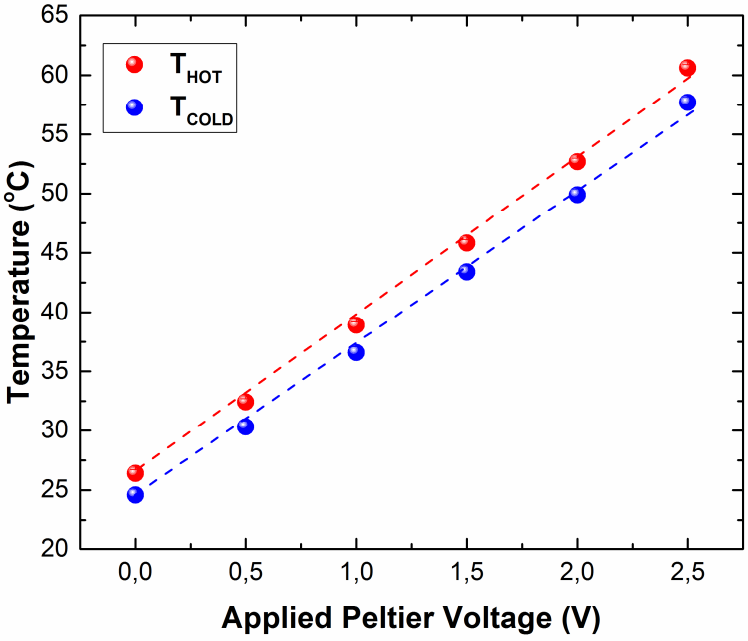

Figure A7.4. – The measured temperature on the hot (T_{HOT}) and the cold (T_{COLD}) site as a function of applied Peltier heating voltage.

The measured temperature is linearly proportional to the applied voltage at the Peltier heating element. Based on these results, the temperature difference across the thermoelectric device as a function of the applied voltage at the Peltier heating element is plotted in figure A7.5.

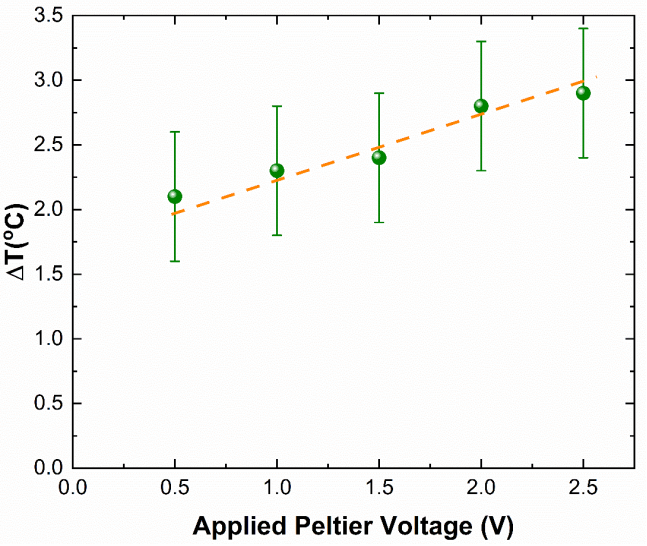

Figure A7.5. – Temperature measurements across the nanowire-based thermoelectric generator.

Appendix A7.5. Simulations of the temperature profile.

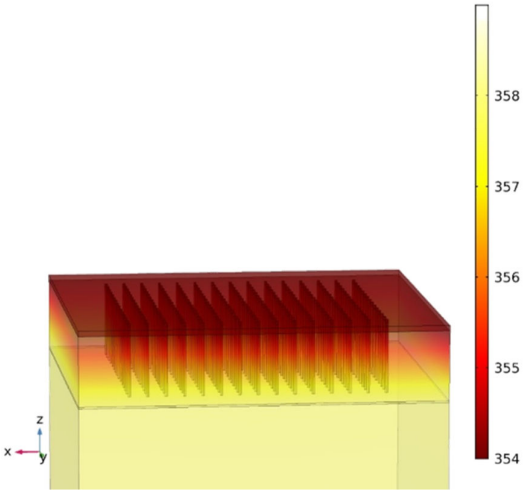

Figure A7.6. – Simulated temperature distribution across the simplified nanowire-based thermoelectric generator consisting of a 15 by 15 nanowires array.

Appendix A7.6. Seebeck coefficient.

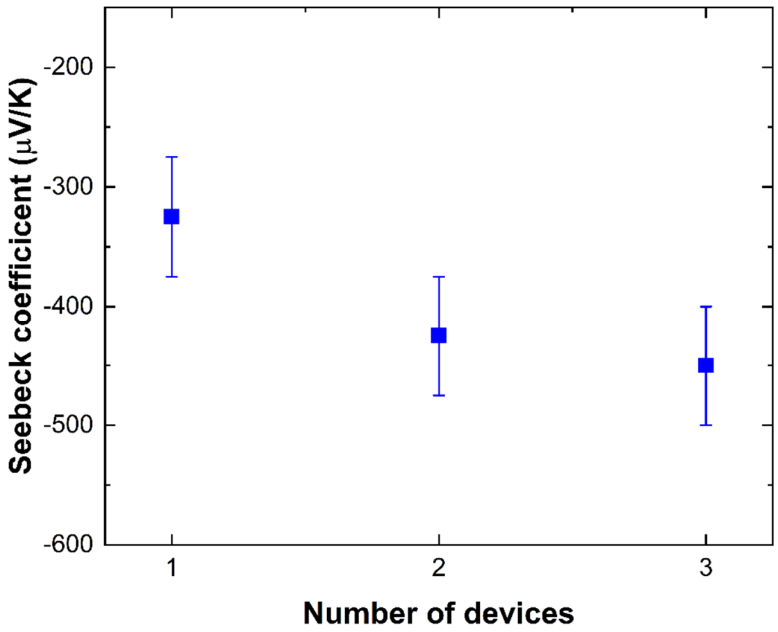

Figure A7.7. – Normalized Seebeck coefficient of InSb nanowires for the calculated temperature difference across the thermoelectric device.

7.7. References.

1. Pb/TAGS 400°C-600°C HIGH EFFICIENCY (up to 12%) TEG MODULES - Thermoelectric Generator. https://thermoelectric-generator.com/pbtags-400c-600c-high-efficiency-up-to-12-teg-modules/.
2. Narducci, D. Thermoelectric harvesters and the internet of things: technological and economic drivers. *J. Phys. Energy* **1**, 024001 (2019).
3. Nakagawa, K. & Suzuki, T. A Highly Efficient Thermoelectric Module with Heat Storage Utilizing Sensible Heat for IoT Power Supply. *J. Electron. Mater.* **48**, 1939–1950 (2019).
4. Li, Y., Buddharaju, K., Singh, N. & Lee, S. J. Top-Down Silicon Nanowire-Based Thermoelectric Generator: Design and Characterization. *J. Electron. Mater.* **41**, 989–992 (2012).
5. Domnez Noyan, I. *et al.* SiGe nanowire arrays based thermoelectric microgenerator. *Nano Energy* **57**, 492–499 (2019).
6. Dávila, D., Huber, R. & Hierold, C. Bottom-up silicon nanowire-based thermoelectric microgenerators. in *Journal of Physics: Conference Series* vol. 660 (Institute of Physics Publishing, 2015).
7. Li, Y., Buddharaju, K., Tinh, B. C., Singh, N. & Lee, S. J. Improved vertical silicon nanowire based thermoelectric power generator with polyimide filling. *IEEE Electron Device Lett.* **33**, 715–717 (2012).
8. Li, Y., Buddharaju, K., Singh, N., Lo, G. Q. & Lee, S. J. Chip-level

thermoelectric power generators based on high-density silicon nanowire array prepared with top-down CMOS technology. *IEEE Electron Device Lett.* **32**, 674–676 (2011).

9. Zhan, T. *et al.* Miniaturized planar Si-nanowire micro-thermoelectric generator using exuded thermal field for power generation. *Sci. Technol. Adv. Mater.* **19**, 443–453 (2018).
10. Hicks, L. D. & Dresselhaus, M. S. Thermoelectric figure of merit of a one-dimensional conductor. *Phys. Rev. B* **47**, 16631–16634 (1993).
11. Zhan, T. *et al.* Miniaturized planar Si-nanowire micro-thermoelectric generator using exuded thermal field for power generation. *Sci. Technol. Adv. Mater.* **19**, 443–453 (2018).
12. Caballero-Calero, O. & Martín-González, M. Thermoelectric nanowires: A brief prospective. *Scr. Mater.* **111**, 54–57 (2016).
13. Hochbaum, A. I. *et al.* Enhanced thermoelectric performance of rough silicon nanowires. *Nature* **451**, 163–167 (2008).
14. Zianni, X. & Chantrenne, P. Thermal conductivity of diameter-modulated silicon nanowires within a frequency-dependent model for phonon boundary scattering. *J. Electron. Mater.* **42**, 1509–1513 (2013).
15. Thumfart, L. *et al.* Thermal transport through Ge-rich Ge/Si superlattices grown on Ge(0 0 1). *J. Phys. D. Appl. Phys.* **51**, (2018).
16. Jones, R. E., Winters, H. F. & Maissel, L. I. Effect of Oxygen on the rf-Sputtering Rate of SiO2. *J. Vac. Sci. Technol.* **5**, 84–87 (1968).
17. Properties: Silica - Silicon Dioxide (SiO2). https://www.azom.com/properties.aspx?ArticleID=1114.
18. Huang, C., Qian, X. & Yang, R. Thermal conductivity of polymers and polymer nanocomposites. (2018).
19. Thermal Conductivity of selected Materials and Gases. https://www.engineeringtoolbox.com/thermal-conductivity-d_429.html.
20. Haras, M. & Skotnicki, T. Thermoelectricity for IoT – A review. *Nano Energy* vol. 54 461–476 (2018).
21. US4292579A - Thermoelectric generator - Google Patents. https://patents.google.com/patent/US4292579A/en.
22. Mingo, N. Thermoelectric figure of merit and maximum power factor in III-V semiconductor nanowires. *Appl. Phys. Lett.* **84**, 2652–2654 (2004).
23. Dayeh, S. A., Fontcuberta i Morral, A. & Jagadish, C. (Chennupati). *Semiconductor Nanowires. II, Properties and Applications*.
24. Badawy, G. *et al.* High Mobility Stemless InSb Nanowires. *Nano Lett.* **19**, 3575–3582 (2019).
25. Zheng, J.-F. *et al.* Novel planarization and passivation in the integration of III-V semiconductor devices. in *Optoelectronic Integrated Circuits VI* vol. 5356 81 (SPIE, 2004).
26. Dow CYCLOTENE™ 3022-57 Bisbenzocyclobutene (BCB) Electronic Resin. http://www.matweb.com/search/DataSheet.aspx?MatGUID=a73261999203463a9c26a010da0d1b37&ckck=1.

27. Thermocouple - Definition, Construction, Working Principle, and Applications. https://www.elprocus.com/what-is-a-thermocouple-definition-working-principle-diagram-applications/.
28. Seebeck, T. J. Ueber die magnetische Polarisation der Metalle und Erze durch Temperatur-Differenz. *Ann. Phys.* **82**, 1–20 (1826).
29. How Thermoelectric Generators Work | Applied Thermoelectric Solutions LLC. https://thermoelectricsolutions.com/how-thermoelectric-generators-work/.

Summary

Nowadays with the depletion of fossil fuels and the ever-increasing climate change, the quest for renewable and "green" energy sources is getting more relevant every day. Thermoelectric generators are a helpful tool to improve energy yield. These generators can directly transform waste heat into electricity. These devices can be used to improve the efficiency of existing power sources or in any other situation where heat would be wasted. Nevertheless, the low efficiency of commercially available thermoelectric generators limits their applications. Theoretically, it has been predicted that nanowires can significantly increase the thermoelectric energy conversion because not only the thermal conductivity can be reduced without a loss of electrical conductivity, but also the power factor, is expected to be enhanced due to the modified density of states.

In this thesis, the results of the experimental research of thermoelectric energy conversion in semiconductor nanowires are presented. More specifically, the thermal and electron transport through nanowires was studied using microdevices. The device using for thermal measurements is consisting of two suspended Si_3N_4 membranes with platinum meanders. The nanowire is placed in the way that it is bridging between the two membranes. The platinum meanders can be used as heaters and thermometers; thus, the thermal conductance of a nanowire can be measured.

According to Fourier's law, a temperature difference across a material results in a linear temperature profile and a thermal conductance that decreases inversely proportional to the system length. These are the hallmarks of diffusive heat flow. When phonon mean free paths exceed system dimensions, phonon-mediated heat flow may become non-diffusive. In the thesis, heat flow in ultrathin (25 nm) GaP nanowires is studied and concluded that the heat conductance is independent of nanowire length. These observations deviate from Fourier's law and are direct proof of ballistic heat flow, persisting for wire lengths up to at least 15 μm at room temperature. When doubling the wire diameter, a remarkably sudden transition to diffusive heat flow is observed. The results of the ballistic heat flow can be explained by Anderson localization in the ultrathin wires of phonons that reflect diffusely at the nanowire surface, decoupling them from ballistic phonons with very long mean free paths. The heat flow in both the diffusive and ballistic regime is modeled by Landauer's formalism. Controlled ballistic heat flow over long distances can be relevant to novel devices such as phonon transistors and phonon waveguides and may lead to new cooling solutions for computer chips.

Furthermore, the measurement technique of thermoelectric (power factor) properties of nanowires is developed. The device using for power factor characterization is consisting of two heaters and two thermometers. The nanowire is placed on the SiO_2 sample, the thermometers, as well as electric contacts, positioned in the way that they are located on top of the nanowire. A temperature gradient across the nanowire created when the heating current is applied. The presence of the temperature gradient generates a thermoelectric voltage, which can be measured by the top electrical contacts. The established temperature difference built along the nanowire is measured using the

thermometers. By knowing the generated voltage and the temperature difference, the Seebeck coefficient can be calculated. This technique has been applied to measure the thermoelectric properties of InSb nanowires experimentally. Finite element analysis simulations of the Seebeck measurement device are made and compared to the temperature profile measured by resistance thermometers and thermal reflectance imaging. The electrical conductivity and Seebeck coefficient as a function of the diameter of the InSb nanowires are experimentally studied at different temperatures. Finally, the power factor and thermoelectric figure of merit of the InSb nanowires are estimated.

Based on the obtained results, the design of a prospective thermoelectric generator has been proposed. Few prototypes of the novel thermoelectric generator based on InSb nanowires have been built and experimentally tested. The developed fabrication technique allows for scalability. The proposed design and fabrication technique of the thermoelectric generator has been patented. Additionally, higher efficient materials may be used to further increase the thermoelectric conversion. The proposed thermoelectric generator is prospective to find applications in the Internet of Things devices.

Acknowledgement

It has been a bit more than four years since the time I came to the Netherlands – the land of the giants, windmills, and tulips for my PhD project. I remember very well the first day I arrived at rainy Eindhoven in August 2015. Time flies, and now I am about to write the last pages of my PhD dissertation.

First, I would like to thank my promoter, Prof. Erik Bakkers, for allowing me to do this research project and your advice and support. I enjoyed working under your guidance. Thank you, Erik, for being the best boss.

I want to acknowledge my copromoter Prof. Peter Bobbert for giving this work a theoretical framework and for all the time you spent providing me detailed comments.

Additionally, I would like to thank Dr. Jos Haverkort for help and support.

I would like to thank my entire defense committee for the evaluation of my thesis: Prof. Ekkes Brück, Prof. Maria Loi, Prof. Thomas Schäpers, Prof. Ilaria Zardo. Thank you that you kindly accepted to be in the committee and provided valuable feedback that improved my thesis.

I would like to acknowledge the academic staff of the Advanced Nanomaterials and Devices and Photonics and Semiconductor Nanophysics group for the inspirations, and valuable discussions: Dr. Rob van der Heijden, Dr. Andrei Silov, and Dr. Marcel Verheijen.

I would like to thank Dr. Milo Swinkels, who shared with me all the secrets of thermoelectrics. It was a great pleasure working with you. Dr. Ruben Chavez, thanks a lot for your help with the thermal imaging setup.

I would like to acknowledge my colleagues at the Eindhoven University of Technology. The warmest memories I have with my officemates, labmates, colleagues, and friends: Alain, Alessandro, Antony, Claudiu, Danielle, Diana, Dick, Elham, Francesco, Ghada, Ilya, Jason, Jim, Luca, Manu, Marcone, Marco, Marvin, Maurangelo, Philipp, Roy, Saša, Sebastian, Simone, Subash, Victor, Xin, Yizhen. Thank you all for the best moments of my PhD journey.

During my PhD project, I was lucky to work with a wide range of people. Andy van der Velde, thank you for all the work you have done on the GaP nanowires. Cody Nettecoven, thank you for the very first gating experiments on InAs nanowires. Bart Goelema, thank you for your help with the development of the power factor measurements setup. Thijs van der Sande, thank you for the work you have done on InSb nanowires Tijn Swinkels, thank you for your motivation and ambitions you have put on the development of the nanowire-based thermoelectric generator. David Rodriguéz, thank you for being my first master student and for the first results on PbTe nanowires. Thank you all for willing to work under my supervision. We have become not only colleagues but friends. It was a great pleasure working with you, and I wish you good luck in your further carrier development.

Sander Schellingerhout, Max Hoskam, Vince van der Sande, Maarten Kumphuis, Jelte Schaltmann, and Mathijs Mientjes it has been a pleasure to handing the knowledge and share some essential experience with you and I wish you best of luck in the future.

Additionally, I would like to thank Innovation Space and Innovation Lab people: Mark Cox, Steven van Huiden, Mathijs Bulsink, Rachel de Greef, and Monique Grave for giving me a business-oriented mindset.

This dissertation could not have been completed without support from the NanoLab@TU/e staff members that keep cleanroom running Erik Jan Geluk for always being available for help, Barry Smalbrugge, Patrick Bax for all the support, Tjibbe de Vries, Robert van de Laar for all the helpful discussions and advices.

Thank you, Simone Krooswijk-Manche and Thérèse-Anne Botman-van Amelsvoort, for your help and for organizing awesome group-outings.

Additionally, I would like to thank Dr. Coen Jaspars and Dr. Niek Schepel for their essential help and relevant suggestions.

Ksenia, Nika, Ronis, Cyrill, Nastya, Karina, Quentin, you guys are incredible. The amount of fun I had with you the amount of support I got from you is unmeasurable. You helped me to overcome every hardship I faced during my PhD years.

I would also like to thank my Parents for their endless support and love they transmitted through over 2800 km. And to my brother Zakhar for being the best brother. Without you, I would not have been able to complete this challenge.

Dank je wel! Thank you! Большое Спасибо! Danke schön! Grazie Mille! Merci! Ευχαριστώ! Хвала! Děkuji!

List of publications

- Ballistic phonons in ultra-thin nanowires – **Vakulov D.**; Gireesan S.; Swinkels M.Y.; Chavez R.; Vogelaar T.; Gagliano L.; van der Velde A.; Torres P.; Campo A.; De Luca M.; Verheijen M.A.; Koelling S.; Haverkort J.E.M.; Alvarez F.X.; Zardo I.; Bobbert P.A.; Bakkers E.P.A.M. – *Nano Letters* (2020). – Submitted.
- Measuring the Optical absorption of single nanowires – Swinkels M.Y.; Campo A.; **Vakulov D.**; Wongjong K.; Gagliano L.; Steinvall S.E.; Detz H.; De Luca M.; Lugstein A.; Bakkers E.P.A.M.; Foncuberta i Moral A.; Zardo I. – *Physical Review Applied* (2020). – Submitted.
- US Patent (2019): 'Flexible and transparent thermoelectric generator' – **Vakulov D.**; Swinkels M.A.P.M.; Bakkers E.P.A.M.
- Thermopower characterization of InSb nanowires using thermoreflectance – Chavez R.; **Vakulov D.**; Gazibegovic S.; Car D; Kendig D.; Tay A.A.O.; Schakouri A.; Bakkers E.P.A.M. – *23rd International Workshop on Thermal Investigations of ICs and Systems (THERMINIC), IEEE.* (2017), P. 1 - 5.
- InSb nanowires for thermoelectric energy generation – **Vakulov D.**; van de Sande T.L.P.; Goelema M.G.B.; Badawy G.; Gazibegovic S.; Bakkers E.P.A.M. – In preparation.
- Electrical properties of lightly Ga-doped ZnO nanowires. – Alagha S.; Heedt S.; **Vakulov D.**; Mohammadbeigi F.; Kumar E; Schaepers T.; Isheim D.; Watkins S.; Kavanagh K. — *Semiconductor Science and Technology.* Vol.22. (2017), P.125010 - 125022.
- Electronic properties of complex self-assembled InAs nanowire networks. – Heedt S.; **Vakulov D.**; Rieger T.; Rosenbach D.; Trellenkamp S.; Grutzmacher D.; Lepsa M.I.; Schapers T. — *Advanced Electronic Materials.* Vol. 2, Issue 6. (2016). P. 1500460-1500466.
- Crystal phase transformation in self-assembled InAs nanowire junctions on patterned Si substrates. – Rieger T.; Rosenbach D.; **Vakulov D.**; Heedt S.; Schapers T.; Grutzmacher D.; Lepsa M.I. — *Nano Letters.* Vol. 16. (2016). Issue 3. P. 1933-1941.
- Electrical and optical properties of zinc-oxide films deposited by the ion-beam sputtering of an oxide target. – Dostanko A.P.; Ageev O.A.; Golosov D.A.; Zavadski S.M.; Zamburg E.G.; **Vakulov D.E.**; Vakulov Z.E. — *Semiconductors.* Vol. 48. Issue 9. (2014). P. 1242-1247.
- Nanocrystalline ZnO films grown by PLD for NO_2 and NH_3 sensor. – Ageev O.A.; Gusev E.Y.; Zamburg E.G.; **Vakulov D.E.**; Vakulov Z.E.; Shumov A.V.; Ivonin M.N. – *Applied Mechanics and Materials.* Vol. 475-476. (2014). P. 446-450.
- Study of the effect of ion-stimulated deposition assisted by a pulsed laser on the properties of zinc oxide nanocrystalline films. – Ageev O.A.; Dostanko A.P.; Dzuplin V.N.; Zamburg E.G.; **Vakulov D.E.**; Vakulov Z.E.; Alekseev A.M.; Golosov D.A.; Zavadski S.M. – *Surface Engineering and Applied Electrochemistry.* Vol. 50. Issue 5, (2014). P. 371-376.

Curriculum Vitae

Daniel Vakulov was born on 05-03-1992 in Taganrog, Russia. After finishing High School in 2008, he studied Nanotechnology at the Southern Federal University in Rostov-on-Don, Russia. He did his Bachelor Project internship at the National University of Singapore, studying the growth of complex oxide thin films by laser molecular beam epitaxy for sensing applications. In 2014 he worked at the Forschungszentrum Jülich (Germany) for six months on the research internship on Quantum magnetotransport in InAs nanowire junctions. In 2015 he graduated cum Laude, obtaining the Master of Science degree in Nanotechnology, supervised by Prof. Ageev, with a thesis on fabrication technology of gas-sensor based on nanocrystalline ZnO films. In 2015 he started a PhD project at the Eindhoven University of Technology, the Netherlands, the results of which are presented in this dissertation. He obtained the Raith Micrograph Art Award in 2018. In 2019 he attended the executive training program on New Business Development via the European Venture Programme.